Addis Ababa University

College of Technology and Built Environment

School of Chemical and Bio Engineering

Development and Evaluation of Plant-Mediated Nanocomposite Materials for the Disinfection and Removal of Heavy Metals and Fluoride from Drinking Water

---

Genet Tsegaye Araya

Supervisor: Prof. Zebene Kiflie

A Ph.D. Dissertation Submitted to the School of Chemical and Bio Engineering in Partial Fulfillment of the Requirements for the Degree of Doctor of Philosophy (Ph.D.) in Chemical Engineering (Environmental Engineering).

Addis Ababa University

Addis Ababa, Ethiopia

May, 2025

APPROVAL SHEET

ADDIS ABABA UNIVERSITY
COLLEGE OF TECHNOLOGY AND BUILT ENVIRONMENT

SCHOOL OF CHEMICAL AND BIO ENGINEERING

This is to certify that the PhD Dissertation prepared by Genet Tsegaye Araya, entitled: **"Development and Evaluation of Plant-Mediated Nanocomposite Filters for the Disinfection and Removal of Heavy Metals and Fluoride from Drinking Water"** and submitted in partial fulfillment of the requirements for Degree of Doctor of Philosophy in Chemical Engineering (Environmental Engineering Stream) complies with the regulations of the university and meets the accepted standards with respect to originality and quality.

Examining Committee:

Internal Examiner	**Signature**	**Date**
Dr.Sintayehu Mekuria		
External Examiner	**Signature**	**Date**
Prof Ajay Kumar Mishra		18 November 2025
Supervisor	**Signature**	**Date**

School Dean/ Graduate Program Coordinator

____

DECLARATION

I declare that this dissertation, entitled "Development and Evaluation of Plant-Mediated Nanocomposite Filter Materials for Disinfection and Removal of Heavy Metals and Fluoride from Drinking Water," is my own original work, conducted under the guidance of my advisor. All sources have been explicitly acknowledged. This work has not been submitted, in whole or in part, for any other degree or professional qualification. Portions of this research have been published in the *Journal of Biomass Conversion and Biorefinery* and the *Chinese Journal of Chemical Engineering*.

Author: Signature, Date:

Mrs. Genet Tsegaye Araya ______________________________

Witnessed by:

Name of student Supervisor Signature, Date:

Prof. Zebene Kiflie ______________________________

ABSTRACT

Water pollution remains a critical threat to public health and environmental sustainability, especially in low- and middle-income countries where access to efficient and affordable purification technologies is often limited. Conventional treatment systems frequently fail to effectively remove key contaminants such as pathogenic microorganisms, toxic heavy metals, and excess fluoride from drinking water. This study seeks to address these challenges by developing green-synthesized nanocomposite materials, mediated by coffee husk extract (CHE), for advanced water treatment applications including microbial disinfection and the removal of both cationic (Pb^{2+}, Cr(VI)) and anionic (F^-) pollutants.

The specific objectives of this study were to: (1) synthesize CHE-capped ZnO nanoparticles (ZnO NPs) for the disinfection of waterborne pathogens; (2) enhance the properties and antibacterial activity of bare CHE-capped ZnO NPs through the incorporation of CHE-capped Fe_3O_4/PU nanocomposites (NCs); (3) develop a CHE-capped magnetite-based pumice silica nanocomposite (CHE-M/PU/Si-NC) for lead ion adsorption; and (4) incorporate CHE-capped MgO NPs and amine functional groups into the CHE-capped M/PU/Si-NC to improve surface charge for the removal of anionic pollutants.

For the plant-mediated synthesis of nanomaterials, coffee husk extract (CHE) was obtained using an ethanol-based solid–liquid extraction method. The study focused on optimizing the synthesis parameters of ZnO nanoparticles (ZnO-NPs) by employing CHE as an effective reducing and capping agent to improve nanoparticle size control and functional performance. The optimization involved key parameters such as temperature, zinc precursor-to-CHE ratio, reaction time, and pH. Moreover, the total phenolic content of indigenous CHE, which is essential for understanding its reducing potential, was evaluated and applied throughout all synthesis procedures.

The initial formation of the synthesized nanomaterial was visually indicated by a noticeable color change. This was followed by thorough characterization using ultraviolet–visible (UV–Vis) spectroscopy, Fourier-transform infrared spectroscopy (FTIR), and X-ray diffraction (XRD). Further analysis of the physicochemical properties of the synthesized materials was carried out using scanning electron microscopy (SEM), zeta potential analysis, dynamic light scattering (DLS), Brunauer–Emmett–Teller (BET) surface area analysis, and thermogravimetric analysis (TGA).The functional performance of the nanocomposites was assessed through antibacterial activity using agar well diffusion assays, heavy metal quantification via atomic absorption spectroscopy (AAS), and fluoride removal efficiency using a fluoride ion-selective electrode.

The optimized CHE-ZnO NPs synthesis conditions included a 1:1 zinc precursor-to-extract ratio, pH 10, reaction temperature of 80 °C, and a 1h reaction time. The resulting ZnO nanoparticles exhibited strong antibacterial activity, against *S. aureus and E. coli.* Their performance was further improved by forming a composite with Fe_3O_4/PU, yielding particles with enhanced colloidal stability (zeta potential −23.8 mV), reduced size (11.2 nm), and broader-spectrum antibacterial efficacy against both *S. aureus* and *E. coli* .

For heavy metal adsorption, a green-synthesized CHE capped magnetite-pumice-silica nanocomposite (M/PU/Si-NC) was fabricated and tested for lead removal. The material demonstrated a high surface area (313 m^2/g), good thermal stability (up to 690 °C), and a strong negative surface charge (−37.7 mV). It achieved 95% lead removal efficiency at 2 g/L dosage and 100 mg/L Pb^{2+} concentration. Adsorption followed the Langmuir isotherm model with a maximum capacity of 150 mg/g and pseudo-second-order kinetics. The CHE-capped M/PU/Si-NC maintained its initial adsorption capacity after five cycles highlighting its reusability. However, its negatively charged surface limited its ability to capture anionic species such as fluoride and Cr (VI). To address this, the material was modified by incorporating magnesium oxide and amine functional groups, resulting in a positively charged surface under acidic conditions. The amine-functionalized magnetite-magnesium silica nanocomposite achieved removal efficiencies of 92% for fluoride and 86% for Cr (VI), the material maintained a relatively high removal efficiency even after multiple cycles. The adsorption behaviors for both pollutants conformed to the Langmuir isotherm and pseudo-second-order kinetics, confirming the efficiency and stability of the modified adsorbent. In conclusion, this research successfully demonstrates the potential of plant-mediated nanotechnology for the development of sustainable water purification materials. The synthesized aforementioned nanocomposites effectively addressed key challenges in water treatment by combining disinfection capabilities with the removal of hazardous ions. Their high performance, environmental compatibility, and reusability make them strong candidates for practical implementation in decentralized or resource-constrained communities, offering a scalable solution to global water quality concerns.

Keywords: phenolic compound; pollutant; drinking water; biogenic-synthesis; Water treatment.

ACKNOWLEDGEMENTS

I would like to express my sincere gratitude to God for granting me the health and perseverance to complete this study. I am deeply indebted to my supervisor, Prof. Zebene Kiflie, for his invaluable advice, guidance, encouragement, and support throughout my PhD journey. I also extend my sincere thanks to Dr. Tizazu Mekonnen and Dr. Mulissa Jida for their kind support and for helping me overcome challenges with the laboratory analysis required for my research.

I gratefully acknowledge Addis Ababa University, College of Technology and Built Environment and the Bio and Emerging Technology Institute (BETin) for sponsoring and providing the resources that enabled me to complete this PhD study.

I would also like to thank Dr. Abera Demeke, Dr. Jemal Fito, Ms. Hana Asrat, and Dr. Abiy Lolasa for their unforgettable support and encouragement.

Finally, I express my deepest gratitude to my husband Mr.Addisu Zenebe, my parents, and my children for their unwavering support, encouragement, and patience.

TABLE OF CONTENTS

LIST OF FIGURES

LIST OF TABLES

LIST OF PUBLICATIONS

1. G. Tsegaye, Z. Kiflie, T. H. Mekonnen, and M. Jida, “Synthesis and characterization of coffee husk extract (CHE)- capped ZnO nanoparticles and their antimicrobial activity,” Biomass Convers. Biorefinery, no. 0123456789, 2023, doi: 10.1007/s13399-023-049080.
2. G. Tsegaye, Z. Kiflie, T. H. Mekonnen, and M. Jida, “Synthesis and characterization of coffee husk extract (CHE)-capped Fe3O4/PU/ZnO nanocomposites with antimicrobial activity,” Biomass Convers. Biorefinery, no. 0123456789, 2024, doi: 10.1007/s13399-024-05918-2.
3. G. Tsegaye, Z. Kiflie, J. Fito Nure, and A. D. Ambaye, “Magnetite-based pumice silica nanocomposite for lead adsorption from aqueous solution: The green synthesis approach,” Chinese J. Chem. Eng., Mar. 2025, doi: 10.1016/J.CJCHE.2025.01.013.
4. G. Tsegaye, Z. Kiflie, T. H. Mekonnen, and M. Jida, “Amine-functionalized magnetic bio-nanocomposite for fluoride and chromium removal in water Genet,” *Mater. Today Sustain.*, p. 100130, 2025, doi: 10.1016/j.rechem.2025.102685.

LIST OF ACRONYMS

ANOVA	Analysis of variance
AOPs	Advanced oxidation processes
APTES	Amino propyltriethoxysilane-modified silica gel
At-PU	Acid treated pumice
BA	Bagasse ash
BET	Brunauer-Emmett-Teller
CH	Coffee husk
CHE	Coffee husk extract
CHE-Si	CHE-capped SiO_2 NPs
DBP	Disinfection by product
DI	Deionized
DLS	Dynamic light scattering
DTA	Differential thermal analysis
DTG	Derivative Thermogravimetry
EDA	Ethylenediamine
EDS	Energy dispersive spectroscopy
FE-SEM	Field emission scanning electron microscopy.
FTIR	Fourier transform infrared spectroscopy
IPD	Intraparticle diffusion
NC	Nanocomposite
NZI	No zone of inhibition
PFO	Pseudo-first-order

PSO	Pseudo-second-order
PU	Pumice
SEM	Scanning Electron Microscopy Analysis
Si-NPs	Silica nanoparticles
Sol-Si-NPs	Sol gel synthesized silica nanoparticles
TEM	Transmission electron microscopy
TEOS	Tetraethyl orthosilicate
UV-Vis	Ultraviolent-visible spectrophotometer
WASH	Water, Sanitation, and Hygiene
WHO	World Health Organization
XRD	X-ray diffraction
XRF	X-ray fluorescent

CHAPTER ONE

1. INTRODUCTION

1.1. Background and justification

Water is the most abundant source of necessary substances for all life on Earth and has been a driving force in human civilization's evolution. However, the world is currently facing a severe water shortage, affecting 1.1 billion people globally [1]. The primary causes of water shortages include climate change, leading to altered weather patterns like droughts and floods, increased pollution, and excessive human water use. Water resources can become polluted due to various natural and human-made factors. Natural sources of pollution include volcanic activity, soil erosion, biological processes, and the weathering of rocks and minerals. One significant natural pollutant is fluoride, which becomes harmful at high concentrations (above 1.5 mg/L) [2].

Regions with high fluoride levels often coincide with areas of volcanic or geothermal activity, such as the mountainous regions from Iraq and Iran to Syria, Turkey, Algeria, and Morocco, parts of the United States, Europe, and the former Soviet Union, as well as along the East African Rift Valley, including Ethiopia, Eritrea, and Malawi [3]. In the Ethiopian Rift Valley, groundwater fluoride levels exceed the WHO standard at 6.03 mg/L [2] as shown in Fig.1.1. Excessive fluoride exposure can lead to various health problems, including dental fluorosis, skeletal fluorosis, tooth decay, and bone deformities. Additionally, fluoride can cause non-skeletal fluorosis by damaging red blood cells, ligaments, sperm, the thyroid gland, and muscle tissue, resulting in muscle weakness [3].

Anthropogenic pollutant sources include landfills, fuel combustion, street run-off, sewage, agricultural activities, mining, and industrial pollutants [4]. Among these, wastewater pollutants, particularly heavy metals and pathogens, are of significant concern [5]. Over 50 elements can be classified as heavy metals, 17 of which are extremely toxic and readily accessible [6]. Particularly in Ethiopia, toxic heavy metals such as copper (Cu), manganese (Mn), zinc (Zn), chromium (Cr), cadmium (Cd), nickel (Ni), lead (Pb), iron (Fe), and arsenic (As) are produced by various industries, including textile and garment, tanning, dye, and industrial parks [7]. Additionally, agriculture, fuel stations (using leaded petroleum products), and garage operations contribute to heavy metal pollution [8]–[10]. These heavy metals pollute groundwater and surface waters, including rivers, leading to significant pollution in downstream areas where the water is used for domestic purposes and irrigation [11]. Due to their non-biodegradability, mobility, toxicity, and bioaccumulation potential in the liver, kidney, and other human organs, these well-known toxic heavy metals pose serious global threats to public health [12].

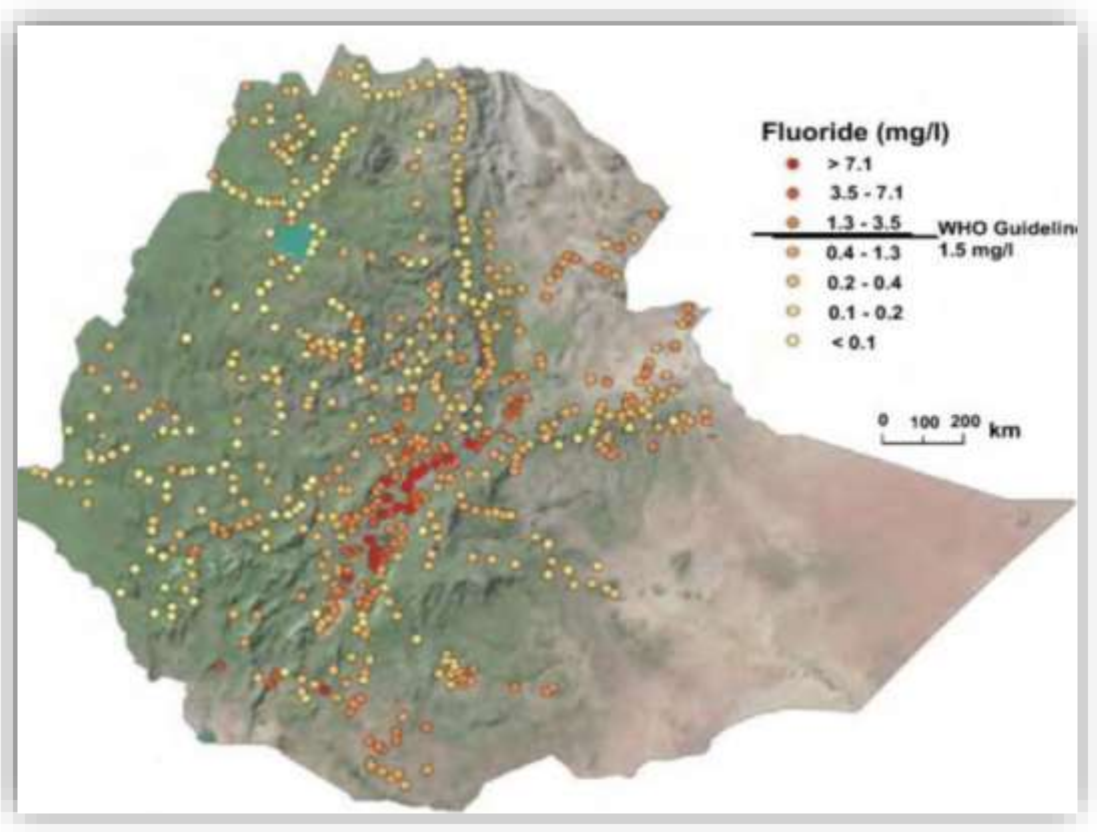

Fig.1. 1. Fluoride distribution map of Ethiopia [13]

Other anthropogenic water pollutants include pathogens, originating from human waste, animal waste, wildlife excreta, and waterfowl droppings [14]. Fecal contamination, often resulting from poor sanitation, leads to the proliferation of *E. coli*, a bacterium that can pollute water bodies and beaches [15]. The E. coli O157:H7 strain, in particular, produces a potent toxin that damages the intestinal lining, causing severe illness, including bloody diarrhea [15]. In Ethiopia, poor Water, Sanitation, and Hygiene (WASH) practices contribute significantly to the national disease burden, with diarrheal diseases accounting for 70% of cases [16]. This challenge affects both rural and urban communities. Although small-scale and household water treatment devices have been widely promoted globally, their adoption in Ethiopia remains low. Consequently, access to safe drinking water is extremely limited [17].

To mitigate the impact of these pollutants, various water treatment technologies have been developed. These include chemical precipitation, ion exchange, adsorption, membrane filtration, reverse osmosis, solvent extraction, and electrochemical treatment. However, many of these methods are costly and energy-intensive [18]. Adsorption emerges as a promising technique due to its low cost, and ease of operation. Adsorbents, such as activated carbon, zeolite, and various waste materials, can remove pollutants [19]. However, the adsorption efficiency of the aforementioned conventional adsorbent mechanisms is low. As a result, finding more efficient adsorbents has become critical [20]. The use of nanomaterials in wastewater treatment has recently received significant attention. These are natural, incidental, or manufactured materials with particles ranging in size from 1 nm to 100 nm. Nanostructured adsorbents offer higher surface area, higher efficiencies, and faster adsorption rates in water treatment compared to conventional materials [21]. Some of the nano-based materials for water and wastewater treatment include nano-sorbents, metal oxide nanoscale materials, polymer-based nano-sorbents, nano-scale membrane materials (nanomembranes), carbon nanotubes (CNTs), and silver nanoparticles (AgNPs).

However, some studies have reported that nanoparticles can dissolve into toxic ions, posing risks to human and environmental health [22]. To mitigate this issue, several strategies can be employed: replacing toxic species with less toxic elements, capping nanoparticles with a shell [23], and adopting green synthesis methods. Green synthesis involves using plants or plant parts for bio-reduction of metal ions into their elemental form within the 1-100 nm size range and stabilizing their size, as well as using bio-based precursors for nanoparticle production [24]. Additionally, the incorporation of natural surfactants during nanoparticle synthesis can act as stabilizers, inhibiting overgrowth and preventing aggregation/agglomeration in colloidal synthesis, ultimately affecting the toxicity of nanoparticle dispersions [25].

Therefore, the combination of nanoparticles and biotechnology is crucial for implementing these improvement strategies in the synthesis of nanomaterials for wastewater adsorption. Nanotechnology offers numerous benefits and applications for enhancing water quality for human consumption and promoting sustainability [26]. Consequently, significant efforts are being directed towards developing novel strategies for synthesizing various types of nanoparticles with specific compositions and sizes from biological sources for wastewater treatment applications [27].

As a result, in this study, the nano-biotechnology approach was used to synthesize the major heavy metal and fluoride adsorbent (Silica NPs) and disinfectant (ZnO-NPs) nanomaterials. The primary reason for selecting ZnO for this study is that it has strong activity even in small amounts, is regarded as a good antibacterial agent due to its stability under harsh processing conditions, and is considered a safe material for humans and animals. It has greater durability, selectivity, and heat resistance, can treat water without forming disinfection by product (DBP), and is significantly less expensive than other disinfection mechanisms [28]. Silica nanoparticles were selected for this study due to their low toxicity, biocompatibility, environmental friendliness, ease of modification, high recovery rate, resistance to microbial growth, and outstanding surface properties [29]. Furthermore, we will extract the precursor of silica nanoparticles from agricultural waste (bagasse), as bio-based economies and the use of renewable biomass as raw materials have recently been identified as viable solutions to the problems associated with local and global pollution [29].

Silica and ZnO nanoparticles have traditionally been synthesized using various chemical and physical methods. While some research has explored green synthesis methods for ZnO nanoparticles utilizing plant extracts, no study has combined magnetite pumice to enhance plant-mediated CHE-capped ZnO-NPs. Coffee husk, a rich source of bioactive phenolic compounds [30], offers a promising reducing and capping agent for ZnO nanoparticle synthesis in disinfection applications. Pumice, a highly porous material with an average porosity of 90 % , exhibits excellent chemical, thermal, and mechanical stability and initial buoyancy, making it an ideal support [31]. Similarly, for plant-mediated synthesized Si-NPs, no research has been conducted on incorporating magnetite pumice nanocomposite for the immobilization and regeneration of CHE-capped silica nanoparticles derived from bagasse ash, utilizing phenolic compounds from CHE as a replacement for chemical stabilizing agents. This dissertation focuses on the removal of heavy metals (Pb & Cr(VI)) and fluorides from drinking water using magnetic pumice-supported SiO_2 for cationic pollutants and amine-functionalized magnetic pumice magnesium silicon oxide nanocomposites for anionic pollutants, as well as the disinfection of *E. coli* and *S. aureus* using magnetic pumice-CHE-capped ZnO NCs.

1.2. Problem statement

A critical water crisis looms in Ethiopia, as highlighted by a survey from the Ministry of Water Resources. The data reveals a staggering reality: 33 million Ethiopians lack access to clean water, and sanitation facilities are inadequate for a further 89 million [16], [32]. This situation is particularly dire in rural areas where communities are heavily reliant on rivers and lakes as their primary sources of drinking water. Unfortunately, these water sources are often severely contaminated with harmful E. coli bacteria and heavy metals [33]. These combination of limited access to clean water and inadequate sanitation poses a significant public health risk.

In Addis Ababa, research by Belete found the average Pb^{+2} concentration in drinking water from the Akaki, Legedadi, and Gefersa sub-systems to be 62.37 μg/L, significantly exceeding the WHO's recommended limit of 10 μg/L [34]. This elevated exposure poses a serious health risk, particularly to children, with an estimated 20% expected to have blood lead levels above the safe threshold. Furthermore, research by Debebe documented high levels of lead accumulation in Chamo Lake, highlighting the widespread nature of this environmental pollutant [35].Studies have documented concerning levels of chromium contamination in various water bodies across Ethiopia. Such as, Alemu & Gabbiye reported that chromium levels in the Abay River near the Habesha Tannery discharge point (8.420 mg/L) drastically exceeded the WHO's safe limit for drinking water (0.05 mg/L) [36]. Similarly, Gebreyohannes & Asgedom found elevated chromium levels in the Ellala River in Mekelle, surpassing the WHO standards [37]. Further evidence of chromium contamination comes from studies in the Akaki River, Gondar City, and Akaki groundwater [38]. In addition to chromium, fluoride contamination poses a significant challenge in many regions, particularly in the Rift Valley (Fig.1.1) where deep wells are the primary source of drinking water. Demelash et al. found that fluoride levels in groundwater often exceed the WHO's recommended limit of 1.5 mg/L [2]. This necessitates the development and implementation of cost-effective water treatment technologies to ensure safe drinking water access from these valuable resources.

One of the difficulties in developing an antibacterial agent, and a limitation of conventional disinfection methods, is their inability to effectively eliminate water pathogens and the formation of disinfection by-products (DBPs) [39]. To address these challenges, this study prepared CHE-capped Fe_3O_4/PU/ZnO NC, which is easily recyclable and separable from water after disinfection, does not form DBPs, and exhibits efficient activity even in small amounts due to its large surface area [28]. As a result, this research synthesized novel, sustainable drinking water purification materials by combining CHE-capped Fe_3O_4/Pu/Si NC for the removal of fluoride and heavy metals from water and CHE-capped Fe_3O_4/PU/ZnO NC for water disinfection.

1.3. Objective

1.3.1. General Objective

The general objective of the present study is to synthesize and characterize plant-mediated nano-composite filter materials for disinfection and removal of heavy metals (lead ion and hexavalent chromium) and fluoride from drinking water.

1.3.2. Specific objectives

a. To synthesize and characterize coffee husk extract (CHE)-capped ZnO nanoparticles and evaluate their antimicrobial activity.

b. To synthesize and characterize CHE-capped Fe_3O_4/PU/ZnO nanocomposites, evaluate their antimicrobial activity, and compare it with that of bare CHE-capped ZnO-NPs.

c. To synthesize and characterize plant-mediated magnetite-based pumice silica nanocomposite for lead adsorption from aqueous solution.

d. To synthesize and characterize plant-mediated amine-functionalized magnetite-based pumice magnesium silica nanocomposite for hexavalent chromium and fluoride adsorption from aqueous solution.

1.4. Scope of the Study

This study focuses on the laboratory-scale development of a hybrid drinking water purifier capable of effectively removing heavy metals (chromium and lead), fluoride, and bacterial contaminants (*S. aureus* and *E. coli*) from polluted water sources. The work emphasizes the synthesis and batch-type performance evaluation of the purification system using locally available and sustainable materials. The scope of the study is limited to laboratory experimentation and does not extend to large-scale field implementation.

1.5. Significance of the Study

This research is significant for several reasons. It aims to improve access to safe drinking water through the development of an effective and affordable household purification system. The study also promotes environmental sustainability by utilizing agro-industrial solid wastes in the development of filter materials, reducing pollution and encouraging resource recycling. Additionally, by offering a low-cost alternative to commercial water treatments, the system can help reduce healthcare expenses associated with waterborne diseases, thus contributing to economic improvement. Furthermore, the findings can provide valuable insights for policymakers in developing guidelines and strategies that enhance the use of alternative water sources and promote sustainable water treatment practices.

1.6. Structure of the dissertation

Chapter One

This chapter introduces the issue of water scarcity at both global and national levels, provides an overview of the sources of water pollutants along with the target pollutant of the study, and presents a general introduction to existing water treatment technologies. It also outlines the problem statement, research scope, significance, and objectives of the dissertation.

Chapter Two

This chapter presents a literature review on water pollution in the country, with a specific focus on pollution caused by the study's target pollutants Cr (VI), Pb^{2+}, F^-, and pathogens such as E. coli and S. aureus and their associated health impacts. It summarizes existing water treatment technologies, including adsorbents for the removal of cationic and anionic pollutants, as well as disinfection methods for pathogens. The chapter also discusses nanomaterial-based adsorbents, nanoparticle synthesis methods, adsorption kinetics and isotherms, and adsorbent reusability. It concludes by identifying current technological gaps and highlighting how the present research aims to address them.

Chapter Three

Chapter Three details the extraction of phenolic compounds from indigenous coffee husk, the

synthesis of ZnO nanoparticles using coffee husk extract (CHE) as a reducing agent, and the characterization of the synthesized nanoparticles. It also investigates the effect of synthesis parameters on plant-mediated CHE-capped ZnO nanoparticles and evaluates their antimicrobial activity.

Chapter Four

Focuses on the synthesis and characterization of coffee husk extract (CHE)-capped Fe_3O_4/PU/ZnO NCs, assessing their antimicrobial activity. The chapter compares the properties of bare CHE-capped ZnO-NPs with those of the magnetic pumice nanocomposite-incorporated ZnO nanoparticles and evaluates their antimicrobial properties.

Chapter Five

Chapter five deals with the synthesis and characterization of plant-mediated silica nanoparticles derived from bagasse ash, comparing their properties to those of sol-gel synthesized silica nanoparticles. The chapter then explores the enhancement of these silica nanoparticles by incorporating them into magnetite-based pumice silica nanocomposites for the removal of lead ions from aqueous solutions. Furthermore, it evaluates the adsorbent's Pb^{2+} removal efficiency in batch mode, analyzes adsorption isotherms and kinetics to understand the adsorption process, and investigates the adsorbent's reusability

Chapter Six

Details the synthesis and characterization of amine-functionalized CHE-capped Fe_3O_4/PU/Mg@SiO_2 nanocomposites. This chapter investigates the impact of amine functionalization and the incorporation of MgO NPs on the surface charge properties of the magnetite-based pumice silica nanocomposite. It evaluates the adsorption performance of these modified nanocomposites for the removal of anionic pollutants F^- and Cr (VI) and assesses their reusability.

Chapter Seven

Provides a comprehensive summary of the conclusions drawn from the study and offers recommendations for future research.

CHAPTER TWO

2. LITERATURE REVIEW

2.1. Water pollution overview

Water pollution is one of the most pressing global environmental challenges, affecting both developed and developing nations [40]. According to the United Nations World Water Development Report (2023), nearly 80% of the world’s wastewater is discharged into the environment without adequate treatment, contaminating rivers, lakes, and groundwater [41]. An estimated 2 billion people rely on drinking water sources that are contaminated with feces, leading to the transmission of diseases [42]. Furthermore, industrialization and urbanization have intensified the release of chemical pollutants, including heavy metals, pesticides, and pharmaceutical residues, into aquatic environments [43].

Globally, the major causes of water pollution include industrial effluents, agricultural runoff, domestic sewage, mining activities, oil spills, and improper waste disposal [44]. Agricultural practices, in particular, contribute large quantities of nitrogen and phosphorus from fertilizers, leading to eutrophication, which depletes oxygen and disrupts aquatic ecosystems [45]. Industrial discharges introduce toxic metals such as lead, chromium, and mercury, while untreated municipal wastewater adds pathogens and organic matter [46].

The effects of water pollution are wide-ranging and severe. Contaminated water poses serious public health risks, contributing to millions of deaths annually, especially in low-income countries[47]. Environmentally, it leads to the degradation of aquatic habitats, loss of biodiversity, and disruption of the food chain [48]. Economically, it increases the cost of water treatment and reduces agricultural productivity due to the use of polluted irrigation water [49]. Overall, the increasing levels of global water pollution underscore the urgent need for sustainable water management strategies, effective wastewater treatment technologies, and strengthened environmental regulations to safeguard human health and ecosystem integrity

2.2. Water pollutants in Ethiopia

Ethiopia, known as the "water tower of East Africa," faces a paradox. Despite abundant water resources, only 42 % of the population has access to clean water. This disparity is further compounded by the fact that just 11 % of its population benefit from adequate sanitation services [50]. This limited access to clean water and proper sanitation poses a significant public health risk, contributing to the spread of waterborne diseases such as diarrhea, cholera, typhoid, and dysentery.

One major threat comes from toxic heavy metals like lead (Pb), arsenic (As), chromium (Cr), and nickel (Ni) contaminating water sources. Studies have shown high levels of these metals in tap water from Gullele and Akaki-Kality sub cities, linked to an increased risk of cancer [51]. Lead contamination is another widespread issue. Even after conventional treatment, lead levels in tap, lake, and river water exceed WHO standards [52]. The ineffectiveness of these treatment plants in removing heavy metals underscores the urgent need for innovative solutions. Most conventional water treatment systems are limited in their capacity to remove heavy metals to handle heavy metal contamination, necessitating the development of portable water purifiers for individual use.

Pathogenic contaminants pose an additional substantial danger to water quality. Contaminants from urban garbage and animal feces wash into water sources during rainfall. Over half of rural communities rely on unimproved surface water for drinking [53]. The situation is even more dire where water sources are shared with livestock. Unsafe and inadequate water supply, coupled with poor sanitation, leads to high rates of illness and death, especially in rural areas [42]. Diarrhea remains a leading cause of death among children under five, accounting for 23 % of all under-five deaths (more than 70,000 children per year) [33]

Another significant water quality issue in Ethiopia is fluoride contamination. This naturally occurring pollutant can be found in high concentrations (above 1.5 mg/L) in rift valley waters. The Ethiopian Rift Valley, a seismically active region, stretches across the country from south to north. This area features active volcanoes in the Danakil Depression in the north and young volcanic rocks in the middle and southern parts of the rift valley. Fluoride levels in the rift valley lakes consistently exceed the WHO recommended limit [54]. Shala (264.0 mg/L), Abijata (202.4 mg/L), and Beseka (32.2 mg/L) are among the lakes with the highest fluoride concentrations [55]. Fluoride values ranged from 0.65 mg/L to 11 mg/L in Hawassa city shallow hand-dug wells [54]. Fluoride levels in both the Hawassa and Halaba districts were found to be higher than the drinking water standard [56]. Fluoride concentrations in drinking water samples were greater than 6.8 mg/L in most rift valley rural areas [2]. In rift valley areas, approximately 8 million people drink high-fluoride water [57]. Groundwater accounts for more than 70 % of Ethiopia's water supply [58].

2.3. Health effects of E coli, excessive heavy metals and fluoride in water

Pollution of water and food from anthropogenic activities, including industrial waste and agricultural runoff, poses a significant global health threat. Microbial contamination of water leads to acute diseases like diarrhea, while heavy metals, fluoride, and other toxins cause insidious illnesses that can lead to long-term health issues and death [59]. Heavy metals such as lead (Pb), chromium (Cr), and nickel (Ni) are of particular concern due to their non-biodegradability, mobility, toxicity, and bioaccumulation potential in human organs like the liver and kidneys [60]. Chronic exposure to lead and hexavalent chromium can negatively impact bone and kidney health, increase blood pressure, and contribute to cancer. With a biological half-life of 10 to 33 years, these metals can bioaccumulate in organisms and ecosystems [12]. Fluoride can also adversely affect human reproductive organs. More "immobile and deformed births" and a decrease in birth rates have been reported in locations with high fluoride concentrations [61].

2.4. Water treatment technologies

Researchers have extensively studied various techniques for removing E. coli, heavy metals, and fluoride from water. Common treatment methods for heavy metals and fluoride include coagulation/precipitation, membrane processes, electrochemical treatments, ion exchange, and adsorption [62]. However, these conventional methods often suffer from limitations such as low efficiency, high cost, generation of toxic by-products, slow operation, limited selectivity for specific pollutants, and complex treatment processes [63].

Other conventional water treatment methods, such as chlorination, UV treatment, and ozonation, are used to disinfect water and eliminate waterborne pathogens. However, each of these methods has its own limitations. Chlorination, while effective against many pathogens, can be less effective against highly resistant strains and can lead to the formation of carcinogenic disinfection by-products (DBPs). These DBPs—such as trihalomethanes (THMs) and haloacetic acids (HAAs)—are produced when chlorine reacts with natural organic matter (NOM), bromide, or iodide that are present in the source water. Natural organic matter originates from the decay of plant and animal materials in surface or groundwater, while bromide and iodide are usually present in water from seawater intrusion, industrial discharges, or the natural dissolution of minerals in soils and rocks [64]. As bacteria develop resistance to disinfectants, higher doses are required, leading to increased DBP formation [65]. Ozonation, although less prone to DBP formation, is more expensive than chemical disinfection and can produce harmful bromate when ozone reacts with bromide ions [66]. UV treatment, while effective, does not leave a residual disinfectant to protect against re-contamination in the distribution system. To address these limitations, innovative approaches are needed to improve water disinfection efficiency. Several technologies listed in Table 2.1, which are currently available, can be used to remove fluoride, heavy metals, and waterborne pathogens from water.

Table 2. 1. Current removal mechanism of heavy metal, fluoride and pathogens from water.

Technology	Pollutant	Advantage	Disadvantage	Ref.
Coagulation/precipitation: calcium hydroxide; aluminum hydroxide	Heavy metal, *E,coli*	Commercially available chemicals	Expensive, efficiency depends of pH and presence of co-ions in water, adjustment and formation of sludge with high amount of toxic complex compound and unable to achieve a stable coliform removal which requires coupled with additional treatment process to improve the overall pathogen removal efficiency.	[67], [68]
Ion-exchange:	Heavy metal, Fluoride,	High efficiency	Expensive, vulnerable to interfering ions (sulfate, phosphate,chloride, bicarbonate, *etc.*), replacement of media after multiple regenerations, used media present toxic solid waste, regeneration creates toxic liquid waste, efficiency highly pH-dependent.	[69]
Adsorptive materials:	Heavy metal, Fluoride, E, coli	Greater accessibility, low cost, simple operation, availability of wide range of adsorbents.	High efficiency often demands adjustment and readjustment of pH, some common water ions can interfere pollutant adsorption	[21], [70]
Bio sand filtration.	Turbidity, E, coli	It can be easily Constructed using raw materials that are locally sourced.	The treated water does not meet the WHO drinking waterguideline.	[71]
Membrane filtration: reverseosmosis; Nano filtration	Heavy metal, Fluoride, E, coli	High efficiency; remove other contaminates	High capital, high running and maintenance costs, toxic wastewater produced	[72], [73]
Electrochemical treatments: dialysis; electro-dialysis; electro-coagulation	Heavy metal, Fluoride, E. coli	High efficiency; high selectivity	High cost during installation and maintenance	[74]

Advanced oxidation processes (AOPs), membrane technology, and nanotechnology are among the most recent and cutting-edge water purification technologies.

Advanced oxidation processes (AOPs)

AOPs, in broad terms, are chemical treatment processes designed to remove organic (and sometimes inorganic) materials from water and wastewater. This is achieved through oxidation reactions with hydroxyl radicals (•OH). While the hydroxyl radical has traditionally been considered the primary active species responsible for pollutant destruction [75], AOPs have also proven effective in eliminating disease-causing pathogens. Researchers have successfully employed AOPs to remove a wide range of contaminants, including pharmaceuticals, endocrine disruptors, pesticides, surfactants, and various industrial toxicants like phenols, humic acids, and benzene derivatives, commonly found in surface, ground, and wastewater [76]. Among the most well-known AOP technologies are photochemical degradation processes (UV/O_3, UV/H_2O_2), photocatalysis (TiO_2/UV, photo-fenton), and chemical oxidation processes (O_3, O_3/H_2O_2, H_2O_2/Fe^{2+}, H_2O_2/Fe^{3+}). These processes generate highly reactive and non-selective hydroxyl radicals (•OH) [77], [78].

However, AOPs have several drawbacks. One is their high cost, particularly in terms of operating and maintenance expenses due to energy consumption and chemical reagent requirements [79]. Additionally, the effectiveness of these processes is dosage-dependent, necessitating careful control of the •OH molecule concentration to achieve the desired treatment level [80]. Hydrogen peroxide levels must also be closely monitored to avoid potential negative impacts on subsequent oxidation processes and human health [81].

Membrane Technology

Membrane separation is becoming increasingly important in applications such as water treatment, wastewater treatment, water reclamation, and desalination. Pressure-driven processes like microfiltration (MF), ultrafiltration (UF), and nanofiltration (NF) are used to remove a variety of contaminants from water and wastewater [68]. These membranes are also widely employed in industrial applications, such as water recycling and process intensification.

Membrane bioreactor (MBRs) represent a significant advancement in wastewater treatment technology. Their high efficiency, compact footprint, and versatility make them a valuable tool for addressing the growing challenges of water scarcity and environmental pollution [82].As technology continues to evolve, MBRs are poised to play an increasingly important role in sustainable water management practices worldwide [83].

Reverse osmosis (RO) is a water purification technology that uses a semipermeable membrane to remove dissolved salts and other impurities from water. By applying pressure greater than the osmotic pressure, RO forces water molecules to pass through the membrane while leaving behind contaminants. This process is widely used in desalination, water purification for drinking and industrial purposes, and wastewater treatment.

Beyond reverse osmosis, other membrane processes such as electrodialysis (ED), membrane distillation (MD), and forward osmosis (FO) present promising alternatives for desalination. ED utilizes an electric field to transport ions across charged membranes, separating them from the water. MD relies on a temperature difference to drive water vapor through a hydrophobic membrane [84]. FO leverages a concentration gradient to draw water across a membrane, potentially offering lower energy consumption compared to traditional RO [85].

Membrane technology, while offering numerous advantages, faces several challenges. Fouling, where particles and organic matter clog the membrane surface, significantly reduces efficiency and necessitates frequent cleaning, increasing operational costs [86]. High initial investment costs associated with the membranes and equipment can be a significant barrier. Furthermore, membranes are susceptible to damage from chemicals, high pressures, and temperature fluctuations. Desalination processes, particularly reverse osmosis, generate concentrated brine, requiring careful disposal to avoid environmental harm [87]. While more energy-efficient than some traditional methods, membrane processes still consume energy, contributing to the overall carbon footprint. Addressing these drawbacks through careful design, operation, and maintenance practices is crucial for ensuring the long-term viability and sustainability of membrane technologies [88].

Nanotechnology

The application of nanotechnology in water treatment has gained significant attention due to its ability to address global challenges associated with water scarcity, pollution, and contamination (Hairom et al., 2021). Nanotechnology employs materials at the nanoscale (1–100 nm), exhibiting unique properties such as high surface area, reactivity, and tunable functionality. These properties enable advanced solutions for water purification, desalination, and contaminant removal [89]. A variety of nanomaterials have been explored for water treatment, each with specific roles and advantages.

However, the release of nanomaterials into the environment during and after water treatment raises concerns about potential ecological and human health impacts. Therefore, it's crucial to consider the impact of nanomaterials on aquatic organisms. Nanoparticles, particularly TiO_2 nanoparticles, silver nanoparticles, and carbon nanotubes (CNT), are primarily responsible for these negative effects. To mitigate these risks, improved mechanisms are needed to prevent the dissolution of hazardous nanoparticles into toxic ions following water treatment [22].

2.4.1. Nanomaterials and nanoparticles on removal of heavy metal, fluoride and water born pathogen.

Numerous nanotechnological studies in the last two decades have demonstrated novel approaches to improving water treatment techniques. Nanoparticles, with sizes ranging from 1 to 100 nanometers, exhibit distinct properties and a significantly higher specific surface area compared to their conventional macro-scale counterparts. These unique characteristics render nanoparticles more efficient in water treatment applications [26], [90]

2.4.1.1. Removal of bacterial pathogens from water using different nanomaterial

In an attempt to remove bacterial pathogens from water, nanotechnology emerges as a promising approach. Several categories of nanoscale materials demonstrate the ability to effectively eliminate microbes from wastewater [91]. High perm selectivity and enhanced hydrophilicity of nano-sized composite integrated with inorganic materials render them efficient tools for the enhanced treatment of contaminated water [89]. Numerous previous studies have demonstrated the efficacy of metal ions in disinfecting water. These metal ions exhibit altered capacities, contributing to their antibacterial properties. A variety of nanoscale materials, including silver, titanium, and zinc, exhibit the potential to disinfect water from various waterborne disease-causing microorganisms.

TiO_2 Nanoparticles

Titanium dioxide nanoparticles (TiO2 NPs) exhibit antibacterial properties due to their ability to generate reactive oxygen species (ROS) when exposed to ultraviolet (UV) light [92]. These ROS can damage bacterial cell walls, leading to cell death. However, TiO2 NPs also present several drawbacks [92]. Primarily, their antibacterial activity relies heavily on UV light, limiting their practical applications in many settings. Additionally, concerns exist regarding their potential toxicity, including the potential for oxidative stress, inflammation, and even genotoxicity. Furthermore, the release of TiO_2 NPs into the environment can have detrimental ecological consequences [93]. Finally, their tendency to agglomerate reduces their surface area, thereby diminishing their antibacterial efficacy.

Carbon Nanotubes

The antimicrobial potential of carbon nanotubes (CNTs) in water purification applications is significant, offering promising solutions for addressing waterborne diseases [94]. Their unique nanostructure allows for efficient physical interaction with microorganisms, leading to cell disruption and inactivation. Additionally, CNTs can generate reactive oxygen species, inducing oxidative stress within microbial cells [95]. However, potential drawbacks include the potential for environmental release and toxicity to aquatic organisms [96]. Furthermore, large-scale production and implementation of CNT-based water treatment technologies may pose economic challenges [97]. Continued research is crucial to optimize their use while mitigating potential risks and ensuring their safe and sustainable application in water purification

Silver Nanoparticles

Silver nanoparticles (AgNPs) have emerged as promising antimicrobial agents for water treatment due to their potent antibacterial properties [98]. Their small size and large surface area allow for efficient interaction with microorganisms, leading to disruption of cellular processes and ultimately, cell death. AgNPs can be incorporated into water filtration membranes, enhancing their antimicrobial properties and improving the removal of bacteria and other pathogens [99]. They can also be used as coatings for surfaces in contact with water, such as pipes and storage tanks, to prevent microbial growth [100]. While AgNPs offer significant potential for improving water quality, potential drawbacks include their potential environmental impact, potential human health concerns, and the possibility of the development of microbial resistance [101].

ZnO Nanoparticles

Numerous studies have demonstrated the potential of zinc oxide (ZnO) nanoparticles to effectively remove total coliforms from municipal wastewater treatment plants [102]. ZnO nanoparticles can disrupt bacterial cell membranes, leading to cell death. This disruption occurs through mechanisms such as the aggregation of ZnO nanoparticles within the bacterial membrane and cytoplasm, as well as the increased secretion of reactive oxygen species (ROS) like hydrogen peroxide, which exert toxic effects on the bacteria [103].

ZnO nanoparticles are favored over other disinfectant nanoparticles due to their unique properties. Their large surface area enhances contact with microorganisms, thereby boosting antimicrobial activity [104]. Furthermore, ZnO-NPs exhibit broad-spectrum antimicrobial activity, effectively targeting viruses, fungi, and bacteria [105], [106]. Importantly, ZnO-NPs are non-toxic to humans, release zinc ions gradually for sustained antimicrobial protection, are biodegradable, and have minimal environmental impact [107]. These factors, combined [108]with their relatively low cost, make ZnO-NPs an attractive and affordable disinfection option.

I. ZnO-NPs and its property

Zinc oxide nanoparticles exhibit a unique set of properties that make them valuable in various applications. Key properties include strong antimicrobial activity due to their ability to generate reactive oxygen species that damage microbial cells [108] . Their small size translates to a significantly higher surface area-to-volume ratio compared to bulk ZnO, enhancing their reactivity and interactions. ZnO-NPs also possess photocatalytic activity, utilizing light energy to generate electron-hole pairs that can initiate chemical reactions, further boosting their antimicrobial capabilities [109]. Additionally, ZnO-NPs are generally considered biocompatible, exhibit high thermal conductivity, and possess excellent chemical stability, making them suitable for a wide range of applications in fields such as medicine, environmental remediation, and energy [110].

II. **Synthesis of ZnO-NPs**

Three primary methods can be used to synthesize zinc oxide nanoparticles, as illustrated in Fig.2.1.

a. **Physical Methods for ZnO Nanoparticle Synthesis**:

Physical methods utilize various techniques to synthesize ZnO nanoparticles, such as binding smaller molecules and atoms together to form particles within the nanoscale range [111]. These methods include amorphous crystallization, vapor condensation, colloidal dispersion, and physical fragmentation. Specific examples of physical methods for ZnO NP synthesis encompass ion implantation, ball grinding, sputtering, physical vapor deposition, electric arc deposition, laser ablation, and many others [107]. While offering advantages like precise control over particle size and shape, high purity, and the ability to produce a wide range of nanomaterials, these physical methods often require significant energy input and specialized equipment. Physical methods for synthesizing ZnO nanoparticles, while offering certain advantages, also come with several drawbacks. These methods often require significant energy input, making them potentially expensive and less environmentally friendly [112]. Additionally, they can lead to agglomeration of nanoparticles, reducing their surface area and affecting their properties [112]. Precise control over particle size and distribution can be challenging, and controlling the shape of the nanoparticles is often limited. Furthermore, impurities can be introduced during the synthesis process, affecting the final product's quality, and specialized and often expensive equipment may be required, increasing the overall cost of production [113].

b. Chemical methods for ZnO nanoparticle synthesis

Chemical methods for synthesizing ZnO nanoparticles offer several advantages over physical methods. They generally involve lower energy consumption, making them more energy-efficient and environmentally friendly [114]. These methods often provide better control over particle size and distribution, allowing for the production of more uniform nanoparticles. Additionally, chemical methods can be used to synthesize nanoparticles with specific shapes and morphologies, which is crucial for many applications [115]. However, it's important to note that chemical methods can introduce impurities into the final product and may require careful control of reaction conditions to achieve desired properties [116]. Furthermore, careful control of reaction conditions is crucial to achieve the desired particle size, shape, and distribution. Factors such as temperature, pH, concentration of reactants, and the presence of surfactants or capping agents can significantly influence the final product. Additionally, some chemical methods may involve the use of toxic chemicals or generate hazardous byproducts, raising environmental and safety concerns [117].

c. Biological methods

Biological methods, often referred to as 'green synthesis' or 'bio fabrication,' utilize biological entities such as microorganisms, plants, and algae to produce nanoparticles [118] .These organisms possess the ability to reduce metal ions, leading to the formation of metal nanoparticles, as shown in Fig.2.1. Compared to traditional chemical and physical methods, this approach offers several advantages. Nanoparticles are biocompatible when they possess suitable surface chemistry, such as coatings with non-toxic biomolecules that reduce toxicity and improve hydrophilicity. Their small, uniform size and smooth shape allow safe cellular uptake without causing damage. A moderate surface charge helps maintain stability and prevents harmful interactions with cell membranes. Additionally, high purity, biodegradability, and stability in biological environments ensure safe and efficient performance in biomedical applications [119]. Additionally, these methods are generally more cost-effective due to the readily available and often inexpensive nature of biological agents. Furthermore, green synthesis minimizes the use of harsh chemicals, resulting in a more environmentally friendly process. By leveraging biological systems, the need for toxic chemicals is significantly reduced, improving overall safety [120].

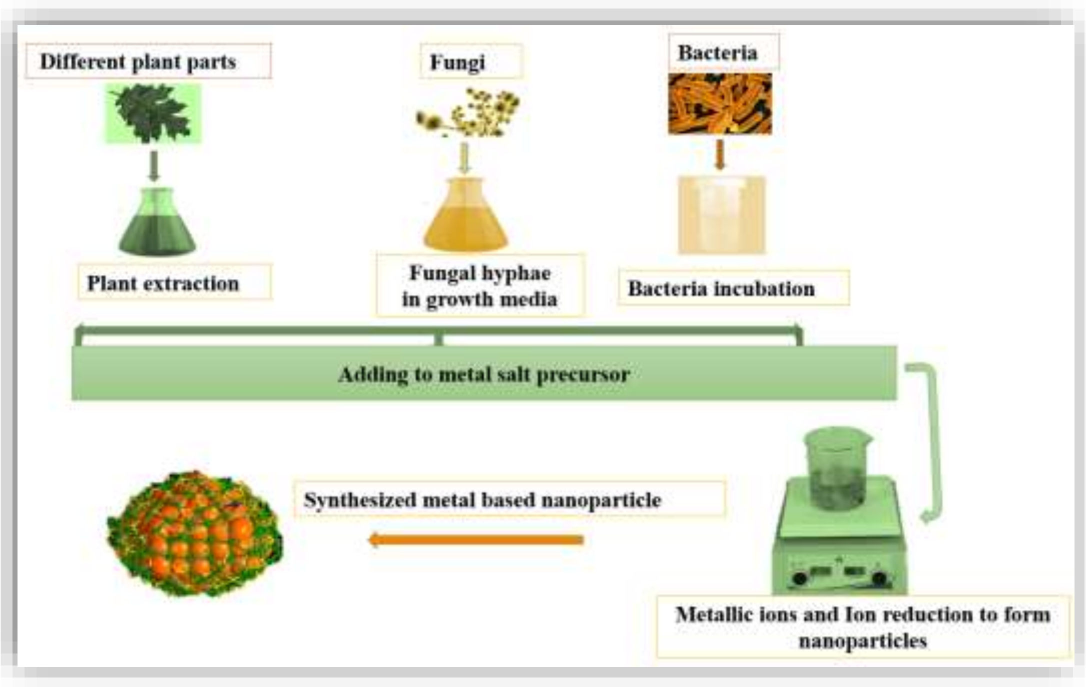

Fig.2. 1. Biologically-mediated synthesis of nanoparticles through green chemistry methods (citation)

Plant-mediated green synthesis of ZnO nanoparticles

Synthesis using natural plant extracts is cost-effective, as these extracts inherently contain biomolecules such as flavonoids, phenols, proteins, and sugars, which can act directly as both reducing and stabilizing agents during nanoparticle formation. Consequently, there is no need to create or add intermediary base groups, since these natural compounds efficiently and sustainably perform those chemical roles [121]. It is time-efficient and requires minimal equipment to generate high-quality, impurity-free, and highly pure products. Plants are the most preferred source for nanoparticle synthesis due to their ability to produce stable nanoparticles with varying sizes for specifc applications on a large scale [122]. Phytochemicals present in plants, including polyphenolic substances, proteins, alkaloid compounds, terpenoids, and polysaccharides, act as reducing agents in the green synthesis process, converting metal ions or metal oxides into metal nanoparticles [123] .

ZnO-NPs extracted from plants are typically washed with double-distilled water and then rinsed with tap water. The dried plant material is subsequently weighed and ground. The required amount of water is added during the boiling of the plant extract, followed by vigorous stirring [124]. The resulting solution is filtered through Whatman filter paper to obtain the plant extract.

Studies have been conducted to optimize plant-mediated synthesis of ZnO-NPs for optimal particle size and desired nano-characteristics. These characteristics are primarily influenced by factors such as precursor concentration, the ratio of plant extract volume to precursor volume, temperature, reaction time, and pH [125]. The effect of these synthesis parameters on nanoparticle formation was evaluated by UV-Vis spectroscopy based on the wavelength of the observed absorbance peaks [126]. The formation of ZnO-NPs is indicated by a visible yellow coloration of the solution after an incubation period. Fig.3 illustrates the green synthesis process of ZnO-NPs. These nanoparticles are then characterized using ultraviolet-visible spectroscopy [36], X-ray Diffraction (XRD) , scanning electron microscopy (SEM), DLS (Dynamic Light Scattering), TGA (Thermogravimetric Analysis) and transmission electron microscopy (TEM) [127].

III. Nanocomposite formation of ZnO-NPs for enhanced antibacterial activity

Incorporating ZnO-NPs enhance the antibacterial activity of nanocomposite materials by generating reactive oxygen species (ROS), releasing Zn^{2+} ions that disrupt bacterial membranes and metabolic processes, and providing a high surface area that ensures close contact with bacterial cells. Incorporation into a nanocomposite matrix promotes uniform dispersion, prevents aggregation, and maintains nanoparticle activity over time, resulting in a material that is more effective against bacteria than ZnO-NPs or the matrix alone. These strategies allow for controlled release of Zn^{2+} ions [128], increased surface area [129], and improved thermal stability [130]. Common support materials for immobilization and nanocomposite formation include inorganic materials like zeolites, pumice, clay minerals [131] , metal oxides [132] , and carbon-based materials [133], [134] as well as organic materials such as polymers and natural fibers. By addressing the limitations of free ZnO-NPs, these approaches offer significant advantages in terms of stability, reusability, controlled release, and synergistic effects, making them promising for various applications.

Indeed, the combination of ZnO-NPs with inorganic support materials and metal oxide nanocomposites has emerged as a highly effective strategy to enhance their antibacterial properties [135]. For instance, Ag/ZnO/bentonite has been shown to exhibit superior bactericidal activity compared to bare ZnO-NPs [136]. Similarly, the fabrication of iron oxide/zinc oxide nanocomposites using plant extracts has demonstrated promising antibacterial applications [137]. To fully realize the potential of these nanocomposites, further research is needed to optimize the synthesis process of plant-mediated ZnO nanocomposites and integrate magnetic nanoparticles to facilitate reuse and incorporate high-surface-area inorganic materials as immobilizers [138], [139].

IV. Mechanism of ZnO-NPs antibacterial activity

Zinc oxide nanoparticles have garnered significant attention due to their potent antibacterial properties. The mechanism of their antibacterial activity is multifaceted and involves several key processes, as shown in Fig.2. 2. These include the release of zinc ions, the generation of reactive oxygen species (ROS), and the exploitation of their large surface area [140]. Released zinc ions can penetrate the bacterial cell wall, disrupting cellular processes and binding to thiol groups in proteins, interfering with their function [140]. Under UV light exposure, generate ROS, which can damage the bacterial cell membrane, DNA, and proteins, leading to cell death [141]. Finally, the large surface area of ZnO-NPs allows for close contact with bacterial cells, disrupting the cell membrane and leading to the leakage of cellular contents [142]. ZnO-NPs can also penetrate the cell wall and interact with intracellular components, further damaging the cell.

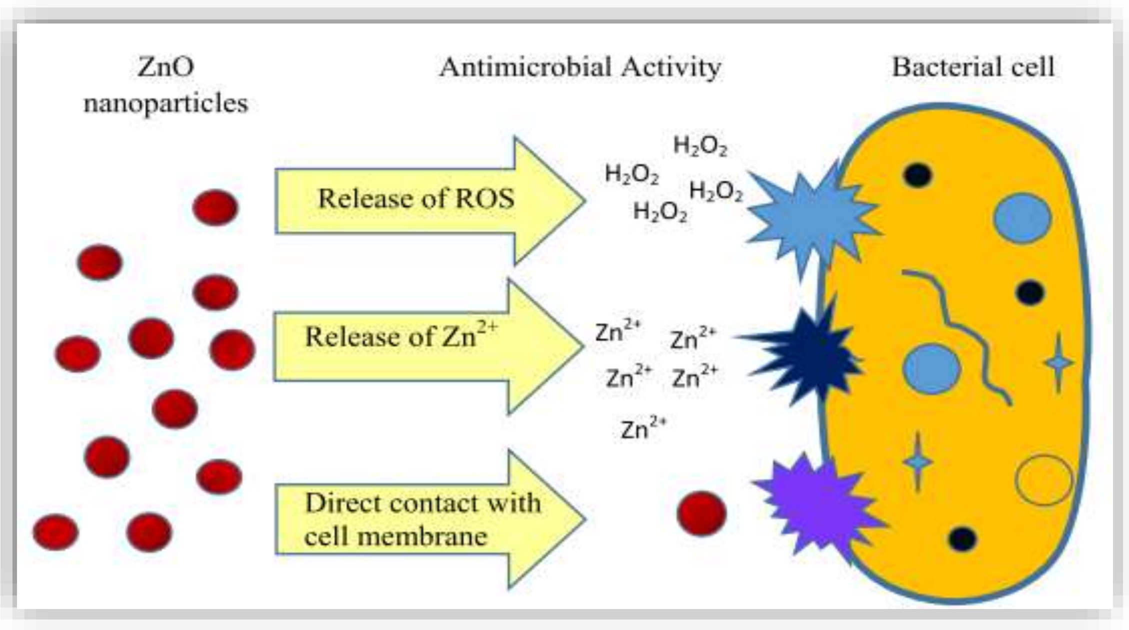

Fig.2. 2. ZnO disinfection mechanisms [28]

It's important to note that the relative contribution of these mechanisms can vary depending on factors such as the size, shape, and surface properties of the ZnO-NPs as well as the specific bacterial strain [104], [111]. Further research is needed to improve the complex mechanisms underlying the antibacterial activity of ZnO-NPs.

2.4.1.2. Nanomaterials in heavy metals and fluoride removal

Industrialization is the main source of the release of various pollutants into the environment, including various organic and inorganic wastes, heavy metal ions such Pb^{2},Cd^{2+},Zn^{2+}, Ni^{2+}, Hg^{2+}, Cu^{2+}, Cr^{3+} and Co^{2+}.These heavy metals are poisonous and not biodegradable [143].

To alleviate these defects, nanomaterials offer significant potential for removing heavy metals and fluoride ions from water due to their unique properties, such as large surface area, high reactivity, and tunable surface chemistry [144]. These properties enable efficient adsorption of contaminants, while surface modifications can enhance selectivity and adsorption capacity. Magnetic nanoparticles facilitate easy separation after adsorption, and some nanomaterials can catalyze redox reactions, enabling the reduction or oxidation of heavy metals into less toxic forms [145]. Several types of nanoparticles have shown significant promise for heavy metal removal such as: metal oxide NPs,polymeric NPs, carbon based NPs.

Nano scale particles synthesized from oxides of metals

Nanomaterials synthesized from metal oxides are inorganic nanomaterials widely used to remove heavy metals from wastewater. Examples include iron oxides, silver nanoparticles, manganese oxides, titanium oxides, magnesium oxides, copper oxides, cerium oxides, etc., which offer large surface areas and specific affinities for heavy metal ions [146]. Metal oxide nanomaterials have shown also promise in removing fluoride from water, such as alumina, iron oxide, and titanium dioxide [60]. Their high surface area provides numerous adsorption sites for fluoride ions, while their surface chemistry can be modified to enhance fluoride binding. For example, surface modifications can introduce functional groups with high affinity for fluoride, improving adsorption capacity and selectivity [147]. Additionally, the small size of these nanomaterials allows for efficient contact with fluoride ions in water, facilitating rapid removal.

However, challenges include difficulties in separating these nanoparticles from wastewater due to their high surface energy and nano size, non-selective adsorption of some metals, and potential toxicity and environmental impact from nanoparticle synthesis precursors and surfactants. Furthermore, these nanoparticles tend to aggregate, reducing their effective surface area. To address these challenges, strategies include surface functionalization to enhance selectivity and adsorption capacity, nanocomposite formation to improve stability and performance, using magnetic nanoparticles for easy separation and recovery, and developing green synthesis methods for nanoparticle production [148].

Polymer-based Nano sorbents

Polymer-based nano sorbents offer significant potential for fluoride and heavy metal removal due to their high surface area, tunable surface chemistry, and potential for selective binding [149]. By incorporating functional groups like chelating agents or ion-exchange sites into the polymer matrix, these materials can effectively capture specific heavy metal ions. However, challenges include potential leaching of polymer components into the environment, potential toxicity of some polymers, and the need for careful design to ensure long-term stability and prevent aggregation, which can reduce adsorption efficiency [150].

Magnetic nanomaterial’s

Magnetic nanomaterials, particularly those based on metal oxides, offer significant advantages in water treatment applications, including fluoride removal [151].These materials exhibit high efficiency in adsorbing fluoride ions while also enabling facile separation of the adsorbent from the aqueous solution after the reaction [152]. This overcomes a major challenge faced by many nanocomposite adsorbents – their difficult recovery from the treated water, which can lead to nanoparticle leaching and potential environmental contamination [153]. The incorporation of magnetic properties into metal oxide nanomaterials provides a convenient and efficient method for solid-liquid separation using external magnetic fields. Iron oxide-based nanomaterials and their composites are prominent examples within this category, offering a promising approach for sustainable and efficient water treatment

Silica-based nanomaterials

Silica-based nanomaterials have emerged as promising candidates for removing heavy metals and fluoride from water due to their unique properties. Their high surface area provides numerous binding sites for pollutants, facilitating efficient adsorption. Additionally, silica's surface chemistry can be readily modified through techniques like silanization, enabling selective adsorption of target contaminants [154]. This tunability, combined with silica's biocompatibility, makes it a versatile material for water treatment applications.

Silica-based nanomaterials demonstrate a wide range of applications in water treatment. synthesized 3-aminopropyltriethoxysilane-modified silica gel (APTES) from rice husk ash, creating a composite adsorbent for effective lead ion removal from metal solutions [155] . Similarly, Milton Manyangadze et al. demonstrated the adsorption of lead ions from wastewater using nano-silica spheres synthesized on calcium carbonate templates. In the context of fluoride removal, Pillai et al. prepared a silica nano-adsorbent from rice husk, an inexpensive and effective material for fluoride removal [156]. Furthermore, Srivastava et al. synthesized chitosan-functionalized mesoporous silica nanoparticles, demonstrating high fluoride sorption efficiency [157]. However, while silica nanoparticles are promising nanomaterials for bioremediation, challenges remain, such as nanoparticle aggregation and the need for efficient methods for separating them from treated water.

I. Silica-nanoparticles (SNPs)

Silica, one of Earth's most abundant materials, can be derived from various sources like agricultural waste (sugarcane, groundnut shells, corn cobs, wheat straw, rice husks, barley, etc. and natural minerals (quartz, olivine). Given the environmental impact of agricultural waste, researchers have increasingly focused on its reuse and reduction. Silica nanoparticles have attracted significant attention due to their versatile physicochemical properties. SNPs are relatively inexpensive to produce on a large scale, possess hydrophobicity, high surface area, pore volume, and biocompatibility, leading to diverse applications [158].

Recent advancements have expanded the applications of SNPs to various fields, including biomedicine, biotechnology, food, personal care products, pesticides, adsorption, semiconductors, ceramics, and water purification. Composed primarily of silicon dioxide, these materials exhibit high surface area, excellent chemical stability, and customizable pore structures [159] . These properties make them effective for removing heavy metals, organic pollutants, and dyes from water [160]. Their adsorption, catalytic, and filtration capabilities contribute to efficient water treatment processes.

II. Synthesis of SNPs

Silica nanoparticles can be synthesized using both chemical and green methods. Chemical synthesis involves the use of silicate precursors under controlled conditions to form uniform nanoparticles. These methods offer precision in size and shape but often require toxic reagents and high energy. Green synthesis utilizes natural sources like plant extracts or microorganisms as reducing and stabilizing agents. This eco-friendly approach eliminates the need for harmful chemicals and supports sustainable nanoparticle production. Both methods aim to produce silica nanoparticles with desired properties for various applications. The choice of method depends on the intended use, scalability, and environmental considerations.

Chemical methods

Traditionally, silica nanoparticles were produced using conventional techniques such as the sol-gel method, Stöber method, flame synthesis, and microemulsion [17]. While these chemical approaches are relatively straightforward to implement and modify, they can be expensive and difficult to control.

a. Microemulsion method

Microemulsion method which relies on surfactants to stabilize the emulsion, faces the significant challenge of surfactant removal from the final product. Surfactants, although crucial for emulsion stability, can negatively impact the nanoparticles' properties, including their surface chemistry and optical characteristics.

b. Chemical Vapor Condensation (CVC)

Another common method for synthesizing silica nanoparticles is Chemical Vapor Condensation (CVC). In this process, a volatile precursor, typically silicon tetrachloride ($SiCl_4$), is vaporized and introduced into a reaction chamber, where it reacts with oxygen and hydrogen at high temperatures to form silica nanoparticles. However, CVC presents several challenges, including high temperature requirements, complex reactor design, high energy consumption, and particle agglomeration.

c. Sol-gel method

The sol-gel method, a versatile technique for synthesizing silica (SiO_2) nanoparticles, involves the hydrolysis and condensation of a silica precursor, typically a silicon alkoxide. This process forms a colloidal suspension (sol), which then evolves into a gel. Subsequent processing yields silica nanoparticles. However, precise control over particle size and morphology remains challenging in sol-gel synthesis. Subtle changes in reaction conditions can significantly affect the final product, often leading to a broad particle size distribution. Uncontrolled aggregation during gelation is another major issue, compromising uniformity.

d. Stöber method

The Stöber method, another technique, synthesizes monodisperse silica spheres through base-catalyzed hydrolysis and condensation of tetraethyl orthosilicate (TEOS) in alcohol. While producing relatively uniform spherical particles, this method is limited in controlling particle shape beyond spheres and achieving precise sizes below 100 nm. The batch process hinders large-scale production, ammonia usage requires safety precautions, and byproduct management is necessary. Additionally, controlling porosity and achieving uniform surface functionalization pose challenges, and high reproducibility can be difficult due to the reaction's sensitivity to parameters. Fig.2. 3 schematically illustrates the most commonly used chemical techniques for synthesizing silica nanoparticles large-scale production, ammonia usage requires safety precautions, and byproduct management is necessary. Additionally, controlling porosity and achieving uniform surface functionalization pose challenges, and high reproducibility can be difficult due to the reaction's sensitivity to parameters.

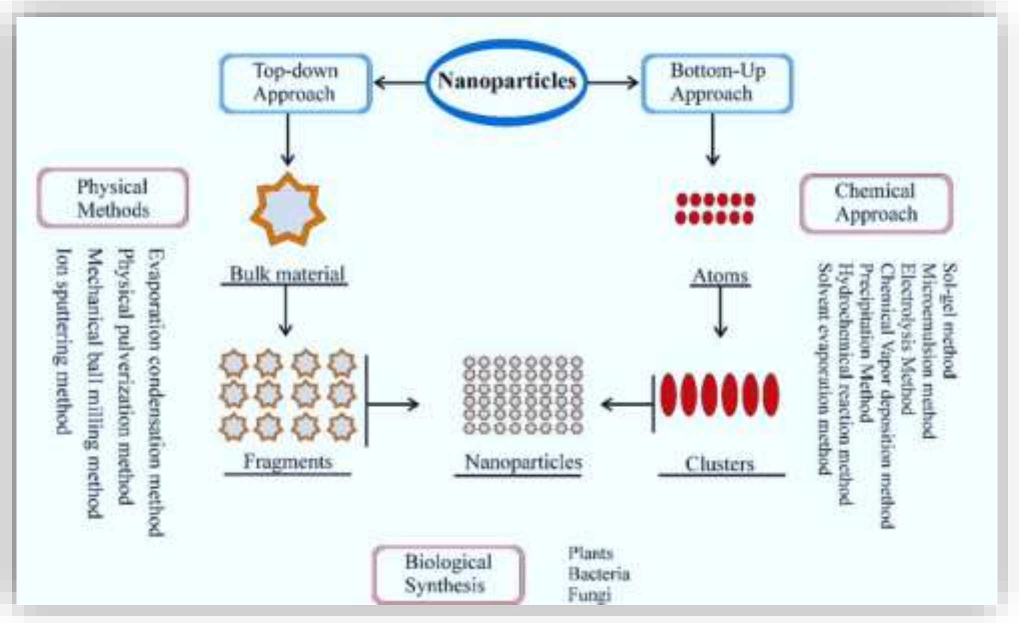

Fig.2. 3. Synthesis of silica nanoparticles by different approaches [161].

Green synthesis method of SNPS (biogenic synthesis of SNPs)

Green synthesis techniques, which utilize plant extracts or microorganisms, have gained popularity for producing silica nanoparticles. Researchers have successfully synthesized amorphous, semi-crystalline, and porous silica nanoparticles from biomass sources like rice husk and sugar beet bagasse. The most recently biogenic synthesis of silica nanoparticles using plant extracts offers a sustainable and eco-friendly approach. By leveraging the reducing and stabilizing properties of plant-derived phytochemicals, this method allows for the controlled synthesis of nanoparticles [162]. The process typically involves mixing a plant extract with a silica precursor solution, such as sodium silicate. Phytochemicals within the extract, including alkaloids, flavonoids, terpenoids, and polysaccharides, play a crucial role in the synthesis process. These compounds act as both reducing and capping agents. Reducing agents facilitate the conversion of the silica precursor into nanoparticles, while capping agents prevent particle aggregation and influence their size and shape. Despite the promising potential of this approach, there remains a significant gap in research on the green synthesis of silica nanoparticles using silica precursors derived from agricultural residues in conjunction with plant extracts as reducing or stabilizing agents.

III. Immobilization, nanocomposite formation, and functionalization of silica-based materials

Silica nano-composites are hybrid materials that combine silica nanoparticles with other materials at the nanoscale, resulting in enhanced properties and functionalities compared to the individual components [163]. The incorporated second phase material can be organic or inorganic, significantly altering the nano-composite's overall properties including polymers, metals, ceramics, magnetic nanoparticles, and carbon-based materials. The resulting nano-composites exhibit tailored properties like increased strength, thermal stability, optical functionality, electrical conductivity, or catalytic activity, depending on the incorporated material.

Recently to enhance the adsorption capacity of silica nanoparticles several inorganic nanoparticles have been incorporated to enhance silica's adsorption capacity, including metal oxides (iron oxide, titanium dioxide, aluminum oxide), metal sulfides (zinc sulfide), and layered double hydroxides (LDH) [164], [165]. The choice of nano-particle incorporated with silica depends on the target pollutants in the water. Such as ,titanium dioxide can enhance the photocatalytic degradation of organic pollutants [166]. While iron oxide nanoparticles are effective for removing heavy metals due to their high surface area and affinity for metal ions and crucial for easy separation of the adsorbent from the treated water using an external magnetic field [167]. Which significantly simplifies the water treatment process and avoids the need for energy-intensive filtration. So many research works have been carried out such as magnetic iron oxide-silica nanocomposites for heavy metal adsorption from aqueous solution [168]. The immobilization of nanoparticles on clay minerals and pumice has emerged as a promising strategy for creating advanced composite materials with enhanced properties [169] . This technique involves anchoring nanoparticles onto the surface or within the interlayer spaces of these natural materials, leading to a synergistic combination of their individual characteristics [170]. And it can be used to control the release of nanoparticles, making them suitable for of environmental remediation [171]. Functionalization markedly improves the adsorption efficiency of silica nanoparticles. Introducing functional groups such as amines, thiols, or carboxylic acids onto the silica surface generates specific binding sites, which facilitate selective interactions with target contaminants through mechanisms like ion exchange, chelation, and hydrogen bonding. For example, amine-functionalized silica exhibits strong affinity for heavy metal ions via electrostatic attraction and ion exchange. In addition, functionalization can alter the zeta potential of silica nanoparticles a key factor in their effectiveness at adsorbing anionic pollutants from aqueous solutions. Zeta potential refers to the electrokinetic potential at the shear plane surrounding a particle in suspension. In their native state, silica surfaces carry a negative charge due to the deprotonation of silanol groups (–Si–OH) in water, which leads to electrostatic repulsion of negatively charged (anionic) pollutants [172]. As depicted in Fig. 2.4, the adsorption behavior of both anionic and cationic pollutants is largely governed by the surface charge, particularly the zeta potential. Through surface modification, the charge properties of silica nanoparticles can be strategically adjusted, allowing for controlled and selective adsorption performance.

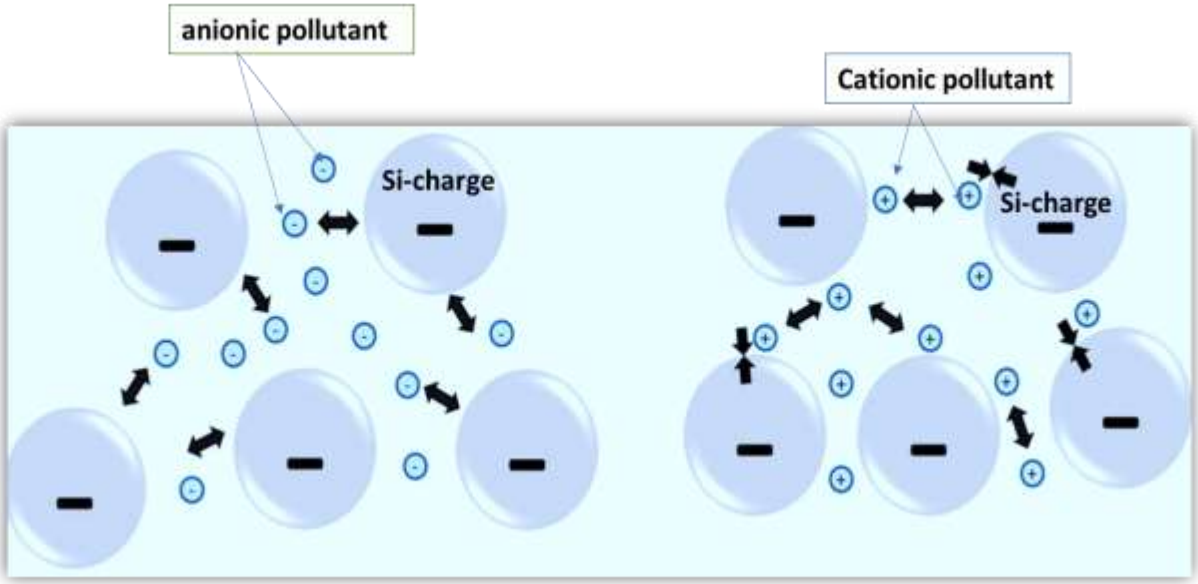

Fig.2. 4. Schematic illustration of the interaction of anionic and cationic pollutants with silica nanoparticle surfaces

IV. Silica adsorption mechanism

The adsorption mechanisms can vary depending on the specific contaminant and the properties of the silica material. The adsorption process forms a layer of adsorbate (metal ions) on the surface of adsorbents. Adsorption can be reproduced for multiple applications via a desorption method (reverse adsorption in which adsorbate ions are transported from the adsorbent surface) because adsorption is a reversible process in certain circumstances [173].

Adsorption on a solid material involves several steps: the contaminant first moves towards the surface, then sticks to it, and finally may move within the material itself. Removing heavy metals from water often involves a combination of different sticking mechanisms [174]. These include electrostatic interactions, where charged metals are attracted to oppositely charged sites on the adsorbent; complexation, where metals form chemical bonds with functional groups on the adsorbent; ion exchange, where metals are exchanged with other ions bound to the adsorbent; precipitation, where metals react to form insoluble compounds; physical adsorption, based on weak van der Waals forces; chemisorption, involving strong chemical bonding; intra-particle diffusion, the movement of metals within the adsorbent's pores; pore adsorption, where metals are adsorbed within the pores; hydrogen bonding between the metal and the adsorbent [173]. The specific mechanisms involved depend on the adsorbent, the metal, and solution chemistry.

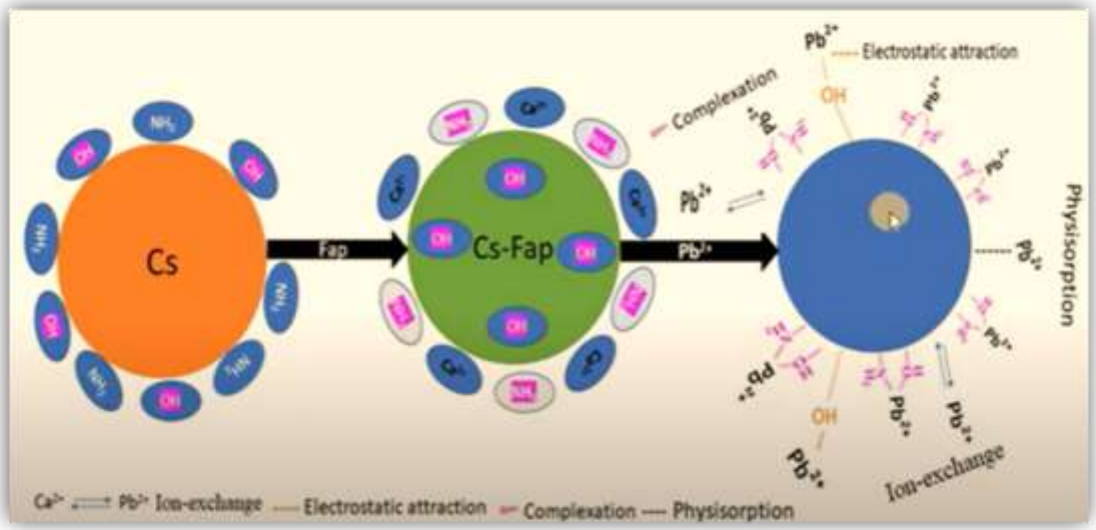

Fig.2. 5. Mechanisms of adsorption process

Generally, electrostatic attraction causes charged pollutants to adsorb on differently charged adsorbents because heavy metals have a vigorous affinity for hydroxyl (OH−) or other functional group surfaces specially for cationic pollutant, as shown in Fig.2.5. The adsorption mechanism of amine-functionalized any silica for anionic pollutants and fluoride involves a combination of electrostatic interactions, hydrogen bonding, and surface complexation. The amine groups on the surface of the adsorbent provide a positive charge, which attracts and binds to negatively charged anionic pollutants and fluoride ions through electrostatic forces [147]. Additionally, the lone pair of electrons on the nitrogen atom in the amine group can form hydrogen bonds with the anionic species, further enhancing the adsorption process [175]. Surface complexation can also occur, where the anionic pollutants and fluoride ions form chemical bonds with the metal ions on the surface of the adsorbent, leading to strong adsorption.

It is relevant to mention that there are many factors which affect heavy metal adsorption such as initial concentration, temperature, adsorbent dose, pH, contact time and stirring speed. However, the pH plays a vital role in deciding the maximum adsorption capacity of the adsorbent such as activated carbons, carbon nanotubes, graphene, bio sorbents, low-cost adsorbents (vegetal and industrial wastes), silica, chitosan, zeolites, alumina, clay, algal biomass, red mud, magnetic composites, and so on. The pH affects the surface charge of the adsorbent, the degree of ionization and speciation of the surface functional groups and metal ions [71–74]. In general, the adsorption of cationic metallic species increases with increasing pH in certain range because at low pH, there a competition between the metallic species and the H^+ ions of aqueous solution.

2.4.1.3. Adsorption performance evaluation models

Adsorption performance evaluation models are used to assess the effectiveness of adsorbents in removing specific substances from a fluid phase (liquid or gas). These models help in understanding the adsorption process, optimizing adsorbent selection, and designing efficient adsorption systems. Here are some key models [176].

Isotherm models

Langmuir Isotherm describes the relationship between the amount of adsorbate adsorbed and its equilibrium concentration in the fluid phase. It assumes a monolayer adsorption on a homogeneous surface with a finite number of adsorption sites [176]. Freundlich Isotherm describes multilayer adsorption on a heterogeneous surface with an infinite number of adsorption sites. It is often used for complex systems where the adsorbent surface is not uniform [177]. Temkin Isotherm considers adsorbent-adsorbate interactions and assumes that the heat of adsorption decreases linearly with coverage [178].

Kinetic models

Pseudo-first-order is useful for describing physical adsorption processes and assumes that the adsorption rate is proportional to the number of unoccupied adsorption sites [179].

Pseudo-second-order Often is used to describe chemisorption processes and assumes that the adsorption rate is proportional to the square of the number of unoccupied adsorption sites [180].

Intraparticle Diffusion Model describes the diffusion of adsorbate molecules within the pores of the adsorbent. And helps to identify if intraparticle diffusion is the rate-limiting step.

2.4.2. Present research fulfillments of technology gaps

In the present study, Coffee husk extracted (CHE) capped magnetite pumice supported CHE capped ZnO and CHE capped SiO_2 nanocomposites were applied as disinfectants and for the removal of lead ions from aqueous solutions, respectively. In addition, amine-functionalized magnesium magnetite pumice silica nanocomposites (CHE Capped Fe_3O_4/PU/Mg@SiO_2 -NH_2 NC) were applied for Cr (VI) and fluoride ion (F^-) removal from aqueous solutions. These materials have the potential to remove heavy metals, fluoride, and be utilized as disinfectants for drinking water treatment. By applying green synthesis-based enhancement mechanisms, this study aimed to fulfill the following research gaps.

Recently, many studies have been carried out on the synthesis of bio-silica nanoparticles from bagasse ash using various techniques, including the sol-gel method, hydrothermal synthesis, flame synthesis, and the reverse microemulsion technique. The sol-gel process is best known for producing SiO_2 NPs from agricultural waste ash [164], [165]. It involves a simultaneous reaction of hydrolysis and condensation. In these studies, mentioned above, sodium silicate solution was extracted from rice ash and bagasse ash and used to produce SiO_2 NPs. The production of SiO_2 NPs is based on the hydrolysis reaction (formation of silanol groups) and condensation (siloxane formation) with sulfuric acid in a two-phase medium in the presence of Cetyl Tri-Methyl Ammonium Bromide (CTAB) was added as a surfactant to control the size of nanoparticles, avoid agglomeration, and modify their surface [181]. According to the study by Dlomo, Silica nanoparticle size can be manipulated by controlling (slowing down) the poly-condensation rate using a small amount of anionic surfactants (ammonium salts of Br, I, and Cl) [183].

However, the utilization of CTAB and anionic surfactants like ammonium salts of Br, I, and Cl for enhancing silica nanoparticle size presents several drawbacks, including potential toxicity and environmental impact due to their chemical nature [184]. Complete removal of these surfactants from the final product can be challenging, which is crucial for applications in sensitive areas like biomedicine and food [185]. Additionally, their use can lead to inconsistent size control and potential aggregation of nanoparticles, complicating the synthesis process and affecting the final product's quality. This study investigated a solution for the aforementioned conventional silica nanoparticle synthesis mechanism, substituting phenolic compounds extracted from coffee husk as a surfactant to manipulate nanoparticle size. Additionally, synthesized silica nanoparticles were endowed with magnetic properties by incorporating green-synthesized magnetite nanoparticles and pumice, facilitating simplified separation and regeneration.

The other area of focus is the synthesis of zinc oxide nanoparticles, where research has been conducted using various green synthesis mechanisms. According to a review by Agarwal et al [186], the size and morphology of zinc oxide nanoparticles are significantly influenced by the specific green synthesis method employed. The primary factors contributing to size fluctuations during plant extract-mediated synthesis are the concentration of phenolic compounds, which play a crucial role in the reduction and capping processes, and pH variations. Acidic conditions can promote excessive nucleation and agglomeration, while alkaline conditions may lead to nanoparticle instability [187]. Consequently, precise regulation of zinc salt concentration, reaction temperature, and time is critical for achieving ZnO-NPs with uniform size and shape [188]. Therefore, this present study aimed to investigate the optimal parameter values for these factors during the synthesis of ZnO-NPs using plant-mediated coffee husk extract (CHE) and we enhanced green-synthesized ZnO-NPs by incorporating them with CHE-capped Fe_3O_4/Pumice to facilitate easy separation, increase surface area, and improve regeneration properties.

In general, based on the descriptions above, significant gaps remain in the application of hybrid drinking water treatment methods capable of simultaneously removing all three types of contaminants water born pathogens, (*E. coli and S.aurus)* , fluoride, and heavy metals using purification systems that rely on affordable, locally available materials. Water sources in many regions contain diverse pollutants that require effective treatment. This study evaluated the individual performance of the synthesized nanocomposite materials and recommended their potential application in water purification.

CHAPTER THREE

3. SYNTHESIS AND CHARACTERIZATION OF COFFEE HUSK EXTRACT (CHE) CAPPED ZNO NANOPARTICLES AND THEIR ANTIMICROBIAL ACTIVITY

3.1. Introduction

Access to safe drinking water and sanitation services for all is a critical public health and development issue that all countries around the world have endorsed. However, more than 1.6 billion people worldwide lack access to safe drinking [1]. In Sub-Saharan Africa, rain and surface water are used for drinking, which is heavily polluted by fecal microorganisms and emerging pathogens [189]. The deposition of fecal material results in *Escherichia coli* (*E. coli)* pollution of waterways. Specifically, the *E. coli O157:H7* strain produces a potent toxin that damages the small intestine lining, causing bloody diarrhea and other health complications.

In Ethiopia, poor water sanitation and hygiene (WASH) are responsible for 23 % of all under-five deaths (more than 70,000 children per year) due to various pathogenic microbes found in the aquatic environment [16]. *E. coli* and *Staphylococcus aureus* (*S. aureus*) are two enteric pathogens that cause various infections [190]. According to several studies, Ethiopia's major causes of water-borne diseases are water source contamination, lack of treatment mechanisms, cross-contamination in the pipeline system, and unsafe household storage. In Addis Ababa (the capital city), 10 %, 7 %, and 3 % of tap water tested positive for bacteriological, total coliforms, and fecal coliforms, respectively [191]. *E. coli* contamination of household stored-water was found in 83.3 % of the cases [192]. In North Eastern Ethiopia, *E. coli* and total coliforms were detected in both bottled drinking water and city tap water, beyond the World Health Organization standard [193]. In Jimma City (Southwest Ethiopia), total coliforms and fecal coliforms were found in all water samples gathered from drinking water reservoirs [194]. These challenges are largely due to the operation and application mechanisms of disinfectants, as well as the conditions of post-disinfection storage systems. Therefore, developing an affordable and effective end-user water disinfection mechanism is critical to addressing these issues.

Water disinfection methods commonly used to kill pathogens include chlorination, UV treatment, and ozonation. Unfortunately, chlorination is not effective in some extremely resistant water pathogens. Moreover, adding chlorine to water produces harmful disinfection by-products (DBP) [195]. However, some pathogens in water have developed resistance to the existing disinfectants, and larger disinfectant dosages are required, resulting in greater DBP residual levels in the treated water [196]. Ozonation creates less contaminant than conventional disinfection, but it is usually expensive. Moreover, it can produce toxic bromates when the ozone reacts with bromide ions in water, which can easily corrode water transmission pipelines. Similar to ozone treatment, UV treatment leaves no remnant in the water afterward. As a result, it does not cause defense from re-infection in the supply chain. Furthermore, it needs ongoing upkeep and does not perform well in turbid water [197], which can be the case in developing countries. Thus, new approaches need to be considered to improve the efficiency of water disinfection.

Some nanomaterials have enormous antimicrobial properties that can inactivate waterborne pathogens in water supplies [198], [199]. However, multiple research investigations have found that nanoparticles (NPs) can disintegrate into dangerous ions harmful to both humans and the environment [200]. To minimize NP's degradation to harmful ions, poisonous species can be substituted with less toxic components that have similar characteristics. As an alternative, NPs can be capped with shells [201], and traditional synthesis methods can be replaced with green synthesis methods. This may include the use of plants or plant parts to bio-reduce metal ions into their elemental form in the size range of 1-100 nm and stabilize their size throughout the synthesis process by inhibiting over-growth and reducing aggregation/agglomeration in colloids [187], [202]. The phyto-fabricated components used in the manufacturing process have more roles than only reduce metal ions; they also modify the nano-particle surfaces, resulting in the generation of synergistic effects required for anti-oxidants, antimicrobial, and medicinal uses [203], [204]. In addition, nano-biotechnology has numerous benefits, including applications for improving the quality of water resources for human consumption, as well as its eminence for sustainability [205]. As a result, combining NPs and biotechnology may be an appropriate strategy for the successful synthesis of nanomaterials for wastewater treatment [204], [205] This is because biotechnology processes are non-toxic, environmentally safe/green, and simple to use [187]. Specially green-process synthesized metallic oxide nanoparticles, such as titanium dioxide (TiO_2), copper oxide (CuO), gold oxide (Au_2O_3), silver oxide (Ag_2O), and other metal oxides, are widely used for water treatment and medical applications, but their toxicity is currently a significant limitation for their widespread use[204]. In this regard, significant effort is being directed to discovering novel ways for synthesizing diverse types of NPs from biological sources for wastewater treatment applications [206]. In contrast to the aforementioned metal oxides, ZnO is a nontoxic metal oxide with bio-compatibility attribute and can be utilized extensively in water disinfection, as antiviral agent, and biomedical and environmental applications [207]. Furthermore, ZnO was chosen for this study because its nanostructure has high antibacterial activity even in minute amounts. It also displays stability under extreme processing circumstances [208], exceptional durability, selectivity, and heat resistance [28], [124], [204]. As a result, the nano-biotechnology technique was applied in this study to synthesize ZnO-NPs using plant extract (CHE) as a source of phytochemicals [209], [210]. Plants have significant benefits over other green synthesis methods such as bacteria, fungus, and algae as bio-templates [211]. The first advantage is that it is safer and easier to handle than microbial nanoparticle production procedures because some bacteria produce toxins during cultivation [187], [212]. The second reason is that microbial fabrication mechanism requires a time-consuming synthesis process and is difficult to manage since it requires microbial growth to be performed under specific conditions to avoid the formation of colonies, which is detrimental to ZnO production. In addition, plant extract takes a few minutes to a few hours for Zn ion reduction synthesis, and also phytochemical extraction from plant components only requires ethanol and water as solvents. In this study, coffee husk (CH) was selected as a suitable plant extract due to its abundant availability in Ethiopia, cost-effectiveness, and high content of phenolic compounds, which serve as effective reducing and stabilizing agents for the biosynthesis of ZnO nanoparticles. It is important to highlight that over 192,000 metric tons of CH is discarded annually in Ethiopia [207], causing severe environmental pollution [206], [208]. Thus, the utilization of CH as a source of aqueous extracts rich in phytochemicals and antioxidants is appealing and inexpensive [209]. The main functional groups of plants that contribute to metal ion size reduction to nanoscales are hydroxyl (OH), carbonyl (C=O), and amine (NH_2), which also act as stabilizing agents [187], [210].

Several studies have been conducted on green synthesis methods for the generation of ZnO-NPs[211]–[216] using plant extract as reducing and capping agents. The major factors for plant mediated NPs synthesis like amount of plant extract concentration, amount of metal salt solution, temperature, pH, reaction time have a detectable effect on the morphologies, shape, size and characteristics of NPs [203]. The value of the synthesis parameters for NPs is determined by the substrate or capping agent employed in the biosynthesis [211], [216], [217]. In this part of the study, the total phenolic content of indigenous CHE was investigated, and the synthesis parameters (temperature, reaction time, pH, and the volume ratio of the precursor to CHE) were optimized to produce CHE-capped ZnO-NPs. The antimicrobial activities of CHE capped ZnO-NPs against *E. coli* and *S. aureus* were also tested.

3.2. Materials and Methods

3.2.1. Materials

Ethanol (C_2H_5OH, 99.02%), folic and Ciocalteu's phenolic reagent, and gallic acid ($C_7H_6O_5{\cdot}H_2O$, 99.5%), were purchased from Loba Chemie Pvt. Ltd. Zinc nitrate hexa hydrate ($Zn(NO_3)_2{\cdot}6H_2O$, 99%) was obtained from Effective Laboratory Supplies. Sodium carbonate (Na_2CO_3, 98%) and LB agar medium were sourced from Blulux Laboratories Ltd., and Sisco Research Laboratories Pvt. Ltd, respectively. Indigenous arabica coffee husk was collected from the eastern part of Ethiopia, Chiro district (9.0795272N, 40.8652187E). Standard bacterial strains of *S. aureus* (ATCC 25923) and *E. coli* (ATCC25922) were obtained from the Ethiopian Biodiversity Institute. All compounds utilized were of analytical quality, and all solutions were made with deionized (DI) water.

3.2.2. Methods

3.2.2.1.Coffee husk extract preparation

Coffee husk was thoroughly washed with distilled water to remove dirt and impurities, then dried to a constant moisture content and ground using a coffee grinder. The extraction method was followed according to the procedure of Silva et al. The solvent for extraction was prepared by mixing equal volumes of ethanol and deionized (DI) water. The coffee husk powder was immersed in the solvent at a 1:10 (g/mL) ratio and heated at 60 °C for 1 h in a water bath. The resulting mixture was centrifuged for 20 min at 6000 rpm, and the obtained coffee husk extract (CHE) was stored at 4 °C until use [218].

3.2.2.2. Green synthesis of ZnO-NPs

The ZnO-NPs were synthesized using the method described by B. Naiel et al. [124] with some modifications. These modifications included adjusting the precursor concentration, changing the reaction temperature, and altering the reaction time to optimize the nanoparticle size and morphology as shown in Fig.3.1. The CHE was poured into a beaker onto which a precursor of ZnO ($Zn(NO_3)_2\cdot 6H_2O$) was added. The beaker was then placed in a water bath and maintained at different temperatures. The mixture was stirred using an overhead stirrer (200 rpm) for different times. The reaction mixture was observed for color change from dark brown to yellowish white (Fig.2.2a and b) as validation of ZnO-NPs synthesis. The dispersion was then cooled and centrifuged (6000 rpm) for 25 min to separate the precipitate. It was then subsequently cleaned with DI water, rinsed with ethanol to eliminate organic materials, and oven dried (60 °C for 24 h) [124] . A Cary 60 UV-Vis spectrometer in the wavelength range of 190-1100 nm was used to probe the formation of NPs [204].

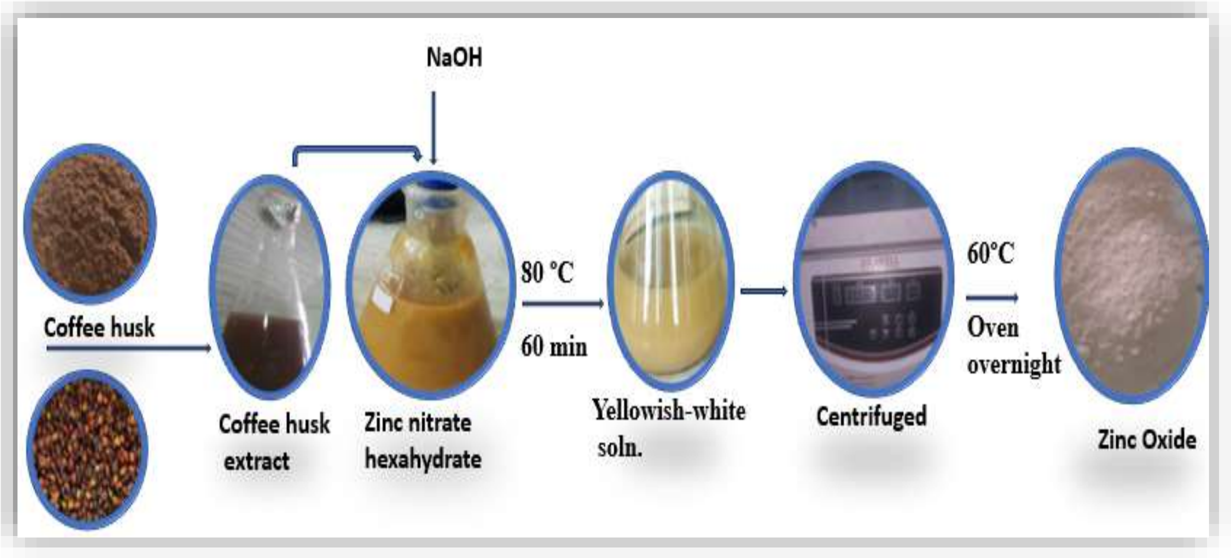

Fig.3.1. Schematic diagram for the green synthesis of CHE capped ZnO- NPs.

3.2.2.3.Effect of synthesis parameters of ZnO-NPs

One-factor-at-a-time (OFAT) approach was used to find the single effects of the study variables on the green synthesis of ZnO-NPs. The investigated synthesis parameters were pH (4,6, 8, 10, and14), temperature (25, 50, 65, 80, 90 °C), volume of precursor to extract ratio (0.25, 0.5, 1), operating time (1 h, 2 h, 3 h, 4 h). The pH was adjusted by using 1M NaOH.

3.2.2.4. Characterization of CHE and its total phenolic content

Folin-Ciocalteu technique was used to quantify the amount of reducing agent found in CHE [219]. The total phenolic contents of the extract were also determined using the Folin Ciocalteau reagent as described by Mohamad et al., [219]. For this, a calibration curve was prepared by combining 1 ml of (0.2, 0.4, 0.6, 0.8 and 1 mg/mL) gallic acid solutions with 10.0 mL of diluted (1:10). Folin Ciocalteu reagent and 8.0 mL of (7.5 g/100 mL) sodium carbonate solution. After 30 min, the absorbance was measured at 765 nm using ultraviolet-visible spectroscopy (Cary 60 UV-Vis-Agilent) for constructing the calibration curve. For the sample preparation, 2 mL of the extract was mixed with the same reagents as standard solution excluding gallic acid. The absorbance was then calculated after 1 h to assess the total phenolic content of the CHE using Eq.3.1 [219].

$$TP = \mathrm{TP1}\, V/m. \tag{3.l}$$

Where TP is total phenolic content (mg/g) in GAE (gallic acid equivalent), TP1 is the concentration of gallic acid obtained from the calibration curve in mg/mL, V is amount of CHE in mL, and m is amount of the plant extract in gram [219].

Phytoconstituents in the CHE were identified using UV-Vis in the wavelength range of 190-1100 nm [220], [221] . FTIR spectroscopy (Thermo Scientific Nicolet 6700 with ATR) was used to analyze CHE and CHE capped ZnO-NPs functional groups as well as to identify the functional groups involved in zinc nitrate reduction and ZnO-NP synthesis at wavenumbers ranging from 400 to 4000 cm^{-1}.

3.2.2.5. Characterization of CHE capped ZnO-NPs

The UV-VIS analysis was also used to determine the optimal synthesis parameters of ZnO-NPs and to confirm their formation. SEM images were obtained using a scanning electron microscope (Quanta FEG-250 SEM Abingdon, UK). The supported energy dispersive X-ray spectroscopy (EDX) was used for surface elemental analysis. X-ray diffraction (XRD- MiniFlex 600, Rigaku) at 40 kV with 30 mA with $CuK\alpha$ (λ = 0.154 Å) radiation was used to analyze the crystalline structure and the sizes of the NP's were calculated using the Debye-Scherrer equation. Diffraction data were collected in the 2θ range of 10 ° - 60 °. The Brunauer-Emmett-Teller (BET) **(**SA-9600 Series Surface Area Analyzer, Horiba**)** was used to determine the surface area of the synthesized nano-particle. The thermal stability and degradation characteristic of the generated ZnO-NPs were investigated using thermo-gravimetric analysis (TGA; HCT-1, China) in the temperature range of 30 - 900 °C. Zeta potential and particle size of the synthesized NPs were measured using Dynamic Light Scattering (DLS, Zeta sizer nano series, Malvern, Westborough, MA, USA).

3.2.2.6.Determination of antimicrobial activity

The antimicrobial activity of the various materials in LB agar medium was evaluated using the agar - well diffusion method. The McFarland 0.5 standard (1.5×10^8 colony-forming unit (CFU))/mL) was used to achieve equivalent bacterial concentrations. Then, a very small amount of pre cultured bacteria was collected using a sterile swab, mixed in sterile saline, and compared to the 0.5 McFarland standard opacity. The opacity was adjusted following the method used by Hudzicki [222] in order to achieve the 0.5 McFarland opacity. Similar bacterial strain dilutions were prepared and inoculated in the media. After that, 8 mm diameter wells were punched into the agar medium. The wells were separately filled with 100 µL of ZnO-NPs at two different concentrations (1 and 2 mg/mL). The plates were then incubated for 24 h in an upright position at 37 °C. After incubation, the diameters of the growth inhibition zones were measured with a graduated ruler.

3.3. Results and discussion

3.3.1. Characteristics of CHE and activity on formation of ZnO-NPs

Both indigenous CHEs, i.e., obtained using a water-ethanol mixture (1:1 ratio) and DI water extraction alone, showed the presence of phenolics in Folin-Ciocalteu analysis. The total phenolic contents (gallic acid equivalents, mg/g) in the water-ethanol and water-only extracts were calculated to be 14.25 mg/g and 12.04 mg/g, respectively, showing that the ethanol-containing solvent gives more phenolic content. Other studies [30], [223] also showed that water-ethanol mixture-based extraction provides high phenolic compounds concentration.

3.3.2. UV-Vis's analysis

To regulate the size and morphology of the NPs, phytochemicals present in CH were used in the biosynthesis processes. Due to the presence of phytochemicals, metal ions in plant extract are changed into metal NPs. Thus UV–Vis spectroscopy [221] was employed to confirm this reaction progress. The UV spectra of the ethanolic extract of CHE showed a characteristic wavelength for the maximum absorption (λ_{max}) at 274 nm and another absorption band at 285 nm (Fig.3.2c). At this wavelength range, the common phenolic compound to be noted is caffeine [41,42]. This is not surprising as caffeine is considered the major phytochemical component of CHE in arabica CH [226]. Because of the existence of -OH groups, this phytochemical may function as a bio-reducing and capping agent [227]. Additionally, due to the antioxidant characteristics and absence of harmful compounds, these plant-based chemicals are particularly efficient at reducing metal ions and maintaining them at the nano size [25].The color of the resulting solution changed from dark brown to yellowish-white, indicating that the zinc ion was reduced to ZnO (Fig.3.2 a and b). Further UV/Vis spectral analysis revealed a surface plasmon resonance (SPR) peak of CHE-capped ZnO-NPs at 365nm (Fig.3.2 e), which confirmed the formation of monodisperse ZnO-NP [221], [228].

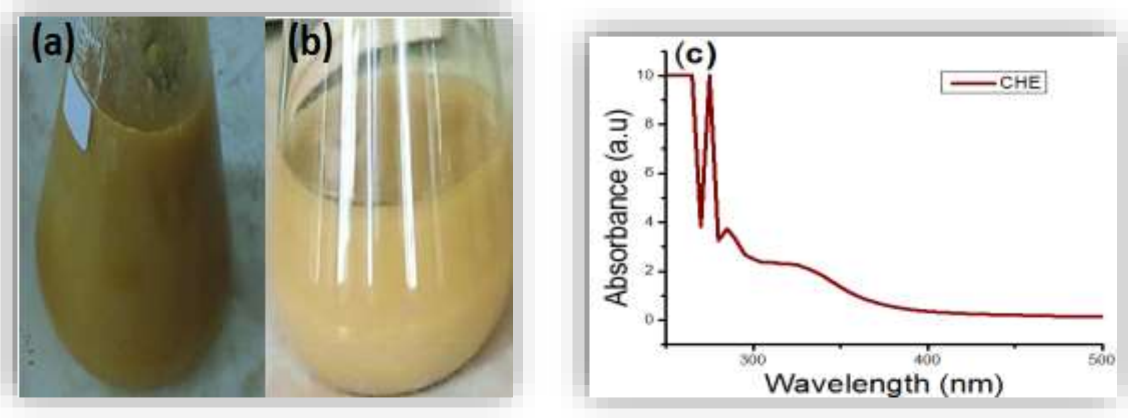

Fig.3. 2. Formation of ZnO-NPs and identification by the color change: (a) mixture of CHE with 0.5M zinc nitrate hexahydrate solution, (b) mixture color change after 1h reaction time and (c) UV-Vis's spectra of CHE.

3.3.3. FTIR spectroscopy analysis

To determine whether CHE functional groups linked to these reductive biomolecules exist and to identify the functional groups that assisted in the reduction of ZnO into NPs, FTIR spectra of the CHE and ZnO-NPs were analyzed.

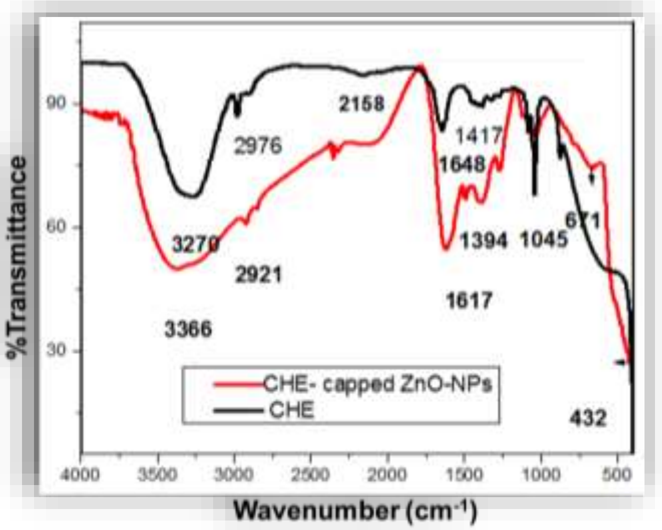

Fig.3. 3. FTIR spectra of CHE and CHE-capped ZnO-NPs

Fig. 3.3 shows the FTIR spectra of prepared ZnO and CHE wherein vibrational bands at 3270, 2976, 2158, 1648, 1417, and 1045 cm^{-1} are observed in relation to CHE. These bands are ascribed to the presence of O–H group of phenolic compounds, C–H from alkane groups, C=O group of amide stretching mode, and C=C group of aromatic compounds, respectively [229]. They demonstrate the presence of potential biomolecules in the CHE that could be responsible for the reduction of zinc ions and their interaction with the produced ZnO-NPs for stabilization. The FTIR spectra of ZnO-NPs revealed intense bands at 3366, 2921, 1617, 1394, 1036, 671 and 432 cm^{-1}. Shifting of some peaks were observed in the nanoparticles FTIR spectra: the O-H group band in CHE associated with the phenolics shifted from 3270 to 3366 cm^{-1}, indicating the phenol activity in the formation of ZnO-NPs [230]. Furthermore, the bands associated with the C=O group of the amide stretching mode (1648 cm^{-1}) shifted to 1617 cm^{-1}. The presence of a primary amide band suggests that proteins can bind to ZnO via carboxylate ions or free amine groups [227]. The amide functional group can act as a stabilizing agent reducing nanoparticle aggregation [25]**.** The bands associated with the C=C group of aromatic compounds (1417-1394 cm^{-1}), and the C-O stretching the frequency of phenolic group (1045-1036 cm^{-1}) inferred the role of these functional groups in the bio-reduction and stabilization of ZnO-NPs. Moreover, additional bands at 432 and 671 cm^{-1} indicate the formation of a Zn-O stretching vibration [231], [232].

3.3.4. Influence of synthesis parameters on the biosynthesis of ZnO-NPs using CHE

3.3.4.1.Effect of temperature

The response of biosynthesized ZnO-NPs to changes in temperature is depicted in Fig. 3.4a. It is revealed that an increase in temperature up to 80 °C (50, 65, 70, and 80 °C) caused an increase in the UV-Vis absorption spectra of ZnO-NPs. However, at 90 °C, the absorption peak was reduced, suggesting the agglomeration of ZnO-NPs at higher temperatures. The sizes of the particles were also estimated from the absorbance spectra using eq. (2.2) [233] and were 7.1 nm and 12.4 nm at 80 °C and 90 °C, respectively. This indicates that particle sizes became larger as the absorbance reduced (Fig.3.4 a) due to the decrease in particle concentration of nanoparticles [228]. Also, when the temperature increased from 65 to 80 °C, the peak absorption wavelength shifted from 355 to 350 nm, indicating that the small-sized NPs were formed at 80°C. Thus, it can be noted that, in the investigated temperature range, the highest activity of CHE as a reducing and capping agent for the formation of ZnO-NPs was found at 80 °C.

$$\mathrm{d(nm)} = \frac{-0.3049+\sqrt{(-26.23012+10240.72)/\lambda p(nm}}{-6.3829+2483.2/\lambda p(nm)} \qquad (3.2)$$

Where *d* and *λ*p are half of particle diameter and the peak absorbance wavelength (nm), respectively.

3.3.4.2.Effect of reaction time

The reaction time is crucial in the synthesis of nanoparticles [234]. Figure 3.4 b depicts the UV-Vis spectra of ZnO-NPs for various reaction times. As can be observed, the position and form of the absorption peak of ZnO-NPs are greatly dependent on particle size. UV-vis peaks displayed up to 360 nm at 1h reaction time. However, the absorption peak shifted to 370 nm and then to 385 nm as the processing time rose from 2 to 3 h, revealing that particle sizes have increased. Furthermore, as contact time increased to 4 h, the absorption spectra shifted to 390 nm in agreement with other studies [234]. Such shifts in UV-vis peaks to higher wavelengths indicate that the particles continued to grow, reducing the free surface energy by increasing particle size and decreasing surface area due to agglomeration [235], [236]. Based on the observation, the best processing time for the synthesis of ZnO-NPs using CHE was taken as 1 h because its UV-vis peaks showed up at the lowest absorption wavelength (360 nm) when compared to the other reaction times (2 h, 3 h, 4 h).

3.3.4.3.Effect of volume ratio of Zinc nitrate to CHE

The effect of CHE concentration on the quantity of NPs and the size of CHE-capped ZnO-NPs is shown in Fig.3.4c. As can be observed from this Figure, when the volume ratio of extract to precursor rose from 0.25 to 0.5, and to 1, the absorption peak at 357 nm increased (the SPR bands became sharper). This result is consistent with the study reported by Christensen et. al. [237], who found that using higher concentrations of extract raised the final concentration of NPs. The presence of larger concentrations of plant extract causes an increase in the amount of NPs. Overall, an equal volume ratio of CHE to precursor was found to be optimal for the synthesis of ZnO-NPs, resulting in well-capped nanoparticles with controlled and smaller particle sizes.

3.3.4.4.Effect of pH

The reduction of metal ions was also significantly influenced by pH. The primary impact of pH is a change in the electrical charges of biomolecules, which could alter their capacity for reducing and capping, and subsequently, the formation of NPs. In Fig.3.4d, at pH 6, absorption peaks related to ZnO-NP are not observed at all because both nano-ZnO and nano-Zn metal are highly soluble at low pH [32. 56]. At high pH, when the pH ascended from 10 to 12, the absorption peak shifted from 355 to 365 nm, which indicated the increment of particle size and reduction in the dissolution of zinc [239], [240]. As the pH increased to 14, the absorption peak further shifted to 370 nm with reduced intensity. This revealed that particle agglomeration is favored at higher pH [215]. Hence, pH 10 was considered optimal for synthesizing ZnO using CHE, similar to other studies [241].

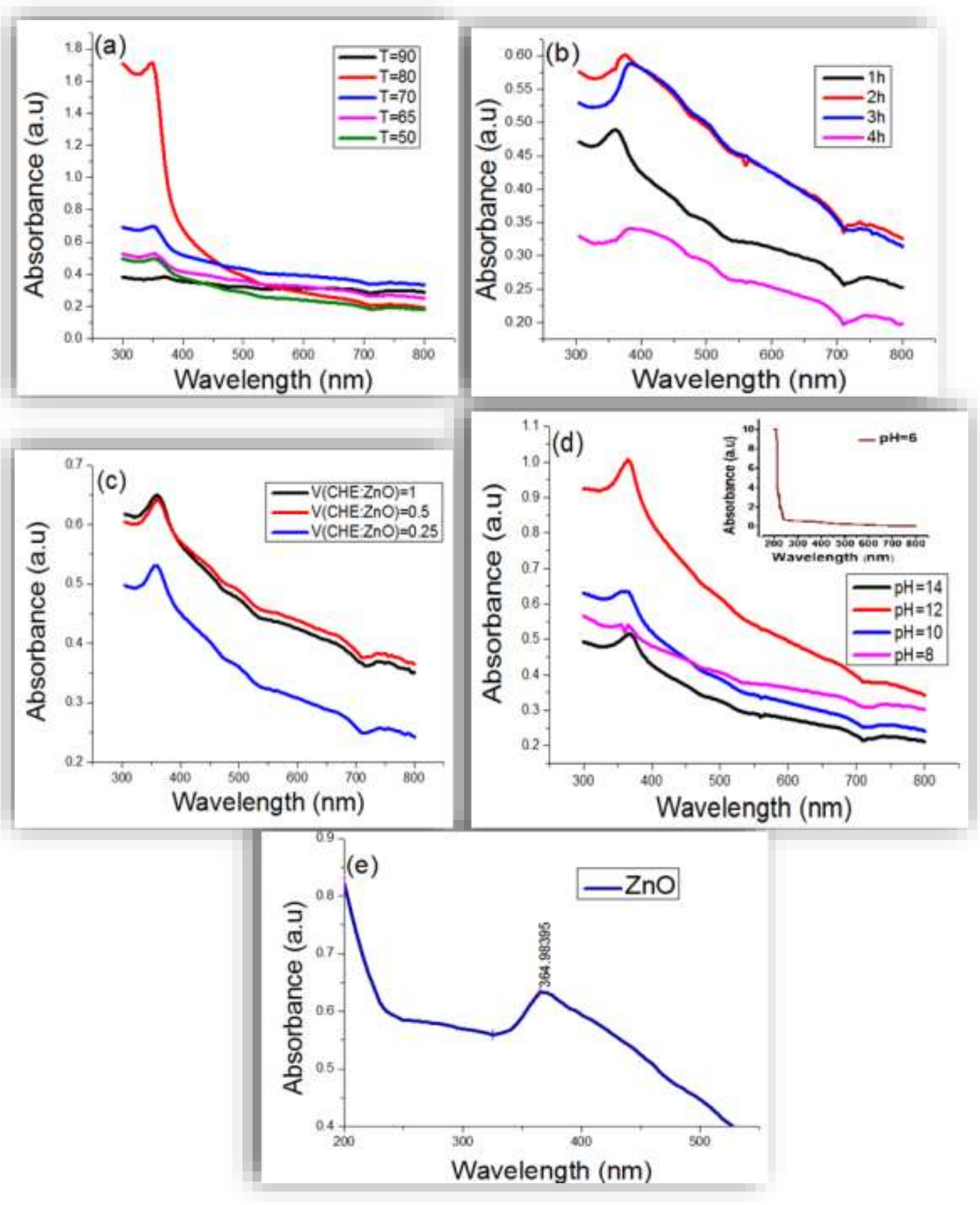

Fig.3. 4. UV-vis absorption spectra showing the effect of ZnO–NPs synthesis parameters: (a) temperature, (b) reaction time, (c) ratio of precursor to CHE, (d) pH, and (e) optimum condition

Thus, the synthesis of ZnO-NPs was carried out at the optimal processing condition for the subsequent sections. These were pH 10, 80 °C reaction temperature, 1 h reaction time, and at 1:1 volume ratio. These conditions produced ZnO-NPs with a strong absorbance peak at 365nm (Fig. 4e). This result is in agreement with the result demonstrated by [228].

3.3.5. Structural Characterization of the CHE capped ZnO-NPs

3.3.5.1.X-ray diffraction (XRD) analysis

The purity, crystal size and structures of CHE-capped ZnO-NPs were assessed using XRD (Fig. 3.5a). Various diffraction peaks were visible in the ZnO-NPs powder's X-ray diffraction (XRD) pattern at 2θ degrees of 31.62°, 34.27°, 36.07°, 47.42°, 56.47° related to the lattice plane of (100), (002), (101), (102) and (110) Miller indices, respectively. The whole XRD spectra is in perfect accordance with the crystallographic database's standards JCPDS 36-1451 [215] similar to earlier reports of [124], [204], [211], [242]. The broadening of the XRD peaks indicates that the synthesized material contains particles in the nanoscale range [243], and it additionally proves that the synthesized nano-powder is without impurities since XRD peaks other than ZnO peaks are not evident. The crystal size of the CHE capped ZnO-NPs was determined using the Debye-Scherrer formula shown below [244].

$$D = k\lambda / (\beta \ \mathrm{Cos}\theta) \tag{3.3}$$

Where D is the crystal size, Scherer constant (k) =0.95, λ is X-ray wavelength, i.e., 1.5406 Å, β= FWHM (Full Width at Half Maximum) and θ = Bragg's angle of diffraction.

The average crystal size of ZnO-NPs using the assigned five peaks in Fig.3.5a was approximately 9.8 nm. This showed that the synthesized CHE capped ZnO-NPs have good performance and CHE is a proficient reducing and stabilizing agent for the biosynthesis of ZnO-NPs due to its lower optimal size compared to ZnO-NPs prepared using other conventional techniques [206] or green synthesis mechanisms reported in the literature [215], [245], [246].

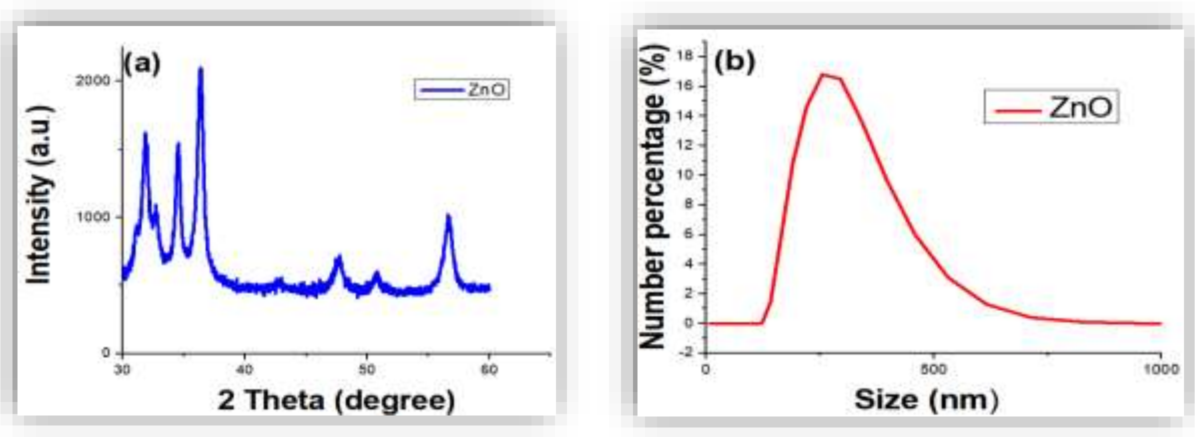

Fig.3. 5. (a) X-ray diffraction pattern of ZnO-NPs, and (b) Particle size intensity-based distribution of ZnO-NPs.

3.3.5.2. Dynamic light scattering and zeta potential analysis

A dynamic light scattering (DLS) technique was employed to investigate the size distribution and zeta potential of bio-synthesized ZnO-NPs in DI water. The average particle size of the biosynthesized ZnO-NPs, as determined using DLS, was found to be 281.89 nm (Fig.3.5b). Similar results were reported elsewhere [32], [66]. However, the aforementioned particle size, which resulted from DLS has become larger than the one estimated based on XRD spectra. Such size increment can be attributed to the repulsive forces between the NPs due to the capping of the NPs with the CHE. In addition, DLS displays a combination of particle size and surrounding diffuse layer of the particle, whereas XRD analysis is attributed only to particle size [215]. Surface analysis via BET revealed that ZnO-NPs had a surface area of 19.096 m^2/g at 150 °C degassing temperature.

Furthermore, the zeta potential of CHE synthesized ZnO-NPs was found to be -20.27mV indicating its potential to generate a colloidally stable [248]. A similar result was reported by [249]. This is attributed to the strong negative charge (strongly anionic), which causes the particles to repel each other with limited tendency to come together and aggregate or agglomerate due to the binding affinity of CHE compounds with the NPs [249], confirming the positive effect of the green synthesis approach on the nanoparticle dispersion capacity. The zeta potential of CHE capped ZnO-NPs is greater than that of ZnO-NPs synthesized utilizing Raphanus sativus var.

Longipinnatus extract as a bio reducing and stabilizing agent [215]. It is commonly accepted that zeta potential greater than or equal to 15 mV result in excellent nanoparticle stability [248].

3.3.5.3.Thermo-gravimetric and differential thermal (TGA/ DTA) analysis

Fig.3.6 reports the TGA/ DTA results of the ZnO-NPs. The figure shows an initial weight loss of 10% around 80 °C, which was attributed to the evaporation of residual moisture and decomposition of volatile phenolic compounds [250], The next stage is distinguished by a 6% weight loss at 236 °C. This stage was likely associated with the transformation of Zn-organic complexes into $Zn(OH)_2$ and the formation of ZnO [250]. The complete formation of ZnO-NPs and the degradation of organic compounds can be attributed to the 10.42% weight loss from 236 to 500 °C. At temperatures above 500 °C, a nearly constant value with a residual weight of 73.58% was observed. Fig.2.6 also shows a ZnO-NPs DTA plot with one endothermic and one exothermic peak at 50 °C and 303.4 °C, respectively. These peaks are associated with the removal of water molecules, organic compound decomposition, and the formation of ZnO-NPs.

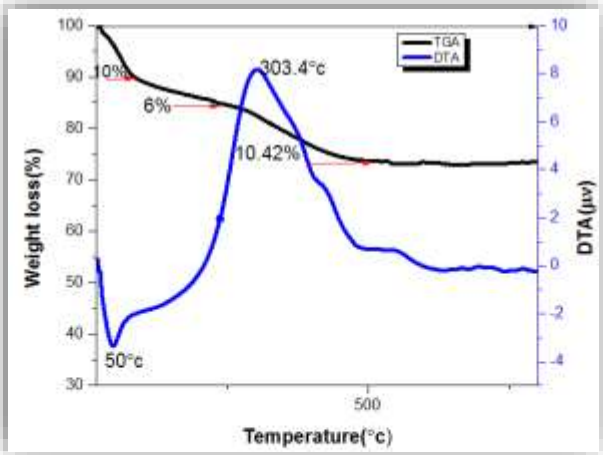

Fig.3. 6.TGA and DTA curves of the fabricated ZnO-NPs

3.3.5.4. Scanning Electron Microscopy Analysis (SEM)

Fig.3.7 depicts the SEM image showing the morphology of CHE capped ZnO-NPs. The presence of spherical nanoparticles was confirmed by SEM scans [124], [251], with aggregation indicating the availability of biological material recognized due to the polarity and electrostatic attraction of ZnO-NPs arising from the capping material [252]. The uniform spherical shapes of the primary particles in Fig.3.7, suggest that the manufactured NPs had not only low surface energy but also good thermodynamic stability, confirming the high zeta potential of the produced ZnO-NPs [253]. On the other hand, the average particle size of ZnO-NPs measured using an image processing software application [254] is around 22 nm, which is the ideal particle size when compared to earlier research on the green synthesis ZnO-NPs [255] Comparison of the XRD data and particle size of SEM indicated good alignment, displaying small crystal size and broad XRD peak resulting from the small particle size of the synthesized nanomaterial [240].

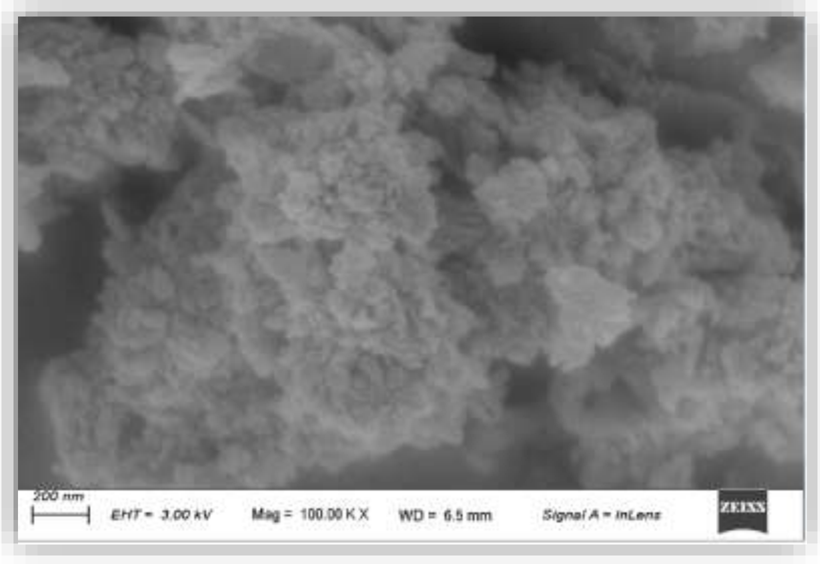

Fig.3. 7.SEM images of CHE capped ZnO-NPs

3.3.5.5. Energy dispersive spectroscopy (EDX) and EDS mapping analysis

To determine the elemental composition and stereochemistry of the synthesized zinc oxide NPs, an EDS analysis was performed. The weight percentages of the Zn and O elements detected in ZnO-NPs (Fig. 3.8a) were 75.9% and 24.1%, respectively. The presence of only Zn and O shows the NPs were synthesized in their pure chemical state. Single zinc and single oxygen peaks are found between 0 keV and 2 keV, and two zinc peaks between 8 keV and 10 keV. These results are consistent with previously reported findings of similar peaks in the biological synthesis of ZnO-NPs using the leaf extract of Candida albicans [256] and Calotropis gigantean [257].

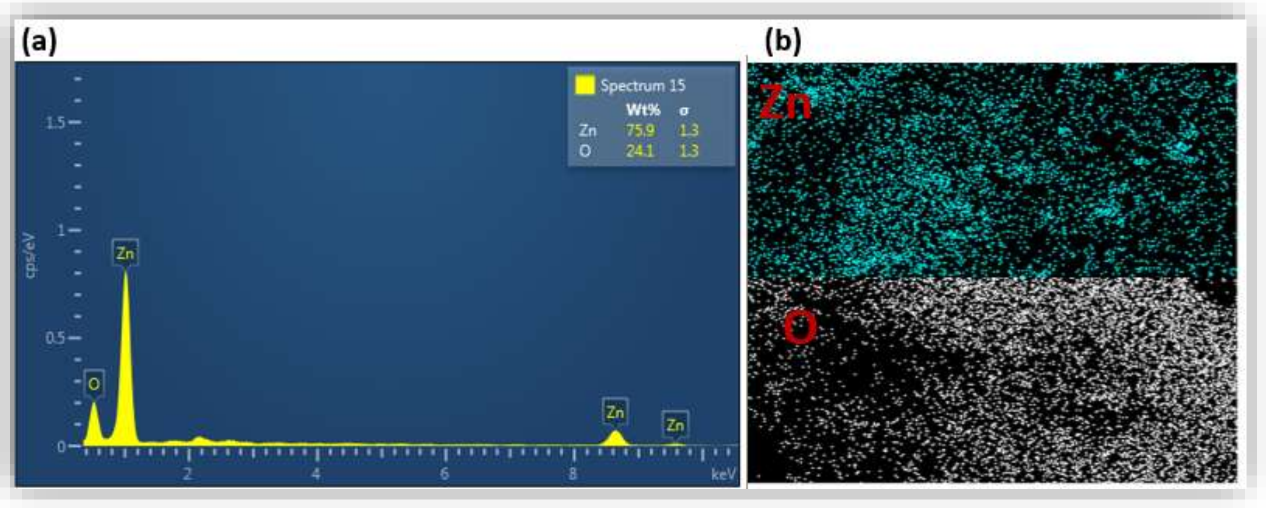

Fig.3. 8. (a) EDS spectrum of biosynthesized Zinc oxide NPs, (b) EDS mapping

The EDS elemental mapping of the ZnO product also describes the excellent uniformity in the spatial distribution of Zn and O (Fig.3.8b), indicating that the two elements are evenly distributed in the spherical structure. Based on the above experimental results, it is reasonable to deduce that spherical ZnO-NPs have been successfully prepared using CHE as reducing and capping agent.

3.3.5.6.Antibacterial activity of CHE capped ZnO-NPs

The antibacterial activities of CHE capped ZnO-NPs were evaluated using the agar well diffusion method, as shown in Fig.3.9 and Table 3.1. The presence of significant inhibition zones indicated that CHE capped ZnO-NPs have potent antibacterial activity against the bacterial pathogens *E. coli* and *S. aureus*. Different concentrations of ZnO-NPs (1 and 2 mg/mL) were tested against *E. coli* and *S. aureus*. The zone of inhibition against *S. aureus* and *E. coli* increased as the concentration of ZnO-NPs increased from 1 to 2 mg/mL. This suggests the antibacterial effectiveness of ZnO-NPs. The biocide activity of ZnO-NPs was determined by their concentration [13], [75], [259].

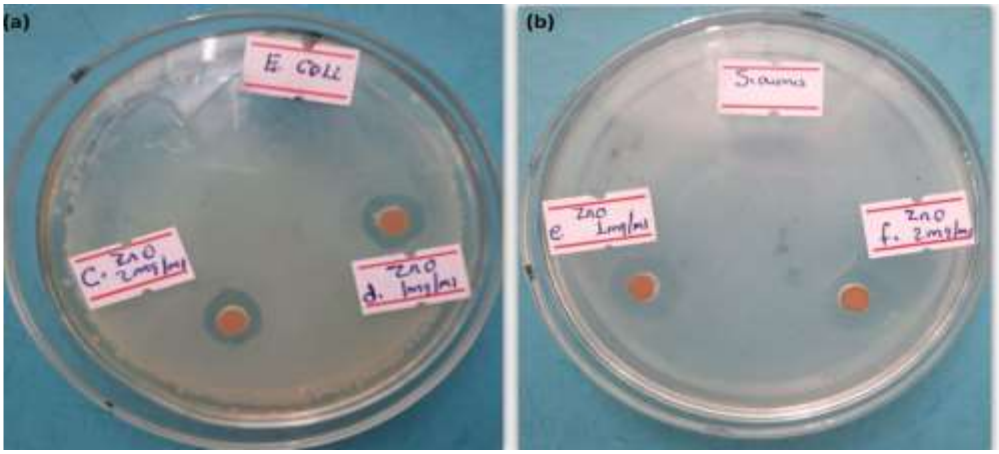

Fig.3. 9. Agar well diffusion for Antibacterial activity of ZnO-NPs against (a) *E. coli*. and (b). *S. aureus*

Table 3. 1**.** ZnO-NPS zone of inhibition on *E. coli* and *S. aureus*

NPS	**Concentration (mg/ml)**	**Zone of inhibition (in cm)**	
		E. coli	*S. aureus*
ZnO	1	1.2	1.3
	2	1.4	1.5

Moreover, the antibacterial activity of green process produced ZnO-NPs may also be related to the action of CHE, which acted as a capping agent in NPs, reducing particle size and enhancing antimicrobial properties [260]. Smaller particles offer a higher surface-to-volume ratio, which gives a more efficient means of antibacterial activity. The shape of NPs is also crucial for anti-pathogen efficacy [260]. Spherical NPs are particularly effective during antibacterial activity due to their capacity to quickly permeate pathogen cell walls [261]. SEM analysis revealed the aggregation of the ZnO- NPs (Fig 2.7), which has an impact on the penetration of nanoparticles into the biofilm matrix of bacteria [262]. However, the synthesized ZnO-NPs in this study has high biotoxicity property, has spherical shape, small particle size, and minimal level of aggregation due to the CHE capping of ZnO-NPs, resulting in excellent antibacterial efficiency (Fig.2.9).As a result, the spherical CHE capped ZnO-NPs have the potential and very useful in pathogen treatment.

3.4. Conclusions

In this study, a facile, efficient, environmentally benign method was developed for synthesizing ZnO-NPs, using indigenous CHE as a stabilizing and reducing agent without using any toxic chemicals. FTIR spectroscopy demonstrated the presence of phenolic functional groups in the CHE, and the quantified total phenolic compound was 14.2 mg GAE/g as gallic acid equivalent. This research utilized UV-Vis spectrophotometry to investigate the biosynthesis of ZnO-NPs using CHE. In order to achieve the best synthesis conditions, the effect of parameters, including pH, temperature, reaction time, and volume ratio of CHE to zinc precursors, were investigated. Spherical zinc oxide NPs with an average crystal size of 9.8 nm were produced using a one-to-one volume ratio of CHE to 0.5 M zinc nitrate under optimal conditions (pH 10, 80 °C, and 1h reaction time). From FTIR investigation, the indigenous CHE had functional groups that contributed to zinc ion reduction. XRD, SEM, EDS, and EDS mapping images validated the synthesis of spherical and pure crystal CHE-capped ZnO-NPs. The synthesized ZnO-NPs were stable due to a strong negative surface charge. It was noted that the CHE-capped ZnO-NPs have strong antibacterial activity against *E. coli* and *S. aureus* bacteria, which was evaluated from the formation of inhibition zones. These results indicated that the CHE has a strong potential for generating ZnO-NPs under optimal synthesis conditions. Because of the CHE capping, the ZnO-NPs have excellent thermal stability, nano-size, and mono-dispersion, and stable spherical shape, which is an appealing sustainable nanomaterial for the disinfection of pathogens in water and other applications. More research is needed to develop the immobilization of ZnO-NPs in polymer matrices and ensure separability after water disinfection.

CHAPTER FOUR

4. SYNTHESIS AND CHARACTERIZATION OF COFFEE HUSK EXTRACT (CHE) CAPPED Fe_3O_4/PU/ZNO NANOCOMPOSITES WITH ANTIMICROBIAL ACTIVITY

4.1. Introduction

Access to clean and safe water remains a critical global challenge, particularly in regions with limited sanitation infrastructure [53], [263] . One of the main challenges is the presence of waterborne pathogens, which severely contaminate drinking water sources. As detailed in Chapter 3 and the literature review section, various conventional methods are employed for water disinfection to eliminate pathogens and bacteria. However, each of these methods has its own set of limitations.

In recent years, nanotechnology has emerged as a promising alternative, offering innovative solutions for water treatment [23]. In Chapter 3, we discussed and reported the performance of CHE-capped zinc oxide nanoparticles (ZnO NPs) for the disinfection of waterborne pathogens. ZnO NPs exhibit strong antibacterial properties, primarily by puncturing bacterial cell walls and damaging internal organelles. Additionally, they generate reactive oxygen species (ROS), which, along with the release of Zn^{2+} ions into the solution, are highly detrimental to bacteria. [264].

However, ZnO NPs tend to aggregate into clusters in aqueous environments, reducing their effectiveness in interacting with microbial contaminants [260], [265] . To mitigate this issue, several approaches have been explored, including microwave solvothermal synthesis [266], sonication , and the use of capping agents [23]. Furthermore, numerous efforts have been made to enhance the stabilization and immobilization of antibacterial nanoparticles using various support substrates, such as aluminosilicate nanotubes [267], graphene sheets [268], silica [269], ZnO nanoroads [270], palygorskite clay [271] and talc clay [272].However, these approaches are often costly and may demonstrate limited effectiveness. Although these nanomaterials exhibit promising antibacterial properties, their practical performance is constrained by several factors. Aluminosilicate nanotubes and palygorskite clay frequently show low antibacterial activity due to limited surface functionalization and weak interactions with bacterial cells. Graphene sheets are prone to aggregation, which reduces their active surface area and antimicrobial efficiency. Silica nanoparticles generally require surface modification to achieve significant antibacterial effects, as bare silica has minimal intrinsic activity. ZnO nanoroads possess strong antibacterial potential, but their effectiveness depends heavily on particle size, morphology, and exposure conditions, which can limit practical applications. Similarly, talc clay exhibits only moderate antibacterial activity, often further restricted by poor dispersibility in aqueous media. Overall, while these substrates can stabilize and support antibacterial agents, their inherent material properties, surface interactions, and environmental factors frequently limit their effectiveness. In this study, indigenous volcanic PU and green-synthesized coffee husk extract (CHE) capped Fe_3O_4-NPs were used to address challenges in immobilization and aggregation of ZnO-NPs for antibacterial activity. The green synthesis of NPs using plant extracts is an environmentally friendly, economically viable, and cost-effective method that eliminates the need for hazardous and expensive chemicals. The biological method surpasses physical and chemical approaches in efficiency, although it requires time and multiple steps for preparation. Plant-mediated synthesis relies on the bio-reduction of NPs by various biomolecules present in plants, including vitamins, amino acids, proteins, phenolic acids, and alkaloids [273]. Phenolic acids, potent antioxidants with hydroxyl and carboxyl groups capable of metal binding, contribute to the colloidal stability of plant capped Fe_3O_4-NPs, enabling them to remain suspended in aqueous solution for extended periods without aggregation [274].

Although Fe_3O_4-NPs can function as peroxidase mimics, facilitating the breakdown of H_2O_2 for the oxidative removal of organic pollutants [275], they are not inherently antibacterial. However, in solution, Fe^{2+}/Fe^{3+} reacts with hydrogen peroxide to generate hydroxyl and peroxide radicals. This radical generation can synergize with ZnO-NPs to enhance their antibacterial characteristics [265]. The choice of PU as a support is rooted in its affordability, abundant in the earth's crust having, good porosity, and high silica and alumina content [276]. Pumice has been widely employed in various studies due to its ability to prevent agglomeration and immobilize NPs by dispersing NPs over its surface, as well as its excellent chemical stability and mechanical strength [31], [277], [278]. ZnO-NPs and Fe_3O_4-NPs have been synthesized using green synthesis methods for various applications [279]–[283]. However, to the best of our knowledge, no study has been conducted on the synthesis of CHE-capped magnetic pumice nanocomposite (CHE capped Fe_3O_4/PU-NC) and CHE-capped magnetic pumice zinc oxide nanocomposite (Fe_3O_4/PU/ZnO-NC). Additionally, this work has examined the composite effect on bare ZnO-NPs [284], which was previously published. The antibacterial properties of CHE capped Fe_3O_4/PU/ZnO-NC were also investigated against both *S. aureus* and *E. coli* bacteria.

4.2. Materials and Methods

4.2.1. Materials

Ferric chloride ($FeCl_3$, 99%), Ferrous sulphate ($FeSO_4.7H_2O$,99%),, ethanol (C_2H_5H,99.02%), and ammonium hydroxide (NH_4OH) were purchased from Loba Chemie Pvt. Ltd (Mumbai, India). Zinc nitrate hexahydrate (Zn $(NO_3)_2$. $6H_2O$,99 %) was purchased from Effective Laboratory Supplies (Selby, South Africa) and LB Agar medium from Sisco Research Laboratories (Mumbai, India). Local Coffee husk was gathered from West Harerge, Ethiopia. Volcanic PU was collected from the

Adulala PU area in Bishoftu District, Ethiopia. Standard bacterial strains of *S. aureus* (ATCC 25923) and *E. coli* (ATCC 25922) were obtained from Ethiopian Public Health Institute (EPHI). Gentamicin was obtained from Sigma-Aldrich (WI, USA). All compounds utilized were of analytical quality and all solutions were made with deionized (DI) water.

4.2.2. Methods

4.2.2.1. Synthesis of CHE capped Fe_3O_4-Nps.

For the synthesis of phyto-fabricated CHE-capped Fe_3O_4 nanoparticles (NPs), we followed the method described by A. V. Ramesh et al. [229] with a modification: In our modification, the nitrogen environment was omitted. This change was made because the coffee husk extract (CHE), used as a capping and reducing agent, naturally contains antioxidants and other phytochemicals that protect Fe^{2+} and Fe^{3+} ions from oxidation [218], [285], as shown in Fig.3.1. In brief, 1.39 g Ferrous Sulphate ($FeSO_4.7H_2O$) and 1.62 g Ferric Chloride ($FeCl_3.6H_2O$) were added in 100 mL of distilled water, well mixed and heated on hot plate until it reached 80 °C. Then, 10 mL of coffee husk extract was added. The extraction procedure followed the method outlined by Tsegaye et al in their study [284] . And thoroughly mixed with a magnetic stirrer at 300 rpm for 5 min. Then, ammonia was added to the mixture drop-wise until pH 9. After 30 min of continuous mixing, a black colored precipitate was formed which was then made to cool down to room temperature. Finally, the black precipitate was washed several times with distilled water until the pH of the washing solution reached 7 with DI water and dried in oven (80 °C for 24 h). Hence, it was stored in a sealed container until further use.

4.2.2.2. Synthesis of CHE capped Fe_3O_4 /PU-NC

The pumice was pretreated using the method described by Soleimani et al., [286]. 1 g of pretreated pumice was dispersed in 100 mL of DI water and sonicated for 10 min [287]. Subsequently, 1.39 g Ferrous Sulphate ($FeSO_4.7H_2O$) and 1.62 g Ferric Chloride ($FeCl_3.6H_2O$) were added and well stirred using magnetic stirrer (300 rpm) and then heated to 80°C. Afterwards, CHE was added and thoroughly mixed for 5 min. Ammonia was added to the mixture drop by drop until the pH reached 9.0. Consequently, a black-colored CHE capped Fe_3O_4 /PU-NC was obtained, which was cooled to room temperature after 30 min of continuous stirring. The black precipitate was separated using an external ferrite magnet and washed several times with deionized water until the pH of the wash reached 7. Finally, the obtained product (Fe_3O_4-NPs) was oven-dried (24h at 80 °C).

4.2.2.3. Synthesis of CHE capped Fe_3O_4/PU/ZnO-NC

CHE capped ZnO/Fe_3O_4/PU nanocomposite was prepared based on the method reported by

Sajjadi et al. [288], with slight modification. Briefly, 1.25 g magnetic PU nanocomposite, 35 mL of 0.5M Zinc nitrate, and 35 mL coffee husk extract were placed in a 250 mL round-bottom flask. The reaction mixture was stirred for 1h at 80 ºC using magnetic stirrer at 300 rpm and then cooled to room temperature. The CHE capped ZnO/Fe_3O_4/PU nanocomposite product was separated with an external ferrite magnet and washed 3 times with ethanol and DI water (until pH was 7.0), and finally dried in vacuum oven at 60 °C overnight.

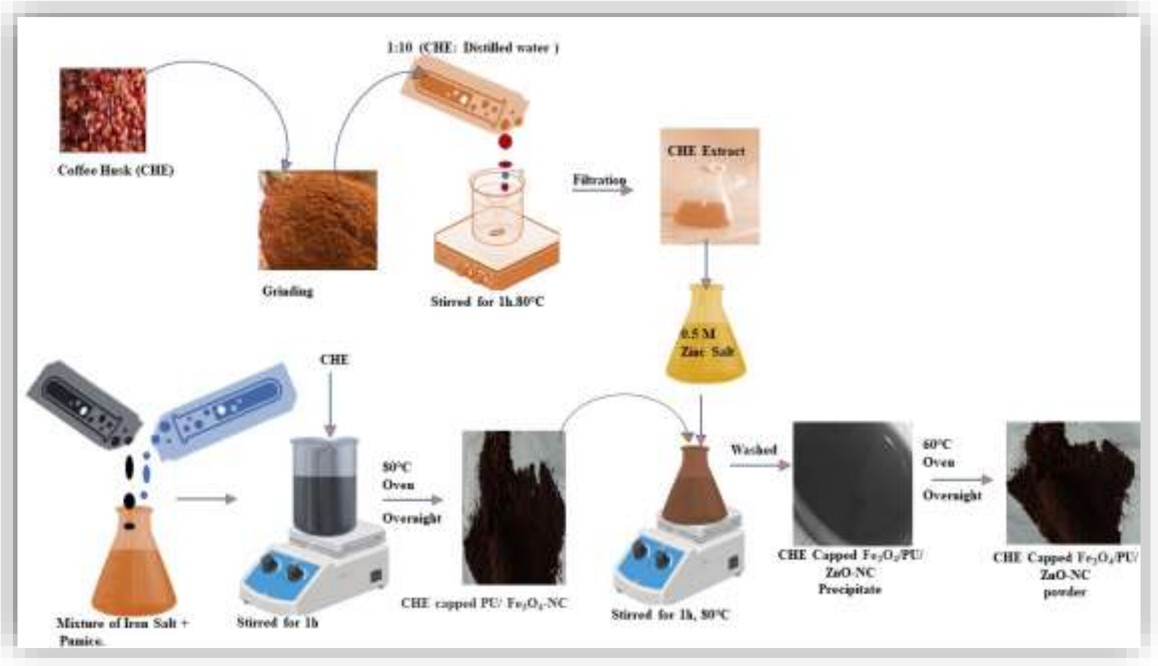

Fig.4. 1. Schematic Diagrams of the Biosynthesis of CHE capped Fe_3O_4/PU/ZnO -NC.

4.2.2.4.Physicochemical Characterization

The synthesized material was characterized using the methods described in Chapter 3, Section 3.2.2.5, which include X-ray diffraction, scanning electron microscopy with energy-dispersive X-ray spectroscopy, thermogravimetric analysis, dynamic light scattering, Fourier-transform infrared spectroscopy, and Brunauer–Emmett–Teller surface area analysis.

4.2.2.5. Data Analysis

The raw data from the characterization instrument was analyzed and graphed using Origin software. The same software was used to calculate the mean and standard deviation of the data.

Additionally, ImageJ software was employed to extract the average particle size from the SEM image. In addition, all statistical analyses regarding the antimicrobial activity of zone of inhibitions were performed by using the IBM SPSS (v. 26.0). All of the collected data were analyzed using one-way analysis of variance (ANOVA).

4.2.2.6. Antibacterial performance evaluation

The antibacterial performance evaluation was conducted using the method described in Chapter 3, Section 3.2.2.6. The agar diffusion method was employed to assess the antibacterial properties of Fe_3O_4, PU, and CHE-capped Fe_3O_4/PU/ZnO nanocomposites. The details of the procedure are provided in the referenced section.

4.3. Results and discussions

4.3.1. X-ray fluorescence (XRF) analysis of samples

Analyses of the XRF data confirmed that the collected volcanic rock was pumice (PU), assessed the effects of acid treatment on PU, and verified the composite formation of Fe_3O_4 and PU. The major and minor element compositions of the samples are expressed as weight percent (wt%) of oxides (Table 4.1). The table illustrates that the pumice powder contained both major (SiO_2, Al_2O_3, CaO, Fe_2O_3) and minor components (K_2O, MgO, MnO, Na_2O, P_2O_5, TiO_2, and H_2O). Particularly noteworthy is the high silica content (over 50%), confirming the material as pumice [289]. Furthermore, acid-treated PU (Table 4.1) has increased the SiO_2 and Al_2O_3 content, thereby enhancing the quality of PU with reduced metallic impurities due to acid leaching of heavy metals**.** The confirmation of Fe_3O_4/PU-NC formation (Table 4.1) revealed that the magnetic PU nano-composite contains 42.88% Fe_2O_3, which is higher than the PU content of Fe_2O_3 (4.68%), indicating the successful deposition of the magnetic Fe_3O_4 onto the PU substrate.

Table 4. 1. Oxide composition of pumice (PU), Acid treated PU (At-PU) and Fe_3O_4/PU (%)

Sample	Oxide Composition (wt%)											
	SiO_2	Al_2O_3	Fe_2O_3	CaO	MgO	Na_2O	K_2O	MnO	P_2O_5	TiO_2	H_2O	LOI
Fe_3O_4/PU	24.98	9.36	42.88	<0.01	<0.01	3.4	5.16	<0.01	0.19	<0.01	4.31	10.50
At- PU	69.8	11.31	4.5	<0.01	<0.01	2.96	4.98	<0.01	0.10	<0.01	1.54	5.81
PU	69.76	10.49	4.68	0.62	0.18	3.02	5.14	<0.01	0.07	<0.01	1.58	5.60

4.3.2. Formation of CHE capped Fe_3O_4-NPs confirmation

The antioxidant properties of these phyto- fabricated NPs, coupled with their safety profile, render them particularly effective at reducing metal ions [30]. The formation of CHE capped Fe_3O_4-NPs was confirmed by the color change in the mixture of iron salt from brown to black precipitate (**Fig.4.2a and b**), and its magnetic property was demonstrated by the attraction of the black precipitate with an external magnet, as depicted in **Fig.4.2c**. These observations indicate that the presence of -OH groups in the caffeine phytochemicals of CHE played a significant role in reducing the iron salt to Fe_3O_4 NPs [218], [284].

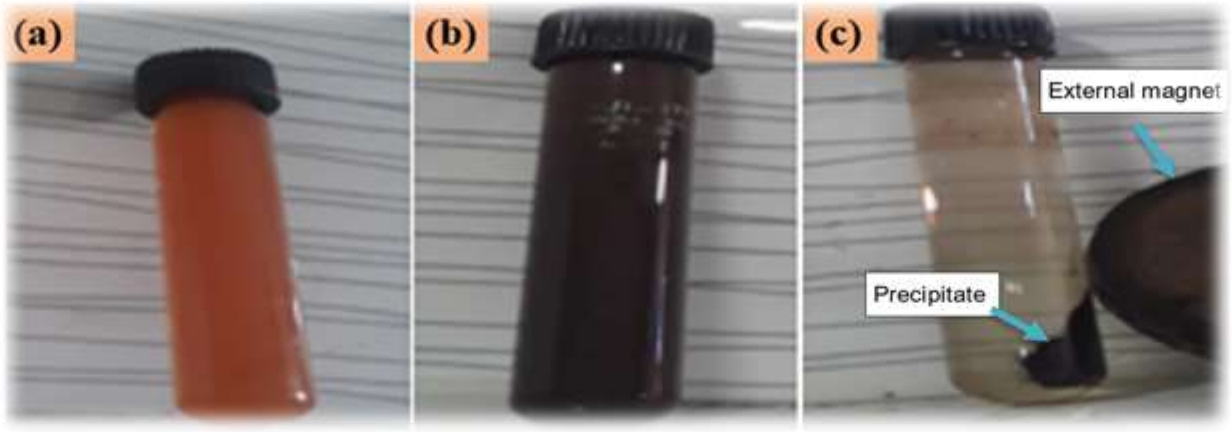

Fig.4. 2.(a) Mixtures of iron salt (b) CHE capped Fe_3O_4-Nps Formation (c) External magnetic attraction of CHE capped Fe_3O_4-NPs

4.3.3. Impact of CHE on bio synthesized CHE capped Fe3O4-Nps, CHE capped Fe3O4/PU/ZnO-NC and their Structural Characterizations

4.3.3.1. Scanning Electron Microscopy (SEM) analysis

SEM was employed to assess the surface morphology and particle size of CHE capped Fe_3O_4/PU/ZnO-NC. As can be seen in Fig. 4.3a, PU exhibits a porous structure with a tortuous shape. These porous and tortuous structures support strong nanoparticle immobilization due to their complex pore network and large internal surface area. Such structures provide suitable substrates for the formation of CHE-capped Fe_3O_4 nanoparticles and ZnO nanoparticles, as indicated by the presence of rectangular-shaped particles in Fig 4.3b, [287]. Rod-shaped CHE capped Fe_3O_4-NPs and spherical shaped ZnO-NPs were observed on the surface of PU particles, which are denoted by arrows and circles in Fig. 4.3b, respectively. Additionally, the SEM images were used to determine the particle size distribution of CHE-capped Fe_3O_4/PU/ZnO-NC using ImageJ software (version 1.8.0 and compared to CHE-capped ZnO-NPs) [33]. The histograms of

CHE-capped Fe_3O_4/PU/ZnO-NC (Fig. 3.3c) reveal smaller particles with an average size of 11±1.4 nm compared to bare CHE-capped ZnO-NPs with an average size of 22±1.5 nm in appendix (Fig,S_1) [283].

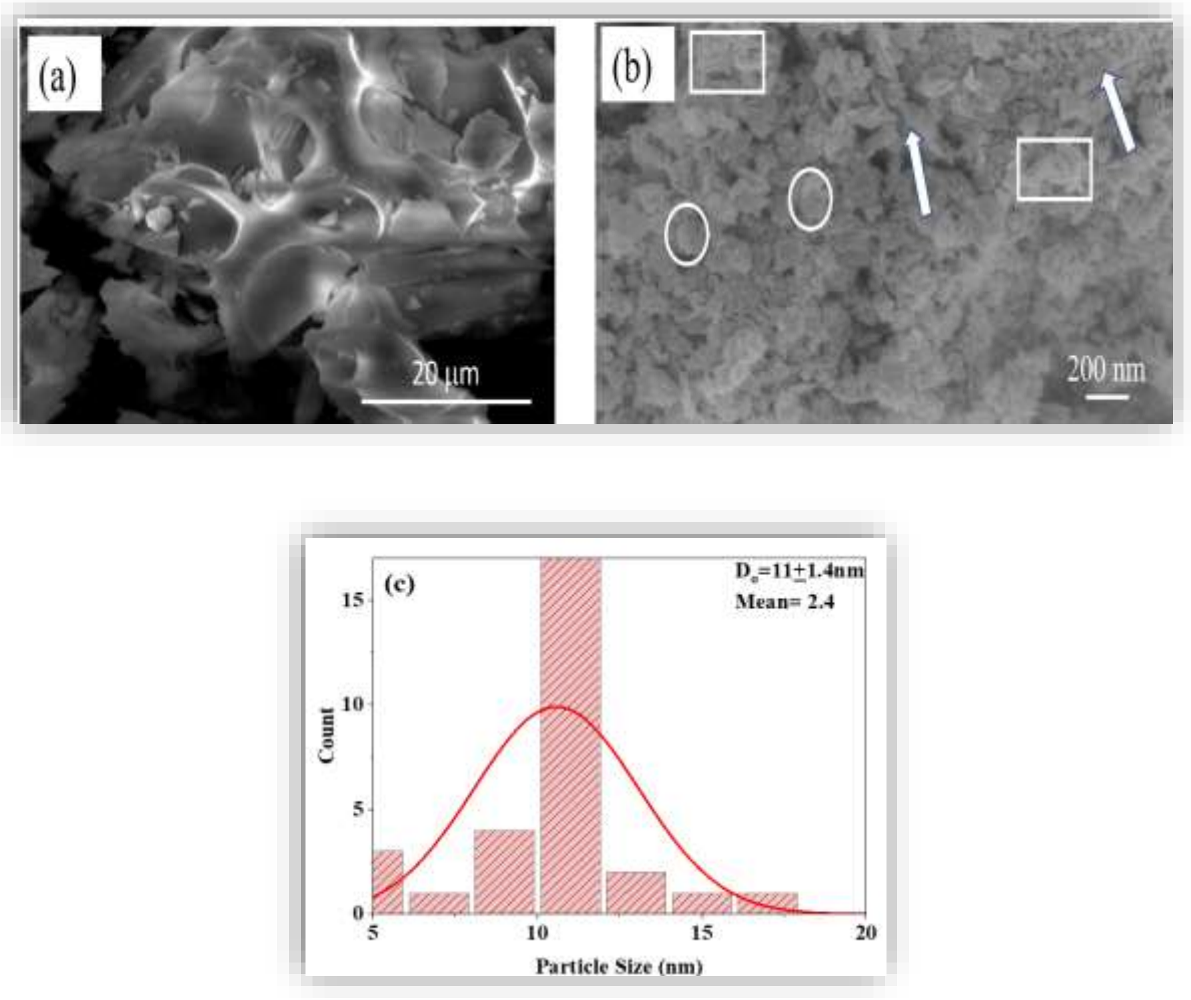

Fig.4. 3. SEM images of (a) Pumice, (b) CHE capped Fe_3O_4/PU/ZnO-NC, and (c) Particle Size distribution.

4.3.3.2.Energy dispersive spectroscopy (EDS) mapping and analysis

Energy dispersive spectroscopy (EDS) was utilized to unequivocally confirm the presence of the anticipated elements in the synthesized nanomaterial. Fig.4.4a demonstrates that PU’s elemental composition includes Fe, Al, Si, O, and K, which validating the accuracy of the raw material collected from PU site, which aligns with XRF analysis, with prominent Si peak at 1.8 keV.

Additionally, Fig. 4.4b reveals that the elemental composition of CHE capped Fe_3O_4/PU/ZnO- NC exhibits peaks around 0.9, 6.4, and 7.1 keV corresponding to the binding energies of Fe [290] , along with an oxygen peak at 0.5 keV. These results are consistent with those obtained by Rahman et al [291]. Two strong zinc peaks were identified at 1 keV and 8.6 keV, corroborating findings from Shamsuzzaman et al. [292], and the presence of Si in the composite was confirmed by the 1.8 keV peak. The weight percent composition of the observed elements in the CHE capped Fe_3O_4/PU/ZnO-NC (Fig.4.4b) was 74.3% Zn, 1.6% Fe, 24% O, and 0.10% Si. Overall, EDS spectrum analysis showed that the synthesized materials constituted approximately 100 % of the identified elements, indicating high purity and free of extraneous impurities.

EDS elemental mapping of PU and CHE capped Fe_3O_4/PU/ZnO-NC is presented in Fig. 4.4a and 4.4c. The PU EDS maps (Fig. 4.4a) demonstrate the purity of the employed PU as well as the evenly distributed elements O, Si, Al, and K. The CHE capped Fe_3O_4/PU/ZnO-NC EDS mapping (Fig. 4.4c**)** shows good homogeneity and spatial dispersal of Fe, Si, Al, Zn, and O, showing that all elements are uniformly dispersed and that CHE capped Fe_3O_4/PU/ZnO-NC was effectively Phyto-fabricated.

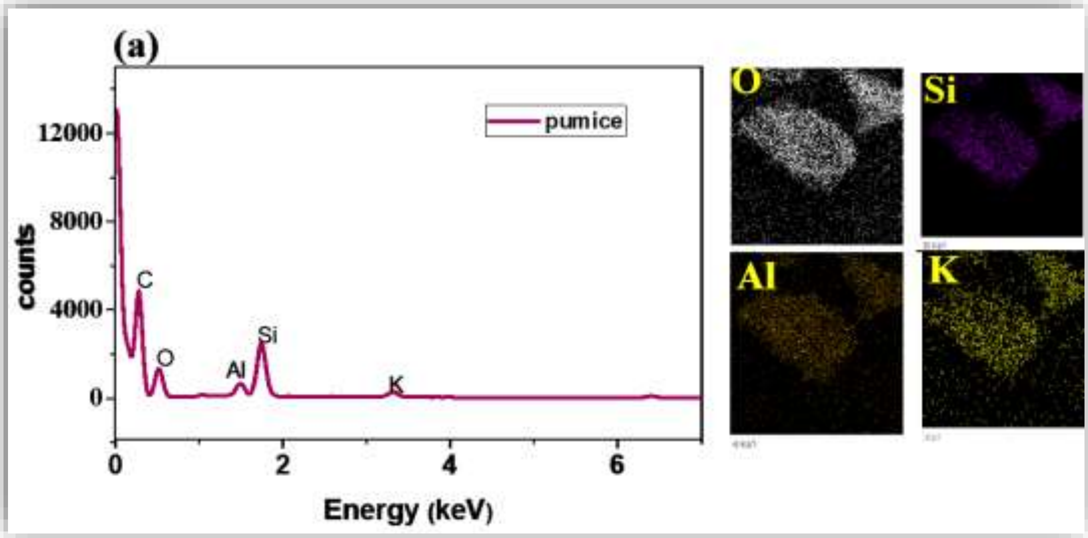

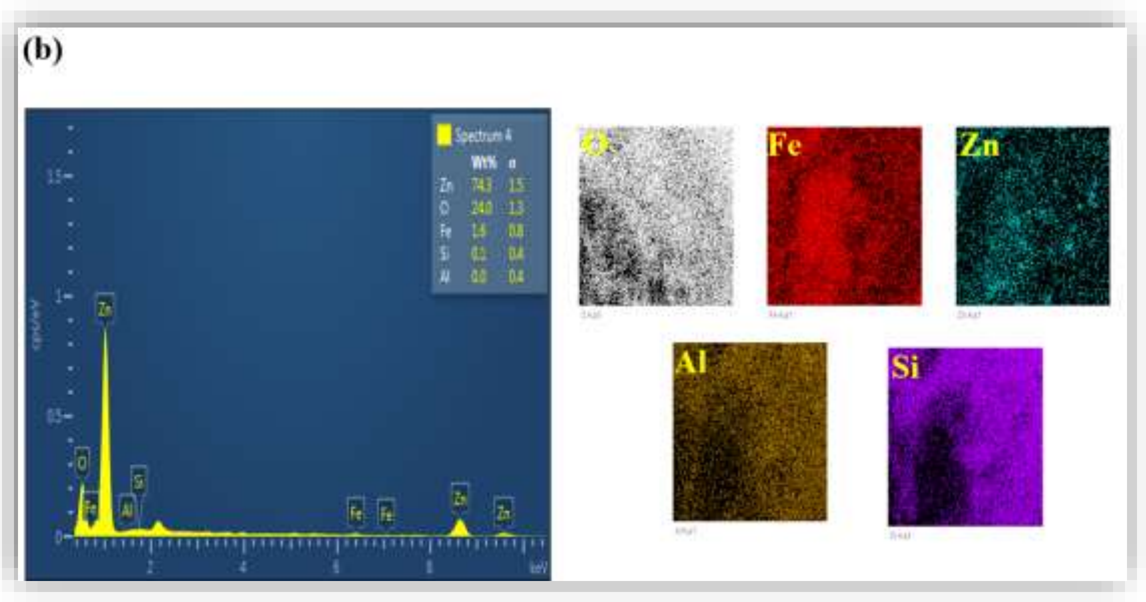

Fig.4. 4. EDS spectrum and elemental mapping of (a) Pumice and (b) CHE capped Fe_3O_4/PU/ZnO NC

4.3.3.3. X-ray diffraction (XRD) analysis

Crystal size, structures, and formation of PU and the synthesized NC were assessed using X-ray diffraction (XRD). XRD patterns of PU, CHE capped Fe_3O_4/PU-NC, and CHE capped Fe_3O_4/PU/ZnO-NC are shown in Fig. 4.5. According to the XRD patterns (Fig. 4.5a), the broad maximum peak at 2θ = 15–30° of the diffractogram profile can be associated with an amorphous matrix (glass), similar to the study reported by Correcher et al. [293]. Another study also found an XRD pattern of amorphous PU with a broad peak in the 20°-30° range [294]. For CHE capped Fe_3O_4/PU-NC) in Fig. 4.5b, several major diffraction peaks at 2θ degree of 30.6°, 35.86 ^{o}, 43.46 ^{o}, 54.01 ^{o}, 57.4 ^{o} , 63.60 ^{o} and 74.46 ^{o} were observed for CHE capped Fe_3O_4-NPs corresponding to (220), (311), (400), (422) (511) (440) and (620), respectively, as per standard data for magnetic cores (JCPDS card No.75-0449) [50, 51]. Additionally, new peaks at 18° were observed due to the amorphous structure of PU. The XRD spectra of CHE capped Fe_3O_4/PU/ZnO -NC (Fig. 4.5c) revealed common peaks with paternal CHE capped Fe_3O_4-NPs (Fig. 4.5b) and ZnO-NPs (Fig. 4.5d) (30.6 ^{o}, 31.62 ^{o}, 34.27 ^{o} , 36.1 ^{o}, 43.62 ^{o}, 47.42 ^{o}, 54.8 ^{o}, 56.47 ^{o} , 57.4 ^{o} , 63.60 ^{o} and 74.46 ^{o}) [249] as well as PU peak formation at 18^{o} similar to CHE capped Fe_3O_4/PU-NC **(**Fig. 4.5b**).** Furthermore, the crystal size of the synthesized material was assessed using Scherrer's method (Eq.4.1).

$$D = k\lambda / (\beta \cos\theta) \quad (4.1)$$

Where D is the size of the crystal, λ is the X-ray wavelength, β – full width at half maximum intensity of the peak [rad], and θ = Bragg's angle of diffraction.

Using equation (4.1), the average crystal size of CHE capped Fe_3O_4 /PU-NC was estimated to be 4.3 nm. On the contrary, the average particle size of CHE capped Fe_3O_4/PU/ZnO - NC particles was determined to be 6.17 nm. Comparing the crystal size of pure Zn--NPs (9.8 nm) [284] to CHE capped Fe_3O_4/PU/ZnO-NC in this study (6.17 nm), the composite's particle size had reduced by 37% than the pure CHE capped ZnO-NPs. These results aligned well with the SEM particle size analysis observation (11nm). Thus, both XRD and SEM indicate that the composite has smaller particle sizes than the bare CHE capped ZnO-NPs.

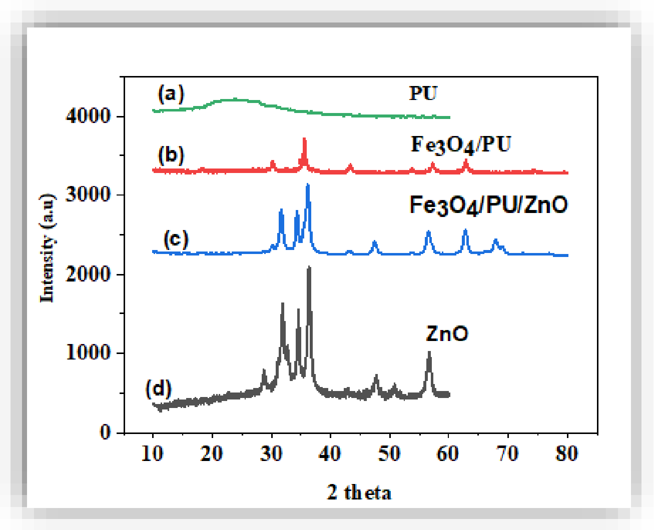

Fig.4. 5. XRD patterns of (a) PU (b) CHE capped Fe_3O_4/PU (c) CHE capped Fe_3O_4/PU/ZnO (d) CHE capped ZnO NC.

4.3.3.4.Nitrogen adsorption-desorption study

The N_2 gas Brunauer-Emmett-Teller (BET) method was employed to calculate the surface areas of the synthesized materials. The surface areas of PU, CHE capped Fe_3O_4-NPs, CHE capped Fe_3O_4/PU-NC, and CHE capped Fe_3O_4/PU /ZnO-NC were 8.9 m^2/g, 143.9 m^2/g, 66.6 m^2/g, and 47.2 m^2/g, respectively. When compared to other materials, CHE capped Fe_3O_4-NPs exhibited the largest surface area, enabling CHE capped Fe_3O_4/PU/ZnO-NCs to significantly enhance the surface area of pure ZnO-

NPs [284]. This BET investigation corroborated the findings of XRD, DLS, and SEM, affirming the beneficial effects of CHE-capped Fe_3O_4/PU/ZnO-NC on the particle size and surface area enhancement of pure CHE-capped ZnO-NPs.

4.3.3.5. FTIR studies

FTIR analysis was employed to identify the functional groups present in the nanocomposite and elucidate the contribution of CHE phenolic compounds to the formation of Fe_3O_4 NPs, ZnO-NPs and nanocomposites. It also served as a reliable tool for confirming the discernible presence of PU material within the synthesized nanocomposite. Fig.4.6 illustrates that the functional group of CHE capped Fe_3O_4-NPs (3215,1620,1432,1116 and 534 cm^{-1}) are significantly influenced by the presence of caffeine in the CHE phenolic molecule (3278, 2976, 1648, 1417, and 1045 cm^{-1}) [284]. The O-H of the phenols serves as a reducing agent in the formation of magnetic CHE capped Fe_3O_4 NPs, as evidenced by the band shifting from 3278 to 3215 cm^{-1} (Fig.4.6) [229]. The bands related to carboxylic acid group (C=O) shifted from 1648 to 1620 cm^{-1}. Additionally, the bands associated with the aromatic compound C=C band shifted from 1417 to 1432 cm^{-1}, and the aliphatic group C-O (1045-1116 cm^{-1}) also exhibited shifts [297]. A new band at 534 cm^{-1} corresponding to the vibration stretching of Fe-O [298] was also observed. These observations indicate that CHE actively participates in the formation of CHE-capped Fe_3O_4-NPs through band shifting of the functional groups of phytochemicals and the formation of new Fe-O bands. Confirmation of the identity of PU and its incorporation into CHE capped Fe_3O_4 /PU-NC and CHE capped Fe_3O_4 /PU /ZnO-NC (Fig.4. 6) was corroborated by an additional Si-O-Si stretching vibration peak at 1006 cm^{-1} [299]. It is important to note that the high silicon oxide composition was validated in XRF analysis (Table 4.1). The merging peaks attributed to various metal oxides present in PU (such as Al_2O_3) were also discerned [31], and the stretching vibration of Si-O-Al was observed at ~ 775 cm^{-1}. In addition, the FTIR spectrum of CHE capped Fe_3O_4/PU/ZnO-NC in Fig.4.6 exhibited a characteristic Zn–O stretching at 428 cm^{-1}, confirming the formation of ZnO-NPs [300]. Meanwhile, peaks observed at 560 cm^{-1} and 554 cm^{-1} in CHE capped Fe_3O_4 / PU-NC and CHE capped Fe_3O_4 /PU /ZnO-NC could be assigned to the Fe-O stretching mode [55, 57, 58]. Overall, the FTIR analysis revealed that the phytochemicals found in coffee husk extract act as reducing, capping, and stabilizing agents for the formation of CHE capped Fe_3O_4 /PU /ZnO - NC.

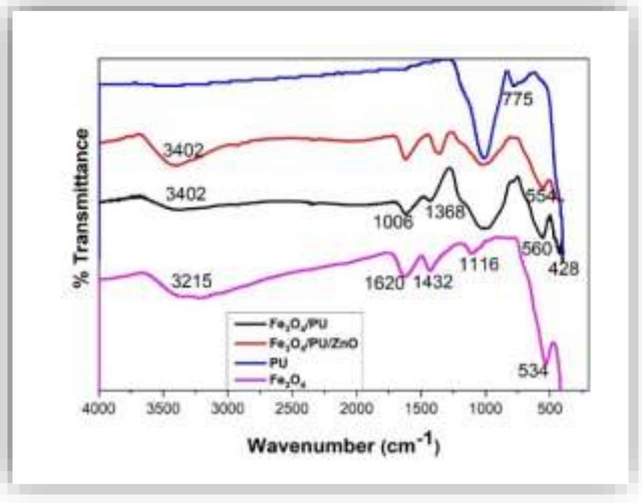

Fig.4. 6. FT-IR spectra of PU, CHE capped Fe_3O_4-NPs, CHE capped Fe3O4 /PU-NC and CHE capped Fe_3O_4/PU/ZnO-NC.

4.3.3.6. Dynamic light scattering (DLS) Analysis

The DLS method was used to evaluate the size distribution and zeta potential of phyto-fabricated NCs in aqueous solutions in order to study the NPs stability. The zeta potential of CHE capped Fe_3O_4/PU-NC, PU, and CHE capped Fe_3O_4 /PU /ZnO-NC was measured to be -18 mV, -15 mV, and -23.8 mV, respectively. This indicates that the zeta potential of CHE capped Fe_3O_4 /PU /ZnO-NC was higher than ZnO-NPs [284], indicating that the addition of magnetic PU to CHE capped ZnO-NPs can improve the stability of CHE capped Fe_3O_4/PU/ZnO NC. This indicates that the suspensions' zeta potential is larger than or equal to 15 mV, implying that these NPs are colloidally stable [248].

Form the DLS measurement, the mean particle size of the synthesized PU, CHE capped Fe_3O_4-NPs, CHE capped Fe_3O_4/PU-NC, and CHE capped Fe_3O_4 /PU /ZnO-NC were 76.29 nm, 32.91, 72.7 nm, and 46.13 nm, respectively, as shown in Fig.4.7. The particle size of green synthesized magnetic NPs were similar to those reported in previous research [60, 61]. The particle size of pure ZnO-NPs was notably high (216 nm) [284] compared to CHE capped Fe_3O_4/PU/ZnO-NC, likely because the particle size of CHE capped Fe_3O_4-NPs is very low and has a high surface area, capable of enhancing the particle size of bare ZnO-NPs. This suggests the biosynthesis of hybrid ZnO-NPs and CHE capped Fe_3O_4/PU-NC are effective combinations for enhancing particle sizes.

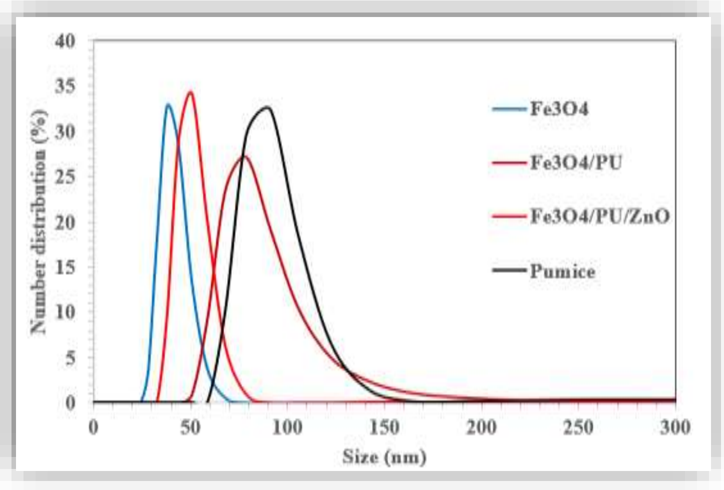

Fig.4. 7. Particle size intensity-based distribution PU, CHE capped Fe_3O_4 -NPs, CHE capped Fe_3O_4/PU-NC, and CHE capped Fe_3O_4/PU/ZnO-NC.

4.3.3.7. Thermal stability analysis

Thermogravimetric and differential thermal analyses (TGA/ DTA) tests were conducted on the CHE capped Fe_3O_4 / PU-NC and CHE capped Fe_3O_4/PU/ZnO nanocomposites, and the TGA curves are presented in Fig.4.8a and b. The results indicate an initial weight loss of 3% around 98 °C and 4% at 179 °C for CHE capped Fe_3O_4/PU-NC and CHE capped Fe_3O_4/PU/ZnO-NC, respectively. This weight loss is likely attributed to absorbed moisture evaporation and the decomposition of volatile phenolic compounds [250].

The subsequent phase is characterized by a 3.56% weight loss for CHE capped Fe_3O_4 /PU-NC in the temperature range of 98 to 260 ^{o}C. This stage is associated with the transformation of Fe $(OH)_2$ to CHE capped Fe_3O_4-NPs [301]. In the case of CHE capped Fe_3O_4/PU/ZnO-NC, the 4.4% weight loss occurring at temperatures ranging from 179 to 275 °C can plausibly be attributed to the conversion of Fe $(OH)_2$ into CHE capped Fe_3O_4-NPs and Zn-organic complexes into Zn $(OH)_2$ and the subsequent production of ZnO-NPs.

The third phase is shown in Fig.4.8a and b, which entailed the last and complete production of CHE capped Fe_3O_4/PU-NC and CHE capped Fe_3O_4/PU/ZnO-NC in the temperature ranges of 260 to 686 ^{o}C with 5.9% weight loss and 275 to 576 ^{o}C with 5.6% weight loss, respectively. For CHE capped Fe_3O_4/PU-NC, no additional degradation or weight loss occurred above 686 °C, retaining around 88%

of its weight. On the other hand, the CHE capped Fe_3O_4/PU/ZnO-NC retained 86% weight above 576 °C with no further weight loss with temperature increase. Due to the inherent thermal stability of PU, the CHE capped Fe_3O_4/PU/ZnO-NC [290] was made to have better thermal stability than pure ZnO-NPs (73.58%) [284]. Pumice can sustain the thermal stability of NPs until temperatures reach 900°C [305].

DTA curves of CHE capped Fe3O4 /PU-NC displayed exothermic reactions as temperature increases, with peaks at 445 °C and 756 °C (Fig. 4.8a). CHE capped Fe_3O_4/PU/ZnO-NC exothermic reactions with peaks at 312 °C and endothermic reactions with peaks at 76 °C (Fig. 4.8b) were notable. The decomposition of the stabilizing and reducing agents of various organic compounds was revealed at lower endothermic temperature peaks. Exothermic peaks of 445 °C and 312 °C were associated with the formation of CHE capped Fe_3O_4-Nps and ZnO- NPs [306], and exothermic peaks at 756 °C revealed that PU's degradation [307].

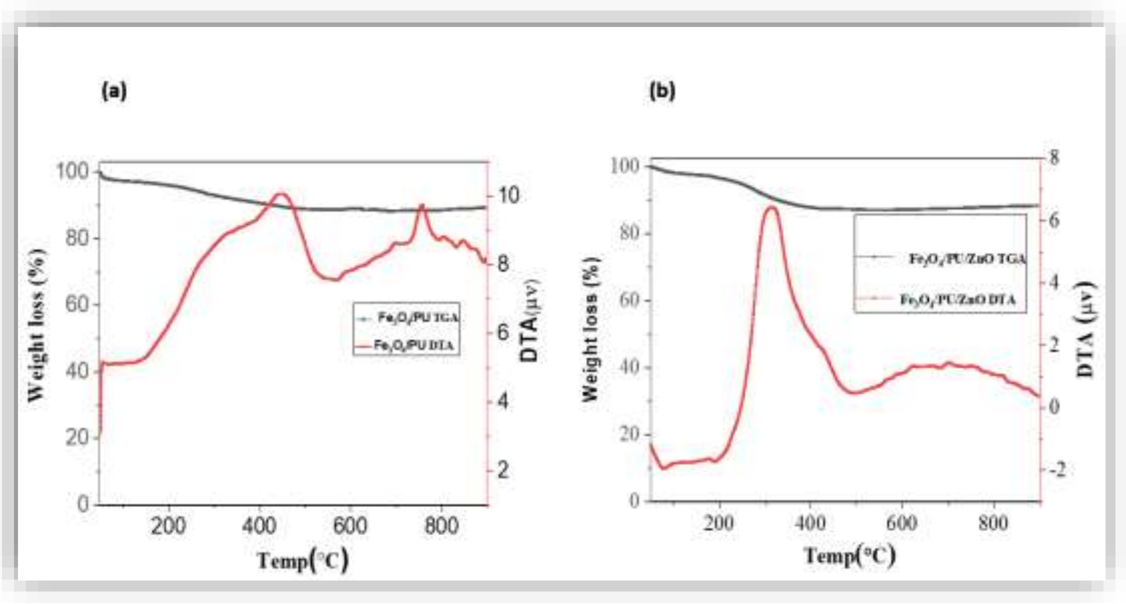

Fig.4. 8. TGA and DTA curves of the synthesized (a) CHE capped Fe_3O_4 /PU-NC (b) CHE capped Fe_3O_4/PU/ZnO – NC,

4.3.3.8.Antibacterial activity of PU, CHE capped Fe3O4 NPs and CHE capped Fe_3O_4/PU/ZnO NC.

The antibacterial activity of PU, CHE-capped Fe_3O_4 nanoparticles, and CHE-capped Fe_3O_4/PU/ZnO nanocomposites was investigated against *Staphylococcus aureus* and *Escherichia coli* using the agar well diffusion method, as illustrated in Fig. 4.9 and Table 4.2. The agar well diffusion images for bare PU and Fe_3O_4 nanoparticles are provided in the Appendix (Fig.A_2 and Fig.A_3) in the Annex. According to Table 4.2, all tested materials have antibacterial activity except PU which showed no inhibition zone at concentration of 1 and 2 mg/ml. The bare CHE capped ZnO-NPS demonstrated better antibacterial activity than Fe_3O_4-NPs attributed to ZnO-NPs inherent antibacterial activity through direct contact, membrane breakdown, release of zinc ions (Zn^{2+}) by interrupting key enzymes required for bacterial growth, and release of reactive oxygen species (ROS) from the surface leading to cell death [308]. Comparatively, CHE-capped Fe_3O_4/PU/ZnO-NCs were more effective than ZnO-NPs in suppressing *S. aureus* and *E. coli*. The heightened effectiveness of the CHE-capped Fe_3O_4/PU/ZnO-NC is likely attributed to several factors. As per Sharaf's study, the presence of the magnetite species Fe^{+2} and Fe^{+3} in the nanocomposite material activates the formation of ROS [67], [68] and analysis using Zeta potential and BET methods suggests greater stability and a larger surface area. Additionally, SEM analysis revealed smaller particle size. These features collectively provide more active sites on the material's surface, facilitating interaction with the bacterial biofilm matrix [310], [311]. This elucidates why smaller NPs, with their increased surface area, generate more reactive oxygen species and exhibit stronger antibacterial activity [312], [313].

Table 4. 2. CHE capped Fe_3O_4/PU/ZnO-NC, CHE capped ZnO-NPs, CHE capped Fe_3O_4 and PU inhibitory zone for *E. coli and S. aureus*

Test materials	Concentration (mg/ml)	Zone of inhibition (in mm) *E. coli*	*S. aureus*
CHE capped Fe_3O_4/PU/ ZnO NC	1	13± 1.2	14 ±1.4
	2	15 ±1	16 ±1.3
CHE capped ZnO-NPs	1	12± 1.7	13 ± 1.4
	2	14 ±1.3	15 ± 1.5
CHE Capped Fe_3O_4 NP	1	3 ±1.4	4± 1.25
	2	5± 1.3	6± 1.04
PU	1	NZI	NZI
	2	NZI	NZI

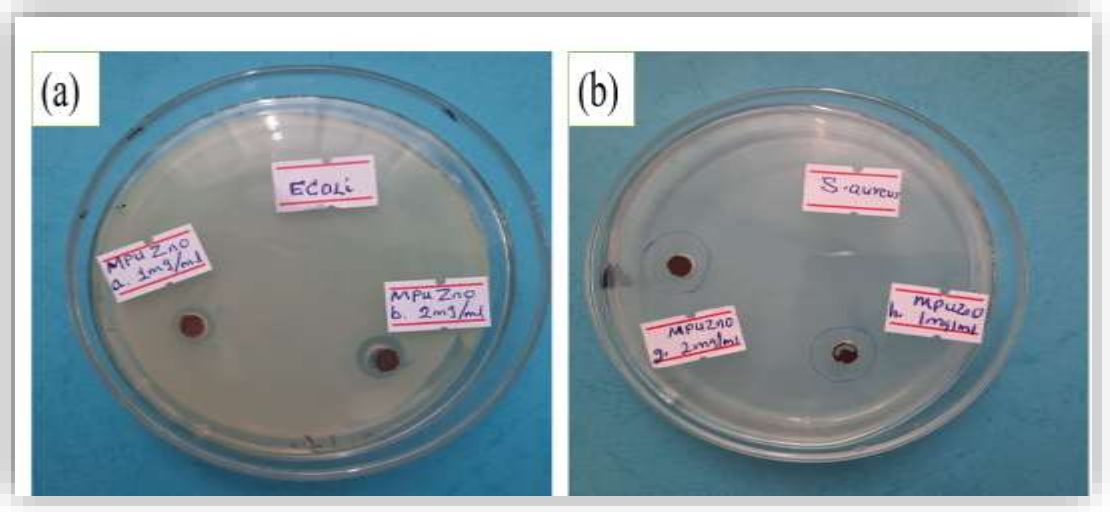

Fig.4. 9. Antimicrobial capacity of CHE capped Fe_3O_4/PU/ZnO NCs' against (a) E. coli. *and (b).* S. aureus

Furthermore, the boost in bactericidal efficacy of bio synthesized CHE capped Fe_3O_4/PU/ZnO-NCs could be due to the reduced agglomeration (Fig. 4.3b) compared to bare CHE capped ZnO-NPs [284]. Nanoparticle aggregation limits nanoparticle entry into the biofilm layer of microorganisms [314] thereby altering the surface properties of NPs, such as charge and chemistry, which can affect their interaction with bacterial cells [315]. This aggregation can also hinder the antibacterial mechanism, as well as the cytotoxicity and immunological reactions of nanomaterials [262].

The inhibition zone against *S. aureus* and *E.coli* expanded as the concentration increased from 1 to 2 mg/ml [316]. It was also observed that the antibacterial activity against *S. aureus* was more effective than against *E. coli*. This variation can be attributed to the presence of lipopolysaccharide (LPS) [316], a molecule found in the outer membrane of gram-negative bacteria like *E. coli* [317]. This membrane acts as a protective barrier, and LPS specifically makes it difficult for antimicrobial agents to penetrate the bacteria. On the other hand, gram-positive bacteria have a simpler cell wall primarily composed of peptidoglycan, a mesh-like layer [258], which is relatively easier for some antimicrobial agents to pass through.

Therefore, it can be deduced that the biocidal activity of CHE capped Fe_3O_4/PU/ZnO-NC is heavily influenced by its particle size, surface area and concentration of the composite [198], [258].

4.3.4. Data analysis

The data analysis results using one way ANOVA test showed that the inhibitory zone diameter data of CHE capped Fe_3O_4/PU/ZnO-NC, CHE capped ZnO-NPs, CHE capped Fe_3O_4-NPs and PU in their antibacterial activity against the growth of *S. aureus* and *E. coli* were significantly different at the 0.05 level.

Table 4. 3. One way ANOVA test result of CHE capped Fe_3O_4/PU/ZnO-NC, CHE capped ZnO-NPs, CHE capped Fe_3O_4-NPs and PU against E. coli

	Sum of Squares	Df	Mean Square	F	Sig.
Between Groups	471.000	3	157.000	64.609	.000
Within Groups	19.440	8	2.430		
Total	490.440	11			

Note: the data is significantly different if the significance value is less than 0.05

Tables 4.3 and 4.4 show the results of data analysis using the one way ANOVA test, which revealed that the diameter of inhibition zones of CHE capped Fe_3O_4/PU/ZnO-NC, CHE capped ZnO-NPs, CHE capped Fe_3O_4-NPs and PU differed significantly at the 0.05 level in their antibacterial activity against the growth of *E.coli* and *S. aureus*. This is because the significance level for *E.coli* and *S. aureus* was zero and 0.015, respectively.

Table 4. 4. One way ANOVA test result of CHE capped Fe_3O_4/PU/ZnO-NC, CHE capped ZnO-NPs, CHE capped Fe_3O_4 and PU against *S. aureus*

	Sum of Squares	Df	Mean Square	F	Sig.
Between Groups	339.690	3	113.230	6.628	.015
Within Groups	136.667	8	17.083		
Total	476.357	11			

Note: the data is significantly different if the significance value is less than 0.05

4.4. Conclusions

In this study, a simple, effective, and environmentally friendly approach to biosynthesize CHE capped Fe_3O_4/PU / ZnO-NC was employed, utilizing indigenous CHE as a stabilizing and reducing agent without the need for hazardous chemicals. SEM imaging revealed spherical and rod-shaped CHE-capped ZnO-NPs and CHE-capped Fe_3O_4-NPs attached to the surface of pumice, respectively, with a more favorable nanocomposite particle size (11 nm) than bare ZnO-NPs. Furthermore, BET and TGA measurements unveiled that the nanocomposite possesses a larger surface area (47.2 m^2/g) and better thermal and surface stability than bare CHE-capped ZnO-NPs. The antibacterial activity of the synthesized materials against *E. coli* and *S. aureus* was evaluated using agar well diffusion. The results indicated that CHE-capped Fe_3O_4/PU/ZnO-NC inhibited both *E. coli* and *S. aureus* in a concentration-dependent manner. As the concentration of the nanocomposite increased, so did the antibacterial activity, with stronger biocidal activity observed against *E. coli* compared to *S. aureus*. CHE-capped Fe_3O_4/PU/ZnO-NC exhibited higher bacteriostatic activity than bare ZnO-NPs, attributed to the inclusion of CHE-capped Fe_3O_4/PU-NC in the nanocomposite synthesis. Overall, the combination of biosynthesized CHE-capped Fe_3O_4/PU nanocomposite and ZnO-NPs demonstrated improved nanomaterial properties and enhanced biocidal activity. This finding confirms the effectiveness of CHE capped Fe_3O_4/PU / ZnO-NC in exhibiting potent antibacterial activity.

CHAPTER FIVE

5. MAGNETITE-BASED PUMICE SILICA NANOCOMPOSITE FOR LEAD ADSORPTION FROM AQUEOUS SOLUTION: THE GREEN SYNTHESIS APPROACH.

5.1. Introduction

Heavy metals pose serious problems due to their toxicity and are categorized as the most dangerous pollutants to the environment [318]. In addition, most toxic metals can adversely impact the health of humans and animals [319]. Although heavy metals serve as valuable inputs for numerous industries, their direct release into the environment results in their buildup in soil and water. Subsequently, during irrigation and agricultural activities, these metals can readily accumulate in the human body. Lead, a toxic heavy metal, originates from both natural and human activities. Natural sources include lead-containing minerals in the Earth's crust, while anthropogenic sources encompass mining, smelting, industrial processes, lead-based paints, water distribution systems, vehicle emissions, and improper recycling and waste disposal. Lead pollution poses serious health risks, especially to children, causing neurological damage, developmental issues, and other health problems. Efforts to mitigate lead contamination involve regulations, the banning of lead-based products, improved waste management, and lead-safe practices in various industries. Nevertheless, the removal of lead from aquatic ecosystems stands as a significant global concern [320].

Recent technologies have been used for the removal of heavy metals including ion exchange resins [18], electrocoagulation and electrochemical depositions [321], nanofiltration, and reverse osmosis [322], [323]. However, these methods have still some gaps that need to be addressed to further improve their efficiency and effectiveness. Recently, the development of advanced adsorbent materials for heavy metal removal has gotten significant attention in the field of water treatment [324]. An effective water treatment mechanism is nanotechnology which utilizes engineered NPs and nanomaterials to clean up polluted water [325]. Nanoparticle-based technologies are often cost-effective compared to other technologies [326]. This is because NPs can be easily synthesized using low-cost precursors and the synthesizing process can be scaled up for high performance in industrial applications [114]. Furthermore, nano adsorbents can be regenerated and reused multiple times, thus reducing the amount of waste generated during the treatment process [327]. Several studies have shown that nanomaterials such as iron oxide, titanium dioxide, and carbon nanotubes can effectively be used to remove heavy metals including lead, chromium, and cadmium [328]. Silica NPs have shown great potential in adsorbing heavy metals due to their large surface area, high adsorption capacity, and tunable surface properties compared to other NPs [329]. However, there are still several gaps and challenges that exist in utilizing silica NPs for heavy metals adsorption.

Silica NPs often exhibit rapid adsorption kinetics at the initial stage but the rate of adsorption decreases over time as the NPs become saturated. Understanding and optimizing the kinetics of heavy metal adsorption on silica NPs is an area that requires further investigation [173]. Moreover, silica NPs tend to form agglomerates in aqueous environments. Developing strategies to enhance the stability of silica NPs and prevent aggregation is crucial for improving their performance in heavy metal adsorption [330]. The other drawback is related to the regeneration and reusability of silica NPs for heavy metal adsorption. Developing effective regeneration techniques and understanding the long-term stability and performance of silica NPs during multiple adsorption-desorption cycles is, therefore, important[331]. So far, several studies have been carried out on the incorporation of magnetite with silica for heavy metal removal: silica-coated magnetic nano-composites for Pb^{2+} removal from aqueous solution [332], silica-coated $Cu0.50Mg0.50Fe_2O_4$ magnetic adsorbent for wastewater treatment [329], magnetic mesoporous silica microspheres with accessible carboxyl functionalized surfaces for the removal of heavy metal ions [165], magnetic silica-based hybrid organic-inorganic nano-composite for the removal of lead (II) and nickel (II) ions from aqueous solutions [333] and network–polymer–modified super-paramagnetic magnetic silica NPs for the adsorption and regeneration of heavy metal ions [334]. All aforementioned studies employed synthesis mechanisms based on chemical methods, such as the sol-gel method, Stöber method, flame synthesis, and microemulsion. While these chemical approaches are relatively straightforward to implement and modify, they can be expensive, energy-intensive, environmentally unfriendly, and difficult to control. Conversely, green synthesis of metallic NPs involves synthesizing NPs using natural sources or biodegradable agents, providing eco-friendly and sustainable alternatives to conventional methods [335]. The green synthesis approach uses natural reducing and stabilizing agents extracted from plants, algae, fungi, bacteria, and yeasts to form metal NPs [336], [337].This study has attempted to address the gap in the synthesis of silica nanoparticles (SiO_2-NPs) from agricultural residue as a silica precursor reported in the literature [182], [331], [332], [338]–[343]. All aforementioned studies utilized green synthesis in the first stage to produce sodium silicate (Na_2SiO_3), followed by chemical synthesis in the second (final) stage to produce SiO_2 NPs. The novelty of this study lies in its utilization of green synthesis to manufacture SiO_2-NPs directly from their first product (Na_2SiO_3), thus completing the approach entirely using green synthesis. This investigation is a continuation of our ongoing research in the green synthesis of NPs by employing CHE phenolic compounds as reducing and stabilizing agents for silica NPs in sodium silicate (Na_2SiO_3). This approach eliminated the need for chemical surfactants, resulting in the production of novel CHE-capped silica NPs. In addition, the present study has aimed to identify the key differences between CHE-capped silica NPs synthesized using this method and those produced through conventional sol-gel methods.

Although prior studies have investigated the use of combinations of magnetic materials and silica NPs for lead adsorption [344]–[346], none have previously coupled them with phytochemically generated silica NPs and magnetite incorporated into pumice. Pumice, a naturally abundant and cost-effective volcanic rock, possesses a high surface area for adsorption due to its porous nature [78], [347]. Moreover, the addition of magnetic components renders the plant-mediated NC magnetically responsive, enabling easy separation and recovery from water. Green-synthesized magnetic silica NCs have emerged as a promising solution for the adsorption of lead ions from water. This study also determined the optimal lead adsorption parameters values using the synthesized NC. In general, the present study developed a novel, green, and efficient adsorbent for lead removal from water by synthesizing a plant-mediated magnetite-based pumice silica NC. The significance of this study relies in its relevance to advancing research in NP synthesis, the synthesis of bio-based surfactants, and green approaches to remediate environmental pollution.

5.2. Materials and Methods

5.2.1. Materials

Lead nitrate ($Pb(NO_3)_2$), ferric chloride ($FeCl_3$, 99%), ferrous sulfate ($FeSO_4 \cdot 7H_2O$, 99 %), ethanol (C_2H_5H, 99.02 %), and ammonium hydroxide (NH_4OH) were purchased from Loba Chemie Pvt. Ltd. CH was gathered from *Harer*, Ethiopia. Volcanic pumice was collected from the *Adulala* pumice area, *Bishoftu* District, Ethiopia. BA was obtained from the *Wonji/Shoa* Sugar Factory in Ethiopia.

5.2.2. Methods

5.2.2.1.Silica nanoparticle synthesis

Sodium silicate was primarily extracted from HCl acid pretreated [348] BA by melting a mixture of sodium hydroxide and HCl pretreated ash at 550°C for 1 h at a weight ratio of 1:1.5. After cooling to room temperature, distilled water was added to the mixture and refluxed (at boiling point) for 4 h to dissolve all of the sodium silicate, which was then used to synthesize silica [182]. Silica NPs were synthesized using both chemical (sol-gel) and green synthesis techniques. Sol-gel SiO_2-NPs were prepared by adjusting sodium silicate to pH 9 with 2.5 M HCl and aging it at room temperature for 24 h [342]. After filtering, sol-gel silica (Sol-Si) was washed with hot water and dried at 100°C for 5 h. Silica NPs synthesized through a green (plant-mediated) approach were also produced following the modified method of Rahimzadeh et al. [32]. The filtrate Na_2SiO_3 and CHE were mixed and stirred at 60℃ in a 2:1 volume ratio. The procedure was carried out under reflux for 12 h at pH 9. After centrifugation at 7000 rpm for 25 min, the precipitate was carefully washed with double distilled water three times and with ethanol as well. The CHE-capped SiO_2 NPs (CHE-Si) were then heated in a furnace at 550°C for 45 min for removal of the contaminants and organic elements. Then, the residue was dried in an oven and kept for further characterization and application activities.

5.2.2.2. Preparation of CHE capped M/PU/Si NC

CHE-capped M/PU/Si-NC was synthesized by first preparing a magnetite pumice NC solution using a method adapted from our previous work [349]. Pumice was initially washed, dried in an oven, ground, sieved, and acid-pretreated with HCl to remove metallic impurities and rinsed with deionized water until a neutral pH was achieved [286].

It was then dispersed in deionized water and sonicated. As illustrated in Fig.5.1, iron salt precursors (ferrous sulfate and ferric chloride) were subsequently added and thoroughly mixed using a magnetic stirrer until 80°C was reached. CHE was then introduced and mixed for 5 min., followed by the dropwise addition of ammonia until the pH reached 9.0. This process resulted in the formation of a black-colored CHE-capped Fe_3O_4/PU-NC, which was cooled to room temperature after 30 min of continuous stirring. The precipitate was separated using an external ferrite magnet and washed repeatedly with deionized water. Finally, the product was dried in an oven at 80°C for 24 h. Then, CHE-capped M/PU/Si-NC was synthesized by slowly dropping the magnetic pumice solution into the nano-silica solution with continuous mixing for 2 h, after which the solution was centrifuged as indicated in Fig.5.1 and dried in an oven at 80ºC for 3 h [350].

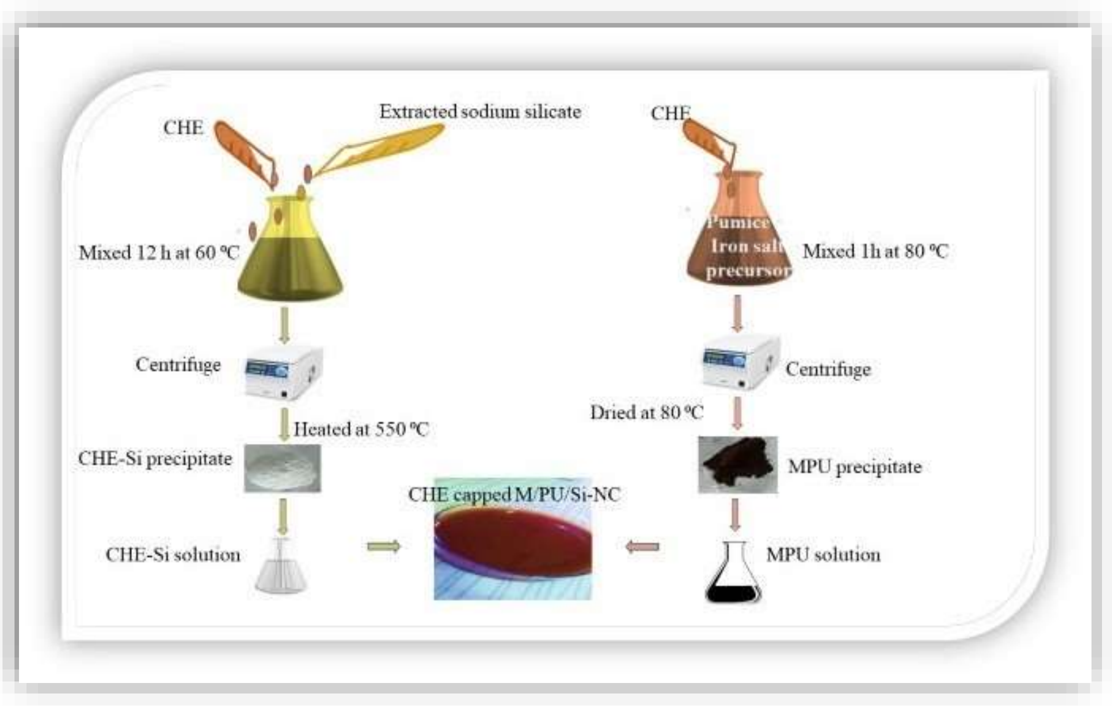

Fig. 5. 1. Schematic illustration of the synthesis of CHE capped M/PU/Si NC.

5.2.2.3.Adsorbent characterization

X-ray fluorescence spectrometers (PANalytical Epsilon 3, XRF, Monterrey, México) were used for the analysis of the oxide composition of BA. XRD (Bruker D8 Advance model) was employed to better understand the behaviors of the synthesized material and confirmation of silica and CHE-capped M/PU/Si NC formation. FTIR spectra were used (IR Prestige, 21 Shimadzu, Japan) to determine the functional groups present in synthesized materials in the 400-4000 cm^{-1} range. Zeta potential analysis (Zetapotential Nano series, Malvern, Westborough, MA, USA) was performed to determine the stability and surface charge while BET analysis (SA-9600 Series SurfaceArea Analyzer, Horiba) was carried out for the surface area, pore volume, and pore size determination. The thermal stability and degradation behavior of the synthesized materials were characterized using thermogravimetric analysis (TGA; HCT-1, China) in a temperature range of 30 to 900°C (20°C/min) SEM with EDX (JCM-6000, PLUS, Japan) was employed to study the formation and morphology of CHE-capped M/PU/Si NC and also for surface elemental analysis, respectively [17] , [41].

5.2.2.4.Adsorption experiment

The adsorption process was investigated under the effects of dose (0.1-0.6 g), contact time (10-150 min), pH (2- 9), and concentration (1-250 mg/L) for lead removal using CHE-capped M/PU/Si-NC. All batch adsorption experiments were carried out in 100 mL rubber-stopped volumetric flasks. The flasks were placed inside an incubator shaker (Excella E24R) and shaken at 200 rpm for the specified times. At the end of the specified times, the CHE-capped M/PU/Si-NC were separated and the remaining metal ion concentration in the solutions was determined using an Atomic Absorption Spectrophotometer (model AA-7000). The pH of the solutions was kept stable by adding 0.1 M of HCl and NaOH solution as needed. The highest lead adsorption capacities were chosen as the optimal condition, and that value was applied to the next affecting factor of the study. The removal efficiency (R%) and adsorption capacities (q_t, q_e) of the CHE-capped M/PU/Si-NC for Pb^{2+} removal were calculated using equations (5.1 - 5.3).

$$R = (Co - Ce) * 100/Co \tag{5.1}$$

$$qt = (Co - Ct) * V/m \tag{5.2}$$

$$qe = (Co - Ce) * V/m \tag{5.3}$$

where qt and qe are the amounts of Pb^{2+} adsorbed at time t and at equilibrium (mg/g), respectively. C_o, C_t, and C_e are concentrations of Pb^{2+} (mg/L) at time 0, t, and equilibrium, respectively. V is the volume of Pb^{2+} solution used (L) and *m* is the mass of adsorbent dosage that was used (g).

5.2.2.5. Adsorption kinetics

Adsorption kinetics models are frequently used to examine adsorption rate and rate-determining steps [173]. Pseudo-first-order (PFO), pseudo-second-order (PSO) models, and intraparticle diffusion (IPD) were used to understand the adsorption process of CHE-capped M/PU/Si-NC adsorbent. The pseudo-first-order model describes the physisorption limits of the adsorption rate of the particles onto the adsorbent. The non-linear form of the PFO model adsorbent capacity-based rate expression is given by equation 5.4 [352].

$$qt = qe(1 - e^{-k_1 t}) \tag{5.4}$$

where k_1 (1/min) is the PFO rate constant, q_e (mg/g) and qt (mg/g) are the amounts of Pb^{2+} adsorbed at equilibrium and at time t (min), respectively [353]. However, the PSO kinetic model describes the adsorption processes achieved via the chemical binding of adsorbates onto the surface of adsorbents. This kinetic model is expressed by equation 5.5:

$$q_t = {q_e}^2 k_2 t/(1 + q_e k_2 t) \tag{5.5}$$

where k_2 denotes the PSO equilibrium rate constant (g / mg**.** min). The other one is the IPD model which is the rate-limiting steps in the overall adsorption process if the line passes through the origin. The IPD model is expressed by equation 5.6.

$$q_t = K_{id}\, t^{1/2} + \mathrm{C} \tag{5.6}$$

where K_{id} is IPD rate constant (g/mg **.**min^{-}) and q_t (mg/g) is the amount of lead ion adsorbed at any time t

5.2.2.6. Adsorption isotherms

Adsorption isotherm models were used to study the effect of lead adsorbed from lead concentration per unit mass of CHE-capped M/PU/Si-NC adsorbent. The models can give important insights into the adsorption mechanism [354], [355]. Langmuir, Freundlich, and Temkin models were used to identify the mechanism of Pb^{2+} adsorption onto CHE-capped M/PU/Si-NC adsorbent. The Langmuir adsorption isotherm describes non-interactive monolayer adsorption on a limited homogeneous surface [356]. The equilibrium correlation of Pb^{2+} and CHE-capped M/PU/Si-NC adsorbent is explained by the non-linearized equation (5.7).

$$\mathrm{qe} = \mathrm{Qm} * KL * Ce/(1 + K_L * Ce) \tag{5.7}$$

where q_e is the amount of adsorbed lead (mg) per g of adsorbent at equilibrium (mg/g), Q_m (mg/g) is the maximum adsorption capacity of the system (mgg) and C_e is the adsorbate concentration in solution at equilibrium (mg/L), K_L is the Langmuir model constant. In contrast, the Freundlich isotherm describes multilayer adsorption at heterogeneous sites. Adsorption affinity and energy vary between adsorbent surfaces. Stronger binding sites are occupied first and binding strength decreases as site occupancy increases. The non-linear form of this model is described by equation (5.8).

$$q_{e= K_f . C_e}{}^{1/nf} \tag{5.8}$$

K_f and n_f are specific constants that correspond to the adsorbent's relative adsorption capacity and the intensity of adsorption, respectively [357]. Likewise, the Temkin isotherm model accounts for the indirect interactions between adsorbates and adsorbents. Essentially, it posits that as the surface coverage of the adsorbent increases, there will be a uniform decrease in the adsorption heat for all molecules on that surface [178]. The Temkin isotherm can be expressed by Equation (5.9).

$$q_e = BLn\ (A_T\, C_e) \tag{5.9}$$

where A_T is the Temkin equilibrium binding constant, B is the constant related to the heat of adsorption ($B= R_T/ b_T$), R is the universal gas constant (8.314 $J{\cdot}mol^{-1}{\cdot}K^{-1}$)

5.3. Results and Discussion

5.3.1. Characteristics of the adsorbent

5.3.1.1. X-ray Fluorescence (XRF) analysis

XRF analysis was conducted to study the oxide composition of BA which was used as a silica source. The XRF analyses show that the oxide compositions of BA were SiO_2 (65.8 %), Fe_2O_3 (7.3 %), Al_2O_3(13.0 %), and K_2O (8.6 %) with a small LOI value of 1.6 % which is similar to other studies [358], [359]. Interestingly, acid pre-treatment significantly altered the oxide composition of BA. Silicon dioxide (SiO_2) became the dominant component, increasing to 85.8 %. Conversely, the content of metal oxides like iron oxide (Fe_2O_3), aluminum oxide (Al_2O_3), and potassium oxide (K_2O) all decreased to 3.3 %, 7.0 %, and 4.0 %, respectively. This reduction in metallic impurities may be attributed to the effective leaching action of hydrochloric acid [348], [359]. These findings confirm that BA has a high content of SiO_2, making it a promising precursor for silica production [360], [361].

5.3.1.2. FTIR Analysis

To investigate the functional groups of the synthesized material and the role of phenolic compounds in their formation, Fourier-Transform Infrared Spectroscopy (FTIR) analysis was performed on both the raw BA and the synthesized material. Fig. 5.2a shows the FTIR spectra of the BA. The BA spectra exhibit vibrational bands at 983 cm^{-1}, 788 cm^{-1}, and 430 cm^{-1}. These peaks correspond to asymmetric and symmetric stretching vibrations of Si-O-Si (at 983 cm^{-1} and 788 cm^{-1}, respectively) [181]. Similarly, the Si-O bending was found at 430 cm^{-1} [362]. The strong intensity of the Si-O

peak suggests a high content of silicon oxide in BA, which is consistent with the high silicon oxide percentage found in the XRF analysis [359], [363]**.** Fig. 5.2b shows the functional groups present in CHE-Si-NPs, CHE-capped M/PU/Si-NCs, and Sol-Si-NPs. The FTIR spectra of CHE-capped M/PU/Si-NCs exhibit peaks at 3430, 1625, 1109, 808, 570, and 460 cm^{-1}. CHE-Si-NPs show peaks at 3430, 1625, 1109, 808, and 460 cm^{-1}, while Sol-Si-NPs exhibit peaks at 3430, 1625, 1036, 808, and 460 cm^{-1}. The FTIR spectra of the synthesized materials reveal four common peaks (Fig. 5.2b). The strong, broad peak at 3430 cm^{-1} in CHE-capped Si and CHE-capped M/PU/Si-NC corresponds to stretching vibrations of Si-O-H groups. This peak is characteristic of the OH groups present in the phenolic compounds of CHE, suggesting their contribution to the formation of silica and Fe_3O_4-NPs [56], [57]. In contrast, the weak, broad peak at 3430 cm⁻¹ observed in Sol-Si-NPs likely arises from surface water adsorption [331]. The second common peak at 1625 cm⁻¹ originates from bending vibrations within the silanol groups (Si-OH) [365]. The third peak at 808 cm⁻¹ signifies symmetric stretching of siloxane bonds (Si–O–Si) as reported in various studies [182], [332], [365]. Finally, the last common peak at 460 cm⁻¹ represents the bending vibrations of Si-OH bonds [48]. Interestingly, CHE-Si-NPs and CHE-capped M/PU/Si-NCs exhibit additional strong narrow peaks at 1109 cm⁻¹. This peak indicates the presence of asymmetric siloxane bonds (Si–O–Si) and bending vibrations of functional groups [366]. In contrast, analysis of Sol-Si-NPs reveals a weak and broad peak at 1036 cm⁻¹ which is associated with Si-O-Si asymmetric stretching vibrations [367]. This peak indicates a lower abundance of silica functional groups in the sample [368]. Furthermore, the FTIR spectra of CHE-capped M/PU/Si-NCs reveal an additional peak at 570 cm⁻¹. This peak is attributed to Fe–O–Si stretching vibrations within magnetite [17], [18], [62] and indicates the successful formation of Fe_3O_4 in the CHE-capped M/PU/Si-NC material. Generally, the FTIR analyses confirmed the phytochemicals present in the CHE acted as a reduction and capping agent in CHE-Si-NPs, and CHE-capped M/PU/Si-NCs.

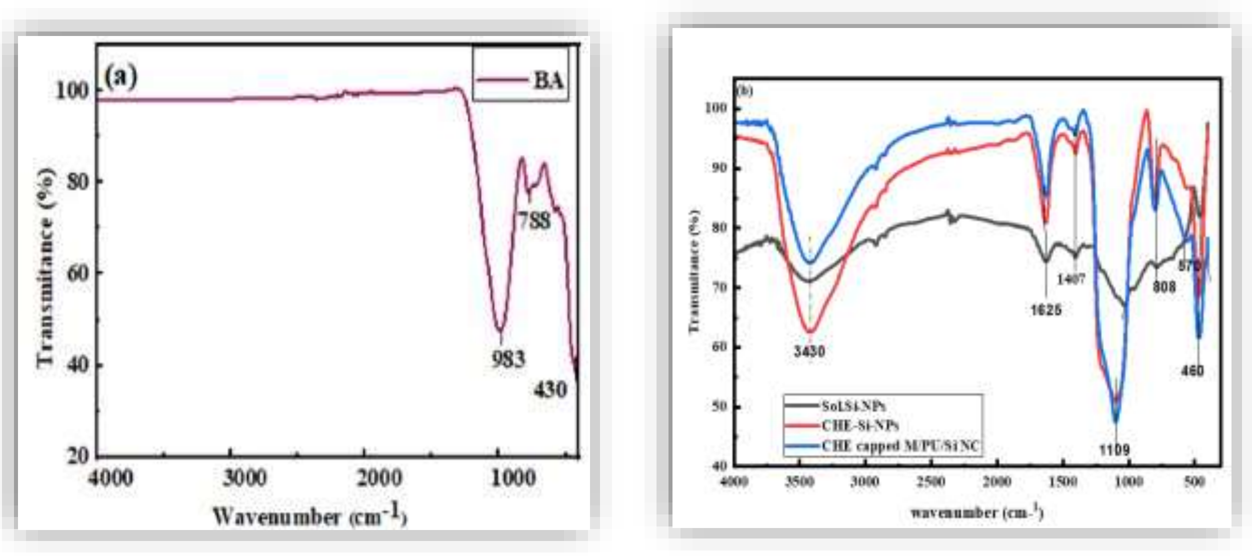

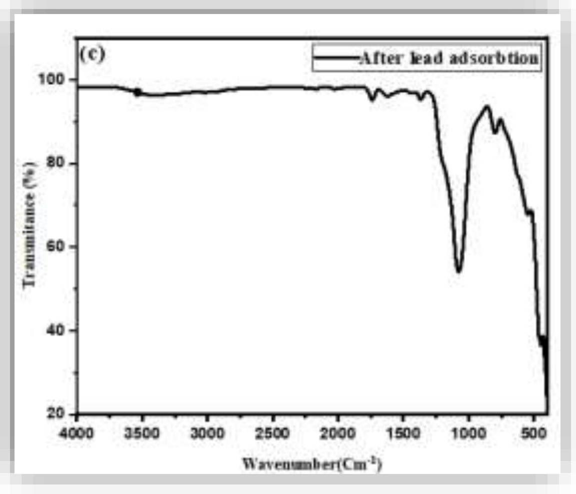

Fig. 5. 2. FTIR spectra (a) BA (b) Sol-Si-NPs, CHE-Si-NPs, and CHE capped M/PU/Si-NC (c) after lead adsorbtion CHE capped M/PU/Si-NC

As illustrated in Fig. 5.2c, the FTIR spectra confirm the presence of surface functional groups, including –SiOH, –OH, and –COOH, on the NCs. During heavy metal ion adsorption, Pb^{2+} ions form strong coordinate covalent bonds with these groups. This interaction is facilitated by the overall negative surface charge of the synthesized material across the pH range of 0 to 10, which enhances the electrostatic attraction and binding of the positively charged metal ions.

5.3.1.3. X-ray Diffractometer (XRD) analysis

The physical properties such as phase composition, crystal structure, and orientation of Sol-Si, CHE-Si, and CHE-capped M/PU/Si-NC which were investigated using the XRD are shown in Fig. 5.3. The broad peaks around 2θ = 15–30° in Fig.s 5.3a and 5.3b confirm the presence of amorphous silica NPs in both samples synthesized using the plant-mediated and sol-gel methods, respectively [162], [181], [350]. Plant-mediated synthesis appears to yield SiO_2-NPs with less background noise compared to those produced by sol-gel synthesis. Notably, the diffraction peaks in both cases match the reference pattern for SiO_2 in JCPDS file No. 89-0510 [370]. Fig. 5.3c shows the X-ray diffraction (XRD) pattern of the CHE-capped M/PU/Si-NC. The pattern reveals both crystalline and amorphous peaks. The crystalline peaks correspond to Fe_3O_4-NPs at 2θ values of 30.6, 35.9, 43.5, 54.0, 57.4, 63.0, and 74.5 degrees. This observation is consistent with previous XRD results [17], [40], [65]. Additionally, a broad peak around 2θ = 15–30° indicates the presence of amorphous pumice [294] and silica NPs [372].

This XRD analysis confirms the formation of the composite material with a combination of crystalline Fe_3O_4 and amorphous SiO_2. Furthermore, the absence of impurity peaks in the entire pattern suggests high purity of the synthesized CHE-capped M/PU/Si-NC.

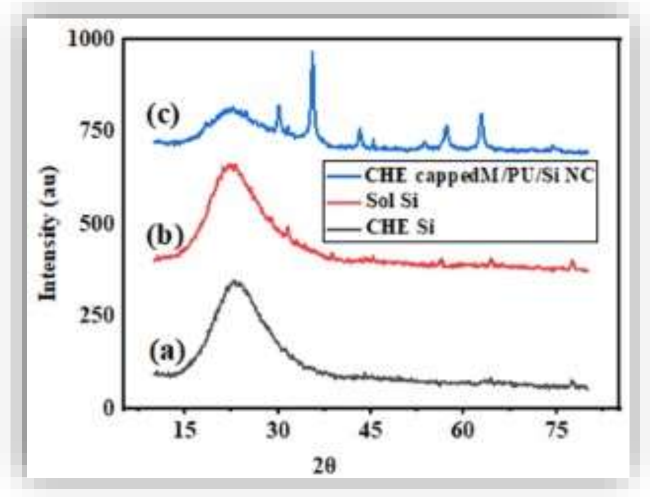

Fig. 5. 3. XRD patterns of (a) CHE-Si-NPs, (b) Sol. Si-NPs, (c) CHE capped M/PU/Si-NC.

5.3.1.4. TGA and DTG analysis

TGA and DTG were used to evaluate and compare the thermal stability of Sol-gel synthesized silica NP (Sol-Si), CHE capped silica NP (CHE-Si), and CHE capped magnetic pumice silica nanocomposite (CHE capped M/PU/Si-NC) are presented in Fig.5.4a and b. The relative comparison between weight losses of Sol-Si and that of CHE-Si is 6 % at 129 ºC and 3% at 250 ºC, respectively.

This condition is related to evaporation of physically and chemically adsorbed water. The second stage of decomposition observed in the range of CHE-Si from 250 ºC–650 ºC with weight loss of 2.5 % and Sol-Si 129–450 ºC with weight loss of 3.5 % was due to dehydration and evaporation of chemically adsorbed water molecules. This could also be associated with the removal of hydroxyl groups which is the surface dihydroxylation of silica [373]. This result confirms the successful synthesis of high thermally stable green capped silica NPs with high purity of silica (94.5%) at a higher temperature (650 ºC) than Sol- Si NPs which is 89.7 % purity at 463 ºC. This is a very good indicator that the capping and stabilizing agents around the CHE-Si-NPs are strong enough to resist high temperatures [374]. The CHE-capped M/PU/Si-NC residue was 95 % at the highest temperature (690 ºC) [374].

Similar results have been found by other authors [162]. This revealed that the plant-mediated CHE-capped M/PU/Si-NC have better thermal stability compared to the bare silica NPs.

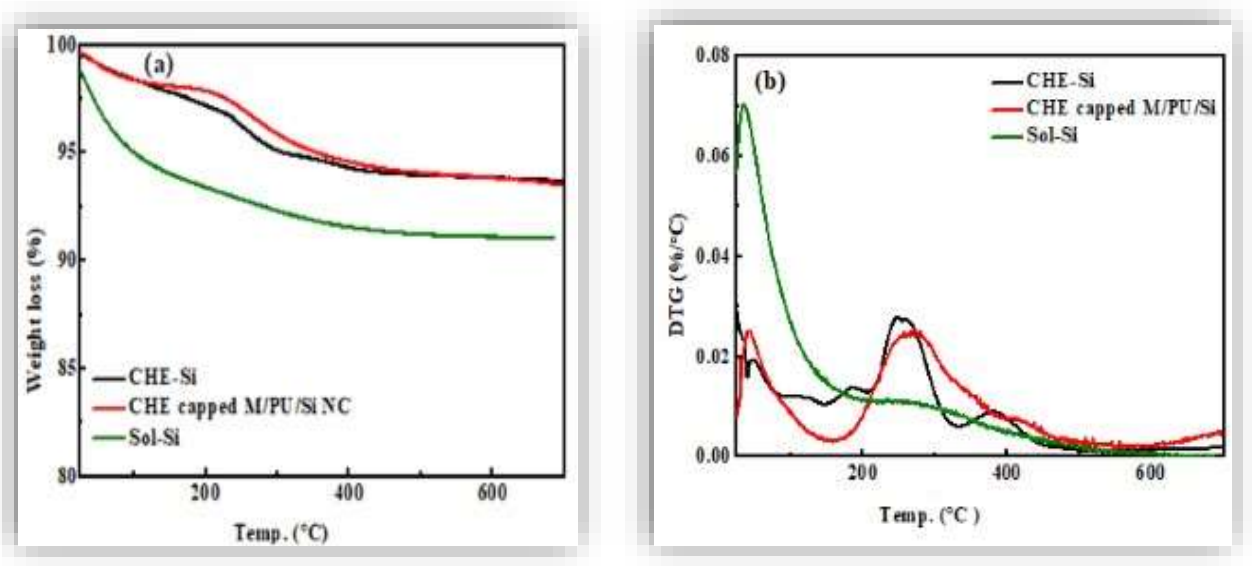

Fig. 5. 4. (a). TGA curves of the synthesized Sol-Si, CHE-Si, and CHE capped M/PU/Si NC. (b) DTG curves of the synthesized Sol-Si, CHE-Si, and CHE capped M/PU/Si NC.

5.3.1.5. BET surface area determination

BET analysis was performed on microporous silica to assess its surface area and pore characteristics as shown in Table 5.1. The analysis revealed a surface area of 338 m^2/g, a pore radius of 1.324 nm, and a pore volume of 0.1367cm^3/g. This confirms the microporous nature of the synthesized material with pores predominantly less than 2 nm in size [375]. Compared to silica NPs synthesized using CTAB surfactant (323 m^2/g), CHE-capped Si-NPs displayed superior surface area [344]. Similarly, Sol-Si exhibited lower surface area (309 m^2/g) and pore volume (0.1066 cm^3/g) compared to CHE-capped silica. Furthermore, CHE-capped Fe_3O_4/PU/Si-NC possessed a surface area of 313.6 m^2/g, pore volume of 0.16 cm^3/g, and pore radius of 1.3 nm. This is significantly higher than the surface area of magnetic silica NCs (275 m^2/g) and (172 m^2/g) reported by Nicola et al. [332] and Faaliyan [376], respectively. These findings suggest that the use of phytochemical capping and stabilizing agents enhances both surface area and pore volume in CHE-capped M/PU/Si-NC and CHE-Si-NPs compared to Sol-Si NPs.

Table 5. 1. N_2 adsorption-desorption analysis

Name of nanomaterial	Surface area (m^2/g)	Pore volume (cm^3/g)	Pore size (nm)
Si-sol gel	309	0.1066	1.60
CHE-Si	338.1	0.1367	1.32
CHE capped M/PU/Si NC	313.6	0.1600	1.30

5.3.1.6. Zeta potential analysis

Zeta potential is an important parameter in evaluating CHE-capped M/PU/Si-NC stability and surface charge [377]. In this study, the zeta potential of CHE-capped M/PU/Si-NC surfaces was tested using the method used by Bakatula in solution at pH values of 2-10 [378]. The zeta potential of CHE capped M/PU/Si NC (Fig. 5.5) was negatively charged throughout the entire pH range but with increasing zeta potential charges from pH 2 to 6 due to increasing of SiO species [379], [380] which became less negative when the pH of the aqueous solution increased from 7 to 10 which may be due to the repulsive forces occurring between the magnetite NPs and the negative charges of the basic medium [338]. Higher zeta potential charges were seen around pH 5 and 6 implying strong surface stability at this point and following optimal adsorption of positively charged lead ion (Fig. 5.5) on the surface of synthesized material due to the electrostatic attraction [352].

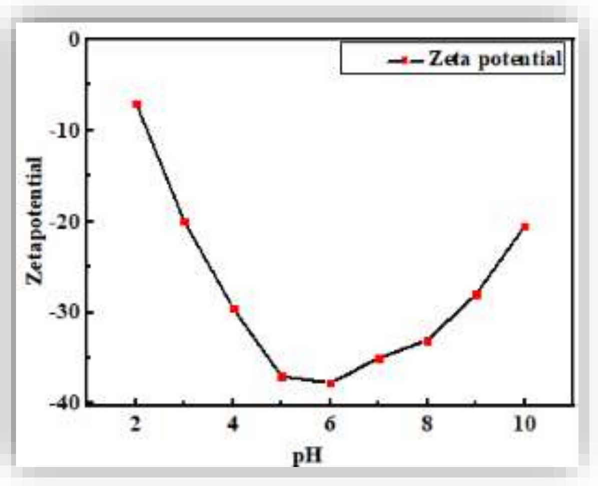

Fig. 5. 5. Zeta potential versus pH for CHE capped M/PU/Si NC

5.3.1.7. Scanning Electron Microscopy (SEM) analysis

SEM was employed to investigate the surface morphology of the CHE-capped M/PU/Si-NC before and after lead (Pb^{2+}) adsorption (Fig. 5.6). The pre-adsorption image (Fig. 5.6a) revealed spherical NPs, consistent with observations in other studies [331], [339]. However, the morphology differed significantly after Pb^{2+} loading (Fig. 5.6b). The post-adsorption image displayed aggregates or clusters on the surface, suggesting the successful adsorption of Pb^{2+} ions. This highlights the crucial role of the microporous structure of the CHE-capped M/PU/Si-NC in Pb^{2+} capture from water as reported previously [381]. In essence, the SEM analysis confirms the well-established anionic and microporous nature of the NC surface which effectively attracts and adsorbs the cationic Pb^{2+}.

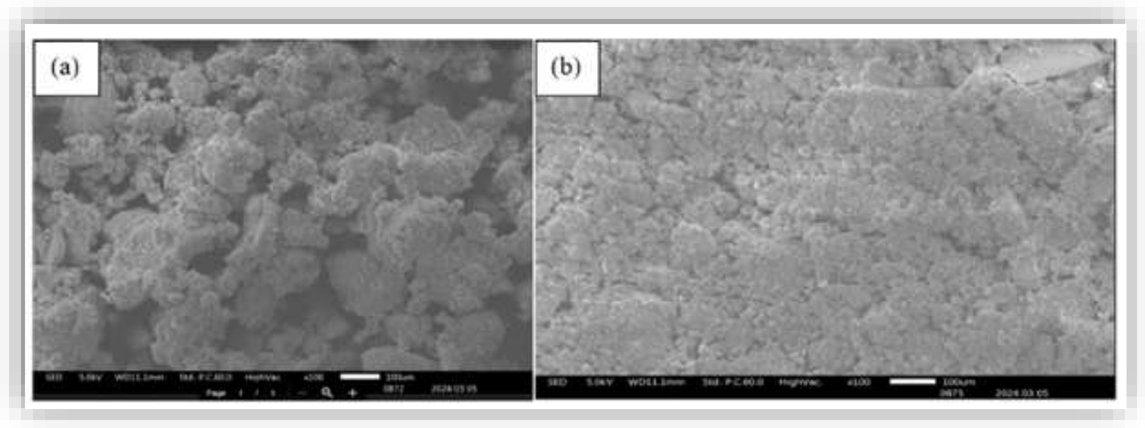

Fig. 5. 6. SEM image of (a) CHE capped M/PU/Si-NC (b) CHE capped M/PU/Si-NC after Pb^{2+} absorption

5.3.1.8. Energy dispersive spectroscopy (EDS) and EDS mapping analysis

An EDS study was conducted to prove unequivocally that the synthesized nanomaterial contains the anticipated elements. Fig. 5.7a shows that the elemental composition of CHE-capped Si includes Si and O, indicating that the NPs are silica [382]**.** According to the results, impurity elements such as Na and Cl are present because HCl and NaOH were used for pH adjustment, while the additional Au and C peaks were due to coating the sample during analysis. Furthermore, Fig. 5.7b shows that the chemical composition of CHE-capped M/PU/Si-NC exhibits peaks around 0.9 and 6.4 keV which corresponds to the Fe binding energies [290]. The oxygen peak at 0.5 keV and the Si peak at 1.8 keV confirm the presence of silica in the composite. The results are consistent with those reported by Rahman et al [291]. The synthesized materials constituted about 100 % of the identified elements, indicating high purity and free of extraneous impurities. The EDS elemental mappings of CHE-capped Si-NPs and CHE-capped M/PU/Si-NC are presented in Fig.5.7a and b. The CHE-capped Si EDS maps (Fig. 5.7a) show the purity of the synthesized CHE-capped Si NPs as well as the evenly distributed O and Si elements. The CHE-capped Fe_3O_4/PU/Si-NC EDS mapping (Fig.5.7b) shows good homogeneity in the spatial dispersal of Fe, Si, O, Al, and O, showing that all elements are uniformly dispersed and that CHE-capped Fe_3O_4/PU/Si-NC was effectively Phyto-fabricated.

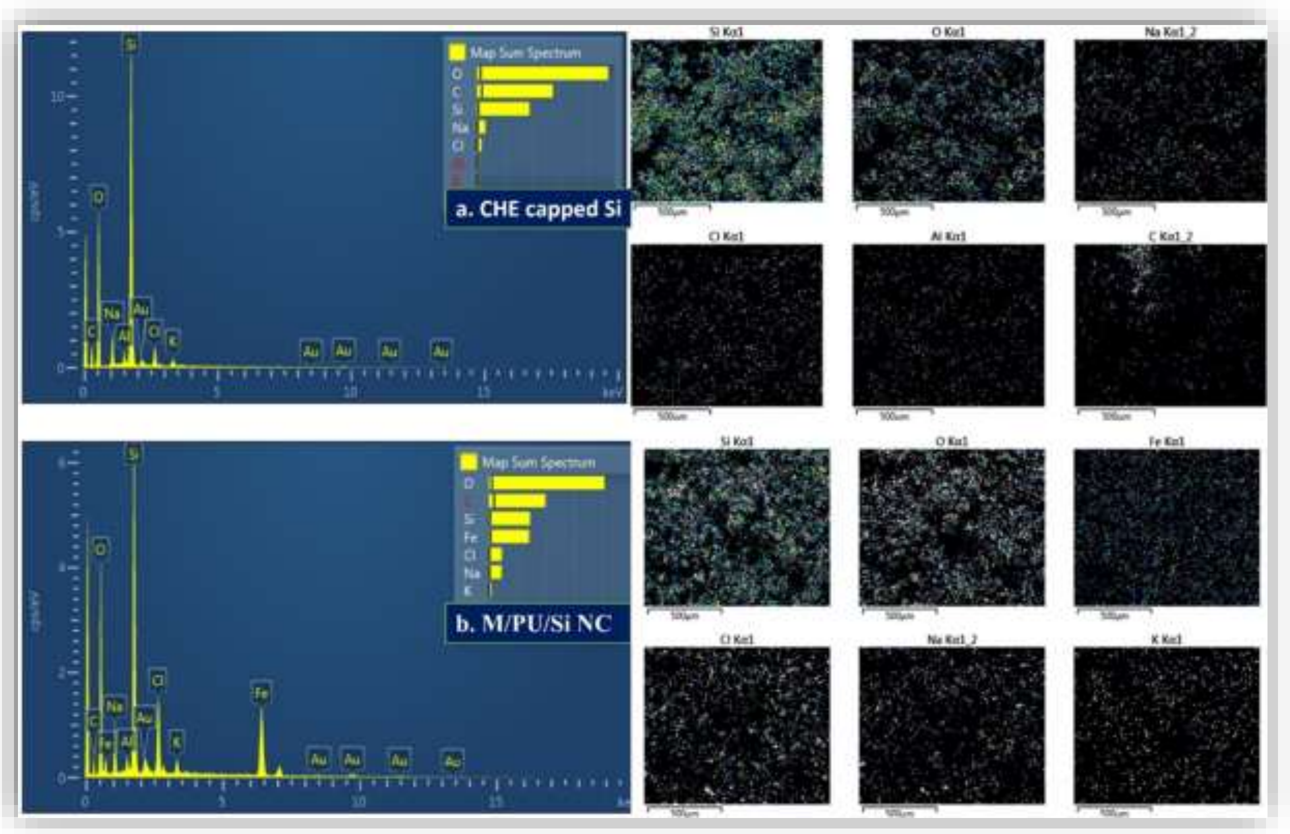

Fig. 5. 7. Energy dispersive spectroscopy (EDS) and EDS mapping analysis of (a). CHE capped Si. (b) M/PU/Si NC

5.3.2. Adsorption performances

5.3.2.1. Effect of pH

CHE-capped M/PU/Si-NC was used for lead ion adsorption, and it is crucial to identify the pH conditions that give the greatest adsorption capacity. As a result, this study investigated and demonstrated (Fig.5.8) the impacts of starting solution pH on Pb^{2+} adsorption by CHE-capped

M/PU/Si-NC in the pH range of 1-9. The graph indicates that the adsorption of Pb^{2+} increases with increasing solution pH up to a pH of 5. This is due to a reduction in the quantity of H^+ ions in the solution, which results in reduced competition [383]. Furthermore, as the pH increased, the negative charges of the adsorbent and active site increased, promoting electrostatic attraction complexation between the CHE-capped M/PU/Si-NC and Pb^{2+} [332]. Additionally, the ionization of functional groups, such as hydroxyl (-OH) and silanol (-SiOH), varies with pH. At pH 5, more hydroxyl groups may be deprotonated, increasing the availability of active sites for lead complexation and lead ion adsorption [384]. Even if the deprotonation of the CHE-capped M/PU/Si-NC was enhanced, the adsorption efficiency was observed to decrease above the pH of 5. This can be because lead ions may form insoluble hydroxides and precipitate, limiting their availability for adsorption [332]. As a result, an initial pH of 5 was selected as the best setting for the sorption of lead ions in the subsequent adsorption studies [383], [385].

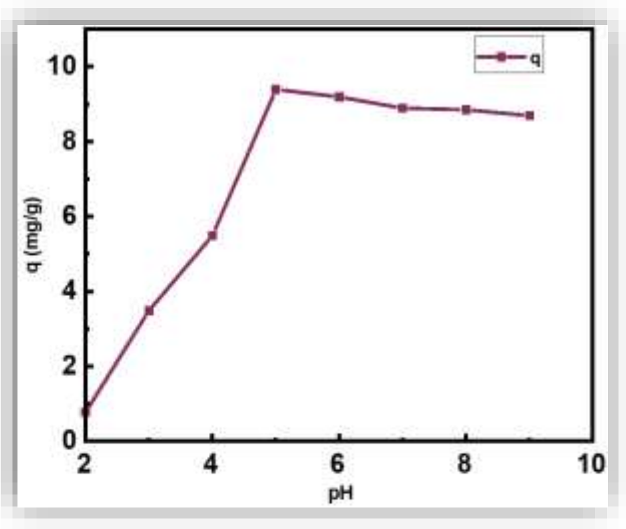

Fig. 5. 8. Adsorption capacity of CHE-capped M/PU/Si-NC at different pH (adsorption conditions were, t= 60 min C_{o} =10 mg·L^{-1}, agitation speed = 200 rpm, T = 25 ℃ , Adsorbent dose = 1 g/L

5.3.2.2. Effect of contact time

As shown in Fig. 5.9, lead ion adsorption increases initially until it reaches equilibrium at 60 min. This is due to the abundance of adsorption sites on NC which the lead ions can easily access and bind to. The adsorption capacity of the NC rises as more lead ions meet it. After 60 min, there is an approximately constant effect on adsorption, and lead ion adsorption achieves equilibrium. At this moment, the rate of adsorption equals the rate of desorption, resulting in the saturation of accessible adsorption sites on the NC surface [386]. At equilibrium, additional contact time does not result in considerable additional adsorption. Beyond 60 min, the adsorption capacity shows a limited reduction as well as a slight fall in adsorption capacity. This occurs due to the desorption of previously adsorbed lead ions due to the limited access to adsorption sites due to mass transfer restrictions [387].

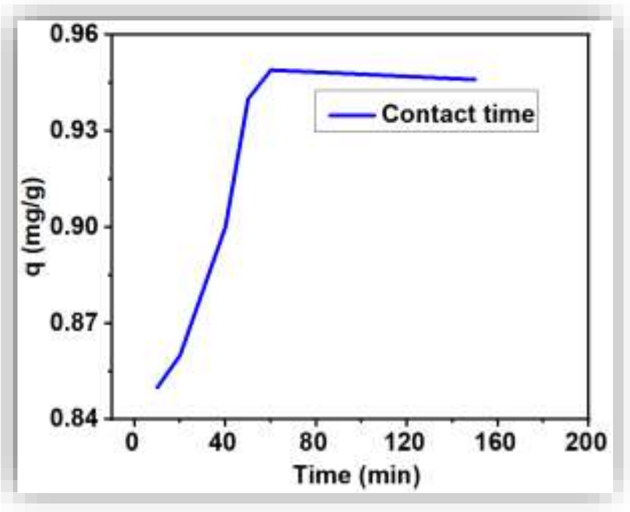

Fig. 5.9. Adsorption capacity of CHE-capped M/PU/Si NC at different contact times (adsorption conditions were pH =5, C_o = 10 mg/L, Adsorbent dose = 1 g/L, agitation speed = 200 rpm, T = 25 ℃).

5.3.2.3. Effect of adsorbent dose

To investigate the effect of CHE-capped M/PU/Si NC adsorbent dose on lead ion adsorption capacity and removal efficiency by varying the CHE-capped M/PU/Si NC dose from 1 to 6 g/L while maintaining the other adsorption parameters constant. As illustrated in Fig.5.10, the CHE-capped M/PU/Si NC adsorption capacity (q) reduced as the CHE-capped M/PU/Si NC dose increased. However, as the CHE-capped M/PU/Si NC dose increased from 0.1 to 2 g/L, the removal (R) increased. The availability of more adsorption sites has been connected to increases in removal efficiency as the CHE-capped M/PU/Si NC increased. The higher the adsorbent dose, the more binding active sites were provided, and the metal ions had a higher probability of adsorption, resulting in increased removal of the metal ions from the solution. As the dose rose to 6 g/L, the adsorption capacity declined while the removal efficiency remained nearly constant. This could be because Pb^{2+} occupied the pore space in the CHE-capped M/PU/Si NC, leaving the active sites, (-SiOH, -OH, and -COOH) saturated. Excess amounts of adsorbent can result in overcrowding of particles which can impede the mass transfer of the target compounds. Particle aggregation or dispersion may also occur at very high adsorbent dosages. Aggregation can result in the creation of bigger aggregates with lower adsorption effectiveness than individual particles. Dispersion occurs when adsorbent particles separate excessively, resulting in diminished adsorption capacity due to reduced contact with the target chemicals. Therefore, 2 g/L of CHE capped M/PU/Si NC dose was chosen for further adsorption studies, considering both adsorption capacity and removal efficiency.

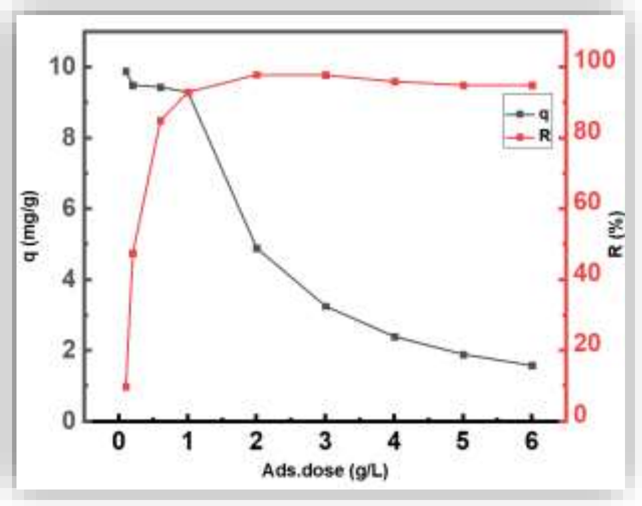

Fig. 5. 10. Adsorption capacity of CHE-capped M/PU/Si-NC at different adsorbent doses (adsorption conditions were pH = 2, Co = 10 mg/L, t = 60 min, agitation speed = 200 rpm, T = 25 °C).

5.3.2.4. Initial concentration effect

As shown in Fig.5.11, the removal efficiency (R %) of Pb^{2+} by the CHE-capped M/PU/Si-NC decreased with increasing concentration of both ions in the solution while the adsorption capacity (q) increased. Initially, the removal efficiency was 93.3 % for Pb^{2+} at 50 mg/L which decreased to 90 % for Pb^{2+} when the initial concentration was increased to 100 mg/L. The adsorption capacity of the CHE-capped M/PU/Si-NC increased sharply as the initial concentrations increased from 50 mg/L to 100 mg/L. This is because a higher concentration of lead ions means a greater number of target ions available for adsorption [388]. More lead ions can bind to the available adsorption sites on the NC surface, resulting in a higher adsorption capacity. The adsorption capacity was reduced beyond the

100 mg/L concentration increment. This may probably be because the adsorption capacity of the NC may reach saturation, even if the initial concentration of lead ions continues to increase. The saturation point corresponds to the maximum adsorption capacity that can be achieved for a given NC and concentration range. Beyond this point, increasing the initial concentration may not significantly enhance the adsorption efficiency or capacity. Also, this surface saturation occurs when all available adsorption sites are occupied by lead ions, and the NC is unable to adsorb additional lead ions. Thus, considering both adsorption capacity and removal efficiency, a concentration of 100 mg/L was chosen for subsequent adsorption experiments.

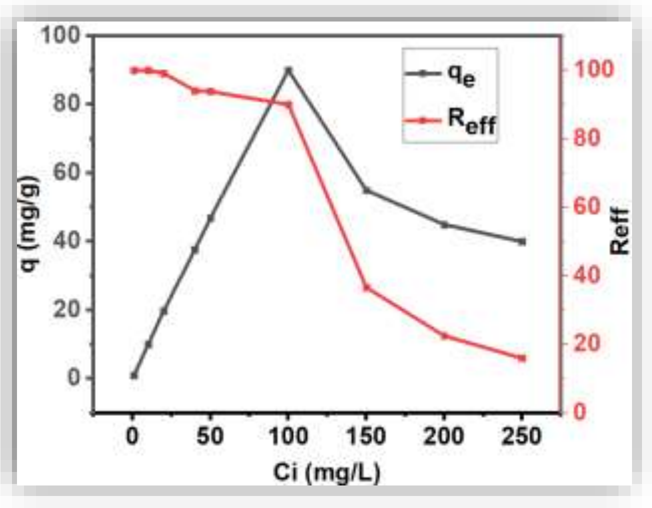

Fig.5.11. Adsorption capacity of CHE-capped M/PU/Si-NC at different Pb^{2+}ions initial concentration (adsorption conditions were pH = 5, t = 60 min, adsorbent dose = 2 g/L, agitation speed = 60 rpm, T = 25 ℃)

5.3.2.5. Adsorption kinetics

PFO, PSO, and IPD kinetic models were studied to analyze the rate of adsorption of Pb^{2+} by CHE-capped M/PU/Si-NC beads. The adsorption kinetic models' results are presented in Table 5.2 and illustrated in Fig.s 5.12a and b. As revealed in Table 5.2, the R^2 value of the PSO model (R^2 0.99) is higher than that of the PFO model (R^2 0.80). Similarly, q_{cal} for PSO (Table 5.2) better fits to q_{exp} than that of PFO. In many cases, the PSO model aligns well with the mechanism of adsorption onto CHE-capped M/PU/Si-NC. This result suggests that chemisorption is the predominant mechanism underlying the adsorption of lead ions and the adsorbent surface. This phenomenon is commonly seen during the adsorption of heavy metal ions onto NCs, where strong coordinate covalent bonds form between the metal ion (Pb^{2+}) and surface functional groups such as –SiOH, –OH, and –COOH, as illustrated in Fig. 5.2c. [389].

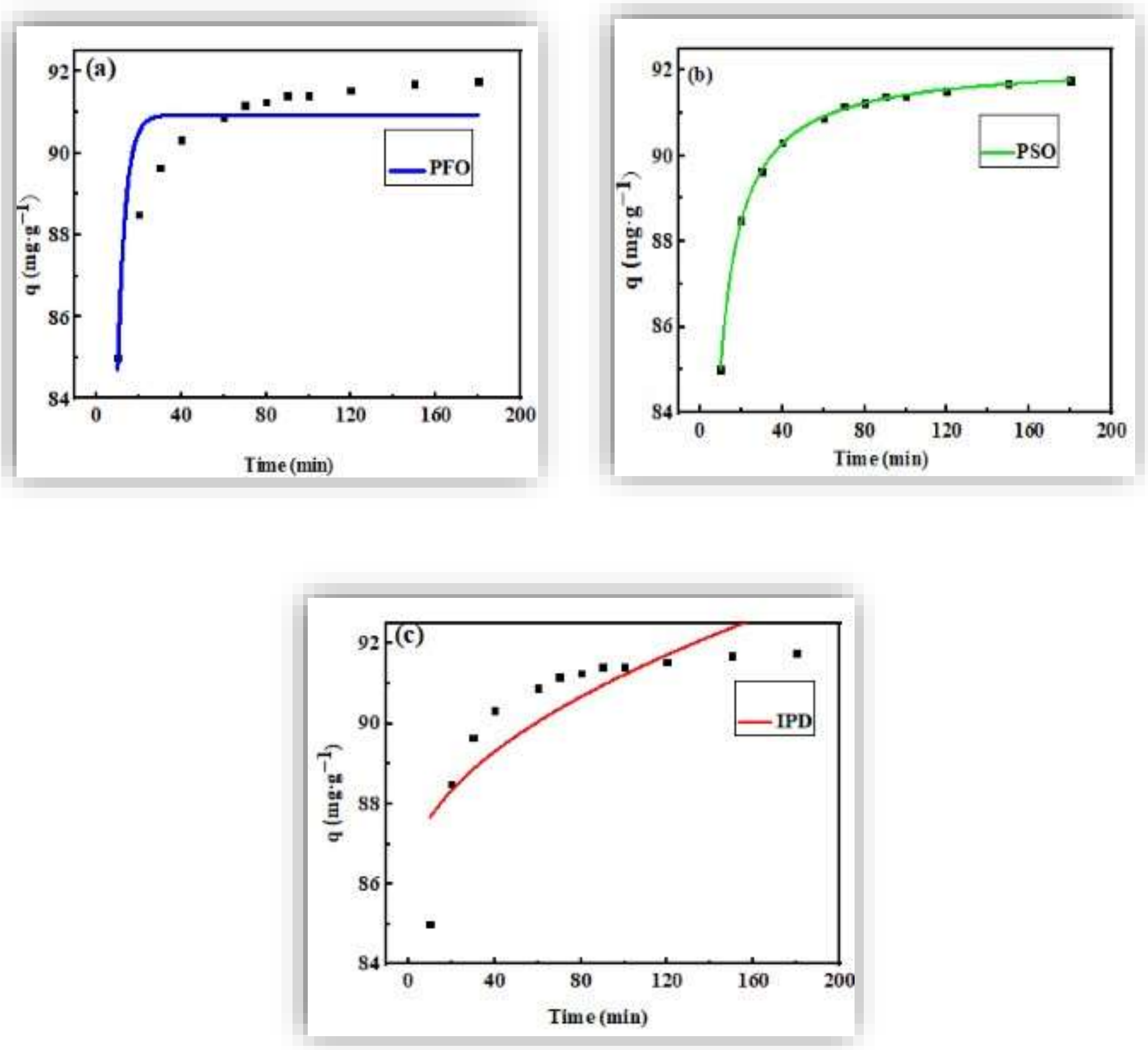

Fig. 5.12. Adsorption kinetic models for adsorption of Pb $^{+2}$ on CHE capped M/PU/Si NC (a) PFO (b) PSO (c) IPD (Adsorption conditions were at pH = 5, Co = 100 mg/L, adsorbent dose = 2 g/L, agitation speed = 200 rpm, T = 25 °C).

In addition, as shown in Table 5.2, the IPD model plot has a low regression coefficient (R^2 0.69) and the intercept is not equal to zero. Besides, one can observe that **(**Fig. 5.12c) the plot does not pass through the origin indicating that IPD was not the rate-limiting step and external diffusion might be involved in the process [390]. Therefore, the formation of the micropore structure of CHE-capped M/PU/Si-NC makes it easy for the diffusion of the lead ions to the active sites because of a microporous material successfully used for adsorbing heavy metals from water solutions [391].

Table 5. 2. Summary of adsorption kinetic model parameters

Kinetic model	**Parameter**	**Pb^{2+}**
Pseudo First Order	q_{exp} (mg/g)	91.8
	q_{cal} (mg/g)	90.9
	R^2	0.80
	K_1	0.2681
Pseudo second order		
	q_{exp} (mg/g)	91.8
	q_{cal} (mg/g)	92
	R^2	0.99
	K_2	0.0128
Intra particle diffusion		
	C	86
	K_{diff}	0.522
	R^2	0.69

5.3.2.6. Adsorption isotherms

To investigate the relationship between initial Pb^{2+} concentration and Pb^{2+} uptake on CHE-capped M/PU/Si-NC adsorbents, Langmuir, Freundlich, and Temkin isotherm models were employed. The study was conducted at 25°C for 60 min at a pH of 5. The initial Pb^{2+} concentration was varied from

1 to 100 mg/L while maintaining a CHE-capped M/PU/Si-NC dose of 2 g/L. Fig. 5.13a and b illustrate the non-linear fitting plots of the Langmuir, Freundlich, and Temkin isotherm models for Pb^{2+} adsorption onto CHE-capped M/PU/Si-NC. The adsorption isotherm parameters are presented in Table 4.3. Table 5.3 reveals that the Langmuir adsorption isotherm has a higher R^2 value (0.999) compared to Freundlich (0.991) and Temkin (0.977), indicating a better fit to the experimental data. The findings suggest that CHE-capped M/PU/Si-NC forms monolayer adsorption without interactions between adsorbed Pb^{2+} ions [356]. The maximum adsorption capacity (qm) of the CHE-capped M/PU/Si-NC adsorbent for Pb^{2+} was found to be 151 mg/g. A comparison of adsorption capacities of different magnetic silica-based adsorbents for Pb^{2+} removal is summarized in Table 5.3. Although the Freundlich model did not fit the data well, the empirical constant n value was greater than 1, suggesting a favorable adsorption process. This indicates a strong interaction between Pb^{2+} and the adsorbent surface [385]. Additionally, the Temkin adsorption isotherm's b_t value was very high (91.8 Kj/mol), suggesting a strong heat of adsorption [178], [392]. This implies the formation of strong attractive forces between the Pb^{2+} ions and the adsorbent surface, confirming the presence of chemisorption [177], [393], [394].

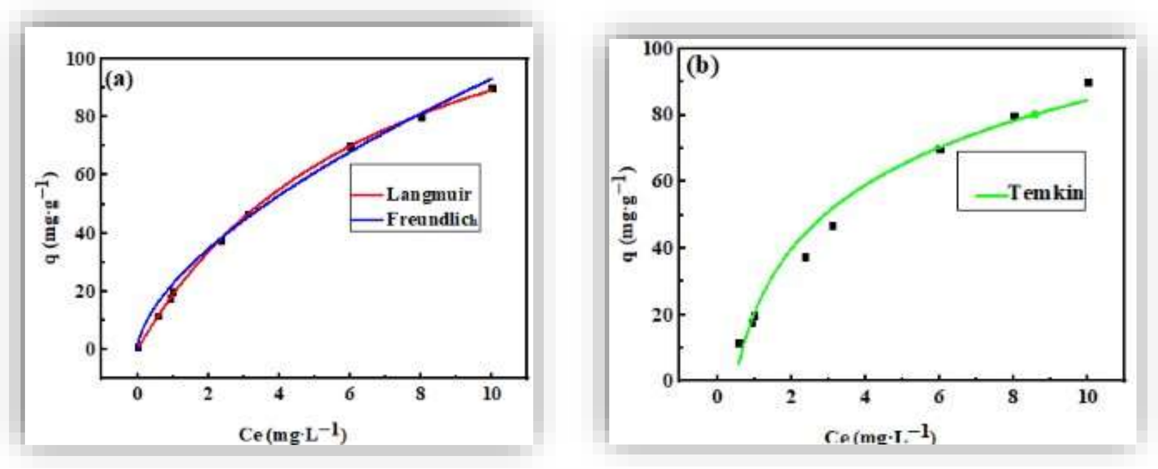

Fig.5.13. (a) Langmuir and Freundlich adsorption isotherm. (b) Temkin adsorption Isotherm (adsorption conditions were at pH = 5, t = 60 min, speed = 200 rpm., adsorbent dose = 2 g/L.

Table 5. 3. Summary of isotherm model parameters

Isotherm	$Q_{m\,(mg\cdot g-1)}$	parameters	R^2

Langmuir	151	K_L=0.1426 (L/mg)	0.999
Freundlich		K_f = 22.66 (g/mg ·min), n=1.624	0.991
Temkin		A_t=2.08 (L/g) b_t=91.8 (KJ/mol)	0.977

5.3.3. Comparison of the adsorption performances

An adsorbent's adsorption capacity is significantly influenced by its surface charge, surface area, and functional groups [395]. The surface charge also determines its stability, biocompatibility, and interactions with other molecules. Our CHE-mediated synthesized NC has good stable electrostatic

properties and is negatively charged (-37 mv). This increases the adsorbent's electrostatic attraction to cationic pollutants. And also CHE/M/PU/Si-NC has a larger surface area (313.9 m^2/g) than the earlier magnetic silica NC adsorbent [332]. Overall, the properties of CHE/M/PU/Si-NC suggest that it possesses a high adsorption capacity compared to other adsorbents. Table 5.4 presents a comparison of the maximum adsorption capacity (q_m) of our synthesized CHE-capped M/PU/Si-NC with values reported in the literature.

Table 5. 4. Comparison of adsorption capacities of different magnetic silica-based adsorbents for Pb^{2+} removal.

Adsorbent	Adsorption capacity (mg/g)	Reference
Silica-Coated Magnetic Nanocomposites	14.9	[332]
Magnetic Mesoporous Silica	143.47	[341]
Magnetic sepiolite/iron(III) oxide composite	90.1	[396]
Magnetite Nanoparticles	108.23	[397]
CHE capped M/PU/Si NC	151	This study

To understand the performance of adsorbents in real-world water samples, comparing their competitive adsorption behaviors is essential. Lead adsorption can be significantly influenced by the presence of other cations, such as cadmium and copper [398]. This study investigated the selectivity of CHE/M/PU/Si-NC for Pb^{2+} adsorption in solutions containing multiple ions. As depicted in Fig. 5.14, the adsorption efficiency for lead alone (control) was 97.5 %. The addition of cadmium ions slightly reduced the adsorption efficiency to 97.35 %, demonstrating a stronger competitive effect due to its smaller ionic radius and similar chemical properties [381]. While copper ions (97.45 %) also competed with lead, their effect was generally less pronounced [399]. When all three ions were present, the combined effect on lead adsorption was greater than their individual effects (96.3 %). Overall, CHE/M/PU/Si-NC remained effective in removing lead even in the presence of competing ions, indicating minimal competitive interference

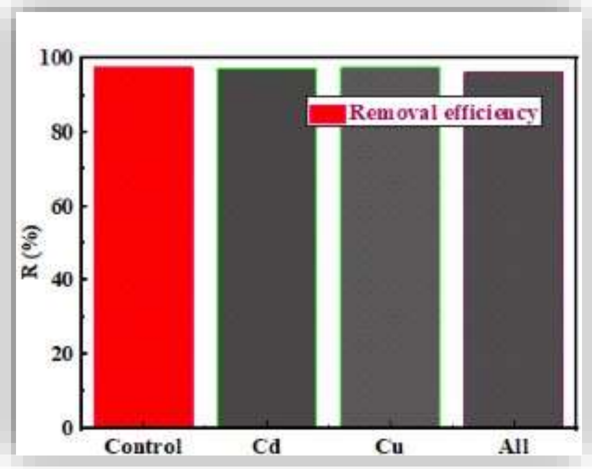

Fig. 5. 14. Effect of competing ions on Pb^{2+} adsorption in aqueous solution (adsorption conditions were C_o = 100 mg/L, adsorbent dose = 2 g/L, pH = 5, t = 60 min, agitation speed = 200 rpm, T =25 ℃).

5.3.4. Reusability of CHE capped M/PU/Si-NC

Reusability of adsorbents is a key component of their economic viability, determining production costs. As a result, determining the reusability of adsorbent materials is critical. The spent CHE-capped M/PU/Si-NC adsorbent was regenerated with 5 % HCl as the desorbing agent [332]. Fig. 5.15 shows the Pb^{2+} uptake onto CHE-capped M/PU/Si NC for various reuse cycles. The Pb^{2+} uptake was 82, 76, 72, 67, and 64 mg/g for the first, second, third, fourth, and fifth reuse cycles. The observed decrease in Pb^{2+} uptake could be attributed to a reduction in adsorbent active sites. As shown in Fig. 5.15, the CHE-capped M/PU/Si-NC maintained nearly 69.6 % of its initial adsorption capacity after five cycles, indicating its excellent recoverability when removing Pb^{2+} from water.

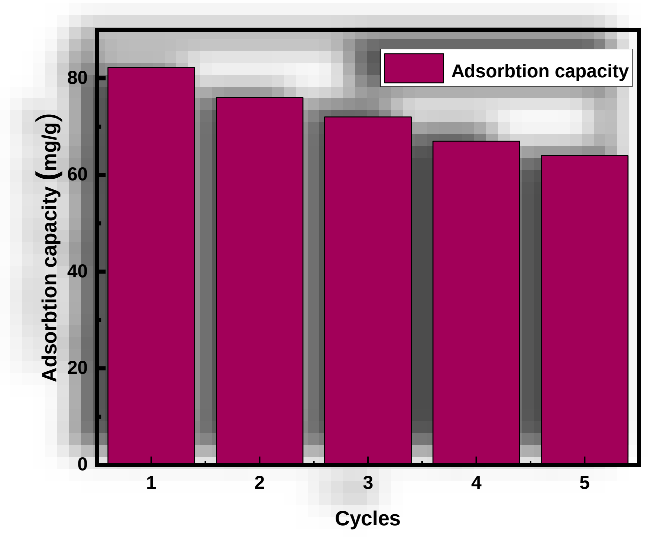

Fig. 5. 9. Regeneration and adsorption capacity of CHE capped M/PU/Si-NC after lead adsorption

5.4. Conclusions

In this study, CHE/M/PU/Si-NC was synthesized and applied for the efficient removal of Pb^{2+} ions from aqueous environments. CHE-capped silica NPs synthesized via plant-mediated methods exhibit superior thermal stability and a remarkable surface area of 338 m^2/g , surpassing that of their sol-gel synthesized counterparts, which demonstrated a surface area of 309 m^2/g. Furthermore, the CHE/M/PU/Si-NC emerged as a standout, boasting an extensive surface area alongside a significantly negative surface charge (-37 mV). This unique combination of physical properties renders it exceptionally suitable for adsorbing cationic lead ions. The adsorption capacity remained robust, with Pb^{2+} uptakes recorded at 82.2, 76, 72, 67, and 64 mg/g for the first through fifth cycles, respectively. The adsorption efficacy of the CHE/M/PU/Si-NC was rigorously evaluated and found to be in excellent agreement with the Langmuir adsorption isotherm and the pseudo-second-order (PSO) kinetic models. This suggests that the silica matrix within the NC, through its silanol (-Si-OH) groups, facilitates the chemisorption and monolayer adsorption of lead ions. The recyclability of the CHE/M/PU/Si-NC adsorbent demonstrated commendable reuse potential across five cycles. The inclusion of magnetic NPs enhanced the post-adsorption separation efficiency and facilitated the recovery and subsequent reuse of the adsorbent material. The demonstrated efficacy of the CHE/M/PU/Si-NC in laboratory conditions paves the way for its application on a larger scale and underscores the need for further studies to evaluate its performance in real-world water treatment scenarios.

CHAPTER SIX

6. AMINE-FUNCTIONALIZED MAGNETIC BIO-NANOCOMPOSITE FOR FLUORIDE AND CHROMIUM REMOVAL FROM WATER.

6.1. Introduction

Water contamination remains one of the most urgent global environmental concerns, significantly threatening both human health and ecological integrity. Among the wide array of water pollutants, hexavalent chromium (Cr(VI)) and fluoride (F^-) stand out due to their high toxicity and potential for long-term adverse health impacts. International assessments reveal that fluoride levels in groundwater exceed the World Health Organization (WHO) guideline of 1.5 mg/L in over 100 countries. Africa alone accounts for the highest number of affected countries 38 in total [3]. The continent represents approximately 37–46% of the global fluoride-affected regions, even though only 6.5% of the world's population resides there. Additionally, Africa is home to 14 of the 20 countries with the highest population at risk from fluoride exposure [400].

In Ethiopia, especially in the Rift Valley region, high fluoride concentrations are frequently detected in groundwater extracted from deep boreholes the primary source of drinking water [401], [402]. While several epidemiological studies have explored the distribution and health impacts of fluoride, the results remain scattered, highlighting the need for a comprehensive synthesis to improve practical implementation [403]. Fluoride levels in Ethiopian water sources show considerable variation, ranging from 0.1 mg/L to as much as 75 mg/L [57]. A meta-analysis by Demelash et al. [2] reported an average fluoride concentration of 6.03 mg/L and a dental fluorosis prevalence of around 28%, with severity levels differing across communities. The region’s main aquifer system consists of weathered and fractured geological formations characterized by high porosity and permeability, making them vulnerable to both natural and human-induced contamination [404]. Geochemical studies indicate that fluoride concentrations ranging from 0.65 mg/L to 11 mg/L are largely driven by rock water interactions [54] .

On the other hand, Cr (VI) contamination primarily stems from industrial activities. In natural environments, chromium exists mainly in two oxidation states: trivalent chromium (Cr(III)) and

hexavalent chromium (Cr(VI)). While Cr(III) is a vital micronutrient involved in glucose metabolism [405], it can become toxic at elevated levels. In aqueous systems, Cr (VI) can exist in several forms such as $HCrO_4^-$, $Cr_2O_7^{2-}$, and $HCr_2O_7^-$depending on pH and other environmental conditions [406]. Cr(VI), however, is highly toxic and carcinogenic, with potential entry routes into the human body including ingestion, inhalation, and dermal absorption. Unlike Cr(III), Cr(VI) is resistant to biodegradation and not easily removed through natural attenuation processes . The World Health Organization (WHO) has set the maximum permissible limit for Cr(VI) in drinking water at 0.05 mg/L [407].

In numerous developing nations, including Ethiopia, the rise in Cr (VI) pollution is closely associated with rapid industrial growth, especially in urban settings where facilities like tanneries, textile mills, and metal-processing plants are situated near rivers and residential zones. Alemu and Gabbiye reported that chromium concentrations in the Abay River near the Habesha Tannery discharge site reached 8.420 mg/L [36], far exceeding the WHO's permissible limit for drinking water (0.05 mg/L). Likewise, Gebreyohannes and Asgedom [37] found high chromium levels in the Ellala River in Mekelle [37], also surpassing WHO standards. Additional studies have documented chromium pollution in the Akaki River, Akaki groundwater, and in the Gondar City area [38]. Moreover, research conducted in central Oromia identified Cr (VI) concentrations up to 0.12 mg/L in groundwater during the rainy season, indicating potential contamination from both direct industrial discharge and subsurface leaching. The coexistence of naturally elevated fluoride and anthropogenic Cr (VI) in shared water sources poses a compounded health threat in regions like Ethiopia's Rift Valley. This overlapping contamination exacerbates the burden on affected populations and complicates water treatment and management strategies. As a result, there is an urgent demand for innovative and cost-effective technologies capable of simultaneously removing both pollutants. Conventional treatment methods such as ion exchange, membrane filtration, and chemical precipitation are often limited by high operational costs, complexity, and poor adaptability in low-resource settings.

Among the available techniques for removing anionic contaminants like F^- and Cr (VI), adsorption has gained widespread attention due to its operational simplicity, design flexibility, efficiency, low energy demand, and environmental compatibility [82]. Recent advancements in nanotechnology have further enhanced the adsorption process, with nanomaterials demonstrating strong potential for removing a wide range of inorganic and organic contaminants from water [408]. Nano adsorbents such as metal oxides [409], silicates [160], and surface-modified mesoporous silica [111] offer numerous advantages including low toxicity, high surface area, chemical stability, superior dispersion, and compatibility with biological systems. Among these, silica-based nanoparticles have attracted particular interest due to their environmental benignity and structural versatility. Silica exhibits excellent resistance to heat and chemicals and can be easily functionalized with various chemical groups [410]. Functional groups on the silica surface enhance its adsorption capacity and selectivity by enabling targeted interactions with specific contaminants [389]. Notably, amine functional groups possess dual binding capabilities, facilitating the removal of both positively and negatively charged ions from aqueous media [411].

In the present study, an amine-functionalized magnetic magnesium–pumice–silica nanocomposite was synthesized for the efficient removal of fluoride and Cr(VI) from contaminated water. The selection of silica as the base material was based on its large surface area, which provides abundant binding sites for pollutant capture [412]. Magnesium (Mg) was incorporated due to its known affinity for fluoride and its role in enhancing the surface charge of the composite, promoting improved adsorption of anionic species [413]. Amine functionalization was employed to further increase surface protonation, thus enhancing electrostatic attraction toward negatively charged contaminants [175]. The inclusion of magnetite (Fe_3O_4) in the nanocomposite enables magnetic separation, allowing for convenient recovery and reuse of the material [414], [415]. Pumice was also incorporated due to its highly porous structure with an average porosity of approximately 90% as well as its excellent chemical, thermal, and mechanical stability, and natural buoyancy, making it a suitable support material [31]. Rich in silicate content, pumice offers abundant active functional groups that facilitate the attachment of metal oxide nanoparticles, thereby enhancing the composite's adsorption performance [416]. Moreover, the addition of pumice improves the dispersion of magnetic and functional components, minimizes nanoparticle aggregation, and reinforces the structural integrity of the nanocomposite [131]. Moreover, CHE was employed as an eco-friendly capping and stabilizing agent during nanomaterial synthesis [417]. Utilizing CHE as a natural source of phytochemical- and antioxidant-rich aqueous extracts represents an economical and sustainable strategy [209]. The presence of functional groups such as hydroxyl (–OH), carbonyl (C=O), and amine ($-NH_2$) in plant extracts plays a pivotal role in the reduction of metal ions to the nanoscale, while simultaneously acting as stabilizers and capping agents [187], [210].

This work introduces a novel, eco-friendly synthesis approach to produce multifunctional nanocomposites capable of removing both fluoride and Cr(VI) from water. To the best of our knowledge, this is the first study to integrate amine functionalization, CHE-capped MgO nanoparticles, and CHE-capped magnetite–pumice–silica into a single composite, specifically designed to enhance positive surface charge and improve anion adsorption. The silica nanoparticles used in this study were derived from bagasse ash, and the CHE served not only as a stabilizer but also as a plant-based reducing and capping agent. This green synthesis route significantly enhanced the composite's adsorption efficiency by increasing electrostatic attraction between the nanocomposite surface and targeted anionic contaminants. This unique approach improved adsorption efficiency by increasing electrostatic attraction between the nanocomposite and anionic contaminants, offering a sustainable and highly effective solution for water purification.

6.2. Materials and methods

6.2.1. Materials

Analytical-grade reagents, including sodium fluoride (NaF), potassium dichromate ($K_2Cr_2O_7$), ferric chloride ($FeCl_3$, 99%), ferrous sulfate heptahydrate ($FeSO_4 \cdot 7H_2O$, 99%), ethanol (C_2H_5OH, 99.02%), ethylenediamine ($C_2H_4(NH_2)_2$), ammonium hydroxide (NH_4OH) and magnesium nitrate hexahydrate ($Mg(NO_3)_2 \cdot 6H_2O$) were procured from Shandong Luba Chemical Co., Ltd. Agricultural and mineral-based precursors were locally sourced: coffee husk from Hierna, Ethiopia; pumice from the Adulala Kebele in the Oromia region; and bagasse boiler ash from the Wenji Sugar Industry.

6.2.2. Methods

6.2.2.1.Synthesis of CHE capped MgO NPs

The green synthesis of MgO NPs was carried out by mixing CH extract with 1 M Mg $(NO_3)_2 \cdot 6H_2O$ solution in a volume ratio of 1:2 at room temperature [284]. The mixture was then heated at 60 °C with continuous agitation using a magnetic stirrer for twenty minutes, resulting in the formation of a turbid brown solution [418], as illustrated in Fig.6.1. Subsequently, stirring was maintained for an additional 2 h while 1 M sodium hydroxide was gradually introduced dropwise until the pH level was adjusted to 12.[419]. The resulting mixture was subjected to centrifugation and subsequently dried in an oven at 60 °C for 12 h. It was subsequently calcined at 500 °C for 3 h to obtain CHE-capped MgO nanoparticles, which were stored for subsequent experimental work.

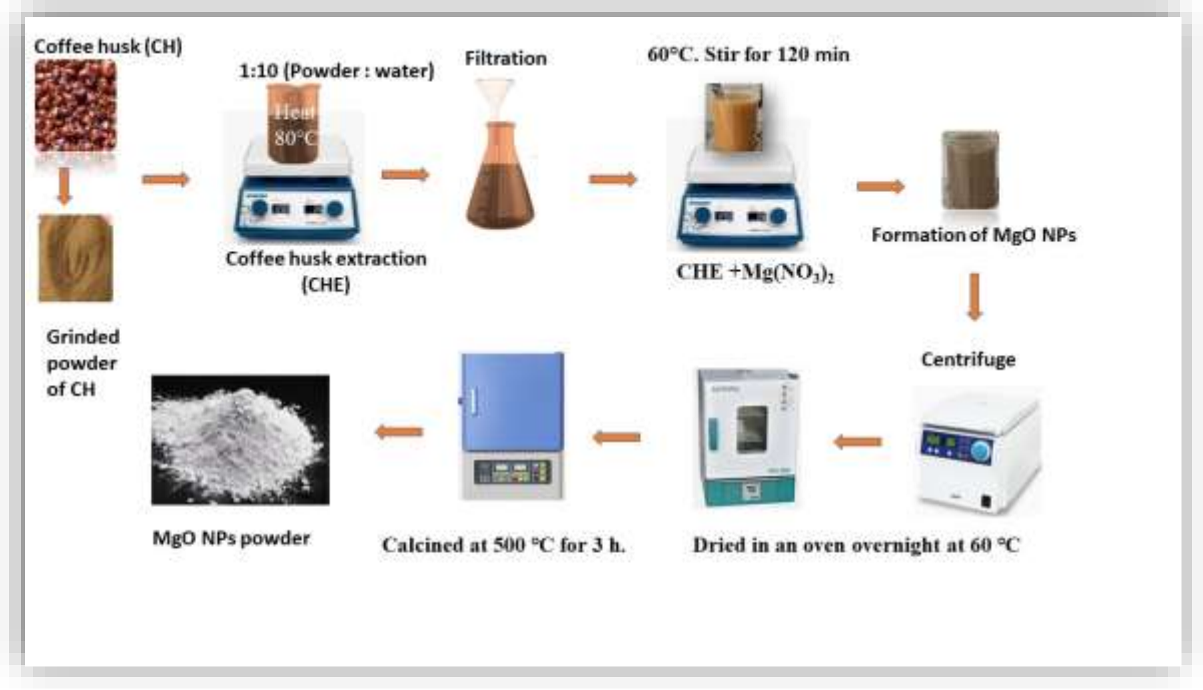

Fig.6. 1. Schematic representation of the preparation of CHE-MgO NPs

6.2.2.2.Synthesis of Fe_3O_4/PU/Mg@SiO_2- Nanocomposite

MgO nanoparticles were incorporated into the CHE-capped Fe_3O_4/PU@SiO_2 composite using a modified coprecipitation-assisted wet impregnation method, as adapted from Ul Ain et al..[420]. The Fe_3O_4/PU nanocomposite was synthesized following the procedure outlined in our previous study [349]. The CHE-capped Fe_3O_4/PU@SiO_2 nanocomposite was then prepared according to the method detailed in our previous work [416]. To integrate MgO, 1 g of the CHE-capped Fe_3O_4/PU@SiO_2 was dispersed in distilled water and homogenized to achieve a uniform suspension. Subsequently, 0.5 g of MgO was added to the solution [421] followed by vigorous stirring for 1 hour. The mixture was further mixed for an additional hour and then placed in a water bath to form a viscous, gel-like mass. Finally, the resulting Fe_3O_4/PU/Mg@SiO_2 nanocomposites were oven-dried and finely ground.

6.2.2.3.Synthesis of Fe_3O_4/PU/Mg@SiO_2-NH_2 Nanocomposite

The approach outlined by Prabu et al. [422] was employed to prepare the amino-functionalized magnetic ,pumice magnesium silica nanocomposite (Fe_3O_4/PU/Mg@SiO_2-NH_2 NC). First, 4g of Fe_3O_4/PU/Mg@SiO_2 nanocomposite was dispersed in 9 mL of ethylenediamine (EDA), and then combined with an aqueous/ethanol solution (76 mL, 1:1). The resulting dispersion was stirred at 80°C for 3 hours. A bar magnet was used to collect the amino-functionalized magnetic pumice magnesium silica nanocomposites. After synthesis, the nanocomposite underwent multiple washes with DI water, followed by vacuum drying at 80 °C for around 12 hours.

6.2.2.4.Adsorbent characterization

X'Pert PRO diffractometer was employed to conduct XRD analysis. to characterize the crystalline structure of the synthesized material and confirm the successful formation of MgO and Fe_3O_4/PU/Mg@SiO_2-NH_2 nanocomposites. A Thermo Scientific Nicolet iS10 spectrometer was used to carry out FTIR spectroscopy for the identification of functional groups in the synthesized materials. The zeta potential and colloidal stability of the nanocomposite were assessed using a Zetasizer Ultra (Malvern Panalytical, UK). Surface features and elemental distribution were characterized through SEM integrated with EDX, utilizing a JEOL JSM-7610F instrument.

6.2.2.5.Adsorption experiments

A set of batch tests was carried out to investigate the impact of variables such as adsorbent amount, interaction time, pH level, and initial concentrations of ions on the adsorption performance for fluoride (F^-) and Cr(VI) using CHE-capped Fe_3O_4/PU/Mg@SiO_2-NH_2 nanocomposite (NC). For fluoride removal, the parameters tested included adsorbent dose (0.1–0.5 g), contact time (10–160 minutes), pH values (2–8), and initial F^- concentration (1–30 mg/L). For Cr (VI) removal, the adsorbent dose (0.2–1.2 g), contact time (10–100 minutes), pH (2–6), and initial Cr(VI) concentration (1–50 mg/L) were examined. The batch tests were conducted in 100 mL rubber-stoppered flasks and placed on an incubator shaker set to 120 rpm (Excella E24R) for the definite durations. After the adsorption process, the nanocomposite was recovered from the suspension via magnetic attraction. To analyze the remaining levels of F^- and Cr (VI), a fluoride-selective electrode was used for fluoride (Turki, Hamdouni, and Enesca 2023), while chromium was quantified using a PerkinElmer Analyst 400 atomic absorption spectrophotometer. pH levels were controlled and maintained through the use of 0.1 M HCl or NaOH. The conditions that resulted in maximum adsorption capacity were identified as optimal and subsequently used for further studies. Eq. (6.1) and (6.2) served to assess both the adsorption capacity (mg/g) and the removal performance (%).

$$q_e=(c_o-c_e)*v/m \tag{6.1}$$

$$R=(c_o-c_e)*100/c_o \tag{6.2}$$

Where q_e is the amounts of F^- and Cr (VI) ion adsorbed at equilibrium (mg/g), c_o, and c_e are concentrations of F^- and Cr (VI) (mg/L) at time 0 and equilibrium, respectively, v is the volume of F^- and Cr (VI) solution used (L) and m is the mass of adsorbent dosage that used (g).

6.2.2.6.Adsorption kinetics

Adsorption kinetics models are commonly used to investigate the adsorption rate and rate-determining stages, which determine how rapidly adsorbate molecules are adsorbed onto the surface of an adsorbent [423]. The Fe_3O_4/PU/Mg@SiO_2-NH_2 NC adsorbent's adsorption process was studied using pseudo-first-order and pseudo-second-order models, as well as intraparticle diffusion. The pseudo-first-order model describes how physisorption limits particle adsorption onto the adsorbent. The nonlinear form of the PFO model's adsorbent capacity-based rate formulation is expressed in Eq. (6.3).

$$qt=qe(1-e^{-K1t}) \tag{6.3}$$

where K_1 (1/min) is the PFO rate constant, and qe (mg/g) and qt (mg/g) are the amounts of F^- and Cr (VI) adsorbed at equilibrium and time t (min), respectively [424] .However, the PSO kinetic model depicts adsorption processes that involve the chemical binding of adsorbates to the surface of adsorbents. Eq.6.4 expresses this kinetic model in nonlinear form.

$$q_t = {q_e}^2 k_2 t/(1+q_e k_2 t) \tag{6.4}$$

Here, k_2 denotes the pseudo-second-order (PSO) rate constant (g/mg·min). Additionally, the intraparticle diffusion equation is employed to illustrate the controlling mechanisms in the total sorption pathway, especially when the graph intercepts the coordinate origin. This equation is presented as Eq.5.

$$q_t = K_{id}\, t^{1/2} + \mathrm{C} \tag{5}$$

In this context, Kid refers to the intraparticle diffusion rate coefficient (g/mg·min), and qt (mg/g) represents the quantity of lead ions retained by the adsorbent at a given time t

6.2.2.7.Adsorption isotherms

Isotherm models were applied to characterize the adsorption process and quantify the uptake of fluoride and hexavalent chromium retained per unit mass of the Fe_3O_4/PU/Mg@SiO_2-NH_2 NC sorbent under varying equilibrium conditions. These models help elucidate the interaction dynamics between the sorbate ions and the active sites of the adsorbent surface. To analyze the adsorption performance and interpret the underlying mechanisms, the Langmuir, Freundlich, and Temkin isotherms were applied and compared with data obtained from batch experiments [425]. The Langmuir model, in particular, is based on the assumption of uniform surface binding sites and monolayer coverage without lateral interactions among adsorbed species [426]. The equilibrium behavior of fluoride and hexavalent chromium with the Fe_3O_4/PU/Mg@SiO_2-NH_2 NC was assessed using the non-linear form of the Langmuir equation (Eq.6.6), which provided insight into the adsorption capacity and affinity under studied conditions.

$$\mathrm{qe} = \mathrm{Qm} * KL * Ce/(1 + \mathrm{KL} * Ce) \tag{6.6}$$

Here, qe represents the amount of adsorbate adsorbed per gram of adsorbent at equilibrium (mg/g), Q_m refers to the system's maximum ability to adsorb the substance (mg/g), Ce is the equilibrium concentration of the adsorbate in solution (mg/L), and KL is the Langmuir isotherm constant.

Unlike the Langmuir model, The Freundlich isotherm describes adsorption occurring in multiple layers on surfaces with non-uniform characteristics where the binding capacity and interaction energy at different sites differ among sites. Initially, adsorbate molecules bind to the most energetically favorable sites, with less favorable sites being occupied as adsorption continues. The nonlinear expression of the Freundlich model is presented in Eq. (6.7).

$$q_{e= K_f . C_e}{}^{1/nf} \tag{6.7}$$

K_f and n_f are empirical constants, where K_f indicates the adsorption capacity of the adsorbent, and n_f reflects the adsorption intensity or favorability.

In addition, the Temkin isotherm model takes into account the indirect interactions between the adsorbate and adsorbent. It proposes that as the surface coverage of the adsorbent increases, the heat of adsorption decreases uniformly across all adsorbed molecules. The Temkin isotherm is expressed in Eq. (6.8).

$$q_e = BLn\,(A_T\,C_e) \tag{6.8}$$

Here, AT denotes the Temkin equilibrium binding constant, while B represents a constant related to the heat of adsorption, defined as $B=RT/b_T$. The parameter bT is the Temkin isotherm constant (kJ/mol), R is the universal gas constant (8.314 J/mol· K).

6.2.2.8.Recovery and stability tests of Fe_3O_4/PU/Mg@SiO_2-NH_2 NC

The Fe_3O_4/PU/Mg@SiO_2-NH_2 nanocomposites (NCs) were regenerated chemically. The used NCs were immersed in a 0.1 M sodium hydroxide (NaOH) solution for two hours [427]. Afterward, the regenerated nanocomposites (NCs) were separated using a magnet, flushed multiple times with distilled deionized water until the wash water stabilized at neutral pH, and then employed in repeated adsorption cycles. The performance of the nanomaterials in terms of recovery and reusability was assessed over five successive cycles.

6.2.2.9.Effect of competing ions

Real water contains a variety of ions, especially anions. The presence of these coexisting anions can influence the adsorbent's ability to remove fluorides and chromates from aqueous solutions [428]. To assess how different anions affect adsorption performance, experiments were conducted using sulfate, chloride, and nitrate in the solution [390].

6.3. Results and Discussion

6.3.1. Characteristics of the adsorbent

6.3.1.1. X-Ray diffraction analysis (XRD) analysis

XRD examination confirmed the synthesis of MgO and Fe_3O_4/PU/Mg@SiO_2-NH_2 NC and established their crystal structures, which are shown in Fig.6.2. The XRD pattern of MgO NPs (Fig.6.2a) verified the formation of crystalline nanoparticles, with typical peaks at 2θ values of 36.87°, 42.85°, 62.18°, 74.58°, and 78.49°, corresponding to the (111), (200), (220), (311), and (222) planes, respectively [419].The XRD pattern of Fe_3O_4/PU/Mg@SiO_2-NH_2 NC (Fig.6.2b) showed peaks consistent with the standard Fe_3O_4 pattern (PDF#79-0419), indicating the presence of Fe_3O_4 NPs with crystalline planes at 30.1°, 35.4°, 43.1°, 53.4°, 56.9°, and 62.5° [389]. Additionally, a broad peak at $2\theta \approx 20°$ confirmed the presence of Pumice and SiO_2 nanoparticles within the composite, along with peaks corresponding to the MgO pattern, indicating successful composite synthesis. The crystallite size of

Fe_3O_4/PU/Mg@SiO_2–NH_2 was calculated using the Debye–Scherrer formula, as expressed in Eq. (6.9)[284].

$$D = k\lambda / (\beta \mathrm{Cos}\theta) \tag{6.9}$$

where D is the crystal size; Scherer constant (k) =0.95; λ is X-ray wavelength, i.e., 1.5406 Å; β = FWHM (full width at half maximum); and θ = Bragg's angle of diffraction.

The crystallite size of the green-synthesized MgO nanoparticles was found to be approximately 7.9 nm, while the Fe_3O_4/PU/Mg@SiO_2-NH_2 nanocomposite exhibited a slightly larger size of about 8.3 nm, as determined from XRD data using the Scherrer equation. Thus, the small size difference reflects successful nanocomposite formation without significant agglomeration or loss of nanoscale features, which is crucial for maintaining the dual functionality and high reactivity of the adsorbent. The structural change from amorphous silica to crystalline silica in the nanocomposite during the incorporation of MgO NPs is supported by the appearance of a diffraction peak, as previously reported. [429]

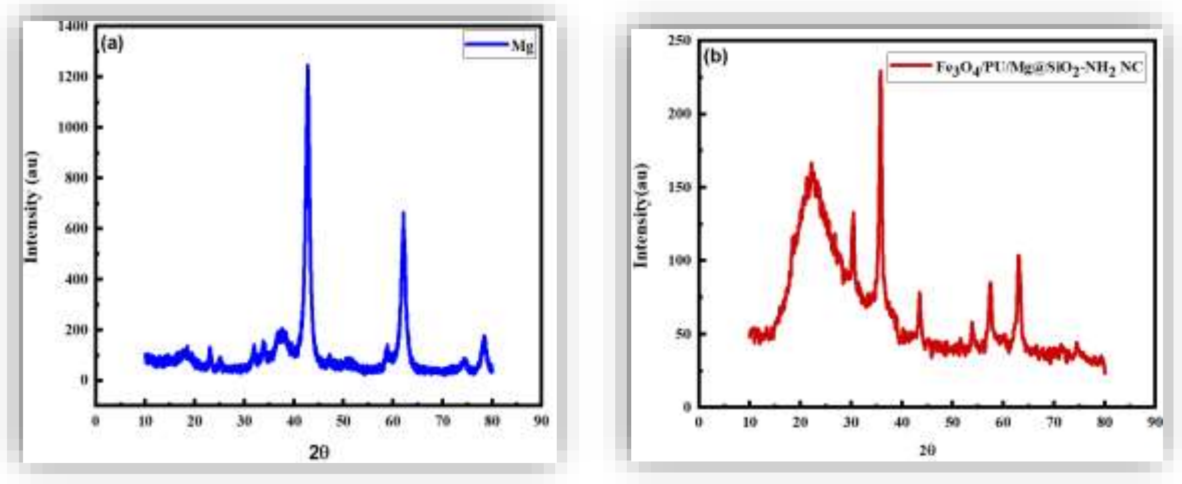

Fig.6. 2. XRD pattern of (a) MgO (b) Fe_3O_4/PU/Mg@SiO_2-NH_2 NC

6.3.1.2.Formation and Functionality of the synthesized material.

The successful synthesis of MgO nanoparticles (NPs), Fe_3O_4/PU@SiO_2-NH_2, and Fe_3O_4/PU/Mg@SiO_2-NH_2 nanocomposites was approved through FTIR spectral analysis, as illustrated in Fig.6.3. The FTIR spectrum of Fe_3O_4/PU@SiO_2-NH_2 (Fig.6.3a) displays several characteristic peaks at 3441, 1640, 1410, 1041, 568, and 455 cm^{-1}. The broad absorption band at 3441 cm^{-1} is attributed to N–H stretching vibrations, indicating successful amine functionalization of the nanocomposite. The peak at 1041 cm^{-1} corresponds to the symmetric vibrations of Si–O–Si [430]. The IR peak at 1640 cm^{-1} corresponds to the bending vibrations of aliphatic amine (-NH_2) [431], confirming the presence of an amine functional group in the Fe_3O_4/PU@SiO_2-NH_2 nanocomposite. Additionally, the peaks around 568 cm^{-1} and 455 cm^{-1} are due to the Fe–O vibration band from the magnetite phase [432].

The FTIR spectrum of the CHE-capped MgO NPs (Fig.6.3c) reveals that the functional groups of possible bioactive molecules present in the CHE acted as reducing agents for the synthesized MgO NPs, as confirmed by the changes in the CHE vibrational bands [284]. In the FTIR spectrum of the prepared MgO nanoparticles, the CHE vibration band shifted from 3270 to 3447 cm^{-1}, suggesting the existence of OH groups derived from the phenolic constituents of CHE. The shift in the peak from 1648 to 1630 cm^{-1} is associated with N–H bond stretching vibrations, while the change from 1417 to 1411 cm^{-1} corresponds to C–C stretching vibrations, likely due to the carboxylic acid group in CHE. The absorption peaks between 876 and 473 cm^{-1} confirm the production of MgO NPs [433].

The FTIR spectrum of the Fe_3O_4/PU/Mg@SiO_2-NH_2 NC, as shown in Fig.6.3b, displays similar peaks to the Fe_3O_4/PU@SiO_2-NH_2 nanocomposite, but with modest shifts and lower intensities, especially for the N–H group on Fe_3O_4/PU/Mg@SiO_2-NH_2. The observed drop in intensity is due to the incorporation of Mg into the Fe_3O_4/PU/Mg@SiO_2-NH_2 nanocomposite. The N–H stretching band shifted from 3441 to 3331 cm^{-1}. Furthermore, the peaks at 568 cm^{-1} indicate the presence of Fe–O stretching vibrations. The peaks also shifted from 455 to 483 cm^{-1} due to the overlapping Fe–O and Mg–O characteristic bands [434]. Additionally, the peaks at 1083 cm^{-1} show the existence of Si–O–Si stretching vibrations. The peak at 802 cm^{-1} reveals Si–O and Mg–O bending vibrations caused by the interaction between Mg–O and silica. The peak at 1640 cm^{-1} confirms the successful attachment of amine groups and matches to the N–H bending vibration of the amine functional groups in Fe_3O_4/PU/Mg@SiO_2-NH_2 nanocomposite.

As shown in Fig. 6.3d and e, several key changes were observed after fluoride and Cr(VI) adsorption onto the Fe_3O_4/PU/Mg@SiO_2–NH_2 nanocomposite, where both ions interacted with the Mg–O bonds, amine groups, and the silica surface. The figure reveals broadening and shifting of peaks, especially in the regions around 3372 cm^{-1} and 1657 cm^{-1} (amine), 1095 cm^{-1} (Si–O), and 467 cm^{-1} (Mg–O), indicating increased surface interactions or the formation of complexes. In acidic conditions, protonated –OH and $–NH_2$ groups form positive sites that attract F^- and $HCrO_4^-$ via electrostatic interactions. Mg–O participates in ion exchange with F^-, while Si–OH and $–NH_2$ contribute through hydrogen bonding [435] and complexation, especially with Cr(VI) [436]. These interactions collectively drive efficient adsorption of both contaminants [436].

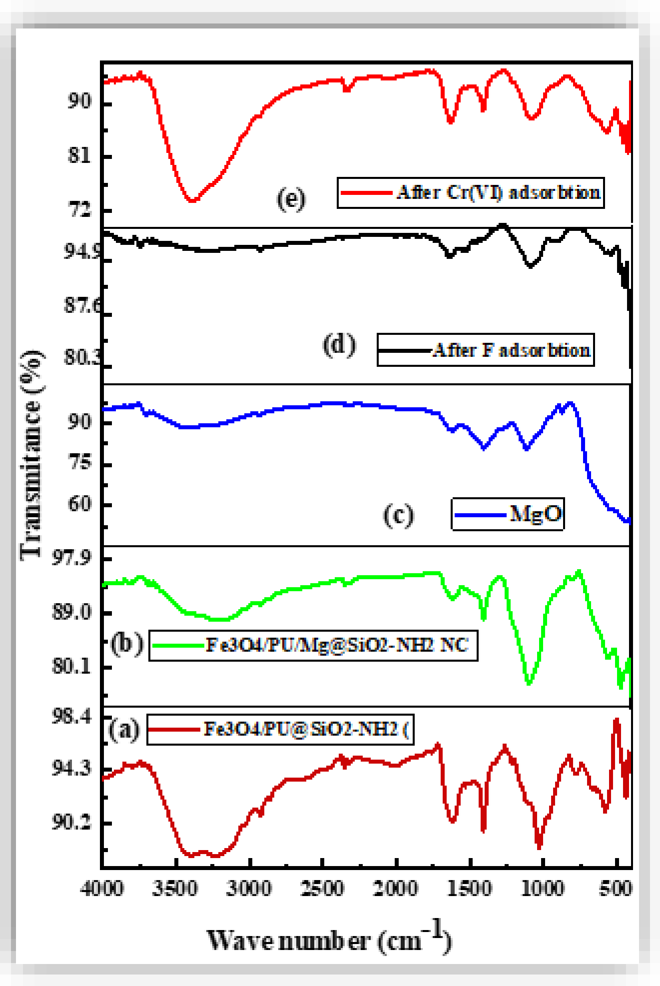

Fig.6. 3. FTIR spectra of (a). Fe_3O_4/PU@SiO_2-NH_2 (b). Fe_3O_4/PU/Mg@SiO_2-NH_2 NC (c). MgO NPs (d). After F^- adsorption (e) After Cr (VI) adsorption

6.3.1.3.Zeta potential analysis

The zeta potential pH curve was employed to evaluate how the surface charge of the nanocomposites changes with pH and to determine their point of zero charge (PZC). This analysis is crucial for understanding surface behavior, colloidal stability, and the adsorption efficiency of materials in water treatment systems. In this study, the zeta potential of Fe_3O_4/PU@SiO_2–NH_2 and Fe_3O_4/PU/Mg@SiO_2–

NH_2 nanocomposites was measured across a pH range of 1 to 10, following the method described by Bakatula et al. [378]. As illustrated in Fig. 6.4, the PZC of Fe_3O_4/PU/Mg@SiO_2–NH_2 was observed at approximately pH 5, while that of Fe_3O_4/PU@SiO_2–NH_2 was around pH 1.5. At neutral pH (pH 7), the measured zeta potentials were –17 mV and –18.4 mV, respectively. Both materials-maintained zeta potential values above –15 mV in neutral conditions, indicating good colloidal stability [349] an important factor for effective dispersion and reliable adsorption performance in aqueous systems.

Additionally, the zeta potential results revealed that Fe_3O_4/PU@SiO_2–NH_2 held a positive surface charge only up to pH 1.5, whereas Fe_3O_4/PU/Mg@SiO_2–NH_2 remained positively charged up to pH 5. This shift toward positive surface charge after amine functionalization aligns with previous studies on NH_2-modified magnetic silica [416], [437]. Furthermore, the incorporation of MgO nanoparticles enhanced the material's surface positivity, as also noted by Cheng et al.[438], thereby increasing the electrostatic attraction between the adsorbent and negatively charged species such as fluoride (F^-) and hexavalent chromium (Cr(VI)). This contributes to improved mass transfer and greater adsorption efficiency.

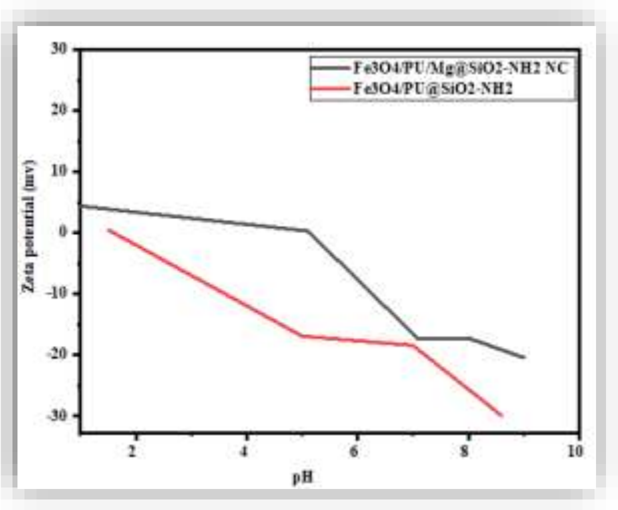

Fig.6. 4. Zeta potential of Fe_3O_4/PU/Mg@SiO_2-NH_2 NC and Fe_3O_4/PU@SiO_2-NH_2

Overall, zeta potential analysis confirmed the dual functionality of the synthesized adsorbent, attributed to the coexistence of both negatively and positively charged surface sites. At pH values above 5, the surface becomes negatively charged, favoring the adsorption of cationic pollutants. In contrast, under acidic conditions (below pH 5), the MgO nanoparticles and amine groups become protonated, enabling effective removal of anionic contaminants. This tunable surface charge behavior allows the adsorbent to efficiently target both cationic and anionic species in aqueous solutions.

6.3.1.4.Scanning Electron Microscopy (SEM) analysis

Scanning Electron Microscopy (SEM) was employed to analyze the surface morphology of Fe_3O_4/PU/Mg@SiO_2-NH_2 nanocomposites before and after the adsorption of fluoride and hexavalent chromium. The SEM image prior to adsorption Fig.6.5a showed spherical nanoparticles featuring a highly porous structure with numerous cavities, which enhances the ability of the adsorbent to capture adsorbate molecules. After adsorption Figs.6.5b and 6.5c, the surface exhibited visible aggregates or layered deposits, and notable morphological changes were observed, indicating the successful attachment of fluoride and hexavalent chromium ions. These outcomes point to the vital contribution of the nanocomposite’s porous architecture in facilitating the efficient elimination of F^- and Cr(VI) from aqueous solutions [414], consistent with previous research [439].

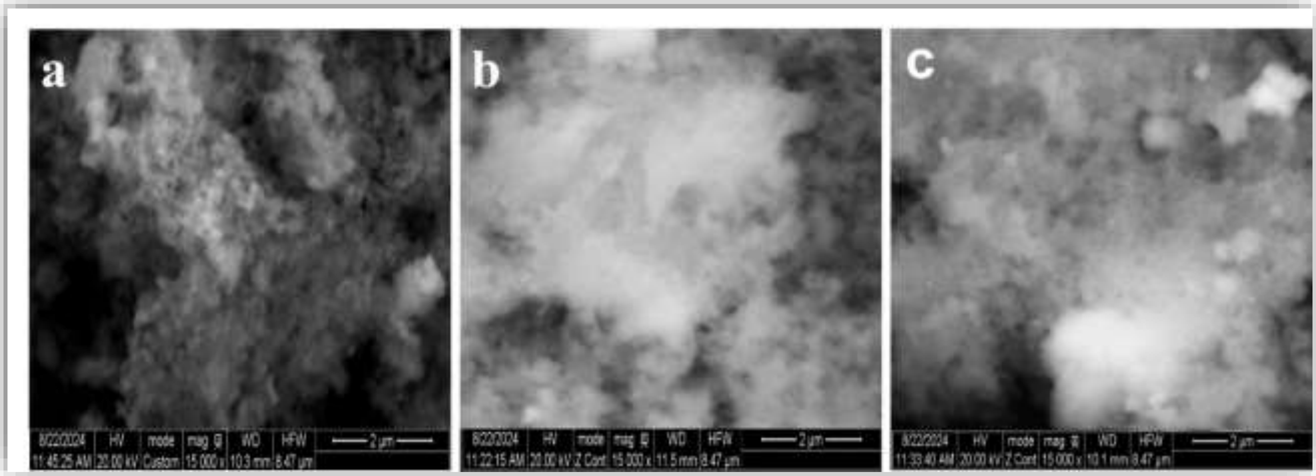

Fig.6. 5. Analysis of SEM for Fe_3O_4/PU/Mg@SiO_2-NH_2 NC (a) before (b)after the F^- (d) after the Cr (IV) sorption.

6.3.1.5.Energy dispersive spectroscopy (EDS) and EDS mapping analysis

To validate the incorporation of the target elements, the synthesized nanomaterial was analyzed using Energy Dispersive Spectroscopy (EDS). Fig.6.6a demonstrates the presence of elements in Fe_3O_4/PU/Mg@SiO_2-NH_2 NC Displays peaks near 0.9 and 6.4 keV, corresponding to the binding energies of Fe [290], as well as an oxygen peak at 0.5 keV and Si peak at 1.8 keV confirms the presence of Si in the composite.. The result agreed with those obtained by Rahman et al [291].

Magnesium (Mg) and nitrogen (N) were also detected, appearing at 1.24 keV [172] and 0.39 keV [440], respectively. The synthesized material was composed almost entirely of the expected elements, suggesting high purity with minimal impurities. Trace amounts of Na and Cl were detected, likely due to the use of NaOH and HCl for pH adjustment during synthesis, while the appearance of C peaks can be attributed to sample coating. Throughout the analytical procedure, as illustrated in Fig. 6.c and d, subsequent to the adsorption of fluoride and hexavalent chromium by Fe_3O_4/PU/Mg@SiO_2-NH_2 nanocomposites, the presence of 7.4% F and 7.26% Cr confirms effective adsorption of these ions onto the nanocomposite surface. The EDS elemental mapping of Fe3O4/PU/Mg@SiO2-NH2 nanocomposite, shown in Fig.6.6b, indicates high purity and uniform distribution of Fe, Si, O, Mg, and N, confirming the effective green synthesis of the nanocomposite.

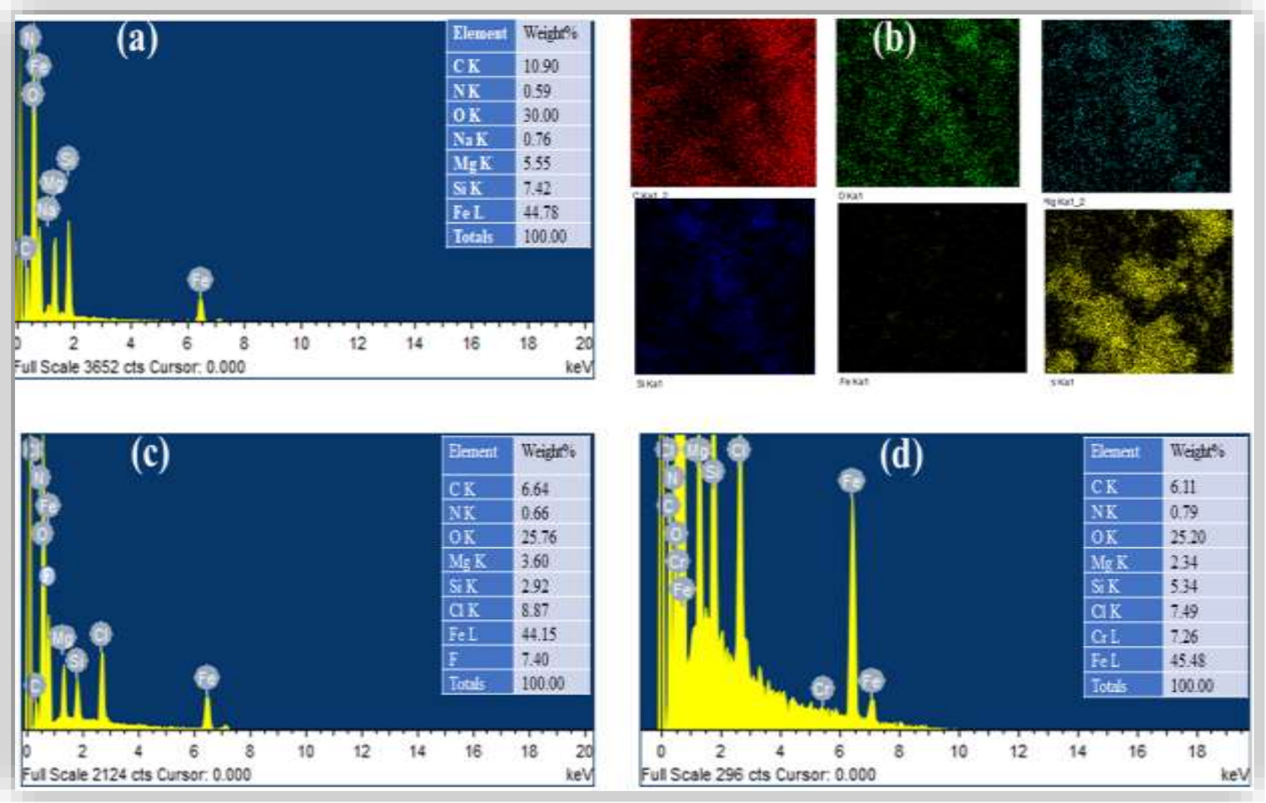

(a)

Element	Weight%
C K	10.90
N K	0.59
O K	30.00
Na K	0.76
Mg K	5.55
Si K	7.42
Fe L	44.78
Totals	100.00

(c)

Element	Weight%
C K	6.64
N K	0.66
O K	25.76
Mg K	3.60
Si K	2.92
Cl K	8.87
Fe L	44.15
F	7.40
Totals	100.00

(d)

Element	Weight%
C K	6.11
N K	0.79
O K	25.20
Mg K	2.34
Si K	5.34
Cl K	7.49
Cr L	7.26
Fe L	45.48
Totals	100.00

Fig.6. 6. Analysis of Fe_3O_4/PU/Mg@SiO_2-NH_2 NC of (a) EDX (b) EDS map (c) EDX after F^- sorption (d) EDX after Cr (VI) sorption.

6.3.2. Adsorption Experiment

6.3.2.1.Effect of pH

The acidity or alkalinity of a solution significantly influences the adsorption of F^- and Cr(VI) ions when utilizing Fe^3O_4/PU/Mg@SiO_2-NH_2. Variations in pH alter the surface charge of the nanocomposite, which in turn affects the electrostatic interactions with F^- and Cr (VI). This relationship is critical for optimizing fluoride removal efficiency. As revealed in Fig.6.7a at lower pH values (from 2 to 4), the uptake of fluoride is very low since a fraction of fluoride becomes unavailable for adsorption and HF is weakly ionized in solution at low pH values [441]. However, Fig.6.7b shows that Cr(IV) adsorption is highest at pH 2. This is likely because at acidic pH, the dominant form of hexavalent Cr (VI) , $HCrO_4^-$, is more strongly attracted to the surface groups of the adsorbent than other forms, such as CrO_4^{2-} or $Cr_2O_7^{2-}$, which predominate at higher pH [442], [443].

And at higher pH (pH > 6), fluoride primarily exists as the dissociated F^- ion, while Cr (VI) is present as $CrO4^{2-}$ and $Cr_2O_7^{2-}$ ions. The adsorption of both F^- and Cr(VI) onto the adsorbent surface decreases at higher pH due to competition from hydroxide ions (OH^-) for adsorption sites on the nanocomposite material [444]. In addition, the surface charge of the adsorbent material, such as amine-functionalized magnetic silica nanocomposites, under alkaline conditions become more negatively charged. The variation in surface charge influences the electrostatic interactions with negatively charged fluoride (F^-) and Cr (VI) ions. In this study, fluoride adsorption was optimal at pH 5. At this pH, protonation of amine groups and MgO likely creates a positively charged surface on the Fe_3O_4/PU/Mg@SiO_2-NH_2 nanocomposite [445], [446]. Specifically, under acidic conditions, the amine groups ($–NH_2$) on the adsorbent are protonated to $–NH_3^+$, which strengthens the electrostatic attraction to fluoride ions. Similarly, the MgO surface gains a positive charge in acidic media due to protonation of surface hydroxyl groups. These positively charged sites promote fluoride adsorption via electrostatic interaction. Generally acidic pH optimized the adsorption of F^- and Cr (VI) onto Fe_3O_4/PU/Mg@SiO_2-NH_2 NC. Because amine protonated (NH_3^+) in acidic conditions and can directly interact with F- and Cr (VI) ions through hydrogen bonding and other interactions, contributing to the overall adsorption process. And the presence of MgO, a basic oxide, further enhances. This effect by contributing to a more positive surface charge at lower pH values, further attracting F^- and Cr (VI) ions forming strong Mg-F and Mg-Cr (VI) complexes on the surface. This complexation mechanism further enhances target pollutant adsorption. While excessively low pH values may adversely affect the stability of the nanocomposite or alter the surface chemistry.

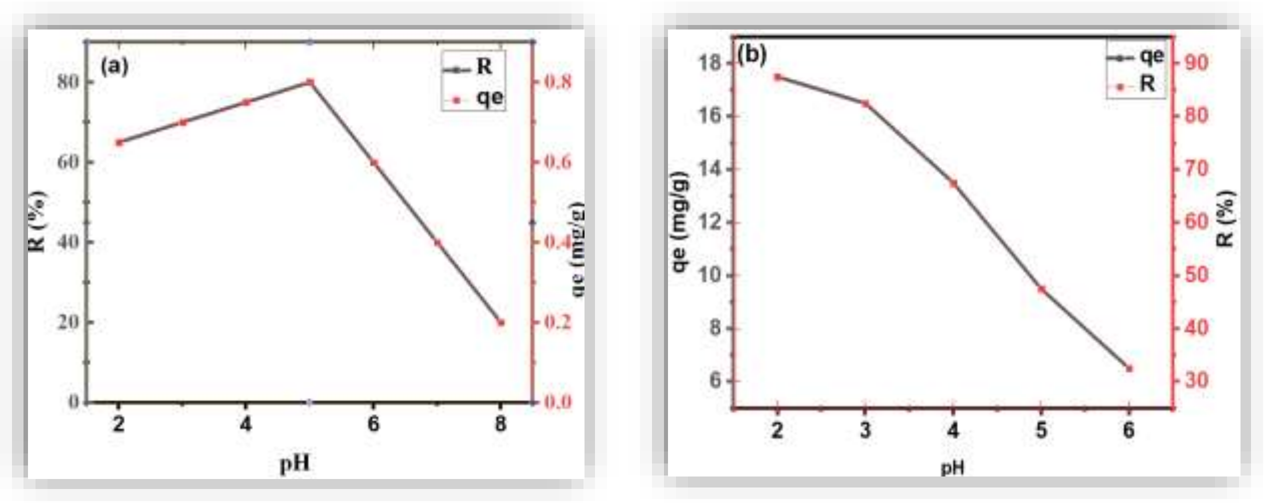

Fig.6. 7. Adsorption capacity of Fe_3O_4/PU/Mg@SiO_2-NH_2 at different pH (a) F^- (b). Cr (VI)

6.3.2.2.Effect of initial concentrations

Figures 6.8a and 6.8b illustrate the influence of the initial concentrations of F^- and Cr(VI) on the removal efficiency and adsorption capacity of Fe_3O_4/PU/Mg@SiO_2-NH_2, respectively. When the initial concentrations of F^- and Cr (VI) increase from 1 to 5 mg/L and 10 to 30 mg/L, respectively, removal efficiency increases by 90% and 80%, respectively, due to ample adsorption sites. However, as concentrations increase further (5-30 mg/L for F- and 30-50 mg/L for Cr (VI)), removal efficiency may decrease due to site saturation. In contrast, adsorption capacity increases with increasing F^- and Cr (VI) concentrations as more ions are adsorbed onto the surface [428], [447], [448].

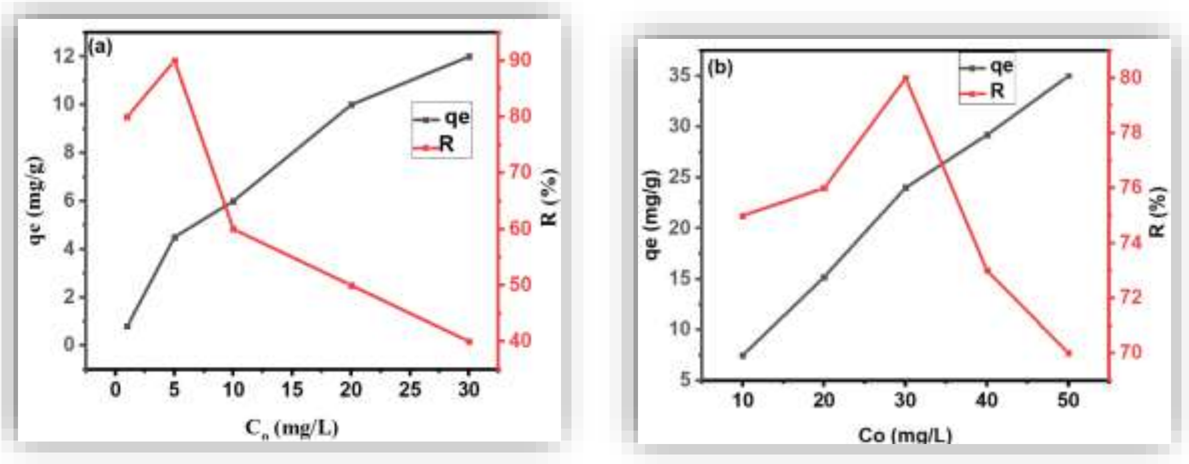

Fig.6. 8. Adsorption capacity of Fe_3O_4/PU/Mg@SiO_2-NH_2 at different initial concentrations of (a) F^- (b). Cr (VI)

6.3.2.3.Adsorbent dosage

The adsorbent dosage plays a critical role in determining the adsorption capacity, efficiency, and overall performance of the adsorption process as shown in Fig.6.9 a and b for F^- and Cr (VI) respectively. At lower adsorbent dosage (1 to 3 gm/L) for F^- and Cr (VI) (2 to 8 gm/L) may result in fewer available adsorption sites on the nanocomposite surface. This can lead to a lower overall adsorption efficiency as not all F^- and Cr (VI) ions in the solution can be effectively captured by the limited number of adsorption sites. Whereas increasing the adsorbent dosage from 3 to 4g/L and 8 to 10g/L can provide more available adsorption sites for F^- and Cr (VI), respectively potentially leading to a higher adsorption efficiency. The higher surface area and more active sites can enhance the adsorption efficiency at high dosages until saturation is reached [449]. Increasing the adsorbent dosage to 5 g/L and 12 g/L led to faster equilibrium but a reduction in the adsorption efficiency for F^- and Cr(VI), respectively. This decline may be due to mass transfer limitations caused by excess adsorbent in the solution [444] . The lower efficiency for Cr(VI) (86% at 10 g/L) compared to F^- (92% at 4 g/L) is attributed to differences in charge and interaction mechanisms. Cr (VI) exists as multivalent oxyanions (CrO_4^{2-}, $HCrO_4^-$) [450], [451], which interact less effectively than monovalent F^- through electrostatic forces. Fluoride is mainly adsorbed via strong electrostatic attraction to protonated amine and MgO sites, whereas Cr (VI) undergoes slower redox or complexation reactions. Generally, as shown in Fig.6.9a and b (right side), increasing adsorbent dosage reduced adsorption capacity, likely due to dense particle packing hindering the diffusion of ions to active sites.

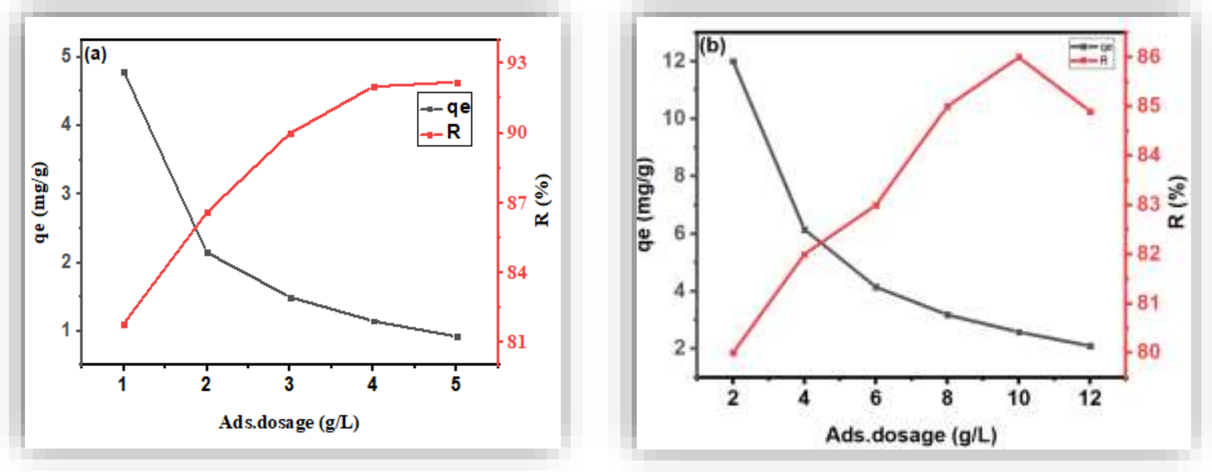

Fig.6. 9. Effect of Adsorbent dosage on adsorption capacity (a) F^- (b) Cr (VI)

6.3.2.4.Effect of contact time

The contact period between the Fe_3O_4/PU/Mg@SiO_2-NH_2 NC and the F- and Cr (VI) containing solution is critical in the adsorption process. As seen in Fig.6.10, Initially, there was an enormous driving force toward fast adsorption. showed an increase in adsorption capacity until 90 min and 50 min for F^- and Cr (VI), respectively. Because of the high concentration of F^- and Cr (VI) ions in the solution and the available adsorption sites on the Fe_3O_4/PU/Mg@SiO_2-NH_2, the F- and Cr (VI) ions adsorbed on the adsorbent surface become reduced after 90 and 50 minutes, respectively, due to the saturation of accessible adsorption sites on the nanocomposite surface. This leads to in a decrease of the adsorption capacity. Then adsorption process the system reaches an equilibrium state where the rate of F^- and Cr (VI) adsorption onto the Fe_3O_4/PU/Mg@SiO_2-NH_2 NC becomes equal to the rate of F^- and Cr (VI) desorption from the Fe_3O_4/PU/Mg@SiO_2-NH_2.

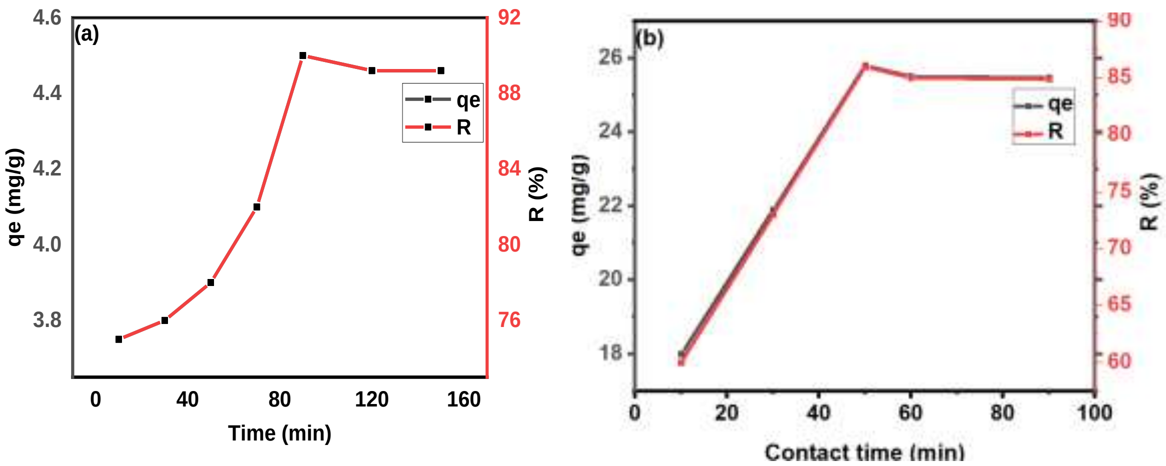

Fig.6. 10. Effect of contact time on adsorption capacity (a) F^- (b) Cr (VI).

6.3.2.5.Adsorption kinetic

A pseudo-first-order (PFO), pseudo-second-order (PSO), and intraparticle diffusion (IPD) kinetic models were applied to investigate the adsorption rates of F^- and Cr(VI) ions onto Fe_3O_4/PU/Mg@SiO_2-NH_2 nanocomposite (NC) beads. The results of the kinetic modeling are summarized in Table 6.1 and illustrated in Figures 6.11a and b. Owing to its higher coefficient of determination (R^2 = 0.99) compared to the PFO model (R^2 = 0.91), along with better agreement between the calculated and experimental adsorption capacities, the PSO model provided a more accurate representation of the experimental data. This suggests that chemisorption is the primary mechanism governing the adsorption of F^- and Cr (VI) ions. Furthermore, FTIR analysis revealed shifts and a weakening of the absorption bands particularly those associated with -NH_2, -OH, Si-O, and Mg-O groups indicating their involvement in the adsorption process.

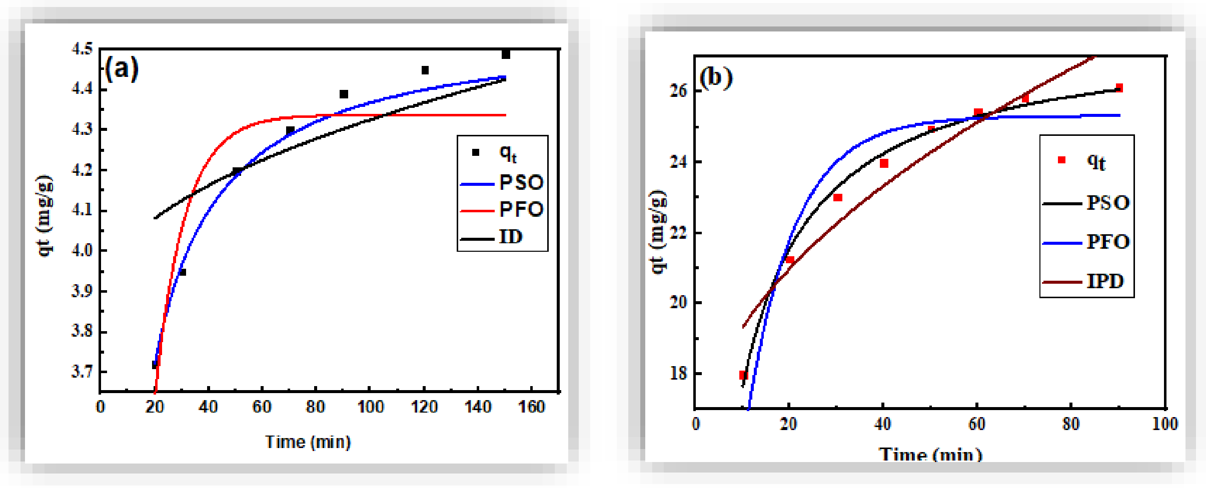

Fig.6. 11. Adsorption kinetic model of (a) F^- (b) Cr (VI)

Table 6.1. Adsorption kinetic modeling results summary

Kinetic model	**Parameter**	**F^-**	**Cr (IV)**
PFO	q_{exp} (mg/g)	4.49	26.14
	q_{cal} (mg/g)	4.33	25.31
	R^2	0.91	0.92
	K_1	0.09	0.099
PSO			
	q_{exp} (mg/g)	4.49	26.14
	q_{cal} (mg/g)	4.57	26.50
	R^2	0.99	0.99
	K_2	0.05	0.006s
IPD	C	3.9	1.6
	Kdiff	0.04	15.33
	R^2	0.52	0.91

According to Table 6.1, the intraparticle diffusion (IPD) model exhibits lower regression coefficients for both F^- (0.69) and Cr (VI) (0.91), along with a non-zero intercept. Furthermore, Fig.6.11a and b illustrate that the plots do not intersect the origin, as evidenced by the non-zero intercepts, which further supports the conclusion that intraparticle diffusion is not the sole rate-limiting mechanism. This behavior suggests the involvement of multiple rate-limiting steps, particularly the contribution of film diffusion, also known as external mass transfer, in the initial stages of adsorption. In this phase, adsorbate ions must first diffuse through the boundary layer surrounding the adsorbent particles before reaching the internal pore surfaces. The deviation from linearity in the IPD plots and the non-zero intercepts reflects this resistance. Therefore, it can be concluded that both film diffusion and intraparticle diffusion play significant roles in the overall adsorption process, with film diffusion dominating in the early stage and intraparticle diffusion becoming more relevant in the later stages. The better fit of the pseudo-second-order model further implies that chemisorption is the primary kinetic mechanism.

6.3.2.6.Adsorption Isotherm

The Langmuir, Freundlich, and Temkin isotherm models were employed to describe the relationship between the amount of F^- and Cr (VI) ions adsorbed onto the Fe_3O_4/PU/Mg@SiO_2-NH_2 nanocomposite and their respective concentrations in solution. As shown in Figure 6.12a and b and summarized in Table 6.2, the Langmuir isotherm yielded the highest coefficient of determination ($R^2 = 0.99$) for both F^- and Cr (VI) ions, outperforming the Freundlich and Temkin models. These results indicate that the Langmuir model best describes the adsorption behavior of the system, suggesting that monolayer adsorption is the dominant mechanism. This aligns with the model’s assumption of uniform and energetically equivalent active sites on the Fe_3O_4/PU/Mg@SiO_2–NH_2 nanocomposite surface. While real adsorbent surfaces are rarely perfectly homogeneous, the strong correlation with the Langmuir model implies that monolayer coverage is more influential under the experimental conditions than multilayer or heterogeneous adsorption, which would be better represented by the Freundlich model. The Langmuir maximum adsorption capacities (q_m) were found to be 14 mg/g for fluoride and 66.4 mg/g for Cr(VI). Although the Freundlich model showed a weaker fit, the adsorption process is still favorable, as indicated by Freundlich constants ($n > 1$), reflecting strong interactions between the adsorbate ions and the nanocomposite surface.

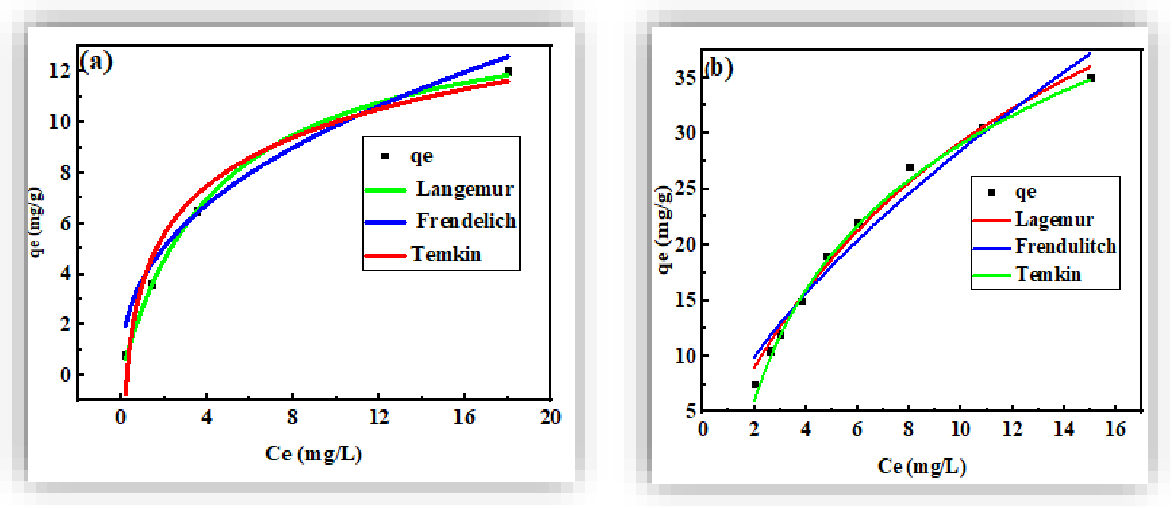

Fig.6. 12. Adsorption isotherm model of (a) F$^-$ (b) Cr (VI)

Table.6.1. Summary of Findings from Isotherm Model Parameters

Isotherm	**parameters**	**F$^-$**	**Cr (VI)**
Langmuir	Qm (mg/g)	14.79	66.41
	K_L (L/mg)	0.22	0.0785
	R^2	0.99	0.99
Freundlich	K_f (g/mg min),	3.8	6.33
	n	1.4	1.1
	R^2	0.95	0.96
Temkin	At (L/g)	4.8	0.76
	bt (KJ/mol)	9.84	14
	R^2	0.94	0.97

Additionally, the Temkin isotherm constants bt for F$^-$ and Cr(VI) were relatively high (9.18 and 14 kJ/mol, respectively), indicating a significant heat of adsorption. This suggests strong attractive interactions between the pollutant anions and the adsorbent surface, supporting the occurrence of chemisorption.

6.3.3. Influence of Competing Anions on the Adsorption of F^- and Cr(VI)

To effectively evaluate the performance of adsorbents in treating real-world water contaminated with F^- and Cr(VI), it is important to investigate their adsorption behavior in the presence of competing anions. Co-existing anions such as sulfate (SO_4^{2-}), nitrate (NO_3^-), and chloride (Cl^-) may interfere with the adsorption process by competing for the active binding sites on the adsorbent surface. The impact of these anions on the removal efficiency of F^- and Cr (VI) is illustrated in Fig.6.13a and b.

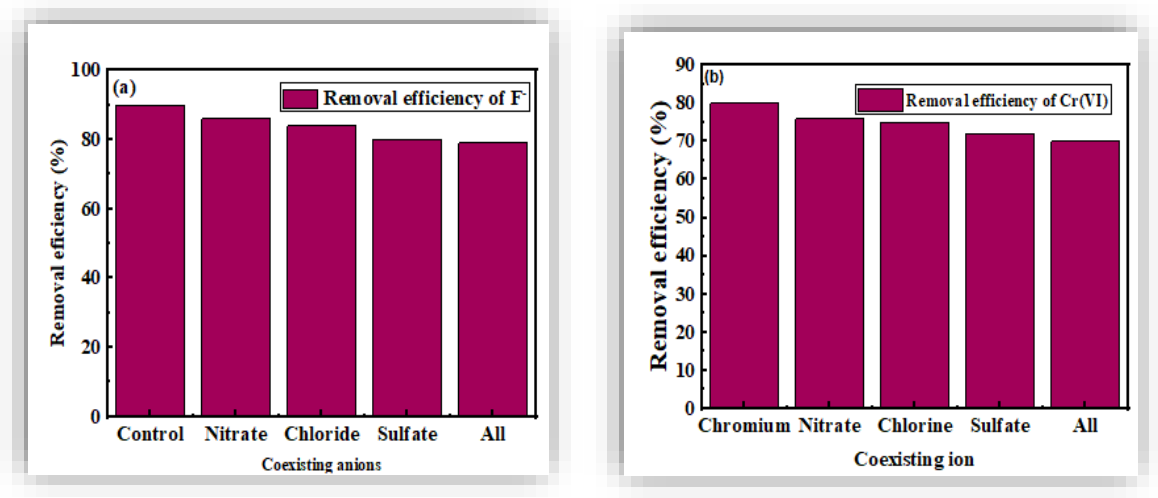

Fig.6. 13. Influence of coexisting anions on the adsorption efficiency of (a) F^- (b) Cr (VI).

Experimental results showed a slight decline in the removal efficiency of F^- and Cr (VI) when competing anions were present, with sulfate (SO_4^{2-}) exerting the greatest effect. In acidic conditions, SO_4^{2-} competes strongly with both F^- and $HCrO_4^-$ due to its divalent nature, moderate ionic radius, and relatively high charge density [451]. Although fluoride has a higher charge density [452] , its monovalent charge and tightly bound hydration shell weaken its competitiveness. Compared to $HCrO_4^-$, sulfate's higher charge and comparable size enable it to more effectively occupy adsorption sites [453] . Conversely, nitrate (NO_3^-) and chloride (Cl^-) showed only a slight influence on F^- and Cr (VI) adsorption. Their larger ionic radii, lower charge densities, and lack of specific surface interactions reduce their ability to compete with F^- and $HCrO_4^-$ for adsorption sites [453], [454].

6.3.4. Comparison of the adsorption performances

Compared to other silica- and magnetic-based adsorbents, the Fe_3O_4/PU/Mg@SiO_2-NH_2 nanocomposite demonstrates a higher adsorption capacity. This improved performance is mainly due to the incorporation of amine functional groups and MgO nanoparticles, which enhance surface interactions with anionic pollutants of Cr (VI) and F^- ions. Table 6.3 presents a comparative evaluation of the maximum adsorption capacity (q_m) of the Fe_3O_4/PU/Mg@SiO_2-NH_2 NC in relation to values reported in previous studies.

Table 6.2. Comparative Review of Adsorption Behavior of Fe_3O_4/PU/Mg@SiO_2-NH_2 NC and other adsorbents for Cr (VI) and F^- removal.

Sorbent	Type of pollutant	pH	Contact time (min)	C_o (mg/L)	q_m (mg/g)	Ref
Silica nanoparticles	F^-	3	10min	10	8	[455]
Si NPs modified with rice husk	F	8	60	10	12	[456]
Iron Oxide (Fe_3O_4)-Supported SiO_2 Magnetic Nanocomposites	F^-	4	10	10	5.59	[449]
Iron functionalized silica particles fluoride from water	F^-	6	45	20	8	[457]
Diatomite Modified with Aluminum Hydroxide	F^-	6	180	10	1.69	[458]
Fe_3O_4/PU/Mg@SiO_2-NH_2 NC	F^-	5	90	5	14.78	This study
Magnetic carbon-based	Cr (VI)	5	90	25	62.7	[459]
nanocomposites	Cr (VI)	2	120	100	42	[435]
Magnetic Fe/C crosslinked NPs	Cr (VI)	6	30	100	48.8	[460]
Chemically functionalized amorphous and mesoporous Si NP	Cr (VI)	2	120	100	42.2	[435]
Fe_3O_4/PU/Mg@SiO_2-NH_2 NC	Cr (VI)	2	50	30	66	This study

6.3.5. Reusability of Fe3O4/PU/Mg@SiO2-NH2 NC

The Fe_3O_4/PU/Mg@SiO_2–NH_2 nanocomposite has demonstrated strong potential as an efficient adsorbent for removing heavy metals such as Cr(VI) and F^- from aqueous environments. Its high adsorption capacity is primarily attributed to its large surface area, magnetic properties, and the presence of amine functional groups that enhance interaction with contaminants. For sustainable and economical use, reusability of the adsorbent is essential. As revealed Fig.6.14 a, there is a gradual decline in removal efficiency for Cr(VI) and F^- over multiple regeneration cycles, mainly due to the gradual exhaustion of active adsorption sites. Nevertheless, the nanocomposite retained about 84.4% and 82.5% of its initial adsorption capacity for F^- and Cr (VI), respectively, after five reuse cycles. These results highlight the material's excellent regeneration capability and reliable performance for long-term water purification.

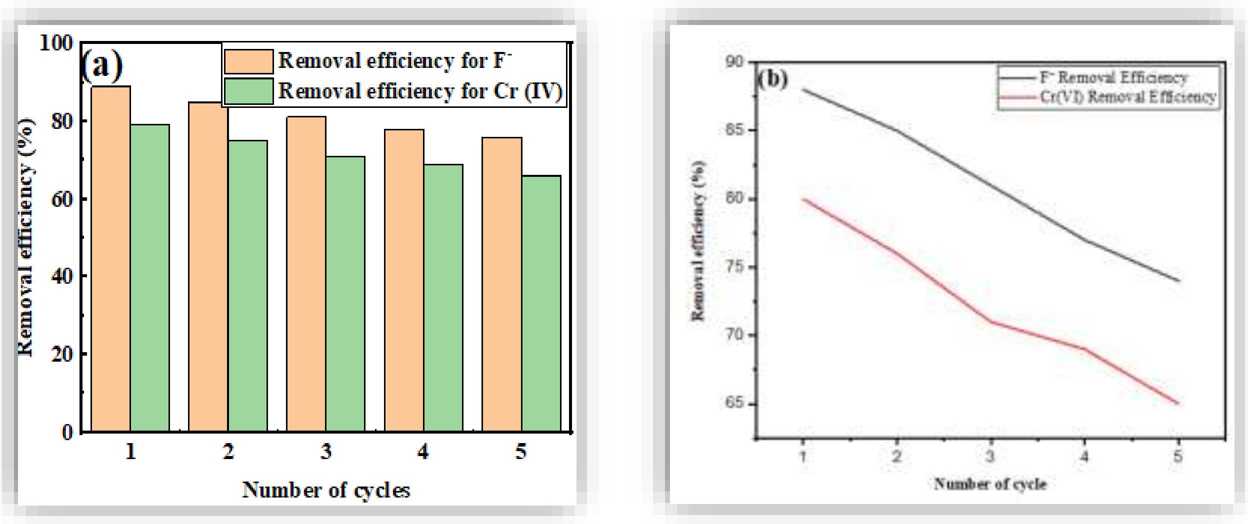

Fig.6. 14. (a) Reusability of Fe_3O_4/PU/Mg@SiO_2-NH_2 NC for Cr (VI) and F^- removal (b) Degradation trend graph

As illustrated in Fig.6.14b, the degradation trend demonstrates a progressive decline in removal efficiency for both F^- and Cr(VI) across five successive adsorption desorption cycles. The initial fluoride removal efficiency of approximately 88% decreased to about 74% by the fifth cycle, while Cr(VI) removal efficiency declined from around 80% to 65%. This reduction is likely due to partial saturation or blockage of active sites [461], structural degradation of the adsorbent, and potential loss or modification of functional groups during the regeneration process [459].

6.3.6. Adsorption Mechanism

Fluoride ions primarily exist in an anionic form and interact with the functional groups present on the surface of the amine-functionalized Fe_3O_4/MgO/SiO_2 nanocomposite. The main adsorption mechanisms include electrostatic attraction between the negatively charged fluoride ions and positively charged protonated amine groups [462], ion exchange processes involving magnesium hydroxide sites [463], and hydrogen bonding with silanol groups [458], [464]. Similarly, hexavalent chromium in acidic media predominantly exists as the monovalent oxyanion $HCrO_4^-$. Its adsorption is mainly driven by electrostatic attraction to protonated amine groups, complexation with magnesium hydroxide groups, and hydrogen bonding interactions with silanol functionalities [436]. These combined interactions explain the effective adsorption of both fluoride and Cr(VI) ions onto the nanocomposite surface, as illustrated in Fig. 6.15.

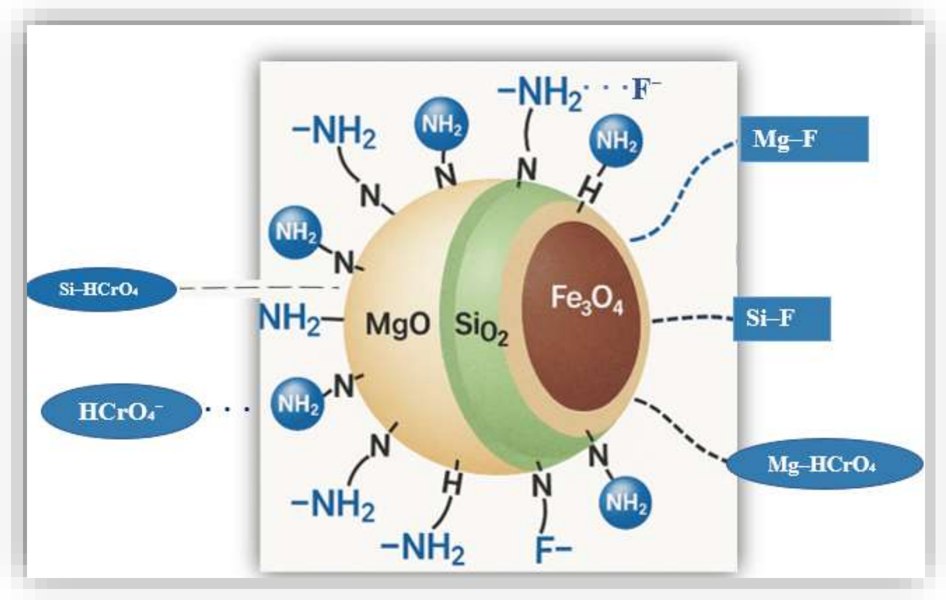

Fig.6. 15. Schematic representation of the dominant adsorption pathways for F^- and Cr(VI) on the adsorbent.

6.4. Conclusion

In this thorough investigation, we produced Fe_3O_4/PU/Mg@SiO_2-NH_2 NC using a green synthesis approach to remove anionic pollutants (F^- and Cr (VI) ion) from aqueous solution. The adsorbent material was evaluated by XRD, SEM with EDX, FTIR, and Zeta potential analysis. The EDX examination confirmed that the produced material contains SiO_2, Fe_3O_4 NPs, PU, and MgO nanoparticles. The Zeta potential study indicated that the addition of magnesium (Mg) was strategically used to increase the adsorbent's positive surface charge. Furthermore, amine functionalization enhances the composite's surface protonation, which promotes the adsorption of negatively charged anion contaminants F- and Cr (VI) ion. The adsorption efficacy of the Fe_3O_4/PU/Mg@SiO_2-NH_2 NC was thoroughly tested and found to be in great accord with the Langmuir adsorption isotherm and pseudo-second-order (PSO) kinetic models. This agreement shows that the Fe_3O_4/PU/Mg@SiO_2-NH_2 NC matrix within the nanocomposite, through its NH_2, -OH, Si-O, and Mg-O groups, enables the chemisorption and monolayer adsorption of F- and Cr (VI) ions, underlining a method of interaction that is both selective and efficient. A critical component of this study is the recyclability of the Fe_3O_4/PU/Mg@SiO_2-NH2 NC adsorbent. At the fifth cycle, the adsorption efficiency of F- and Cr(VI) using Fe_3O_4/PU/Mg@SiO_2-NH_2 NC remained impressively high, at roughly 84.4% and 82.5% of their initial capacities, respectively. The incorporation of magnetic nanoparticles into the composite matrix not only improves separation performance post-adsorption, but also makes it easier to recover and reuse the adsorbent material. The convincing findings of this work not only make major contributions to the realm of environmental remediation, but also encourage further investigation of Fe_3O_4/PU/Mg@SiO_2-NH_2 NC for broader applications in the purification of contaminated water resources.

CHAPTER SEVEN

7. OVERALL CONCLUSION AND RECOMMENDATIONS

This study focused on the synthesis and evaluation of plant-mediated nanocomposite materials for simultaneous pollutant removal in water purification. The research successfully developed eco-friendly nanomaterials with antimicrobial and adsorptive properties, demonstrating their potential as sustainable solutions for water treatment.

7.1. Overall Conclusion

I. Synthesis of CHE-Capped ZnO-NPs:

Zinc oxide nanoparticles (ZnO-NPs) were synthesized using a green approach, employing coffee husk extract (CHE) as both a reducing and stabilizing agent. The resulting ZnO-NPs exhibited strong antimicrobial activity against E. coli and S. aureus, high thermal stability, and a uniform spherical shape with a particle size of 22 nm and a surface area of 19.06 m²/g. These properties suggest their potential for pathogen disinfection in water treatment.

II. Development of CHE-Capped Fe_3O_4/PU/ZnO Nanocomposite:

Incorporating plant-mediated, CHE-capped Fe_3O_4/PU with plant-mediated, CHE-capped ZnO-NPs yielded a nanocomposite with enhanced antibacterial efficacy. This nanocomposite exhibited a larger surface area (47.2 m²/g), improved thermal stability, and superior bacteriostatic and biocidal activity against *E. coli* and *S. aureus* compared to bare ZnO-NPs. The nanocomposite's particle size was 11 nm.

III. Synthesis of CHE/M/PU/Si-NC for lead ion Removal:

A magnetite-based, CHE-capped silica nanocomposite (CHE/M/PU/Si-NC) was synthesized for efficient Pb^{2+} ion adsorption. The incorporation of CHE increased the silica nanoparticles' surface area to 338 m²/g, compared to 309 m²/g for Sol Si NPs. CHE/M/PU/Si-NC exhibited a strong negative surface charge (-37 mV), resulting in a high adsorption capacity for cationic lead ions. Adsorption followed Langmuir isotherm and pseudo-second-order kinetic models. The nanocomposite demonstrated high reusability and maintained 96.3% lead removal efficiency even with competing ions, confirming its potential for heavy metal removal.

IV. Fabrication of Fe_3O_4/PU/Mg@SiO_2-NH_2 NC for Anionic Pollutant Removal:

A green-synthesized nanocomposite, functionalized with amine (-NH_2) and incorporating magnesium (Mg) groups, was developed for fluoride (F^-) and chromium (Cr(VI)) removal from water. The resulting positively charged surface enabled effective adsorption of these negatively charged contaminants. The material maintained high adsorption efficiency over five cycles, retaining approximately 84.4% and 82.5% of its initial F^- and Cr (VI) adsorption capacities, respectively. This demonstrates its reusability and potential for large-scale water purification.

Overall, the synthesized nanomaterials demonstrated remarkable antimicrobial and adsorptive capabilities, making them promising candidates for water purification. The successful incorporation of plant-derived stabilizers ensured an environmentally friendly synthesis process while enhancing the materials' stability and performance. Future research should focus on optimizing these nanocomposites for real-world applications, particularly by exploring their immobilization in polymer matrices to facilitate separation and reuse in large-scale water treatment systems.

7.2. Recommendation and Justification for Future Work

In this study, we evaluated the antibacterial and adsorption performance of the synthesized nanocomposite using model aqueous solutions under controlled laboratory conditions. This approach was selected because pollutants in real drinking water are not uniform and the material itself is novel. As this is among the first studies to examine the adsorption ability of this nanocomposite, future work should validate the following practical applicability by testing it with actual drinking water:

- The antibacterial performance of CHE-capped ZnO NPs and the CHE-capped Fe_3O_4/PU/ZnO nanocomposite should be evaluated in real drinking water samples contaminated with waterborne pathogens.
- To advance the practical application of the developed nanocomposite material in household water treatment systems, it is also recommended to conduct continuous-flow column experiments that simulate real-world operating conditions. These experiments should focus on optimizing key parameters such as flow rate, bed height, contact time, and breakthrough capacity to assess the material’s adsorption performance. The outcomes of these studies will not only contribute to refining purifier design but also support regulatory compliance,

operational safety, and user acceptability for point-of-use water treatment systems in domestic settings.

- Further studies are recommended to optimize the adsorption pH of the CHE/M/PU/Si-NC and Fe_3O_4/PU/Mg@SiO_2-NH_2 nanocomposites for the removal of Pb^{2+}, and (Cr(VI), and F^-) at a pH of suitable for drinking water respectively. Their performance should also be tested using real drinking water.
- Additional research is recommended to optimize the ratio of magnesium oxide nanoparticles incorporation in the CHE/M/PU/Si-NC nanocomposite to enhance surface charge and adsorption efficiency.
- It is recommended to conduct leaching tests and health toxicity level assessments to evaluate the safety and potential release of elements from the developed water purifier materials during operation. These tests are essential to ensure that the purifier meets health and environmental safety standards for long-term use.

REFERENCE

[1] WHO\UNICEF, *Progress on household drinking water, sanitation and hygiene 2000-2020: five years into the SDGs*. 2021.

[2] H. Demelash, A. Beyene, Z. Abebe, and A. Melese, “Fluoride concentration in ground water and prevalence of dental fluorosis in Ethiopian Rift Valley: Systematic review and meta-analysis,” *BMC Public Health*, vol. 19, no. 1, pp. 1–9, 2019, doi: 10.1186/s12889-019-7646-8.

[3] E. Y. Wong and M. K. Stenstrom, “Onsite de fl uoridation system for drinking water treatment using calcium carbonate,” *J. Environ. Manage.*, pp. 6–10, 2017, doi: 10.1016/j.jenvman.2017.06.060.

[4] M. Wołowiec, M. Komorowska-kaufman, A. Pruss, G. Rzepa, and T. Bajda, “Removal of Heavy Metals and Metalloids from Water Using Drinking Water Treatment Residuals as Adsorbents : A Review,” no. August, 2019, doi: 10.3390/min9080487.

[5] M. Manyangadze *et al.*, “Heliyon Adsorption of lead ions from wastewater using nano silica spheres synthesized on calcium carbonate templates,” *Heliyon*, vol. 6, no. August, p. e05309, 2020, doi: 10.1016/j.heliyon.2020.e05309.

[6] S. Mitra *et al.*, “Impact of heavy metals on the environment and human health: Novel therapeutic insights to counter the toxicity,” *J. King Saud Univ. - Sci.*, vol. 34, no. 3, p. 101865, 2022, doi: 10.1016/j.jksus.2022.101865.

[7] D. Dibbisa Itana, T. Daba Bedada, and S. Mohammed Ebu, “A bioremediation approach of some selected heavy metal detected from Bishoftu and Mojo industrial effluents in Ethiopia,” *Egypt. J. Aquat. Res.*, no. August 2024, 2025, doi: 10.1016/j.ejar.2025.03.002.

[8] B. Fei-Baffoe, E. Badu, K. Miezah, L. N. Adjiri Sackey, A. Sulemana, and E. E. Yahans Amuah, “Contamination of groundwater by petroleum hydrocarbons: Impact of fuel stations in residential areas,” *Heliyon*, vol. 10, no. 4, p. e25924, 2024, doi: 10.1016/j.heliyon.2024.e25924.

[9] A. Ahmed, A. . Sara Taha, R. Q. and Sundas, and W. Man-Qun, “Heavy Metals and Pesticides Toxicity in Agricultural Soil and Plants: Ecological Risks and Human Health Implications,”

Toxics, vol. 9, p. 42, 2021.

[10] V. Srivastava, A. Sarkar, S. Singh, P. Singh, A. S. F. de Araujo, and R. P. Singh, "Agroecological responses of heavy metal pollution with special emphasis on soil health and plant performances," *Front. Environ. Sci.*, vol. 5, no. OCT, pp. 1–19, 2017, doi: 10.3389/fenvs.2017.00064.

[11] M. Afzaal *et al.*, "Heavy metals contamination in water, sediments and fish of freshwater ecosystems in Pakistan," *Water Pract. Technol.*, vol. 17, no. 5, pp. 1253–1272, 2022, doi: 10.2166/wpt.2022.039.

[12] P. B. Angon *et al.*, "Sources, effects and present perspectives of heavy metals contamination: Soil, plants and human food chain," *Heliyon*, vol. 10, no. 7, p. e28357, 2024, doi: 10.1016/j.heliyon.2024.e28357.

[13] RiPPLE, "Fluoride Problems in Ethiopian Drinking Watertle," *Http://Www.Rippleethiopia.Org/*, vol. 1, p. 1, 2016.

[14] J. P. S. Cabral, "Water microbiology. Bacterial pathogens and water," *Int. J. Environ. Res. Public Health*, vol. 7, no. 10, pp. 3657–3703, 2010, doi: 10.3390/ijerph7103657.

[15] A. Hernández-Vásquez, F. J. Visconti-Lopez, and R. Vargas-Fernández, "Escherichia coli Contamination of Water for Human Consumption and Its Associated Factors in Peru: A Cross-Sectional Study," *Am. J. Trop. Med. Hyg.*, vol. 108, no. 1, pp. 187–194, 2023, doi: 10.4269/ajtmh.22-0240.

[16] H. Rakotomanana, J. J. Komakech, C. N. Walters, and B. J. Stoecker, "The who and unicef joint monitoring programme (Jmp) indicators for water supply, sanitation and hygiene and their association with linear growth in children 6 to 23 months in east Africa," *Int. J. Environ. Res. Public Health*, vol. 17, no. 17, pp. 1–14, 2020, doi: 10.3390/ijerph17176262.

[17] L. Asefa, A. Ashenafi, D. Dhengesu, H. Roba, and H. Lemma, "Household water treatment practice and associated factors among rural Kebeles (villages) in west Guji zone, southern Ethiopia: Community based cross-sectional study," *Clin. Epidemiol. Glob. Heal.*, vol. 22, no. May, p. 101311, 2023, doi: 10.1016/j.cegh.2023.101311.

[18] N. A. A. Qasem, R. H. Mohammed, and D. U. Lawal, "Removal of heavy metal ions from

wastewater: a comprehensive and critical review," *npj Clean Water*, vol. 4, no. 1, 2021, doi: 10.1038/s41545-021-00127-0.

[19] S. Satyam and S. Patra, "Innovations and challenges in adsorption-based wastewater remediation: A comprehensive review," *Heliyon*, vol. 10, no. 9, p. e29573, 2024, doi: 10.1016/j.heliyon.2024.e29573.

[20] M. S. Akhtar, S. Ali, and W. Zaman, "Innovative Adsorbents for Pollutant Removal: Exploring the Latest Research and Applications," *Molecules*, vol. 29, no. 18, pp. 1–37, 2024, doi: 10.3390/molecules29184317.

[21] D. Sahu *et al.*, "Applications of different adsorbent materials for the removal of organic and inorganic contaminants from water and wastewater – A review," *Desalin. Water Treat.*, vol. 317, no. February, p. 100253, 2024, doi: 10.1016/j.dwt.2024.100253.

[22] L. Xuan, Z. Ju, M. Skonieczna, P. K. Zhou, and R. Huang, "Nanoparticles-induced potential toxicity on human health: Applications, toxicity mechanisms, and evaluation models," *MedComm*, vol. 4, no. 4, pp. 1–39, 2023, doi: 10.1002/mco2.327.

[23] R. Javed, M. Zia, S. Naz, S. O. Aisida, N. ul Ain, and Q. Ao, "Synthesis, Characterization, and Evaluation of Antimicrobial Efficacy of Reduced Graphene–ZnO–Copper Nanocomplex," *J. Nanobiotechnology*, vol. 18, no. 1, pp. 1–15, 2020, doi: 10.1186/s12951-020-00704-4.

[24] C. Pechyen, B. Tangnorawich, S. Toommee, R. Marks, and Y. Parcharoen, "Green synthesis of metal nanoparticles, characterization, and biosensing applications," *Sensors Int.*, vol. 5, no. March, p. 100287, 2024, doi: 10.1016/j.sintl.2024.100287.

[25] A. K. Sidhu, N. Verma, and P. Kaushal, "Role of Biogenic Capping Agents in the Synthesis of Metallic Nanoparticles and Evaluation of Their Therapeutic Potential," *Frontiers in Nanotechnology*, vol. 3. Frontiers Media S.A., Jan. 31, 2022. doi: 10.3389/fnano.2021.801620.

[26] Nishu and S. Kumar, "Smart and innovative nanotechnology applications for water purification," *Hybrid Adv.*, vol. 3, no. March, p. 100044, 2023, doi: 10.1016/j.hybadv.2023.100044.

[27] N. Asghar *et al.*, "Advancement in nanomaterials for environmental pollutants remediation: a

systematic review on bibliometrics analysis, material types, synthesis pathways, and related mechanisms," *J. Nanobiotechnology*, vol. 22, no. 1, 2024, doi: 10.1186/s12951-023-02151-3.

[28] E. A. S. Dimapilis, C. S. Hsu, R. M. O. Mendoza, and M. C. Lu, "Zinc oxide nanoparticles for water disinfection," *Sustain. Environ. Res.*, vol. 28, no. 2, pp. 47–56, 2018, doi: 10.1016/j.serj.2017.10.001.

[29] P. Jain *et al.*, "Silica nanobiocatalyst: Advancements toward sustainable and innovative applications," *Next Nanotechnol.*, vol. 6, no. April, p. 100068, 2024, doi: 10.1016/j.nxnano.2024.100068.

[30] M. de O. Silva, J. N. B. Honfoga, L. L. de Medeiros, M. S. Madruga, and T. K. A. Bezerra, "Obtaining Bioactive Compounds from the Coffee Husk (Coffea arabica L.) Using Different Extraction Methods," *Molecules*, vol. 26, no. 1, 2021, doi: 10.3390/MOLECULES26010046.

[31] S. Parvaz, M. Rabbani, and R. Rahimi, "Fabrication of novel magnetic ZnO hollow spheres/pumice nanocomposites for photodegradation of Rhodamine B under visible light irradiation," *Mater. Sci. Eng. B Solid-State Mater. Adv. Technol.*, vol. 263, Jan. 2021, doi: 10.1016/j.mseb.2020.114863.

[32] UNICEF/WHO, "Progress on Household Drinking Water ," pp. 1–4, 2021, [Online]. Available: https://washdata.org/sites/default/files/2022-01/jmp-2021-wash-households_3.pdf

[33] A. A. Alemu, M. S. Bitew, K. A. Gelaw, L. B. Zeleke, and G. M. Kassa, "Prevalence and determinants of uterine rupture in Ethiopia: a systematic review and meta-analysis," *Sci. Rep.*, vol. 10, no. 1, pp. 1–20, 2020, doi: 10.1038/s41598-020-74477-z.

[34] E. Belete, Z. Getaneh, and D. Debebe, "Assessment of lead contamination in soil and tap water in daycare facilities in Addis Ababa: implications for children's health," *Water Pract. Technol.*, vol. 19, no. 7, pp. 2584–2594, 2024, doi: 10.2166/wpt.2024.159.

[35] D. Debebe, F. Behulu, and Z. Getaneh, "Predicting children's blood lead levels from exposure to school drinking water in Addis Ababa, Ethiopia," *J. Water Health*, vol. 18, no. 4, pp. 595–601, 2020, doi: 10.2166/WH.2020.248.

[36] A. Alemu and N. Gabbiye, "Assessment of chromium contamination in the surface water and soil at the riparian of Abbay r iver caused by the nearby industries in Bahir dar city, Ethiopia,"

Water Pract. Technol., vol. 12, no. 1, pp. 72–79, 2017, doi: 10.2166/wpt.2017.012.

[37] T. Gebreyohannes and A. G. Asgedom, “Toxicological assessment of Pb, Cd and Cr in lettuce and onion grown around Ellala River in Mekelle, Tigray, Ethiopia,” *Ethiop. J. Sci. Technol.*, vol. 11, no. 3, p. 287, 2019, doi: 10.4314/ejst.v11i3.6.

[38] B. K. Dessie, M. Aschale, E. Assegide, T. Alamirew, C. L. Walsh, and G. Zeleke, “Pollution challenges and consequences of the Akaki catchment, Upper Awash Basin, Ethiopia: Evidence for policy reform and action,” *World Water Policy*, vol. 10, no. 1, pp. 363–372, 2024, doi: 10.1002/wwp2.12169.

[39] S. K. Golfinopoulos, A. D. Nikolaou, and D. E. Alexakis, “Innovative Approaches for Minimizing Disinfection Byproducts (DBPs) in Water Treatment: Challenges and Trends,” *Appl. Sci.*, vol. 14, no. 18, p. 8153, 2024, [Online]. Available: https://www.mdpi.com/2076-3417/14/18/8153

[40] A. Plessis, “Commentary Persistent degradation : Global water quality challenges and required actions,” *One Earth*, vol. 5, no. 2, pp. 129–131, 2022, doi: 10.1016/j.oneear.2022.01.005.

[41] H. Shemer, S. Wald, and R. Semiat, “Challenges and Solutions for Global Water Scarcity,” 2023.

[42] G. Berihun *et al.*, “Drinking water contamination potential and associated factors among households with under-five children in rural areas of Dessie Zuria District, Northeast Ethiopia,” *Front. Public Heal.*, vol. 11, no. June, pp. 1–12, 2023, doi: 10.3389/fpubh.2023.1199314.

[43] G. R. Varatharajan and J. C. Ndayishimiye, “Emerging Contaminants : A Rising Threat to Urban Water and a Barrier to Achieving SDG-Aligned Planetary Protection,” pp. 1–41, 2025.

[44] N. Akhtar, M. Izzuddin, S. Ishak, S. A. Bhawani, and K. Umar, “Various Natural and Anthropogenic Factors Responsible for Water Quality Degradation : A Review,” 2021.

[45] J. Lan, P. Liu, X. Hu, and S. Zhu, “Harmful Algal Blooms in Eutrophic Marine Environments :,” pp. 1–64, 2024.

[46] V. Singh *et al.*, “Toxic heavy metal ions contamination in water and their sustainable reduction by eco - friendly methods : isotherms , thermodynamics and kinetics study,” *Sci.*

Rep., pp. 1–13, 2024, doi: 10.1038/s41598-024-58061-3.

[47] O. Ejiohuo *et al.*, “Ensuring water purity : Mitigating environmental risks and safeguarding human health,” *Water Biol. Secur.*, vol. 4, no. 2, p. 100341, 2025, doi: 10.1016/j.watbs.2024.100341.

[48] D. Nimma *et al.*, “Implications of climate change on freshwater ecosystems and their biodiversity,” vol. 321, no. June 2024, 2025.

[49] S. Mishra, R. Kumar, and M. Kumar, “Total Environment Research Themes Use of treated sewage or wastewater as an irrigation water for agricultural purposes- Environmental , health , and economic impacts,” *Total Environ. Res. Themes*, vol. 6, no. March, p. 100051, 2023, doi: 10.1016/j.totert.2023.100051.

[50] G. J. Joshiba, P. S. Kumar, M. Govarthanan, P. T. Ngueagni, A. Abilarasu, and F. Carolin C, “Investigation of magnetic silica nanocomposite immobilized Pseudomonas fluorescens as a biosorbent for the effective sequestration of Rhodamine B from aqueous systems,” *Environ. Pollut.*, vol. 269, p. 116173, 2021, doi: 10.1016/j.envpol.2020.116173.

[51] B. K. Dessie, S. R. Gari, A. Mihret, A. F. Desta, and B. Mehari, “Determination and health risk assessment of trace elements in the tap water of two Sub-Cities of Addis Ababa, Ethiopia,” *Heliyon*, vol. 7, no. 5, p. e06988, 2021, doi: 10.1016/j.heliyon.2021.e06988.

[52] T. T. Gule, B. Lemma, and B. T. Hailu, “Evaluation of the physical, chemical, and biological characteristics of surface water in urban settings and its applicability to SDG 6: The case of Addis Ababa, Ethiopia,” *Sci. African*, vol. 21, 2023, doi: 10.1016/j.sciaf.2023.e01744.

[53] K. C. B.Adelodun, F.Ajibade, J.Ighalo, G.Odey, R.Ibrahim, K.Kareem, H.Bakare, A.Tiamiyu, T.Ajibade, T.Abdulkadir, K.Adeniran, “Assessment of socioeconomic inequality based on virus-contaminated water usage in developing countries: A review,” *Environ. Res.*, vol. 192, no. 7, pp. 110–309, 2021, doi: 10.1016/j.envres.2020.110309.

[54] S. Gulta Abdurahman and M. Zewdie, “Fluoride ion and total dissolved solid distribution in Ethiopian Rift valley: The case of Hawassa city aquifer,” *J. Hydrol. Reg. Stud.*, vol. 19, no. October, pp. 240–249, 2018, doi: 10.1016/j.ejrh.2018.09.003.

[55] G. Ghiglieri *et al.*, “Three-dimensional Shala (264.0 mg/l), Abijata (202.4 mg/l), and Beseka

(32.2 mg/l) are among the lakes with the highest fluoride concentrations," *J. Hydrol. Reg. Stud.*, vol. 32, p. 100756, 2020, doi: 10.1016/j.ejrh.2020.100756.

[56] T. G. Bantero, D. Mulualem, D. T. Desta, G. W. Worancha, B. B. Boricha, and S. J. Whiting, "Potential For Dietary Calcium to Prevent Fluoride Uptake in Children in Halaba Special District, Southern Ethiopia: Knowledge, Attitudes, and Practices of Mothers," *Juniper Online J. Public Heal.*, vol. 6, no. 5, pp. 1–9, 2022, doi: 10.19080/jojph.2022.06.555700.

[57] A. Almebo, H. B. Mangasha, Z. Ashuro, N. E. Soboksa, and G. G. Kanno, "Utilization of Community-Level Fluoride-Filtered Water and its Associated Factors in Dugda Woreda of East Shewa Zone, Oromia Region, Ethiopia," *Environ. Health Insights*, vol. 15, 2021, doi: 10.1177/11786302211052384.

[58] S. Nowicki *et al.*, "Water chemistry poses health risks as reliance on groundwater increases: A systematic review of hydrogeochemistry research from Ethiopia and Kenya," *Sci. Total Environ.*, vol. 904, no. September, p. 166929, 2023, doi: 10.1016/j.scitotenv.2023.166929.

[59] Dr. Amit Krishan, Dr. Shweta Yadav, and Ankita Srivastava, "Water Pollution's Global Threat to Public Health : A Mini-Review," *Int. J. Sci. Res. Sci. Eng. Technol.*, no. December 2023, pp. 321–334, 2023, doi: 10.32628/ijsrset2310643.

[60] P. K. Maurya, D. S. Malik, K. K. Yadav, A. Kumar, S. Kumar, and H. Kamyab, "Bioaccumulation and potential sources of heavy metal contamination in fish species in River Ganga basin: Possible human health risks evaluation," *Toxicol. Reports*, vol. 6, no. January, pp. 472–481, 2019, doi: 10.1016/j.toxrep.2019.05.012.

[61] A. K. Arun, L. Rustveld, and A. Sunny, "Association between Water Fluoride Levels and Low Birth Weight: National Health and Nutrition Examination Survey (NHANES) 2013–2016," *Int. J. Environ. Res. Public Health*, vol. 19, no. 15, 2022, doi: 10.3390/ijerph19158956.

[62] I. B. Obinnaa and E. C. Ebere, "A Review: Water pollution by heavy metal and organic pollutants: Brief review of sources, effects and progress on remediation with aquatic plants," *Anal. Methods Environ. Chem. J.*, vol. 2, no. 3, pp. 5–38, 2019, doi: 10.24200/amecj.v2.i03.66.

[63] M. Ahmed *et al.*, "Recent developments in hazardous pollutants removal from wastewater and water reuse within a circular economy," *npj Clean Water*, vol. 5, no. 1, pp. 1–25, 2022, doi:

10.1038/s41545-022-00154-5.

[64] J. Zheng, C. Su, J. Zhou, L. Xu, Y. Qian, and H. Chen, "Effects and mechanisms of ultraviolet, chlorination, and ozone disinfection on antibiotic resistance genes in secondary effluents of municipal wastewater treatment plants," *Chem. Eng. J.*, vol. 317, pp. 309–316, 2017, doi: 10.1016/j.cej.2017.02.076.

[65] J. Li, C. Feng, Y. Li, W. Yang, and Z. Zhang, "Formation and influencing factors of disinfection by-products from bacterial materials in drinking water distribution systems," *Water Supply*, vol. 22, no. 9, pp. 7319–7336, 2022, doi: 10.2166/ws.2022.319.

[66] C. M. Morrison *et al.*, "Critical Review on Bromate Formation during Ozonation and Control Options for Its Minimization," *Environ. Sci. Technol.*, vol. 57, no. 47, pp. 18393–18409, 2023, doi: 10.1021/acs.est.3c00538.

[67] R. M. El-taweel *et al.*, "A review of coagulation explaining its definition, mechanism, coagulant types, and optimization models; RSM, and ANN," *Curr. Res. Green Sustain. Chem.*, vol. 6, no. October 2022, p. 100358, 2023, doi: 10.1016/j.crgsc.2023.100358.

[68] S. Shivraj, W. Quraishi, and S. Basu, "A Comprehensive Review on the Progress of Coagulation for Natural Organic Matter Removal in Water Treatment," *J. Penelit. dan Pengkaj. Ilmu Pendidik. e-Saintika*, vol. 7, no. 2, pp. 185–216, 2023, doi: 10.36312/esaintika.v7i2.1342.

[69] K. Chruszcz-Lipska and E. Szostak, "A Study of the Structure of an Anion Exchange Resin with a Quaternary Ammonium Functional Group by Using Infrared Spectroscopy and DFT Calculations," *Materials (Basel).*, vol. 17, no. 24, pp. 1–17, 2024, doi: 10.3390/ma17246132.

[70] M. M. Sabzehmeidani, S. Mahnaee, M. Ghaedi, H. Heidari, and V. A. L. Roy, "Carbon based materials: A review of adsorbents for inorganic and organic compounds," *Mater. Adv.*, vol. 2, no. 2, pp. 598–627, 2021, doi: 10.1039/d0ma00087f.

[71] F. South, T. Usf, D. Graduate, G. Usf, D. Theses, and M. L. Rice, "Enhanced Fluoride Removal in Biosand Filters Using Aluminum Enhanced Fluoride Removal in Biosand Filters Using Aluminum Oxide Coated Media and Modified Filter Design Oxide Coated Media and Modified Filter Design Scholar Commons Citation Scholar Commons Ci," no. March, 2020, [Online]. Available: https://digitalcommons.usf.edu/etd/8288

[72] E. O. Ezugbe and S. Rathilal, “Membrane technologies in wastewater treatment: A review,” *Membranes (Basel).*, vol. 10, no. 5, 2020, doi: 10.3390/membranes10050089.

[73] S. Aziz *et al.*, “A comprehensive review of membrane-based water filtration techniques,” *Appl. Water Sci.*, vol. 14, no. 8, pp. 1–17, 2024, doi: 10.1007/s13201-024-02226-y.

[74] H. K. Hansen *et al.*, “Combined Electrodialysis and Electrocoagulation as Treatment for Industrial Wastewater Containing Arsenic and Copper,” *Membranes (Basel).*, vol. 13, no. 3, 2023, doi: 10.3390/membranes13030264.

[75] G. I. Lupu, C. Orbeci, L. Bobirică, C. Bobirică, and L. F. Pascu, “Key Principles of Advanced Oxidation Processes: A Systematic Analysis of Current and Future Perspectives of the Removal of Antibiotics from Wastewater,” *Catalysts*, vol. 13, no. 9, 2023, doi: 10.3390/catal13091280.

[76] J. Derco, A. Ž. Gotvajn, O. Čižmárová, J. Dudáš, L. Sumegová, and K. Šimovičová, “Removal of micropollutants by ozone-based processes,” *Processes*, vol. 9, no. 6, pp. 1–48, 2021, doi: 10.3390/pr9061013.

[77] I. M. F. Cardoso, R. M. F. Cardoso, and J. C. G. Esteves da Silva, “Advanced oxidation processes coupled with nanomaterials for water treatment,” *Nanomaterials*, vol. 11, no. 8, 2021, doi: 10.3390/nano11082045.

[78] M. B. Aregu, S. L. Asfaw, and M. M. Khan, “Identification of two low-cost and locally available filter media (pumice and scoria) for removal of hazardous pollutants from tannery wastewater,” *Environ. Syst. Res.*, vol. 7, no. 1, 2018, doi: 10.1186/s40068-018-0112-2.

[79] G. Gopalakrishnan, R. B. Jeyakumar, and A. Somanathan, “Challenges and Emerging Trends in Advanced Oxidation Technologies and Integration of Advanced Oxidation Processes with Biological Processes for Wastewater Treatment,” *Sustain.*, vol. 15, no. 5, 2023, doi: 10.3390/su15054235.

[80] E. M. Cuerda-correa, M. F. Alexandre-franco, and C. Fern, “Antibiotics from Water . An Overview,” *Water*, vol. 12, p. 102, 2019.

[81] S. Heo, S. Kim, and D. Kang, “The role of hydrogen peroxide and peroxiredoxins throughout the cell cycle,” *Antioxidants*, vol. 9, no. 4, 2020, doi: 10.3390/antiox9040280.

[82] T. U. Rahman, H. Roy, M. R. Islam, M. Tahmid, and A. Fariha, “The Advancement in Membrane Bioreactor (MBR) Technology toward Sustainable Industrial Wastewater Management,” *Membranes (Basel).*, vol. 13, no. 2, 2023, doi: 10.3390/membranes13020181.

[83] M. Issaoui, S. Jellali, A. A. Zorpas, and P. Dutournie, “Membrane technology for sustainable water resources management: Challenges and future projections,” *Sustain. Chem. Pharm.*, vol. 25, no. January, p. 100590, 2022, doi: 10.1016/j.scp.2021.100590.

[84] S. Parani and O. S. Oluwafemi, “Membrane distillation: Recent configurations, membrane surface engineering, and applications,” *Membranes (Basel).*, vol. 11, no. 12, 2021, doi: 10.3390/membranes11120934.

[85] M. Gulied *et al.*, “A review of membrane-based dewatering technology for the concentration of liquid foods,” *J. Environ. Chem. Eng.*, vol. 11, no. 5, p. 110583, 2023, doi: 10.1016/j.jece.2023.110583.

[86] L. Fortunato, F. Lipnizki, and L. F. Dumée, “Editorial: Fouling in Membrane Filtration Systems,” *Front. Chem. Eng.*, vol. 3, no. December, pp. 10–12, 2021, doi: 10.3389/fceng.2021.812625.

[87] M. Khan and M. A. Al-Ghouti, “DPSIR framework and sustainable approaches of brine management from seawater desalination plants in Qatar,” *J. Clean. Prod.*, vol. 319, no. August, p. 128485, 2021, doi: 10.1016/j.jclepro.2021.128485.

[88] A. I. Osman *et al.*, “Membrane Technology for Energy Saving: Principles, Techniques, Applications, Challenges, and Prospects,” *Adv. Energy Sustain. Res.*, vol. 5, no. 5, 2024, doi: 10.1002/aesr.202400011.

[89] J. Tripathy *et al.*, “Advances in Nanoparticles and Nanocomposites for Water and Wastewater Treatment: A Review,” *Water (Switzerland)*, vol. 16, no. 11, pp. 1–26, 2024, doi: 10.3390/w16111481.

[90] S. Kumari *et al.*, “A comprehensive review on various techniques used for synthesizing nanoparticles,” *J. Mater. Res. Technol.*, vol. 27, pp. 1739–1763, 2023, doi: 10.1016/j.jmrt.2023.09.291.

[91] A. Ojha, *Nanomaterials for removal of waterborne pathogens: opportunities and challenges*,

no. January. 2020. [Online]. Available: /pmc/articles/PMC7153326/%0A/pmc/articles/PMC7153326/?report=abstract%0Ahttps://www.ncbi.nlm.nih.gov/pmc/articles/PMC7153326/

[92] C. Xue *et al.*, “Nano titanium dioxide induces the generation of ROS and potential damage in HaCaT cells under UVA irradiation,” *J. Nanosci. Nanotechnol.*, vol. 10, no. 12, pp. 8500–8507, 2010, doi: 10.1166/jnn.2010.2682.

[93] C. Moro, V. Francioso, M. Schrager, and M. Velay-Lizancos, “TiO2 nanoparticles influence on the environmental performance of natural and recycled mortars: A life cycle assessment,” *Environ. Impact Assess. Rev.*, vol. 84, no. February, 2020, doi: 10.1016/j.eiar.2020.106430.

[94] B. Arora and P. Attri, “Carbon nanotubes (CNTs): A potential nanomaterial for water purification,” *J. Compos. Sci.*, vol. 4, no. 3, pp. 1–20, 2020, doi: 10.3390/jcs4030135.

[95] Y. Maksimova, A. Zorina, and L. Nesterova, “Oxidative Stress Response and E. coli Biofilm Formation under the Effect of Pristine and Modified Carbon Nanotubes,” *Microorganisms*, vol. 11, no. 5, pp. 1–16, 2023, doi: 10.3390/microorganisms11051221.

[96] A. Chen, B. Wang, Q. Feng, and R. Wang, “Potential toxicity of carbonaceous nanomaterials on aquatic organisms and their alleviation strategies: A review,” *Ecotoxicol. Environ. Saf.*, vol. 285, no. April, p. 117019, 2024, doi: 10.1016/j.ecoenv.2024.117019.

[97] M. S. Xie, H. C. Luo, X. J. Liu, and C. C. Yin, “Development and challenge of coal-based nanocarbon materials and their application in water treatment: a review,” *Discov. Nano*, vol. 19, no. 1, 2024, doi: 10.1186/s11671-024-04115-4.

[98] T. Bruna, F. Maldonado-Bravo, P. Jara, and N. Caro, “Silver nanoparticles and their antibacterial applications,” *Int. J. Mol. Sci.*, vol. 22, no. 13, 2021, doi: 10.3390/ijms22137202.

[99] H. Barabadi *et al.*, “Antiviral potential of green-synthesized silver nanoparticles,” *Handb. Microb. Nanotechnol.*, pp. 285–310, 2022, doi: 10.1016/B978-0-12-823426-6.00030-9.

[100] M. L. W. Knetsch and L. H. Koole, “New strategies in the development of antimicrobial coatings: The example of increasing usage of silver and silver nanoparticles,” *Polymers (Basel).*, vol. 3, no. 1, pp. 340–366, 2011, doi: 10.3390/polym3010340.

[101] Z. Ferdous and A. Nemmar, *Health impact of silver nanoparticles: A review of the*

biodistribution and toxicity following various routes of exposure, vol. 21, no. 7. 2020. doi: 10.3390/ijms21072375.

[102] S. M. Ezzat and M. T. Moustafa, “Efficient removal of E. coli from wastewater by novel phytofabricated nano-zinc using antibacterial potential, kinetic studies, and response surface methodology,” *Appl. Water Sci.*, vol. 14, no. 4, pp. 1–23, 2024, doi: 10.1007/s13201-024-02140-3.

[103] A. Sirelkhatim *et al.*, “Review on zinc oxide nanoparticles: Antibacterial activity and toxicity mechanism,” *Nano-Micro Lett.*, vol. 7, no. 3, pp. 219–242, 2015, doi: 10.1007/s40820-015-0040-x.

[104] N. Babayevska *et al.*, “ZnO size and shape effect on antibacterial activity and cytotoxicity profile,” *Sci. Rep.*, vol. 12, no. 1, pp. 1–13, 2022, doi: 10.1038/s41598-022-12134-3.

[105] G. Oxide, G. Barrier, A. Activity, R. Castaldo, and B. National, “Materials & Design The effect of ZnO nanoparticles morphology on the barrier and antibacterial properties of hybrid ZnO / graphene oxide / montmorillonite coatings for flexible packaging,” *Surfaces and Interfaces*, vol. 55, no. June, p. 105307, 2024, doi: 10.1016/j.surfin.2024.105307.

[106] S. E. Jin and H. E. Jin, “Antimicrobial activity of zinc oxide nano/microparticles and their combinations against pathogenic microorganisms for biomedical applications: From physicochemical characteristics to pharmacological aspects,” *Nanomaterials*, vol. 11, no. 2, pp. 1–35, 2021, doi: 10.3390/nano11020263.

[107] S. Dey *et al.*, “A critical review on zinc oxide nanoparticles: Synthesis, properties and biomedical applications,” *Intell. Pharm.*, no. June, 2024, doi: 10.1016/j.ipha.2024.08.004.

[108] S. R. Choudhury, J. Ordaz, C. L. Lo, N. P. Damayanti, F. Zhou, and J. Irudayaraj, “Zinc oxide nanoparticles-induced reactive oxygen species promotes multimodal cyto- and epigenetic toxicity,” *Toxicol. Sci.*, vol. 156, no. 1, pp. 261–274, 2017, doi: 10.1093/toxsci/kfw252.

[109] J. Jiang, J. Pi, and J. Cai, “The Advancing of Zinc Oxide Nanoparticles for Biomedical Applications,” *Bioinorg. Chem. Appl.*, vol. 2018, 2018, doi: 10.1155/2018/1062562.

[110] V. Puspasari, A. Ridhova, A. Hermawan, M. I. Amal, and M. M. Khan, “ZnO-based antimicrobial coatings for biomedical applications,” *Bioprocess Biosyst. Eng.*, vol. 45, no. 9,

pp. 1421–1445, 2022, doi: 10.1007/s00449-022-02733-9.

[111] Y. Zhou, X.Q., Hayat, Z., Zhang, D.D., Li, M.Y., Hu, S., Wu, Q., Cao, Y.F., Yuan, "Modification , and applications in food and agriculture," *Processes*, vol. 11, p. 1193, 2023.

[112] A. Nyabadza *et al.*, "A review of physical, chemical and biological synthesis methods of bimetallic nanoparticles and applications in sensing, water treatment, biomedicine, catalysis and hydrogen storage," *Adv. Colloid Interface Sci.*, vol. 321, no. August, 2023, doi: 10.1016/j.cis.2023.103010.

[113] Z. Wang, S. Wang, T. Ma, Y. Liang, Z. Huo, and F. Yang, "Synthesis of Zinc Oxide Nanoparticles and Their Applications in Enhancing Plant Stress Resistance: A Review," *Agronomy*, vol. 13, no. 12, 2023, doi: 10.3390/agronomy13123060.

[114] I. Ijaz, E. Gilani, A. Nazir, and A. Bukhari, "Detail review on chemical, physical and green synthesis, classification, characterizations and applications of nanoparticles," *Green Chem. Lett. Rev.*, vol. 13, no. 3, pp. 59–81, 2020, doi: 10.1080/17518253.2020.1802517.

[115] N. Baig, I. Kammakakam, W. Falath, and I. Kammakakam, "Nanomaterials: A review of synthesis methods, properties, recent progress, and challenges," *Mater. Adv.*, vol. 2, no. 6, pp. 1821–1871, 2021, doi: 10.1039/d0ma00807a.

[116] A. Roy, C. P. Healey, N. E. Larm, P. Ishtaweera, M. Roca, and G. A. Baker, "The Huge Role of Tiny Impurities in Nanoscale Synthesis," *ACS Nanosci. Au*, vol. 4, no. 3, pp. 176–193, 2024, doi: 10.1021/acsnanoscienceau.3c00056.

[117] A. I. Osman *et al.*, *Synthesis of green nanoparticles for energy, biomedical, environmental, agricultural, and food applications: A review*, vol. 22, no. 2. Springer International Publishing, 2024. doi: 10.1007/s10311-023-01682-3.

[118] M. Murali *et al.*, "Zinc oxide nanoparticles prepared through microbial mediated synthesis for therapeutic applications: a possible alternative for plants," *Front. Microbiol.*, vol. 14, no. September, pp. 1–20, 2023, doi: 10.3389/fmicb.2023.1227951.

[119] S. Ahmad, S. Ahmad, S. Ali, M. Esa, A. Khan, and H. Yan, "Recent Advancements and Unexplored Biomedical Applications of Green Synthesized Ag and Au Nanoparticles: A Review," *Int. J. Nanomedicine*, vol. 19, no. April, pp. 3187–3215, 2024, doi:

10.2147/IJN.S453775.

[120] M. A. Azeez *et al.*, “Green synthesized novel silver nanoparticles and their application as anticoagulant and thrombolytic agents: A perspective,” *IOP Conf. Ser. Mater. Sci. Eng.*, vol. 805, no. 1, 2020, doi: 10.1088/1757-899X/805/1/012043.

[121] N. J, K. E, and R. S, “‘Green Synthesis of Zinc Oxide Nanoparticles: Eco-Friendly Advancements for Biomedical Marvels,’” *Resour. Chem. Mater.*, no. October 2023, pp. 1–23, 2024, doi: 10.1016/j.recm.2024.05.001.

[122] S. kazemi *et al.*, “Recent advances in green synthesized nanoparticles: from production to application,” *Mater. Today Sustain.*, vol. 24, p. 100500, 2023, doi: 10.1016/j.mtsust.2023.100500.

[123] M. Thatyana, N. P. Dube, D. Kemboi, A. L. E. Manicum, N. S. Mokgalaka-Fleischmann, and J. V. Tembu, “Advances in Phytonanotechnology: A Plant-Mediated Green Synthesis of Metal Nanoparticles Using Phyllanthus Plant Extracts and Their Antimicrobial and Anticancer Applications,” *Nanomaterials*, vol. 13, no. 19, 2023, doi: 10.3390/nano13192616.

[124] B. Naiel, M. Fawzy, M. W. A. Halmy, and A. E. D. Mahmoud, “Green synthesis of zinc oxide nanoparticles using Sea Lavender (Limonium pruinosum L. Chaz.) extract: characterization, evaluation of anti-skin cancer, antimicrobial and antioxidant potentials,” *Sci. Rep.*, vol. 12, no. 1, pp. 1–12, 2022, doi: 10.1038/s41598-022-24805-2.

[125] S. Zeghoud *et al.*, “A review on biogenic green synthesis of ZnO nanoparticles by plant biomass and their applications,” *Materials Today Communications*, vol. 33. Elsevier Ltd, Dec. 01, 2022. doi: 10.1016/j.mtcomm.2022.104747.

[126] A. Soyucok, B. Kabak, and B. Tosun, “Optimization of Synthesis Reaction Parameters of AgNPs Derived from Laser trilobum Plant for Foodborne Pathogens,” *Food Bioprocess Technol.*, vol. 17, no. 11, pp. 3800–3812, 2024, doi: 10.1007/s11947-024-03359-3.

[127] S. Ullah, A. Gulnaz, S. Anwar, A. Kamal, and H. Wali, “Synthetization and Characterization of Zinc Oxide Nanoparticles by X- Ray Diffractometry (XRD), Fourier Transforms, Infra-Red Spectroscopy (FT-IR), Scanning Electron Microscopy (SEM) and Antibacterial Activity Test,” *Am. J. Phys. Sci.*, vol. 2, no. 1, pp. 1–25, 2024, doi: 10.47604/ajps.2294.

[128] M. Seray, A. Skender, and A. S. Hadj-Hamou, “Kinetics and mechanisms of Zn2+ release from antimicrobial food packaging based on poly (butylene adipate-co-terephthalate) and zinc oxide nanoparticles,” *Polym. Bull.*, vol. 78, no. 2, pp. 1021–1040, 2021, doi: 10.1007/s00289-020-03145-z.

[129] V. Tucureanu, I. Mihalache, A. Iancu, and V. Dediu, “Antibacterial and Photocatalytic Activity of ZnO / Au and ZnO / Ag Nanocomposites,” 2023.

[130] J. Supramaniam *et al.*, “Facile synthesis and characterization of palm CNF-ZnO nanocomposites with antibacterial and reinforcing properties,” *Int. J. Mol. Sci.*, vol. 22, no. 11, 2021, doi: 10.3390/ijms22115781.

[131] B. T. Son, N. V. Long, and N. T. Nhat Hang, “Fly ash-, foundry sand-, clay-, and pumice-based metal oxide nanocomposites as green photocatalysts,” *RSC Adv.*, vol. 11, no. 49, pp. 30805–30826, 2021, doi: 10.1039/d1ra05647f.

[132] S. M. Devi, A. Nivetha, and I. Prabha, “Role of Citric Acid/Glycine-Reinforced Nanometal Oxide for the Enhancement of Physio-chemical Specifications in Catalytic Properties,” *J. Supercond. Nov. Magn.*, vol. 33, no. 12, pp. 3893–3901, 2020, doi: 10.1007/s10948-020-05607-x.

[133] S. Ruan *et al.*, “Effect of zinc oxide/graphene oxide nanocomposites on the cytotoxicity, antibacterial and mechanical properties of polymethyl methacrylate,” *BMC Oral Health*, vol. 24, no. 1, 2024, doi: 10.1186/s12903-024-04754-0.

[134] A. Taha, M. Ben Aissa, and E. Da’na, “Green synthesis of an activated carbon-supported Ag and ZnO nanocomposite for photocatalytic degradation and its antibacterial activities,” *Molecules*, vol. 25, no. 7, pp. 8–16, 2020, doi: 10.3390/molecules25071586.

[135] S. J. Owonubi, N. M. Malima, and N. Revaprasadu, *Metal Oxide e Based Nanocomposites as Antimicrobial and Biomedical Agents*. Elsevier Inc., 2020. doi: 10.1016/B978-0-12-820054-4.00016-1.

[136] A. G. Zewudie, T. A. Segne, H. C. A. Murthy, C. R. Ravikumar, D. Muniswamy, and B. B. Binagdie, “Biosynthesis of Ag / bentonite , ZnO / bentonite , and Ag / ZnO / bentonite nanocomposites by aqueous leaf extract of Hagenia abyssinica for antibacterial activities,” 2023.

[137] H. S. Abbas, A. Krishnan, and M. Kotakonda, “Fabrication of Iron Oxide/Zinc Oxide Nanocomposite Using Creeper Blepharis maderaspatensis Extract and Their Antimicrobial Activity,” *Front. Bioeng. Biotechnol.*, vol. 8, no. December, pp. 1–11, 2020, doi: 10.3389/fbioe.2020.595161.

[138] D. R. Jaishi *et al.*, “Plant-mediated synthesis of zinc oxide (ZnO) nanoparticles using Alnus nepalensis D. Don for biological applications,” *Heliyon*, vol. 10, no. 20, p. e39255, 2024, doi: 10.1016/j.heliyon.2024.e39255.

[139] K. M. Gendo, R. Feyisa Bogale, and G. Kenasa, “Green Synthesis, Characterization, and Evaluation of Photocatalytic and Antibacterial Activities of Co3O4-ZnO Nanocomposites Using Calpurnia aurea Leaf Extract,” *ACS Omega*, vol. 9, no. 26, pp. 28354–28371, 2024, doi: 10.1021/acsomega.4c01595.

[140] M. Li *et al.*, “Brassinosteroid Ameliorates Zinc Oxide Nanoparticles-Induced Oxidative Stress by Improving Antioxidant Potential and Redox Homeostasis in Tomato Seedling,” *Front. Plant Sci.*, vol. 7, no. May, pp. 1–13, 2016, doi: 10.3389/fpls.2016.00615.

[141] C. Liao, Y. Jin, Y. Li, and S. C. Tjong, “Interactions of zinc oxide nanostructures with mammalian cells: Cytotoxicity and photocatalytic toxicity,” *Int. J. Mol. Sci.*, vol. 21, no. 17, pp. 1–49, 2020, doi: 10.3390/ijms21176305.

[142] B. Abebe, E. A. Zereffa, A. Tadesse, and H. C. A. Murthy, “A Review on Enhancing the Antibacterial Activity of ZnO: Mechanisms and Microscopic Investigation,” *Nanoscale Res. Lett.*, vol. 15, no. 1, 2020, doi: 10.1186/s11671-020-03418-6.

[143] O. Dagdag *et al.*, “An Overview of Heavy Metal Pollution and Control,” *ACS Symp. Ser.*, vol. 1456, pp. 3–24, 2023, doi: 10.1021/bk-2023-1456.ch001.

[144] S. F. Ahmed *et al.*, “Nanomaterials as a sustainable choice for treating wastewater,” *Environ. Res.*, vol. 214, no. July, 2022, doi: 10.1016/j.envres.2022.113807.

[145] Q. Ali *et al.*, “Nanoremediation for heavy metal contamination: A review,” *Hybrid Adv.*, vol. 4, no. July, p. 100091, 2023, doi: 10.1016/j.hybadv.2023.100091.

[146] D. B. Olawade *et al.*, “Metal and metal oxide nanomaterials for heavy metal remediation: novel approaches for selective, regenerative, and scalable water treatment,” *Front.*

Nanotechnol., vol. 6, no. October, pp. 1–24, 2024, doi: 10.3389/fnano.2024.1466721.

[147] Y. Luo *et al.*, “Mechanism of Enhanced Fluoride Adsorption Using Amino-Functionalized Aluminum-Based Metal–Organic Frameworks,” *Water (Switzerland)*, vol. 16, no. 20, 2024, doi: 10.3390/w16202889.

[148] F. Ahmad *et al.*, “Unique Properties of Surface-Functionalized Nanoparticles for Bio-Application: Functionalization Mechanisms and Importance in Application,” *Nanomaterials*, vol. 12, no. 8, 2022, doi: 10.3390/nano12081333.

[149] M. S. Fernando *et al.*, “Biopolymer-Based Nanohydroxyapatite Composites for the Removal of Fluoride, Lead, Cadmium, and Arsenic from Water,” *ACS Omega*, vol. 6, no. 12, pp. 8517–8530, 2021, doi: 10.1021/acsomega.1c00316.

[150] V. Kumar, D. Bhatt, J. S. Dhami, and M. Pal, “Recent Advances of Using Polymer Nanocomposites for the Removal of Heavy Metal Ions from Waste Water : A Review”.

[151] S. Panhwar *et al.*, “Magnetic nanomaterials as an effective absorbent material for removal of fluoride concentration in water: a review,” *J. Water Health*, vol. 22, no. 1, pp. 123–137, 2024, doi: 10.2166/wh.2023.116.

[152] S. KK, S. M, K. P, and G. A, “Magnetic nanoparticles as an effective adsorbent for removal of fluoride–a review,” *MOJ Ecol. Environ. Sci.*, vol. 3, no. 3, pp. 207–210, 2018, doi: 10.15406/mojes.2018.03.00088.

[153] R. Kumar, P. Rauwel, and E. Rauwel, “Nanoadsorbants for the removal of heavy metals from contaminated water: Current scenario and future directions,” *Processes*, vol. 9, no. 8, 2021, doi: 10.3390/pr9081379.

[154] B. Moeini, “Exploring Surface Silanization and Characterization of Thin Films : From Surface Passivation to Microstructural Characterization of Porous Silicon / Silica , and Exploratory Data Analysis of X-Ray Photoelectron Spectroscopy Images,” 2023.

[155] S. Barani, S. P. Sebastian, P. Dhevagi, M. Prasanthrajan, and A. Suganthi, “Synthesis of silica nanoparticles (SiNPs) from agro-wastes for removal of heavy metals from an aqueous medium–a mini review,” *Green Chem. Lett. Rev.*, vol. 17, no. 1, pp. 1–18, 2024, doi: 10.1080/17518253.2024.2422416.

[156] P. Pillai, S. Dharaskar, and S. Pandian, “Rice husk derived silica nano doped on calcium peroxide for fluoride: Performance, characterization, kinetic, isotherm, and groundwater treatment,” *Environ. Technol. Innov.*, vol. 19, p. 100901, 2020, doi: 10.1016/j.eti.2020.100901.

[157] A. Srivastava, M. Kumari, A. Ramanathan, K. Selvaraj, B. Prasad, and K. S. Prasad, “Removal of fluoride from aqueous solution by mesoporous silica nanoparticles functionalized with chitosan derived from mushroom,” *J. Macromol. Sci. Part A Pure Appl. Chem.*, vol. 57, no. 9, pp. 619–627, 2020, doi: 10.1080/10601325.2020.1738896.

[158] F. Rizzi *et al.*, “High surface area mesoporous silica nanoparticles with tunable size in the sub-micrometer regime: Insights on the size and porosity control mechanisms,” *Molecules*, vol. 26, no. 14, 2021, doi: 10.3390/molecules26144247.

[159] P. Kazemzadeh *et al.*, “Structure-Property Relationship for Different Mesoporous Silica Nanoparticles and its Drug Delivery Applications: A Review,” *Front. Chem.*, vol. 10, no. March, pp. 1–11, 2022, doi: 10.3389/fchem.2022.823785.

[160] D. Flores, C. M. R. Almeida, C. R. Gomes, S. S. B. And, and C. M. Granadeiro, “Tailoring of Mesoporous Silica-Based Materials for Enhanced Water Pollutants Removal Daniela,” *Molecules*, vol. 28, p. 4038, 2023.

[161] R. Peng, M. Asadullah Khan, and C. Li Liu, “Synthesis of Silica nanoparticles and their application of Dielectric relaxation spectroscopy- a review,” *Results Chem.*, vol. 6, no. July, p. 101218, 2023, doi: 10.1016/j.rechem.2023.101218.

[162] C. Y. Rahimzadeh, A. A. Barzinjy, A. S. Mohammed, and S. M. Hamad, “Green synthesis of SiO2 nanoparticles from Rhus coriaria L. extract: Comparison with chemically synthesized SiO2 nanoparticles,” *PLoS One*, vol. 17, no. 8 August, pp. 1–15, 2022, doi: 10.1371/journal.pone.0268184.

[163] A. Grisolia *et al.*, “Hybrid Polymer-Silica Nanostructured Materials for Environmental Remediation,” *Molecules*, vol. 28, no. 13, 2023, doi: 10.3390/molecules28135105.

[164] M. A. Taleb, R. Kumar, M. A. Barakat, T. Almeelbi, M. K. Seliem, and A. Ahmad, “Recent advances in heavy metals uptake by tailored silica-based adsorbents,” *Sci. Total Environ.*, vol. 955, p. 177093, Dec. 2024, doi: 10.1016/J.SCITOTENV.2024.177093.

[165] M. Irfan, A. Arif, M. A. Munir, and M. Y. Naz, “Statistically Analyzed Heavy Metal Removal Efficiency of Silica-Coated Cu0.50Mg0.50Fe2O4 Magnetic Adsorbent for Wastewater Treatment,” *ACS Omega*, vol. 8, no. 50, pp. 47623–47634, 2023, doi: 10.1021/acsomega.3c05764.

[166] S. Kalidhasan and H. Y. Lee, “Preparation of TiO2-deposited silica-based catalysts for photocatalytic decomposition of chloro-pesticide to environmentally less toxic species,” *Chemosphere*, vol. 290, p. 133300, Mar. 2022, doi: 10.1016/J.CHEMOSPHERE.2021.133300.

[167] R. Bhateria and R. Singh, “A review on nanotechnological application of magnetic iron oxides for heavy metal removal,” *J. Water Process Eng.*, vol. 31, p. 100845, Oct. 2019, doi: 10.1016/J.JWPE.2019.100845.

[168] V. Muşat *et al.*, “Ag-Decorated Iron Oxides-Silica Magnetic Nanocomposites with Antimicrobial and Photocatalytic Activity,” *Nanomaterials*, vol. 12, no. 24, 2022, doi: 10.3390/nano12244452.

[169] O. Dayan *et al.*, “Pumice-Supported Ruthenium nanoparticles as highly effective and recyclable catalyst in the hydrolysis of methylamine borane,” *Int. J. Hydrogen Energy*, vol. 52, pp. 1–10, Jan. 2024, doi: 10.1016/J.IJHYDENE.2022.07.116.

[170] B. I. Harman and M. Genisoglu, “Synthesis and Characterization of Pumice-Supported nZVI for Removal of Copper from Waters,” *Adv. Mater. Sci. Eng.*, vol. 2016, 2016, doi: 10.1155/2016/4372136.

[171] B. Tural, E. Ertaş, M. Güzel, and S. Tural, “Effect of structural differences of pumice on synthesis of pumice-supported nFe0: removal of Cr (VI) from water,” *Appl. Water Sci.*, vol. 11, no. 7, pp. 1–11, 2021, doi: 10.1007/s13201-021-01458-6.

[172] I. K. Abbas and K. A. Adim, “Synthesis and characterization of magnesium oxide nanoparticles by atmospheric non-thermal plasma jet,” *Kuwait J. Sci.*, vol. 50, no. 3, pp. 223–230, 2023, doi: 10.1016/j.kjs.2023.05.008.

[173] Z. Raji, A. Karim, A. Karam, and S. Khalloufi, “Adsorption of Heavy Metals: Mechanisms, Kinetics, and Applications of Various Adsorbents in Wastewater Remediation—A Review,” *Waste*, vol. 1, no. 3, pp. 775–805, 2023, doi: 10.3390/waste1030046.

[174] D. Türkmen, M. Bakhshpour, S. Akgönüllü, S. Aşır, and A. Denizli, “Heavy Metal Ions Removal From Wastewater Using Cryogels: A Review,” *Front. Sustain.*, vol. 3, no. March, pp. 1–17, 2022, doi: 10.3389/frsus.2022.765592.

[175] N. Bouazizi, J. Vieillard, B. Samir, and F. Le Derf, “Advances in Amine-Surface Functionalization of Inorganic Adsorbents for Water Treatment and Antimicrobial Activities: A Review,” *Polymers (Basel).*, vol. 14, no. 3, 2022, doi: 10.3390/polym14030378.

[176] Amrutha, G. Jeppu, C. R. Girish, B. Prabhu, and K. Mayer, *Multi-component Adsorption Isotherms: Review and Modeling Studies*, vol. 10, no. 2. Springer International Publishing, 2023. doi: 10.1007/s40710-023-00631-0.

[177] N. Ayawei, A. N. Ebelegi, and D. Wankasi, “Modelling and Interpretation of Adsorption Isotherms,” *J. Chem.*, vol. 2017, 2017, doi: 10.1155/2017/3039817.

[178] K. H. Chu, “Revisiting the Temkin Isotherm: Dimensional Inconsistency and Approximate Forms,” *Ind. Eng. Chem. Res.*, vol. 60, no. 35, pp. 13140–13147, 2021, doi: 10.1021/acs.iecr.1c01788.

[179] Y. Miyah, A. Lahrichi, M. Idrissi, S. Boujraf, H. Taouda, and F. Zerrouq, “Assessment of adsorption kinetics for removal potential of Crystal Violet dye from aqueous solutions using Moroccan pyrophyllite,” *J. Assoc. Arab Univ. Basic Appl. Sci.*, vol. 23, pp. 20–28, 2017, doi: 10.1016/j.jaubas.2016.06.001.

[180] S. S. Fatima, A. Borhan, M. Ayoub, and N. A. Ghani, “Modeling of CO2 Adsorption on Surface-Functionalized Rubber-Seed Shell Activated Carbon: Isotherm and Kinetic Analysis,” *Processes*, vol. 11, no. 10, 2023, doi: 10.3390/pr11102833.

[181] S. Rovani, J. J. Santos, P. Corio, and D. A. Fungaro, “Highly Pure Silica Nanoparticles with High Adsorption Capacity Obtained from Sugarcane Waste Ash,” *ACS Omega*, vol. 3, no. 3, pp. 2618–2627, 2018, doi: 10.1021/acsomega.8b00092.

[182] S. Rovani, J. J. Santos, P. Corio, and D. A. Fungaro, “An alternative and simple method for the preparation of bare silica nanoparticles using sugarcane waste ash, an abundant and despised residue in the Brazilian industry,” *J. Braz. Chem. Soc.*, vol. 30, no. 7, pp. 1524–1533, 2019, doi: 10.21577/0103-5053.20190049.

[183] K. Dlomo, S. M. Mohomane, and T. E. Motaung, “Influence of silica nanoparticles on the properties of cellulose composite membranes: A current review,” *Cellul. Chem. Technol.*, vol. 54, no. 7–8, pp. 765–775, 2020, doi: 10.35812/CelluloseChemTechnol.2020.54.76.

[184] O. Kaczerewska, R. Martins, J. Figueiredo, S. Loureiro, and J. Tedim, “Environmental behaviour and ecotoxicity of cationic surfactants towards marine organisms,” *J. Hazard. Mater.*, vol. 392, no. February, p. 122299, 2020, doi: 10.1016/j.jhazmat.2020.122299.

[185] A. M. Brokowski C, “乳鼠心肌提取 HHS Public Access,” *Physiol. Behav.*, vol. 176, no. 5, pp. 139–148, 2019, doi: 10.1016/j.tiv.2015.01.017.Cytotoxicity.

[186] H. Agarwal, S. Venkat Kumar, and S. Rajeshkumar, “A review on green synthesis of zinc oxide nanoparticles – An eco-friendly approach,” *Resour. Technol.*, vol. 3, no. 4, pp. 406–413, Dec. 2017, doi: 10.1016/j.reffit.2017.03.002.

[187] C. P. Devatha and A. K. Thalla, *Green Synthesis of Nanomaterials*. Elsevier Ltd., 2018. doi: 10.1016/B978-0-08-101975-7.00007-5.

[188] D. Mutukwa, R. T. Taziwa, and L. Khotseng, “A Review of Plant-Mediated ZnO Nanoparticles for Photodegradation and Antibacterial Applications,” *Nanomaterials*, vol. 14, no. 14, 2024, doi: 10.3390/nano14141182.

[189] P. K. Pandey, P. H. Kass, M. L. Soupir, S. Biswas, and V. P. Singh, “Contamination of water resources by pathogenic bacteria,” *AMB Express*, vol. 4, no. 1, pp. 1–16, 2014, doi: 10.1186/s13568-014-0051-x.

[190] S. Das *et al.*, “Disinfection of the water borne pathogens Escherichia coli and Staphylococcus aureus by solar photocatalysis using sonochemically synthesized reusable Ag@ZnO core-shell nanoparticles,” *Int. J. Environ. Res. Public Health*, vol. 14, no. 7, 2017, doi: 10.3390/ijerph14070747.

[191] A. M. Wolde, K. Jemal, G. M. Woldearegay, and K. D. Tullu, “Quality and safety of municipal drinking water in Addis Ababa City, Ethiopia,” *Environ. Health Prev. Med.*, vol. 25, no. 1, pp. 1–6, 2020, doi: 10.1186/s12199-020-00847-8.

[192] M. Adane, B. Mengistie, G. Medhin, H. Kloos, and W. Mulat, “Piped water supply interruptions and acute diarrhea among under-five children in Addis Ababa slums, Ethiopia: A

matched case-control study," *PLoS One*, vol. 12, no. 7, pp. 1–19, 2017, doi: 10.1371/journal.pone.0181516.

[193] A. Keleb, A. Ademas, T. Sisay, M. Lingerew, and M. Adane, "Bacteriological Quality of Bottled Drinking Water and Municipal Tap Water in Northeastern Ethiopia," *Front. Environ. Sci.*, vol. 10, no. March, pp. 1–9, 2022, doi: 10.3389/fenvs.2022.828335.

[194] D. Chalchisa, M. Megersa, and A. Beyene, "Assessment of the quality of drinking water in storage tanks and its implication on the safety of urban water supply in developing countries," *Environ. Syst. Res.*, vol. 6, no. 1, 2018, doi: 10.1186/s40068-017-0089-2.

[195] S. K. Kassahun, Z. Kiflie, D. W. Shin, S. S. Park, and Y. R. Chung, "Novel multistage fixed-bed photoreactor for bacterial inactivation using N-doped TiO2 nanoparticles under vis-LEDs and sunlight illumination," *Nanotechnol. Environ. Eng.*, vol. 3, no. 1, 2018, doi: 10.1007/s41204-017-0032-9.

[196] K. Gopal, S. S. Tripathy, J. L. Bersillon, and S. P. Dubey, "Chlorination byproducts, their toxicodynamics and removal from drinking water," *J. Hazard. Mater.*, vol. 140, no. 1–2, pp. 1–6, 2007, doi: 10.1016/j.jhazmat.2006.10.063.

[197] G. Zhang, W. Li, S. Chen, W. Zhou, and J. Chen, "Chemosphere Problems of conventional disinfection and new sterilization methods for antibiotic resistance control," *Chemosphere*, vol. 254, p. 126831, 2020, doi: 10.1016/j.chemosphere.2020.126831.

[198] E. O. Ogunsona, R. Muthuraj, E. Ojogbo, O. Valerio, and T. H. Mekonnen, "Engineered nanomaterials for antimicrobial applications : A review," *Appl. Mater. Today*, vol. 18, pp. 100–473, 2020, doi: 10.1016/j.apmt.2019.100473.

[199] P. Singh, B. Mohan, V. Madaan, R. Ranga, P. Kumari, and S. Kumar, *Nanomaterials photocatalytic activities for waste water treatment : a review*. Springer Berlin Heidelberg, 2022.

[200] R. Soni, A. K. Pal, P. Tripathi, J. A. Lal, K. Kesari, and V. Tripathi, "An overview of nanoscale materials on the removal of wastewater contaminants," *Appl. Water Sci.*, vol. 10, no. 8, pp. 1–9, 2020, doi: 10.1007/s13201-020-01275-3.

[201] J. T. Buchman, N. V Hudson-smith, K. M. Landy, and C. L. Haynes, "Understanding

Nanoparticle Toxicity Mechanisms To Inform Redesign Strategies To Reduce Environmental Impact,” 2019, doi: 10.1021/acs.accounts.9b00053.

[202] L. M. Kustov and W. Peijnenburg, “The effect of capping agents on the toxicity of silver nanoparticles to Danio rerio embryos The effect of capping agents on the toxicity of silver nanoparticles,” vol. 5390, 2019, doi: 10.1080/17435390.2018.1498931.

[203] N. Rani, P. Singh, S. Kumar, P. Kumar, V. Bhankar, and K. Kumar, “Plant-mediated synthesis of nanoparticles and their applications: A review,” *Mater. Res. Bull.*, vol. 163, no. January, p. 112233, 2023, doi: 10.1016/j.materresbull.2023.112233.

[204] A. M. Ramesh *et al.*, “Antioxidant and photocatalytic properties of zinc oxide nanoparticles phyto-fabricated using the aqueous leaf extract of Sida acuta,” *Green Process. Synth.*, vol. 11, no. 1, pp. 857–867, 2022, doi: 10.1515/gps-2022-0075.

[205] R. R. Karri, S. Shams, and J. N. Sahu, “4. Overview of Potential Applications of Nano-Biotechnology in Wastewater and Effluent Treatment,” pp. 87–100, 2019, doi: 10.1016/B978-0-12-813902-8.00004-6.

[206] B. T. Amena, H. Altenbach, G. S. Tibba, and H. G. Lemu, “Effect of reaction conditions on particle size of zno nanoparticles via controlled precipitation method and in-vitro antibacterial capacity,” *Eur. Chem. Bull.*, vol. 11, no. 11, pp. 18–26, 2022, doi: 10.31838/ecb/2022.11.11.003.

[207] W. Sime, R. Kasirajan, S. Latebo, A. Mohammed, and E. Seraw, “Coffee Husk Highly Available in Ethiopia as an Alternative Waste Source for Biofuel Production,” *Int. J. Sci. Eng. Res.*, vol. 8, no. 7, 2017, [Online]. Available: http://www.ijser.org

[208] P. Singh *et al.*, “Assessing the biomass-based carbon dots and their composites for photocatalytic treatment of wastewater,” *J. Clean. Prod.*, vol. 413, no. January, p. 137474, 2023, doi: 10.1016/j.jclepro.2023.137474.

[209] V. Escobar, G. P. Blanch, M. I. San, S. Sanchez-fortun, and M. Dolores, “validation of coffee by-products as novel food ingredients,” *Innov. Food Sci. Emerg. Technol.*, p. #pagerange#, 2018, doi: 10.1016/j.ifset.2018.06.010.

[210] P. Suresh, A. Doss, R. P. Praveen Pole, and M. Devika, “Green synthesis, characterization and

antioxidant activity of bimetallic (Ag-ZnO) nanoparticles using Capparis zeylanica leaf extract,” *Biomass Convers. Biorefinery*, no. 0123456789, 2023, doi: 10.1007/s13399-023-03743-7.

[211] A. M. Pillai *et al.*, “Green synthesis and characterization of zinc oxide nanoparticles with antibacterial and antifungal activity,” *J. Mol. Struct.*, vol. 1211, p. 128107, 2020, doi: 10.1016/j.molstruc.2020.128107.

[212] M. Jiménez-Rosado, A. Gomez-Zavaglia, A. Guerrero, and A. Romero, “Green synthesis of ZnO nanoparticles using polyphenol extracts from pepper waste (Capsicum annuum),” *J. Clean. Prod.*, vol. 350, no. March, 2022, doi: 10.1016/j.jclepro.2022.131541.

[213] S. Faisal *et al.*, “Green Synthesis of Zinc Oxide (ZnO) Nanoparticles Using Aqueous Fruit Extracts of Myristica fragrans: Their Characterizations and Biological and Environmental Applications,” *ACS Omega*, vol. 6, no. 14, pp. 9709–9722, 2021, doi: 10.1021/acsomega.1c00310.

[214] P. Jamdagni, P. Khatri, and J. S. Rana, “Green synthesis of zinc oxide nanoparticles using flower extract of Nyctanthes arbor-tristis and their antifungal activity,” *J. King Saud Univ. - Sci.*, vol. 30, no. 2, pp. 168–175, Apr. 2018, doi: 10.1016/j.jksus.2016.10.002.

[215] A. Umamaheswari, S. L. Prabu, S. A. John, and A. Puratchikody, “Green synthesis of zinc oxide nanoparticles using leaf extracts of Raphanus sativus var. Longipinnatus and evaluation of their anticancer property in A549 cell lines,” *Biotechnol. Reports*, vol. 29, Mar. 2021, doi: 10.1016/j.btre.2021.e00595.

[216] F. M. Mohammadi and N. Ghasemi, “Influence of temperature and concentration on biosynthesis and characterization of zinc oxide nanoparticles using cherry extract,” *J. Nanostructure Chem.*, vol. 8, no. 1, pp. 93–102, 2018, doi: 10.1007/s40097-018-0257-6.

[217] A. Aziz, Z. Memon, and A. Bhutto, “Efficient photocatalytic degradation of industrial wastewater dye by Grewia asiatica mediated zinc oxide nanoparticles,” *Optik (Stuttg).*, vol. 272, no. September 2022, p. 170352, 2023, doi: 10.1016/j.ijleo.2022.170352.

[218] M. de O. Silva, J. N. B. Honfoga, L. L. de Medeiros, M. S. Madruga, and T. K. A. Bezerra, “Obtaining Bioactive Compounds from the Coffee Husk (Coffea arabica L.) Using Different Extraction Methods,” *Molecules*, vol. 26, no. 1, 2020, doi: 10.3390/molecules26010046.

[219] N. Siddiqui, A. Rauf, A. Latif, and Z. Mahmood, "Spectrophotometric determination of the total phenolic content, spectral and fluorescence study of the herbal Unani drug Gul-e-Zoofa (Nepeta bracteata Benth)," *J. Taibah Univ. Med. Sci.*, vol. 12, no. 4, pp. 360–363, Aug. 2017, doi: 10.1016/j.jtumed.2016.11.006.

[220] Kavitha D, "Evaluation of phytochemical compound in leaf extract of calanthe masuca (d.don) lindl., using UV-VIS, FTIR and GCMS analysis-An orchidaceae member," *Int. Res. J. Plant Sci.*, vol. 12, no. 5, pp. 1–5, 2021, [Online]. Available: https://www.interesjournals.org/plant-science.html

[221] A. A. Barzinjy and H. H. Azeez, "Green synthesis and characterization of zinc oxide nanoparticles using Eucalyptus globulus Labill. leaf extract and zinc nitrate hexahydrate salt," *SN Appl. Sci.*, vol. 2, no. 5, May 2020, doi: 10.1007/s42452-020-2813-1.

[222] J. Hudzicki, "Kirby-Bauer Disk Diffusion Susceptibility Test Protocol Author Information," *Am. Soc. Microbiol.*, no. December 2009, pp. 1–13, 2012.

[223] T. K. Patle, K. Shrivas, R. Kurrey, S. Upadhyay, R. Jangde, and R. Chauhan, "Phytochemical screening and determination of phenolics and flavonoids in Dillenia pentagyna using UV–vis and FTIR spectroscopy," *Spectrochim. Acta - Part A Mol. Biomol. Spectrosc.*, vol. 242, p. 118717, 2020, doi: 10.1016/j.saa.2020.118717.

[224] S. Ahmad Bhawani, S. S. Fong, and M. N. Mohamad Ibrahim, "Spectrophotometric Analysis of Caffeine," *International Journal of Analytical Chemistry*, vol. 2015. Hindawi Limited, 2015. doi: 10.1155/2015/170239.

[225] G. Navarra, M. Moschetti, V. Guarrasi, M. R. Mangione, V. Militello, and M. Leone, "Simultaneous determination of caffeine and chlorogenic acids in green coffee by UV/Vis spectroscopy," *J. Chem.*, vol. 2017, 2017, doi: 10.1155/2017/6435086.

[226] L. B. Cangussu, J. C. Melo, A. S. Franca, and L. S. Oliveira, "Chemical characterization of coffee husks, a by-product of coffea arabica production," *Foods*, vol. 10, no. 12. 2021. doi: 10.3390/foods10123125.

[227] M. G. M. Kordy *et al.*, "Phyto-Capped Ag Nanoparticles: Green Synthesis, Characterization, and Catalytic and Antioxidant Activities," *Nanomaterials*, vol. 12, no. 3, Feb. 2022, doi: 10.3390/nano12030373.

[228] E. G. Goh, X. Xu, and P. G. McCormick, “Effect of particle size on the UV absorbance of zinc oxide nanoparticles,” *Scr. Mater.*, vol. 78–79, pp. 49–52, May 2014, doi: 10.1016/j.scriptamat.2014.01.033.

[229] A. V Ramesh, D. R. Devi, S. M. Botsa, and K. Basavaiah, “Facile green synthesis of Fe 3 O 4 nanoparticles using aqueous leaf extract of Zanthoxylum armatum DC . for efficient adsorption of methylene blue,” *J. Asian Ceram. Soc.*, vol. 00, no. 00, pp. 1–11, 2018, doi: 10.1080/21870764.2018.1459335.

[230] P. Wongsa, P. Phatikulrungsun, and S. Prathumthong, “FT-IR characteristics, phenolic profiles and inhibitory potential against digestive enzymes of 25 herbal infusions,” *Sci. Rep.*, vol. 12, no. 1, pp. 1–11, 2022, doi: 10.1038/s41598-022-10669-z.

[231] J. Iqbal *et al.*, “Green synthesis of zinc oxide nanoparticles using Elaeagnus angustifolia L. leaf extracts and their multiple in vitro biological applications,” *Sci. Rep.*, vol. 11, no. 1, pp. 1–13, 2021, doi: 10.1038/s41598-021-99839-z.

[232] A. C. Dhanemozhi, V. Rajeswari, and S. Sathyajothi, “Green Synthesis of Zinc Oxide Nanoparticle Using Green Tea Leaf Extract for Supercapacitor Application,” *Mater. Today Proc.*, vol. 4, no. 2, pp. 660–667, 2017, doi: 10.1016/j.matpr.2017.01.070.

[233] S. Talam, S. R. Karumuri, and N. Gunnam, “Synthesis, Characterization, and Spectroscopic Properties of ZnO Nanoparticles,” *ISRN Nanotechnol.*, vol. 2012, pp. 1–6, May 2012, doi: 10.5402/2012/372505.

[234] D. Zhang, X. L. Ma, Y. Gu, H. Huang, and G. W. Zhang, “Green Synthesis of Metallic Nanoparticles and Their Potential Applications to Treat Cancer,” *Front. Chem.*, vol. 8, no. October, pp. 1–18, 2020, doi: 10.3389/fchem.2020.00799.

[235] T. C. Prathna, N. Chandrasekaran, A. M. Raichur, and A. Mukherjee, “Kinetic evolution studies of silver nanoparticles in a bio-based green synthesis process,” *Colloids Surfaces A Physicochem. Eng. Asp.*, vol. 377, no. 1–3, pp. 212–216, Mar. 2011, doi: 10.1016/j.colsurfa.2010.12.047.

[236] B. Gherbi *et al.*, “Effect of pH Value on the Bandgap Energy and Particles Size for Biosynthesis of ZnO Nanoparticles: Efficiency for Photocatalytic Adsorption of Methyl Orange,” *Sustain.*, vol. 14, no. 18, 2022, doi: 10.3390/su141811300.

[237] L. Christensen, S. Vivekanandhan, M. Misra, and A. K. Mohanty, “Biosynthesis of silver nanoparticles using Murraya koenigii (curry leaf): An investigation on the effect of broth concentration in reduction mechanism and particle size,” *Adv. Mater. Lett.*, vol. 2, no. 6, pp. 429–434, Dec. 2011, doi: 10.5185/amlett.2011.4256.

[238] M. Avramescu, P. E. Rasmussen, M. Chénier, and H. D. Gardner, “Influence of pH , particle size and crystal form on dissolution behaviour of engineered nanomaterials,” *Environ. Sci. Pollut. Res.*, 2016, doi: 10.1007/s11356-016-7932-2.

[239] A. U. H. Khan, Y. Liu, R. Naidu, C. Fang, R. Dharmarajan, and H. Shon, “Interactions between zinc oxide nanoparticles and hexabromocyclododecane in simulated waters,” *Environ. Technol. Innov.*, vol. 24, Nov. 2021, doi: 10.1016/j.eti.2021.102078.

[240] A. F. Abdulrahman, S. M. Ahmed, S. M. Hamad, M. A. Almessiere, N. M. Ahmed, and S. M. Sajadi, “Effect of different pH values on growth solutions for the ZnO nanostructures,” *Chinese J. Phys.*, vol. 71, no. January, pp. 175–189, 2021, doi: 10.1016/j.cjph.2021.02.013.

[241] R. Ashraf, S. Riaz, S. S. Hussain, and S. Naseem, *Effect of pH on Properties of ZnO Nanoparticles*, vol. 2, no. 10. Elsevier Ltd., 2015. doi: 10.1016/j.matpr.2015.11.123.

[242] V. Dhiman, N. Kondal, and P. Choudhary, “Bryophyllum pinnatum leaf extract mediated ZnO nanoparticles with prodigious potential for solar driven photocatalytic degradation of industrial contaminants,” *Environ. Res.*, vol. 216, no. P4, p. 114751, 2023, doi: 10.1016/j.envres.2022.114751.

[243] C. F. Holder and R. E. Schaak, “Tutorial on Powder X-ray Diffraction for Characterizing Nanoscale Materials,” *ACS Nano*, vol. 13, no. 7. American Chemical Society, pp. 7359–7365, Jul. 23, 2019. doi: 10.1021/acsnano.9b05157.

[244] S. K. Esthappan, A. B. Nair, and R. Joseph, “Effect of crystallite size of zinc oxide on the mechanical, thermal and flow properties of polypropylene/zinc oxide nanocomposites,” *Compos. Part B Eng.*, vol. 69, pp. 145–153, 2015, doi: 10.1016/j.compositesb.2013.08.010.

[245] M. Sorbiun, E. Shayegan Mehr, A. Ramazani, and S. Taghavi Fardood, “Green Synthesis of Zinc Oxide and Copper Oxide Nanoparticles Using Aqueous Extract of Oak Fruit Hull (Jaft) and Comparing Their Photocatalytic Degradation of Basic Violet 3,” *Int. J. Environ. Res.*, vol. 12, no. 1, pp. 29–37, Mar. 2018, doi: 10.1007/s41742-018-0064-4.

[246] A. M. Pillai *et al.*, “Green Synthesis of Zinc Oxide (ZnO) Nanoparticles Using Ocimum Tenuiflorum Leaves,” *J. Mol. Struct.*, vol. 1211, p. 128107, 2020, doi: 10.1016/j.molstruc.2020.128107.

[247] S.-B. Kim, N.-K. Yoo, and S.-J. Choi, “Interactions between ZnO Nanoparticles and Polyphenols Affect Biological Responses,” *Nanomaterials*, vol. 12, no. 19, p. 3337, 2022, doi: 10.3390/nano12193337.

[248] M. M. Modena, B. Rühle, T. P. Burg, and S. Wuttke, “Nanoparticle Characterization: What to Measure?,” *Advanced Materials*, vol. 31, no. 32. Wiley-VCH Verlag, 2019. doi: 10.1002/adma.201901556.

[249] S. Faisal, H. Jan, S. A. Shah, S. Shah, A. Khan, and M. T. Akbar, “Green Synthesis of Zinc Oxide (ZnO) Nanoparticles Using Aqueous Fruit Extracts of Myristica fragrans: Their Characterizations and Biological and Environmental Applications,” *ACS Omega*, vol. 6, no. 14, pp. 9709–9722, 2021, doi: 10.1021/acsomega.1c00310.

[250] T. S. Aldeen, H. E. Ahmed Mohamed, and M. Maaza, “ZnO nanoparticles prepared via a green synthesis approach: Physical properties, photocatalytic and antibacterial activity,” *J. Phys. Chem. Solids*, vol. 160, pp. 110–313, 2022, doi: 10.1016/j.jpcs.2021.110313.

[251] N. Rana, S. Chand, and A. K. Gathania, “Green synthesis of zinc oxide nano-sized spherical particles using Terminalia chebula fruits extract for their photocatalytic applications,” *Int. Nano Lett.*, vol. 6, no. 2, pp. 91–98, 2016, doi: 10.1007/s40089-015-0171-6.

[252] Y. A. Dallatu, G. A. Shallangwa, and S. N. Africa, “Synthesis and growth of spherical ZnO nanoparticles using different amount of plant extract: characterization and morphology of structures,” *J. Appl. Sci. Environ. Manag.*, vol. 24, no. 12, pp. 2147–2151, 2021.

[253] R. Saemi, E. Taghavi, H. Jafarizadeh-Malmiri, and N. Anarjan, “Fabrication of green ZnO nanoparticles using walnut leaf extract to develop an antibacterial film based on polyethylene-starch-ZnO NPs,” *Green Process. Synth.*, vol. 10, no. 1, pp. 112–124, 2021, doi: 10.1515/gps-2021-0011.

[254] A. Mazzoli and O. Favoni, “Particle size, size distribution and morphological evaluation of airborne dust particles of diverse woods by Scanning Electron Microscopy and image processing program,” *Powder Technol.*, vol. 225, pp. 65–71, 2012, doi:

10.1016/j.powtec.2012.03.033.

[255] N. A. Alenezi, F. Al-qurainy, M. Tarroum, M. Nadeem, and S. Khan, “Zinc Oxide Nanoparticles (ZnO NPs), Biosynthesis,Characterization and Evaluation of Their Impact to Improve Shoot Growth and to Reduce Salt Toxicity on Salvia officinalis In Vitro Cultivated,” pp. 1–16, 2022.

[256] H. Agarwal, S. Venkat Kumar, and S. Rajeshkumar, “A review on green synthesis of zinc oxide nanoparticles – An eco-friendly approach,” *Resour. Technol.*, vol. 3, no. 4, pp. 406–413, 2017, doi: 10.1016/j.reffit.2017.03.002.

[257] S. K. Chaudhuri and L. Malodia, “Biosynthesis of zinc oxide nanoparticles using leaf extract of calotropis gigantea: Characterization and its evaluation on tree seedling growth in nursery stage,” *Appl. Nanosci.*, vol. 7, no. 8, pp. 501–512, Nov. 2017, doi: 10.1007/s13204-017-0586-7.

[258] S. Arunima Rajan, A. Khan, S. Asrar, H. Raza, R. K. Das, and N. K. Sahu, “Synthesis of ZnO/Fe3O4/rGO nanocomposites and evaluation of antibacterial activities towards E. coli and S. aureus,” *IET Nanobiotechnology*, vol. 13, no. 7, pp. 682–687, 2019, doi: 10.1049/iet-nbt.2018.5330.

[259] S. K. Kassahun, Z. Kiflie, H. Kim, and B. T. Gadisa, “Effects of operational parameters on bacterial inactivation in Vis-LEDs illuminated N-doped TiO2 based photoreactor,” *J. Environ. Chem. Eng.*, vol. 8, no. 5, 2020, doi: 10.1016/j.jece.2020.104374.

[260] S. Sharma, K. Kumar, N. Thakur, S. Chauhan, and M. S. Chauhan, “The effect of shape and size of ZnO nanoparticles on their antimicrobial and photocatalytic activities: a green approach,” *Bull. Mater. Sci.*, vol. 43, no. 1, Dec. 2020, doi: 10.1007/s12034-019-1986-y.

[261] M. Naseer, U. Aslam, B. Khalid, and B. Chen, “Green route to synthesize Zinc Oxide Nanoparticles using leaf extracts of Cassia fistula and Melia azadarach and their antibacterial potential,” *Sci. Rep.*, vol. 10, no. 1, Dec. 2020, doi: 10.1038/s41598-020-65949-3.

[262] Y. Dong, H. Zhu, Y. Shen, W. Zhang, and L. Zhang, “Antibacterial activity of silver nanoparticles of different particle size against Vibrio Natriegens,” *PLoS One*, vol. 14, no. 9, pp. 1–12, 2019, doi: 10.1371/journal.pone.0222322.

[263] D. Surendhiran, A. Sirajunnisa, and K. Tamilselvam, "Silver–magnetic nanocomposites for water purification," *Environ. Chem. Lett.*, vol. 15, no. 3, pp. 367–386, 2017, doi: 10.1007/s10311-017-0635-1.

[264] E. A. S. Dimapilis, C. S. Hsu, R. M. O. Mendoza, and M. C. Lu, "Zinc oxide nanoparticles for water disinfection," *Sustain. Environ. Res.*, vol. 28, no. 2, pp. 47–56, 2018, doi: 10.1016/j.serj.2017.10.001.

[265] T. Gordon, B. Perlstein, O. Houbara, I. Felner, E. Banin, and S. Margel, "Synthesis and characterization of zinc/iron oxide composite nanoparticles and their antibacterial properties," *Colloids Surfaces A Physicochem. Eng. Asp.*, vol. 374, no. 1–3, pp. 1–8, 2011, doi: 10.1016/j.colsurfa.2010.10.015.

[266] J. Wojnarowicz, T. Chudoba, I. Koltsov, S. Gierlotka, S. Dworakowska, and W. Lojkowski, "Size control mechanism of ZnO nanoparticles obtained in microwave solvothermal synthesis," *Nanotechnology*, vol. 29, no. 6, 2018, doi: 10.1088/1361-6528/aaa0ef.

[267] G. Ipek Yucelen, R. E. Connell, J. R. Terbush, D. J. Westenberg, and F. Dogan, "Synthesis and immobilization of silver nanoparticles on aluminosilicate nanotubes and their antibacterial properties," *Appl. Nanosci.*, vol. 6, no. 4, pp. 607–614, 2016, doi: 10.1007/s13204-015-0467-x.

[268] S. Bao, T. Hou, Q. Tan, X. Kong, H. Cao, and M. He, "Immobilization of zinc oxide nanoparticles on graphene sheets for lithium ion storage and electromagnetic microwave absorption," *Mater. Chem. Phys.*, vol. 245, no. 7, pp. 122–766, 2020, doi: 10.1016/j.matchemphys.2020.122766.

[269] A. M. Abdelmonem, B. Pelaz, K. Kantner, N. C. Bigall, P. Del Pino, and W. J. Parak, "Charge and agglomeration dependent in vitro uptake and cytotoxicity of zinc oxide nanoparticles," *J. Inorg. Biochem.*, vol. 153, pp. 334–338, 2015, doi: 10.1016/j.jinorgbio.2015.08.029.

[270] S. Agnihotri, G. Bajaj, S. Mukherji, and S. Mukherji, "Arginine-assisted immobilization of silver nanoparticles on ZnO nanorods: An enhanced and reusable antibacterial substrate without human cell cytotoxicity," *Nanoscale*, vol. 7, no. 16, pp. 7415–7429, 2015, doi: 10.1039/c4nr06913g.

[271] D. Violeta, B. Mariana, V. Tucureanu, B. Oana, C. F. I. B. Iliescu, and S. I. Florina,

“Synthesis of ZnO/Au Nanocomposite for Antibacterial Applications,” *Nanomaterials*, vol. 12, no. 21, 2022, doi: 10.3390/nano12213832.

[272] H. Wu, Y. Meng, M. Yu, and H. Yang, “Modulating the antibacterial activity of ZnO/talc by balancing the monodispersity of ZnO nanoparticles,” *Appl. Clay Sci.*, vol. 242, Sep. 2023, doi: 10.1016/J.CLAY.2023.107024.

[273] H. M. Ahmed, M. A. El-khateeb, N. A. Sobhy, M. M. Hefny, and F. M. Abdel-Haleem, “Green Synthesis of Magnetite Nanoparticles Using Waste Natural Materials and Its Application for Wastewater Treatment,” p. 99, 2023, doi: 10.3390/ecws-7-14181.

[274] C. C. Dos Santos, W. R. Viali, E. S. N. Viali, R. F. C. Marques, and M. Jafelicci Junior, “Colloidal stability study of Fe3O4-based nanofluids in water and ethylene glycol,” *J. Therm. Anal. Calorim.*, vol. 146, no. 1, pp. 509–520, 2021, doi: 10.1007/s10973-020-10062-w.

[275] N. Wang, T. Tong, M. Xie, and J. F. Gaillard, “Lifetime and dissolution kinetics of zinc oxide nanoparticles in aqueous media,” *Nanotechnology*, vol. 27, no. 32, pp. 1–10, 2016, doi: 10.1088/0957-4484/27/32/324001.

[276] A. Mourhly, M. Khachani, A. El Hamidi, M. Kacimi, M. Halim, and S. Arsalane, “The synthesis and characterization of low-cost mesoporous silica SiO2 from local pumice rock,” *Nanomater. Nanotechnol.*, vol. 5, 2015, doi: 10.5772/62033.

[277] E. K. S. K.Baran , L.Tim , M.C. Hatice , K.Gulnar, N.G.Zeynep , O.A. Mehmet , K. Cevriye , S. George E., S.M.Yesim , Z.S.Ahmed, S.Mediha, “Fabrication of naturel pumice/hydroxyapatite composite for biomedical engineering,” *Biomed. Eng. Online*, vol. 15, no. 1, pp. 1–20, 2016, doi: 10.1186/s12938-016-0203-0.

[278] A. Khataee, P. Gholami, B. Kayan, D. Kalderis, L. Dinpazhoh, and S. Akay, “Synthesis of ZrO2 nanoparticles on pumice and tuff for sonocatalytic degradation of rifampin,” *Ultrason. Sonochem.*, vol. 48, no. May, pp. 349–361, 2018, doi: 10.1016/j.ultsonch.2018.05.008.

[279] M. M. S. Abdullah, A. M. Atta, H. A. Allohedan, H. Z. Alkhathlan, M. Khan, and A. O. Ezzat, “Green synthesis of hydrophobic magnetite nanoparticles coated with plant extract and their application as petroleum oil spill collectors,” *Nanomaterials*, vol. 8, no. 10, Oct. 2018, doi: 10.3390/nano8100855.

[280] A. Bouafia and S. E. Laouini, “Green synthesis of iron oxide nanoparticles by aqueous leaves extract of Mentha Pulegium L.: Effect of ferric chloride concentration on the type of product,” *Mater. Lett.*, vol. 265, pp. 127–364, 2020, doi: 10.1016/j.matlet.2020.127364.

[281] W. Marimón-Bolívar and E. E. González, “Green synthesis with enhanced magnetization and life cycle assessment of Fe3O4 nanoparticles,” *Environ. Nanotechnology, Monit. Manag.*, vol. 9, no. 42, pp. 58–66, 2018, doi: 10.1016/j.enmm.2017.12.003.

[282] M. Sivakami, K. Renuka Devi, R. Renuka, and T. Thilagavathi, “Green synthesis of magnetic nanoparticles via Cinnamomum verum bark extract for biological application,” *J. Environ. Chem. Eng.*, vol. 8, no. 5, 2020, doi: 10.1016/j.jece.2020.104420.

[283] I. A. S.Khan, G.Bibi , S.Dilbar, A.Iqbal, M.Ahmad, A.Ali , Z.Ullah , M.Jaremko , J.Iqbal, M.Ali , I.Haq, “Biosynthesis and characterization of iron oxide nanoparticles from Mentha spicata and screening its combating potential against Phytophthora infestans,” *Front. Plant Sci.*, vol. 13, pp. 1–8, 2022, doi: 10.3389/fpls.2022.1001499.

[284] G. Tsegaye, Z. Kiflie, T. H. Mekonnen, and M. Jida, “Synthesis and characterization of coffee husk extract (CHE)- capped ZnO nanoparticles and their antimicrobial activity,” *Biomass Convers. Biorefinery*, no. 0123456789, 2023, doi: 10.1007/s13399-023-04908-0.

[285] M. A. Ali and S. Bhowmik, “Sustainability functional properties , applications , and sustainable approach in circular economy,” pp. 4410–4425, 2025, doi: 10.1039/d5su00531k.

[286] M. Z. H.Soleimani, A.Mahvi, H.Amir, K.Yaghmaeian, A.Abbasnia, K.Sharafi, M.Alimohammadi, “Effect of modification by five different acids on pumice stone as natural and low-cost adsorbent for removal of humic acid from aqueous solutions - Application of response surface methodology,” *J. Mol. Liq.*, vol. 290, 2019, doi: 10.1016/j.molliq.2019.111181.

[287] R. Taheri-Ledari, K. Valadi, S. Gharibi, and A. Maleki, “Synergistic photocatalytic effect between green LED light and Fe3O4/ZnO-modified natural pumice: A novel cleaner product for degradation of methylene blue,” *Mater. Res. Bull.*, vol. 130, Oct. 2020, doi: 10.1016/j.materresbull.2020.110946.

[288] M. Sajjadi, M. Nasrollahzadeh, and S. Mohammad Sajadi, “Green synthesis of Ag/Fe3O4 nanocomposite using Euphorbia peplus Linn leaf extract and evaluation of its catalytic

activity," *J. Colloid Interface Sci.*, vol. 497, pp. 1–13, 2017, doi: 10.1016/j.jcis.2017.02.037.

[289] S. Alraddadi and H. Assaedi, "Physical properties of mesoporous scoria and pumice volcanic rocks," *J. Phys. Commun.*, vol. 5, no. 11, p. 115018, 2021, doi: 10.1088/2399-6528/ac3a95.

[290] S. Torgbo and P. Sukyai, "Fabrication of microporous bacterial cellulose embedded with magnetite and hydroxyapatite nanocomposite scaffold for bone tissue engineering," *Mater. Chem. Phys.*, vol. 237, 2019, doi: 10.1016/j.matchemphys.2019.121868.

[291] S. S. U. Rahman, M. T. Qureshi, K. Sultana, and W. Rehman, "Single step growth of iron oxide nanoparticles and their use as glucose biosensor," *Results Phys.*, vol. 7, pp. 4451–4456, 2017, doi: 10.1016/j.rinp.2017.11.001.

[292] Shamsuzzaman, A. Mashrai, H. Khanam, and R. N. Aljawfi, "Biological synthesis of ZnO nanoparticles using C. albicans and studying their catalytic performance in the synthesis of steroidal pyrazolines," *Arab. J. Chem.*, vol. 10, pp. S1530–S1536, 2017, doi: 10.1016/j.arabjc.2013.05.004.

[293] V. Correcher, J. M. Gomez-Ros, T. Dogan, J. Garcia-Guinea, and M. Topaksu, "Optical, spectral and thermal properties of natural pumice glass," *Radiat. Phys. Chem.*, vol. 130, pp. 69–75, 2017, doi: 10.1016/j.radphyschem.2016.08.002.

[294] A. Ali, Y. W. Chiang, and R. M. Santos, "X-Ray Diffraction Techniques for Mineral Characterization: A Review for Engineers of the Fundamentals, Applications, and Research Directions," *Minerals*, vol. 12, no. 2, 2022, doi: 10.3390/min12020205.

[295] M. A. Ebrahimzadeh, S. Mortazavi-Derazkola, and M. A. Zazouli, "Eco-friendly green synthesis of novel magnetic Fe3O4/SiO2/ZnO-Pr6O11 nanocomposites for photocatalytic degradation of organic pollutant," *J. Rare Earths*, vol. 38, no. 1, pp. 13–20, 2020, doi: 10.1016/j.jre.2019.07.004.

[296] K. X. L. . Y. P. Yew, K. Shameli, M. Miyake, N.Kuwano, N.B. Bt Ahmad Khairudin, S. E. Bt Mohamad, "Green Synthesis of Magnetite (Fe3O4) Nanoparticles Using Seaweed (Kappaphycus alvarezii) Extract," *Nanoscale Res. Lett.*, vol. 11, no. 1, 2016, doi: 10.1186/s11671-016-1498-2.

[297] A. A. SA1, A.-H. FA1, A.-K. AG2, and T. A.-D. AM2, "Phytochemical Screening by FTIR

Spectroscopic Analysis in the Methanolic Extracts Coffee (C. Arabica. L) to Seeds and Peels (Unroasted and Roasted) Cultivars Grown in Yemen," *Bioequivalence Bioavailab. Int. J.*, vol. 6, no. 2, pp. 1–8, 2022, doi: 10.23880/beba-16000179.

[298] P. K. Dhar, P. Saha, M. K. Hasan, M. K. Amin, and M. R. Haque, "Green synthesis of magnetite nanoparticles using Lathyrus sativus peel extract and evaluation of their catalytic activity," *Clean. Eng. Technol.*, vol. 3, 2021, doi: 10.1016/j.clet.2021.100117.

[299] R. Taheri-Ledari, M. Saeidirad, F. S. Qazi, A. Fazeli, A. Maleki, and A. E. Shalan, "Highly porous copper-supported magnetic nanocatalysts: made of volcanic pumice textured by cellulose and applied for the reduction of nitrobenzene derivatives," *RSC Adv.*, vol. 11, no. 41, pp. 25284–25295, 2021, doi: 10.1039/d1ra03538j.

[300] N. A. Al-Dhabi and M. V. Arasu, "Environmentally-friendly green approach for the production of zinc oxide nanoparticles and their anti-fungal, ovicidal, and larvicidal properties," *Nanomaterials*, vol. 8, no. 7, 2018, doi: 10.3390/nano8070500.

[301] S. H. Ghoran, M. F. Dashti, A. Maroofi, M. Shafiee, A. Zare-Hoseinabadi, and F. Behzad, "Biosynthesis of Zinc Ferrite Nanoparticles Using Polyphenol-rich extract of Citrus aurantium flowers," *Nanomedicine Res. J.*, vol. 5, no. 1, pp. 20–28, 2020, doi: 10.22034/NMRJ.2020.01.003.

[302] M. M. S. Abdullah, A. M. Atta, H. A. Allohedan, H. Z. Alkhathlan, M. Khan, and A. O. Ezzat, "Green synthesis of hydrophobic magnetite nanoparticles coated with plant extract and their application as petroleum oil spill collectors," *Nanomaterials*, vol. 8, no. 10, 2018, doi: 10.3390/nano8100855.

[303] V. O. Shipunova, P. A. Kotelnikova, U. F. Aghayeva, O. A. Stremovskiy, A. A. Schulga, and M. P. Nikitin, "Data on characterization of magnetic nanoparticles stabilized with fusion protein of Barstar and C-term part of Mms6," *Data Br.*, vol. 21, pp. 1659–1663, 2018, doi: 10.1016/j.dib.2018.10.173.

[304] G. Sathishkumar, V. Logeshwaran, S. Sarathbabu, P. K. Jha, M. Jeyaraj, and C. Rajkuberan, "Green synthesis of magnetic Fe3O4 nanoparticles using Couroupita guianensis Aubl. fruit extract for their antibacterial and cytotoxicity activities," *Artif. Cells, Nanomedicine Biotechnol.*, vol. 46, no. 3, pp. 589–598, 2018, doi: 10.1080/21691401.2017.1332635.

[305] A. T. Almalkawi, S. Hamadna, and P. Soroushian, “One-part alkali activated cement based volcanic pumice,” *Constr. Build. Mater.*, vol. 152, pp. 367–374, 2017, doi: 10.1016/j.conbuildmat.2017.06.139.

[306] P. Kielbik *et al.*, “Preliminary Studies on Biodegradable Zinc Oxide Nanoparticles Doped with Fe as a Potential Form of Iron Delivery to the Living Organism,” *Nanoscale Res. Lett.*, vol. 14, no. 1, 2019, doi: 10.1186/s11671-019-3217-2.

[307] A. Sarı, G. Hekimoğlu, V. V. Tyagi, and R. K. Sharma, “Evaluation of pumice for development of low-cost and energy-efficient composite phase change materials and lab-scale thermoregulation performances of its cementitious plasters,” *Energy*, vol. 207, pp. 1–13, 2020, doi: 10.1016/j.energy.2020.118242.

[308] M. J. Klink, N. Laloo, A. L. Taka, V. E. Pakade, E. Monapathi, and J. S. Modise, “Synthesis , Characterization and Antimicrobial Activity of Zinc Yeast Pathogens,” *Molecules*, vol. 27, no. 3532, 2022.

[309] E. M. Sharaf, A. Hassan, F. A. AL-Salmi, F. M. Albalwe, and H. M. R. Albalawi, “Synergistic antibacterial activity of compact silver/magnetite core-shell nanoparticles core shell against Gram-negative foodborne pathogens,” *Front. Microbiol.*, vol. 13, no. September, pp. 1–12, 2022, doi: 10.3389/fmicb.2022.929491.

[310] A. Jiménez, M. Vargas, and A. Chiralt, *Antimicrobial nanocomposites for food packaging applications: novel approaches*. Elsevier Inc., 2016. doi: 10.1016/B978-0-12-804308-0.00011-X.

[311] R. Paulino, B. Tamburic, R. M. Stuetz, A. Zamyadi, N. Crosbie, and R. K. Henderson, “Critical review of adsorption and biodegradation mechanisms for removal of biogenic taste and odour compounds in granular and biological activated carbon contactors,” *J. Water Process Eng.*, vol. 52, pp. 103–518, 2023, doi: 10.1016/j.jwpe.2023.103518.

[312] N. Padmavathy and R. Vijayaraghavan, “Enhanced bioactivity of ZnO nanoparticles - An antimicrobial study,” *Sci. Technol. Adv. Mater.*, vol. 9, no. 3, 2008, doi: 10.1088/1468-6996/9/3/035004.

[313] B. Lallo da Silva, B. L. Caetano, B. G. Chiari-Andréo, R. C. L. R. Pietro, and L. A. Chiavacci, “Increased antibacterial activity of ZnO nanoparticles: Influence of size and surface

modification," *Colloids Surfaces B Biointerfaces*, vol. 177, pp. 440–447, 2019, doi: 10.1016/j.colsurfb.2019.02.013.

[314] L. Shkodenko, I. Kassirov, and E. Koshel, "Metal oxide nanoparticles against bacterial biofilms: Perspectives and limitations," *Microorganisms*, vol. 8, no. 10, pp. 1–21, 2020, doi: 10.3390/microorganisms8101545.

[315] W. Li, E. S. Thian, M. Wang, Z. Wang, and L. Ren, "Surface Design for Antibacterial Materials: From Fundamentals to Advanced Strategies," *Adv. Sci.*, vol. 8, no. 19, pp. 1–23, 2021, doi: 10.1002/advs.202100368.

[316] N. Ostovar, N. Mohammadi, and F. Khodadadeh, "Photocatalytic, antioxidant and antibacterial potential of bio-synthesized ZnO nanoparticles derived from espresso spent coffee grounds: optimization by central composite design," *Inorg. Nano-Metal Chem.*, vol. 0, no. 0, pp. 1–12, 2023, doi: 10.1080/24701556.2023.2187419.

[317] S. Dabagh, S. A. Haris, B. K. Isfahani, and Y. N. Ertas, "Silver-Decorated and Silica-Capped Magnetite Nanoparticles with Effective Antibacterial Activity and Reusability," *ACS Appl. Bio Mater.*, vol. 6, no. 6, pp. 2266–2276, 2023, doi: 10.1021/acsabm.3c00122.

[318] J. Briffa, E. Sinagra, and R. Blundell, "Heavy metal pollution in the environment and their toxicological effects on humans," *Heliyon*, vol. 6, no. 9, p. e04691, 2020, doi: 10.1016/j.heliyon.2020.e04691.

[319] M. Rezaei, N. Pourang, and A. M. Moradi, "Removal of lead from aqueous solutions using three biosorbents of aquatic origin with the emphasis on the affective factors," *Sci. Rep.*, vol. 12, no. 1, pp. 1–20, 2022, doi: 10.1038/s41598-021-04744-0.

[320] M. Balali-Mood, K. Naseri, Z. Tahergorabi, M. R. Khazdair, and M. Sadeghi, "Toxic Mechanisms of Five Heavy Metals: Mercury, Lead, Chromium, Cadmium, and Arsenic," *Front. Pharmacol.*, vol. 12, no. April, pp. 1–19, 2021, doi: 10.3389/fphar.2021.643972.

[321] S. U. Khan, M. Khalid, K. Hashim, and M. H. Jamadi, "Efficacy of Electrocoagulation Treatment for the Abatement of Heavy Metals: An Overview of Critical Processing Factors, Kinetic Models and Cost Analysis," *Sustain.*, vol. 15, no. 2, 2023, doi: 10.3390/su15021708.

[322] F. Gholami, A. Asadi, and A. A. Zinatizadeh, "Efficient heavy metals and salts rejection using

a novel modified polysulfone nanofiltration membrane," *Appl. Water Sci.*, vol. 12, no. 7, pp. 1–18, 2022, doi: 10.1007/s13201-022-01671-x.

[323] M. Agarwal and K. Chaudhry, "Heavy Metal Sources Impacts & Removal Technologies," vol. 3, no. 03, pp. 1–7, 2015, [Online]. Available: www.ijert.org

[324] A. E. Burakov, E. V. Galunin, I. V. Burakova, and A. E. Kucherova, "Adsorption of heavy metals on conventional and nanostructured materials for wastewater treatment purposes: A review," *Ecotoxicol. Environ. Saf.*, vol. 148, no. November 2017, pp. 702–712, 2018, doi: 10.1016/j.ecoenv.2017.11.034.

[325] R. Baby, M. Z. Hussein, A. H. Abdullah, and Z. Zainal, "Nanomaterials for the Treatment of Heavy Metal Contaminated Water," *Polymers (Basel).*, vol. 14, no. 3, pp. 1–17, 2022, doi: 10.3390/polym14030583.

[326] Z. H. Mohammad, F. Ahmad, S. A. Ibrahim, and S. Zaidi, "Application of nanotechnology in different aspects of the food industry," *Discov. Food*, vol. 2, no. 1, 2022, doi: 10.1007/s44187-022-00013-9.

[327] P. Samaddar, Y. S. Ok, K. H. Kim, E. E. Kwon, and D. C. W. Tsang, "Synthesis of nanomaterials from various wastes and their new age applications," *J. Clean. Prod.*, vol. 197, pp. 1190–1209, 2018, doi: 10.1016/j.jclepro.2018.06.262.

[328] H. Sadegh, G. A. M. Ali, V. K. Gupta, and A. S. H. Makhlouf, "The role of nanomaterials as effective adsorbents and their applications in wastewater treatment," *J. Nanostructure Chem.*, vol. 7, no. 1, pp. 1–14, 2017, doi: 10.1007/s40097-017-0219-4.

[329] M. Irfan, A. Arif, M. A. Munir, M. Y. Naz, and S. Shukrullah, "Statistically Analyzed Heavy Metal Removal Efficiency of Silica- Treatment," 2023, doi: 10.1021/acsomega.3c05764.

[330] L. Spitzmüller, F. Nitschke, B. Rudolph, J. Berson, T. Schimmel, and T. Kohl, "Dissolution control and stability improvement of silica nanoparticles in aqueous media," *J. Nanoparticle Res.*, vol. 25, no. 3, 2023, doi: 10.1007/s11051-023-05688-4.

[331] A. Taufiq, A. Nikmah, A. Hidayat, and S. Sunaryono, "Synthesis of magnetite/silica nanocomposites from natural sand to create a drug delivery vehicle," *Heliyon*, vol. 6, no. 4, 2020, doi: 10.1016/j.heliyon.2020.e03784.

[332] R. Nicola, O. Costişor, M. Ciopec, A. Negrea, and R. Lazău, “Silica-coated magnetic nanocomposites for Pb2+ removal from aqueous solution,” *Appl. Sci.*, vol. 10, no. 8, 2020, doi: 10.3390/APP10082726.

[333] N. Ahmad, H. Sereshti, M. Mousazadeh, H. Rashidi Nodeh, M. A. Kamboh, and S. Mohamad, “New magnetic silica-based hybrid organic-inorganic nanocomposite for the removal of lead(II) and nickel(II) ions from aqueous solutions,” *Mater. Chem. Phys.*, vol. 226, no. Ii, pp. 73–81, 2019, doi: 10.1016/j.matchemphys.2019.01.002.

[334] Y. Xu, Y. Li, and Z. Ding, “Network–Polymer–Modified Superparamagnetic Magnetic Silica Nanoparticles for the Adsorption and Regeneration of Heavy Metal Ions,” *Molecules*, vol. 28, no. 21, 2023, doi: 10.3390/molecules28217385.

[335] V. P. Aswathi, S. Meera, C. G. A. Maria, and M. Nidhin, “Green synthesis of nanoparticles from biodegradable waste extracts and their applications: a critical review,” *Nanotechnol. Environ. Eng.*, vol. 8, no. 2, pp. 377–397, 2023, doi: 10.1007/s41204-022-00276-8.

[336] Y. H. Gonfa, F. B. Tessema, A. Bachheti, and N. Rai, “Anti-inflammatory activity of phytochemicals from medicinal plants and their nanoparticles: A review,” *Curr. Res. Biotechnol.*, vol. 6, no. November, p. 100152, 2023, doi: 10.1016/j.crbiot.2023.100152.

[337] J. Singh, T. Dutta, K. H. Kim, M. Rawat, P. Samddar, and P. Kumar, “‘Green’ synthesis of metals and their oxide nanoparticles: Applications for environmental remediation,” *J. Nanobiotechnology*, vol. 16, no. 1, pp. 1–24, 2018, doi: 10.1186/s12951-018-0408-4.

[338] A. M. Atta, Y. M. Moustafa, A. O. Ezzat, and A. I. Hashem, “Novel magnetic silica-ionic liquid nanocomposites for wastewater treatment,” *Nanomaterials*, vol. 10, no. 1, 2020, doi: 10.3390/nano10010071.

[339] F. Dadvar and D. Elhamifar, “Magnetic silica/graphene oxide nanocomposite supported ionic liquid–manganese complex as a powerful catalyst for the synthesis of tetrahydrobenzopyrans,” *Sci. Rep.*, vol. 13, no. 1, pp. 1–13, 2023, doi: 10.1038/s41598-023-46629-4.

[340] R. G. Digigow, J. F. Dechézelles, and H. Dietsch, “Preparation and characterization of functional silica hybrid magnetic nanoparticles,” *J. Magn. Magn. Mater.*, vol. 362, pp. 72–79, 2014, doi: 10.1016/j.jmmm.2014.03.026.

[341] Y. Liang, Z. Han, Q. Zeng, S. Wang, and W. Sun, “Effective Removal of Pb2+ from Aqueous Solution Using Magnetic Mesoporous Silica Prepared by Rubidium-Containing Biotite Leaching Residues and Wastewater,” *Water (Switzerland)*, vol. 14, no. 17, 2022, doi: 10.3390/w14172652.

[342] G. Falk, G. P. Shinhe, L. B. Teixeira, E. G. Moraes, and A. P. N. de Oliveira, “Synthesis of silica nanoparticles from sugarcane bagasse ash and nano-silicon via magnesiothermic reactions,” *Ceram. Int.*, vol. 45, no. 17, pp. 21618–21624, 2019, doi: 10.1016/j.ceramint.2019.07.157.

[343] P. Worathanakul, P. Mothong, and P. Engkawara, “Fe2O3-SiO2 nanocomposite derived from bagasse ash for Cr(VI) removal,” *J. Biobased Mater. Bioenergy*, vol. 7, no. 2, pp. 219–222, 2013, doi: 10.1166/jbmb.2013.1322.

[344] D. Dhaneswara, A. Tsania, J. F. Fatriansyah, and A. Federico, “Synthesis of Mesoporous Silica from Sugarcane Bagasse as Adsorbent for Colorants Using Cationic and Non-Ionic Surfactants,” *Int. J. Technol.*, vol. 15, no. 2, pp. 373–382, 2024, doi: 10.14716/ijtech.v15i2.6721.

[345] E. M. Papaslioti, P. Le Bouteiller, H. Carreira, J. M. Greneche, A. Fernandez-Martinez, and L. Charlet, “Immobilisation of contaminants by ‘green’-synthesized magnetite as a remediation approach to the phosphogypsum waste leachates model solution,” *J. Environ. Manage.*, vol. 341, 2023, doi: 10.1016/j.jenvman.2023.117997.

[346] S. Karina, A. W. Perdana, V. Prajaputra, N. Isnaini, P. H. Nuufus, and A. Bismi, “Silica-Magnetite Composite as an Eco-Friendly Adsorbent for Aqueous Tetracycline Removal – Kinetic and Isotherm Studies,” *Ecol. Eng. Environ. Technol.*, vol. 25, no. 1, pp. 82–92, 2024, doi: 10.12912/27197050/174225.

[347] X. Wang, D. Li, R. Bai, S. Liu, C. Yan, and J. Zhang, “Evolution of the pore structure of pumice aggregate concrete and the effect on compressive strength,” *Rev. Adv. Mater. Sci.*, vol. 62, no. 1, 2023, doi: 10.1515/rams-2023-0112.

[348] L. A. September, N. Kheswa, N. S. Seroka, and L. Khotseng, “Green synthesis of silica and silicon from agricultural residue sugarcane bagasse ash - a mini review,” *RSC Adv.*, vol. 13, no. 2, pp. 1370–1380, 2023, doi: 10.1039/d2ra07490g.

[349] G. Tsegaye, Z. Kiflie, T. H. Mekonnen, and M. Jida, “Synthesis and characterization of coffee husk extract (CHE)-capped Fe3O4/PU/ZnO nanocomposites with antimicrobial activity,” *Biomass Convers. Biorefinery*, no. 0123456789, 2024, doi: 10.1007/s13399-024-05918-2.

[350] E. Akhayere, A. Vaseashta, and D. Kavaz, “Novel magnetic nano silica synthesis using barley husk waste for removing petroleum from polluted water for environmental sustainability,” *Sustain.*, vol. 12, no. 24, pp. 1–16, 2020, doi: 10.3390/su122410646.

[351] J. A. Flood-Garibay and M. A. Méndez-Rojas, “Synthesis and characterization of magnetic wrinkled mesoporous silica nanocomposites containing Fe3O4 or CoFe2O4 nanoparticles for potential biomedical applications,” *Colloids Surfaces A Physicochem. Eng. Asp.*, vol. 615, no. January, 2021, doi: 10.1016/j.colsurfa.2021.126236.

[352] N. Meky, E. Salama, M. F. Soliman, S. G. Naeem, M. Ossman, and M. Elsayed, “Synthesis of Nano-silica Oxide for Heavy Metal Decontamination from Aqueous Solutions,” *Water, Air, Soil Pollut.*, vol. 235, no. 2, pp. 1–23, 2024, doi: 10.1007/s11270-024-06944-6.

[353] E. D. Revellame, D. L. Fortela, W. Sharp, R. Hernandez, and M. E. Zappi, “Adsorption kinetic modeling using pseudo-first order and pseudo-second order rate laws: A review,” *Clean. Eng. Technol.*, vol. 1, no. October, p. 100032, 2020, doi: 10.1016/j.clet.2020.100032.

[354] S. Mustapha, D. T. Shuaib, M. M. Ndamitso, M. B. Etsuyankpa, and A. Sumaila, “Adsorption isotherm, kinetic and thermodynamic studies for the removal of Pb(II), Cd(II), Zn(II) and Cu(II) ions from aqueous solutions using Albizia lebbeck pods,” *Appl. Water Sci.*, vol. 9, no. 6, pp. 1–11, 2019, doi: 10.1007/s13201-019-1021-x.

[355] A. Tebeje, Z. Worku, T. T. I. Nkambule, and J. Fito, “Adsorption of chemical oxygen demand from textile industrial wastewater through locally prepared bentonite adsorbent,” *Int. J. Environ. Sci. Technol.*, vol. 19, no. 3, pp. 1893–1906, 2022, doi: 10.1007/s13762-021-03230-4.

[356] S. Kalam, S. A. Abu-Khamsin, M. S. Kamal, and S. Patil, “Surfactant Adsorption Isotherms: A Review,” *ACS Omega*, vol. 6, no. 48, pp. 32342–32348, 2021, doi: 10.1021/acsomega.1c04661.

[357] S. Shamohammadi, M. Khajeh, R. Fattahi, and M. Kadkhodahosseini, “Introducing the new model of chemical adsorption for heavy metals by Jacobi activated carbon adsorbents, Iranian

activated carbon and blowy sand," *Case Stud. Chem. Environ. Eng.*, vol. 6, no. June, p. 100220, 2022, doi: 10.1016/j.cscee.2022.100220.

[358] R. Seyoum, B. B. Tesfamariam, D. M. Andoshe, A. Algahtani, G. M. S. Ahmed, and V. Tirth, "Investigation on control burned of bagasse ash on the properties of bagasse ash-blended mortars," *Materials (Basel).*, vol. 14, no. 17, 2021, doi: 10.3390/ma14174991.

[359] P. Chindaprasirt and U. Rattanasak, "Eco-production of silica from sugarcane bagasse ash for use as a photochromic pigment filler," *Sci. Rep.*, vol. 10, no. 1, pp. 1–8, 2020, doi: 10.1038/s41598-020-66885-y.

[360] S. P. Singh and N. Endley, *Fabrication of nano-silica from agricultural residue and their application*. INC, 2020. doi: 10.1016/B978-0-12-817852-2.00005-6.

[361] W. K. Setiawan and K. Y. Chiang, "Crop Residues as Potential Sustainable Precursors for Developing Silica Materials: A Review," *Waste and Biomass Valorization*, vol. 12, no. 5, pp. 2207–2236, 2021, doi: 10.1007/s12649-020-01126-x.

[362] Munasir, A. S. Dewanto, A. Yulianingsih, and I. K. F. Saadah, "Composites of Fe3O4/SiO2 from Natural Material Synthesized by Co-Precipitation Method," *IOP Conf. Ser. Mater. Sci. Eng.*, vol. 202, no. 1, 2017, doi: 10.1088/1757-899X/202/1/012057.

[363] N. S. Seroka, R. Taziwa, and L. Khotseng, "Green Synthesis of Crystalline Silica from Sugarcane Bagasse Ash: Physico-Chemical Properties," *Nanomaterials*, vol. 12, no. 13, 2022, doi: 10.3390/nano12132184.

[364] P. Wongsa, P. Phatikulrungsun, and S. Prathumthong, "FT-IR characteristics, phenolic profiles and inhibitory potential against digestive enzymes of 25 herbal infusions," *Sci. Rep.*, vol. 12, no. 1, pp. 1–11, 2022, doi: 10.1038/s41598-022-10669-z.

[365] R. Kamila, Ridwan, M. P. M. Akhir, A. Patriati, and A. Insani, "Synthesis of silica particles through conventional sol-gel and sonochemistry methods and the effect of catalyst, water concentration and sample environment to the particle size," *J. Phys. Conf. Ser.*, vol. 2193, no. 1, 2022, doi: 10.1088/1742-6596/2193/1/012044.

[366] S. Steven, E. Restiawaty, and Y. Bindar, "Routes for energy and bio-silica production from rice husk: A comprehensive review and emerging prospect," *Renew. Sustain. Energy Rev.*,

vol. 149, no. May 2020, p. 111329, 2021, doi: 10.1016/j.rser.2021.111329.

[367] K. Panwar, M. Jassal, and A. K. Agrawal, “In situ synthesis of Ag-SiO2Janus particles with epoxy functionality for textile applications,” *Particuology*, vol. 19, pp. 107–112, 2015, doi: 10.1016/j.partic.2014.06.007.

[368] A. Sadat and I. J. Joye, “Peak fitting applied to fourier transform infrared and raman spectroscopic analysis of proteins,” *Appl. Sci.*, vol. 10, no. 17, 2020, doi: 10.3390/app10175918.

[369] D. A. de Freitas, J. A. Barbosa, G. Labuto, R. C. F. Nocelli, and E. N. V. M. Carrilho, “Removal of the pesticide thiamethoxam from sugarcane juice by magnetic nanomodified activated carbon,” *Environ. Sci. Pollut. Res.*, vol. 29, no. 53, pp. 79855–79865, 2022, doi: 10.1007/s11356-021-18484-1.

[370] L. Khouchaf, K. Boulahya, P. P. Das, S. Nicolopoulos, V. K. Kis, and J. L. Lábár, “Study of the microstructure of amorphous silica nanostructures using high-resolution electron microscopy, electron energy loss spectroscopy, X-ray powder diffraction, and electron pair distribution function,” *Materials (Basel).*, vol. 13, no. 19, pp. 1–14, 2020, doi: 10.3390/ma13194393.

[371] Munasir, A. S. Dewanto, D. H. Kusumawati, N. P. Putri, A. Yulianingsih, and I. K. F. Sa’Adah, “Structure Analysis of Fe3O4@SiO2 Core Shells Prepared from Amorphous and Crystalline SiO2 Particles,” *IOP Conf. Ser. Mater. Sci. Eng.*, vol. 367, no. 1, 2018, doi: 10.1088/1757-899X/367/1/012010.

[372] D. Chen, T. Awut, B. Liu, Y. Ma, T. Wang, and I. Nurulla, “Functionalized magnetic Fe3O4 nanoparticles for removal of heavy metal ions from aqueous solutions,” *E-Polymers*, vol. 16, no. 4, pp. 313–322, 2016, doi: 10.1515/epoly-2016-0043.

[373] N. Sheth, D. Ngo, J. Banerjee, Y. Zhou, C. G. Pantano, and S. H. Kim, “Probing Hydrogen-Bonding Interactions of Water Molecules Adsorbed on Silica, Sodium Calcium Silicate, and Calcium Aluminosilicate Glasses,” *J. Phys. Chem. C*, vol. 122, no. 31, pp. 17792–17801, 2018, doi: 10.1021/acs.jpcc.8b04233.

[374] N. Wei, M. X. Wei, B. H. Huang, X. F. Guo, and H. Wang, “One-pot facile synthesis of green-emitting fluorescent silicon quantum dots for the highly selective and sensitive

detection of nitrite in food samples," *Dye. Pigment.*, vol. 184, no. March 2020, p. 108848, 2021, doi: 10.1016/j.dyepig.2020.108848.

[375] T. Liu, Y. Pang, X. Xie, W. Qi, and Y. Wu, "Synthesis of microporous Ni/NiO nanoparticles with enhanced microwave absorption properties," *J. Alloys Compd.*, vol. 667, pp. 287–296, 2016, doi: 10.1016/j.jallcom.2016.01.175.

[376] K. Faaliyan, H. Abdoos, E. Borhani, and S. S. S. Afghahi, "Magnetite-silica nanoparticles with core-shell structure: single-step synthesis, characterization and magnetic behavior," *J. Sol-Gel Sci. Technol.*, vol. 88, no. 3, pp. 609–617, 2018, doi: 10.1007/s10971-018-4847-z.

[377] O. Kapusta, A. Zeleňáková, P. Hrubovčák, V. Girman, and V. Zeleňák, "Fe 2 O 3 and Gd 2 O 3 Nanoparticles Embedded in Mesoporous Silica : Magnetic Properties Comparison," vol. 131, no. 4, pp. 860–862, 2017, doi: 10.12693/APhysPolA.131.860.

[378] E. N. Bakatula, D. Richard, C. M. Neculita, and G. J. Zagury, "Determination of point of zero charge of natural organic materials," 2018.

[379] A. Mahtabani, I. Rytöluoto, R. Anyszka, X. He, E. Saarimäki, and K. Lahti, "On the Silica Surface Modification and Its Effect on Charge Trapping and Transport in PP-Based Dielectric Nanocomposites," *ACS Appl. Polym. Mater.*, vol. 2, no. 8, pp. 3148–3160, 2020, doi: 10.1021/acsapm.0c00349.

[380] H. Tabasi, M. T. H. Mosavian, M. Darroudi, M. Khazaei, A. Hashemzadeh, and Z. Sabouri, "Synthesis and characterization of amine-functionalized Fe3O4/Mesoporous Silica Nanoparticles (MSNs) as potential nanocarriers in drug delivery systems," *J. Porous Mater.*, vol. 29, no. 6, pp. 1817–1828, 2022, doi: 10.1007/s10934-022-01259-5.

[381] S. Wonorahardjo, F. Fajaroh, R. Joharmawan, N. Nazriati, and E. Budiasih, "Cadmium and lead ions adsorption on magnetite, silica, alumina, and cellulosic materials," *Sci. Rep.*, vol. 13, no. 1, pp. 1–15, 2023, doi: 10.1038/s41598-023-30893-5.

[382] S. Beisl, R. Herrera Díaz, J. Maroušek, A. Maroušková, and R. Periakaruppan, "Silica Nanoparticles from Coir Pith Synthesized by Acidic Sol-Gel Method Improve Germination Economics," *Polymers (Basel).*, vol. 14, no. 2, p. 266, 2022, [Online]. Available: https://doi.org/10.3390/polym14020266

[383] L. Lemma, Z. Kiflie, and S. K. Kassahun, “Adsorption of Pb2+ and Cd2+ on the l-cysteine-functionalized graphene oxide/chitosan/polyvinyl alcohol hydrogel: Kinetic, isotherm, and thermodynamic study,” *Remediation*, vol. 33, no. 3, pp. 233–248, 2023, doi: 10.1002/rem.21754.

[384] S. C. Ma, Z. G. Wang, J. L. Zhang, D. H. Sun, and G. X. Liu, “Detection analysis of surface hydroxyl active sites and simulation calculation of the surface dissociation constants of aqueous diatomite suspensions,” *Appl. Surf. Sci.*, vol. 327, pp. 453–461, 2015, doi: 10.1016/j.apsusc.2014.12.006.

[385] A. L. Obsa, N. T. Shibeshi, E. Mulugeta, and G. A. Workeneh, “Bentonite/amino-functionalized cellulose composite as effective adsorbent for removal of lead: Kinetic and isotherm studies,” *Results Eng.*, vol. 21, no. November 2023, p. 101756, 2024, doi: 10.1016/j.rineng.2024.101756.

[386] I. H. Ifijen, A. B. Itua, M. Maliki, C. O. Ize-Iyamu, and S. O. Omorogbe, “The removal of nickel and lead ions from aqueous solutions using green synthesized silica microparticles,” *Heliyon*, vol. 6, no. 9, 2020, doi: 10.1016/j.heliyon.2020.e04907.

[387] J. Li, X. Dong, X. Liu, X. Xu, and W. Duan, “Comparative Study on the Adsorption Characteristics of Heavy Metal Ions by Activated Carbon and Selected Natural Adsorbents,” *Sustain.*, vol. 14, no. 23, 2022, doi: 10.3390/su142315579.

[388] A. K. Kushwaha, N. Gupta, and M. C. Chattopadhyaya, “Adsorption behavior of lead onto a new class of functionalized silica gel,” *Arab. J. Chem.*, vol. 10, pp. S81–S89, 2017, doi: 10.1016/j.arabjc.2012.06.010.

[389] Q. Li, W. Shi, and Q. Yang, “Polarization induced covalent bonding: A new force of heavy metal adsorption on charged particle surface,” *J. Hazard. Mater.*, vol. 412, no. December 2020, p. 125168, 2021, doi: 10.1016/j.jhazmat.2021.125168.

[390] E. Lemma, Z. Kiflie, and S. K. Kassahun, “Adsorption of Cr (VI) ion from aqueous solution on acrylamide–grafted starch (Coccinia abyssinicca)–PVA/PVP/chitosan/graphene oxide blended hydrogel: isotherms, kinetics, and thermodynamics studies,” *Sep. Sci. Technol.*, vol. 58, no. 2, pp. 241–256, 2023, doi: 10.1080/01496395.2022.2106441.

[391] N. Kasera, P. Kolar, and S. G. Hall, “Nitrogen-doped biochars as adsorbents for mitigation of

heavy metals and organics from water: a review," *Biochar*, vol. 4, no. 1, 2022, doi: 10.1007/s42773-022-00145-2.

[392] D. Brahma and H. Saikia, "Synthesis of ZrO2/MgAl-LDH composites and evaluation of its isotherm, kinetics and thermodynamic properties in the adsorption of congo red dye," *Chem. Thermodyn. Therm. Anal.*, vol. 7, no. April, p. 100067, 2022, doi: 10.1016/j.ctta.2022.100067.

[393] F. Togue Kamga, "Modeling adsorption mechanism of paraquat onto Ayous (Triplochiton scleroxylon) wood sawdust," *Appl. Water Sci.*, vol. 9, no. 1, pp. 1–7, 2019, doi: 10.1007/s13201-018-0879-3.

[394] O. D. Agboola and N. U. Benson, "Physisorption and Chemisorption Mechanisms Influencing Micro (Nano) Plastics-Organic Chemical Contaminants Interactions: A Review," *Front. Environ. Sci.*, vol. 9, no. May, pp. 1–27, 2021, doi: 10.3389/fenvs.2021.678574.

[395] S. Tamjidi, B. K. Moghadas, H. Esmaeili, F. Shakerian Khoo, G. Gholami, and M. Ghasemi, "Improving the surface properties of adsorbents by surfactants and their role in the removal of toxic metals from wastewater: A review study," *Process Saf. Environ. Prot.*, vol. 148, pp. 775–795, 2021, doi: 10.1016/j.psep.2021.02.003.

[396] O. Uygun, A. Murat, and G. Ö. Çakal, "Magnetic sepiolite/iron(III) oxide composite for the adsorption of lead(II) ions from aqueous solutions," *Clay Miner.*, vol. 58, no. 3, pp. 267–279, 2023, doi: 10.1180/clm.2023.24.

[397] P. B. Hassan, R. O. Rasheed, and K. Zargoosh, "Cadmium and Lead Removal from Aqueous Solution Using Magnetite Nanoparticles Biofabricated from Portulaca oleracea Leaf Extract," *J. Nanomater.*, vol. 2022, 2022, doi: 10.1155/2022/1024554.

[398] A. Lolasa, N. T. Shibeshi, and E. Mulugeta, "A green composite of sodium carboxymethyl cellulose and amino-decorated cellulose reinforced with modified bentonite for removal of lead (II): Kinetics and isotherm studies," *Mater. Today Commun.*, vol. 41, no. April, p. 110412, 2024, doi: 10.1016/j.mtcomm.2024.110412.

[399] M. Kajeiou *et al.*, "Competitive and non-competitive zinc, copper and lead biosorption from aqueous solutions onto flax fibers," *Chemosphere*, vol. 260, no. 33, 2020, doi: 10.1016/j.chemosphere.2020.127505.

[400] J. Podgorski and M. Berg, “Global analysis and prediction of fluoride in groundwater,” *Nat. Commun.*, vol. 13, no. 1, pp. 1–9, 2022, doi: 10.1038/s41467-022-31940-x.

[401] S. M. R. Bonetto, C. Caselle, D. A. de Luca, and M. Lasagna, “Groundwater Resources in the Main Ethiopian Rift Valley: An Overview for a Sustainable Development,” *Sustain.*, vol. 13, no. 3, pp. 1–15, 2021, doi: 10.3390/su13031347.

[402] T. A. Hulluka, S. K. Balcha, B. Yohannes, A. Bantider, and A. Negatu, “Review: Groundwater research in the Ethiopian Rift Valley Lakes region,” *Front. Water*, vol. 5, 2023, doi: 10.3389/frwa.2023.819568.

[403] S. Guth, S. Hüser, A. Roth, G. Degen, and P. Diel, *Toxicity of fluoride: critical evaluation of evidence for human developmental neurotoxicity in epidemiological studies, animal experiments and in vitro analyses*, vol. 94, no. 5. Springer Berlin Heidelberg, 2020. doi: 10.1007/s00204-020-02725-2.

[404] Y. Mathewos, B. Abate, M. Dadi, and M. Mathewos, “Evaluation of the groundwater prospective zone by coupling hydro-meteorological and geospatial evidence in Wabe River Catchment Omo Gibe River Basin, Ethiopia,” *Water Cycle*, vol. 5, no. October 2023, pp. 37–58, 2024, doi: 10.1016/j.watcyc.2024.01.002.

[405] J. B. Vincent, “New evidence against chromium as an essential trace element,” *J. Nutr.*, vol. 147, no. 12, pp. 2212–2219, 2017, doi: 10.3945/jn.117.255901.

[406] A. Bakshi and A. K. Panigrahi, “A comprehensive review on chromium induced alterations in fresh water fishes,” *Toxicol. Reports*, vol. 5, no. March, pp. 440–447, 2018, doi: 10.1016/j.toxrep.2018.03.007.

[407] B. Ren, Y. Jin, L. zhao, C. Cui, and X. Song, “Enhanced Cr(VI) adsorption using chemically modified dormant Aspergillus niger spores: Process and mechanisms,” *J. Environ. Chem. Eng.*, vol. 10, no. 1, p. 106955, 2022, doi: 10.1016/j.jece.2021.106955.

[408] S. Rezania, N. Darajeh, P. F. Rupani, A. Mojiri, H. Kamyab, and M. Taghavijeloudar, “Recent Advances in the Adsorption of Different Pollutants from Wastewater Using Carbon-Based and Metal-Oxide Nanoparticles,” *Appl. Sci.*, vol. 14, no. 24, 2024, doi: 10.3390/app142411492.

[409] Z. Alhalili, “Metal Oxides Nanoparticles: General Structural Description, Chemical, Physical,

and Biological Synthesis Methods, Role in Pesticides and Heavy Metal Removal through Wastewater Treatment," *Molecules*, vol. 28, no. 7, 2023, doi: 10.3390/molecules28073086.

[410] A. M. Aldawsari, I. H. Alsohaimi, and H. M. A. Hassan, "Silica-integrated chemically modified human hair waste: A novel nanocomposite for efficient removal of methylene blue dye from water," *Inorg. Chem. Commun.*, vol. 172, no. August 2024, p. 113747, 2025, doi: 10.1016/j.inoche.2024.113747.

[411] I. Hotan Alsohaimi, M. S. Alhumaimess, A. Abdullah Alqadami, G. Tharwi Alshammari, and R. Fawzy Al-Olaimi, "Adsorptive performance of aminonaphthalenesulfonic acid modified magnetic-graphene oxide for methylene blue dye: Mechanism, isotherm and thermodynamic studies," *Inorg. Chem. Commun.*, vol. 147, no. July 2022, p. 110261, 2023, doi: 10.1016/j.inoche.2022.110261.

[412] P. V. Mane, R. M. Rego, P. L. Yap, D. Losic, and M. D. Kurkuri, *Unveiling cutting-edge advances in high surface area porous materials for the efficient removal of toxic metal ions from water*, vol. 146, no. June. Elsevier Ltd, 2024. doi: 10.1016/j.pmatsci.2024.101314.

[413] H. C. S. Perera, V. Gurunanthanan, A. Singh, M. M. M. G. P. G. Mantilaka, G. Das, and S. Arya, "Magnesium oxide (MgO) nanoadsorbents in wastewater treatment: A comprehensive review," *J. Magnes. Alloy.*, vol. 12, no. 5, pp. 1709–1773, 2024, doi: 10.1016/j.jma.2024.05.003.

[414] I. H. Alsohaimi, M. S. Alhumaimess, H. M. A. Hassan, M. Reda, and A. M. Aldawsari, "Chitosan Polymer Functionalized-Activated Carbon/Montmorillonite Composite for the Potential Removal of Lead Ions from Wastewater," *Polymers (Basel).*, vol. 15, no. 9, 2023, doi: 10.3390/polym15092188.

[415] V. Phouthavong, R. Yan, S. Nijpanich, T. Hagio, and R. Ichino, "Magnetic Adsorbents for Wastewater Treatment: Advancements in Their Synthesis Methods," *Materials (Basel).*, vol. 15, no. 3, 2022, doi: 10.3390/ma15031053.

[416] G. Tsegaye, Z. Kiflie, J. Fito Nure, and A. D. Ambaye, "Magnetite-based pumice silica nanocomposite for lead adsorption from aqueous solution: The green synthesis approach," *Chinese J. Chem. Eng.*, vol. 82, pp. 281–293, 2025, doi: 10.1016/j.cjche.2025.01.013.

[417] I. H. Alsohaimi, "Novel Synthesis of Polystyrenesulfonate@AC Based on Olive Tree Leaves

Biomass for the Photo-Degradation of Methylene Blue from Aqueous Solution," *Polymers (Basel).*, vol. 16, no. 23, 2024, doi: 10.3390/polym16233321.

[418] S. A. Kumar *et al.*, "Facile green synthesis of magnesium oxide nanoparticles using tea (Camellia sinensis) extract for efficient photocatalytic degradation of methylene blue dye," *Environ. Technol. Innov.*, vol. 28, p. 102746, 2022, doi: 10.1016/j.eti.2022.102746.

[419] B. Y. Hirphaye, N. B. Bonka, A. M. Tura, and G. M. Fanta, "Biosynthesis of magnesium oxide nanoparticles using Hagenia abyssinica female flower aqueous extract for characterization and antibacterial activity," *Appl. Water Sci.*, vol. 13, no. 9, pp. 1–12, 2023, doi: 10.1007/s13201-023-01987-2.

[420] S. N. Ul Ain, M. S. Khan, N. Riaz, A. Khan, and A. Sarwar, "Surface-Functionalized Magnetic Silica-Malachite Tricomposite (Fe-M-Si tricomposite): A Promising Adsorbent for the Removal of Cypermethrin," *ACS Omega*, vol. 9, no. 12, pp. 13803–13817, 2024, doi: 10.1021/acsomega.3c08419.

[421] S. Li, Y. Zhang, S. Qiao, and J. Zhou, "MgO coated magnetic Fe3O4@SiO2 nanoparticles with fast and efficient phosphorus removal performance and excellent pH stability," *Chemosphere*, vol. 307, no. May, p. 135972, 2022, doi: 10.1016/j.chemosphere.2022.135972.

[422] D. Prabu, P. S. Kumar, S. Indraganti, S. Sathish, J. A. Kumar, and K. V. Anand, "One-Step Fabrication of Amino-Functionalized Fe3O4@SiO2 Core-Shell Magnetic Nanoparticles as a Potential Novel Platform for Removal of Cadmium (II) from Aqueous Solution," *Sustain.*, vol. 14, no. 4, pp. 1–21, 2022, doi: 10.3390/su14042290.

[423] S. T. Vielee, W. J. Buchanan, S. H. Roof, R. Kahloon, and E. Evans, "Chromium Selectively Accumulates in the Rat Hippocampus after 90 Days of Exposure to Cr(VI) in Drinking Water and Induces Age- and Sex-Dependent Metal Dyshomeostasis," *Toxics*, vol. 12, no. 10, 2024, doi: 10.3390/toxics12100722.

[424] R. J. Singh, C. E. Martin, D. Barr, and R. J. Rosengren, "Cucumber peel bead biosorbent for multi-ion decontamination of drinking water collected from a mine region in New Zealand," *Environ. Technol. (United Kingdom)*, vol. 42, no. 16, pp. 2461–2477, 2021, doi: 10.1080/09593330.2019.1703824.

[425] A. Muhammad, A. ul Haq Ali Shah, and S. Bilal, "Effective adsorption of hexavalent

chromium and divalent nickel ions from water through polyaniline, iron oxide, and their composites," *Appl. Sci.*, vol. 10, no. 8, 2020, doi: 10.3390/APP10082882.

[426] R. Zangi, "Breakdown of Langmuir Adsorption Isotherm in Small Closed Systems," *Langmuir*, 2023, doi: 10.1021/acs.langmuir.3c03894.

[427] M. Anas, T. Rafique, F. Soomro, and S. N. Ali, "Fluoride removal from drinking water using alumina adsorbent: Batch and column experiments and working efficiency of engineered pilot plant," *Desalin. Water Treat.*, vol. 221, pp. 94–104, 2021, doi: 10.5004/dwt.2021.26900.

[428] T. Turki, A. Hamdouni, and A. Enesca, "Fluoride Adsorption from Aqueous Solution by Modified Zeolite—Kinetic and Isotherm Studies," *Molecules*, vol. 28, no. 10, 2023, doi: 10.3390/molecules28104076.

[429] W. M. Saod, I. W. Oliver, D. F. Thompson, S. Holborn, A. Contini, and V. Zholobenko, "Magnesium oxide loaded mesoporous silica: Synthesis, characterisation and use in removing lead and cadmium from water supplies," *Environ. Nanotechnology, Monit. Manag.*, vol. 20, no. December 2022, p. 100817, 2023, doi: 10.1016/j.enmm.2023.100817.

[430] R. Ellerbrock, M. Stein, and J. Schaller, "Comparing amorphous silica, short-range-ordered silicates and silicic acid species by FTIR," *Sci. Rep.*, vol. 12, no. 1, pp. 1–8, 2022, doi: 10.1038/s41598-022-15882-4.

[431] P. B. Angon, M. S. Islam, S. KC, A. Das, and N. Anjum, "Sources, effects and present perspectives of heavy metals contamination: Soil, plants and human food chain," *Heliyon*, vol. 10, no. 7, p. e28357, 2024, doi: 10.1016/j.heliyon.2024.e28357.

[432] S. Hozhabr Araghi and M. H. Entezari, "Amino-functionalized silica magnetite nanoparticles for the simultaneous removal of pollutants from aqueous solution," *Appl. Surf. Sci.*, vol. 333, pp. 68–77, 2015, doi: 10.1016/j.apsusc.2015.01.211.

[433] S. Kiran, A. Ashraf, G. Afzal, S. Abrar, M. Rahmat, and S. Asif, "Green synthesis of magnesium oxide nanoparticles using leaves of Iresine herbstii for remediation of reactive brown 9 dye," *Glob. Nest J.*, vol. 24, no. 2, pp. 291–296, 2022, doi: 10.30955/gnj.003929.

[434] M. Namvar-Mahboub, E. Khodeir, M. Bahadori, and S. M. Mahdizadeh, "Preparation of magnetic MgO/Fe3O4 via the green method for competitive removal of Pb and Cd from

aqueous solution," *Colloids Surfaces A Physicochem. Eng. Asp.*, vol. 589, p. 124419, 2020, doi: 10.1016/j.colsurfa.2020.124419.

[435] E. H. Jang, S. P. Pack, I. Kim, and S. Chung, "A systematic study of hexavalent chromium adsorption and removal from aqueous environments using chemically functionalized amorphous and mesoporous silica nanoparticles," *Sci. Rep.*, vol. 10, no. 1, pp. 1–20, 2020, doi: 10.1038/s41598-020-61505-1.

[436] M. T. Mazibuko, S. C. Onwubu, P. S. Mdluli, V. Paul, M. C. Teboho, and M. Thabang, "Amine-functionalized cellulose-silica composites for the remediation of hexavalent chromium (Cr IV) in contaminated water," *Results Chem.*, vol. 11, no. August, p. 101796, 2024, doi: 10.1016/j.rechem.2024.101796.

[437] W. Sheng *et al.*, "Amine-functionalized magnetic mesoporous silica nanoparticles for DNA separation," *Appl. Surf. Sci.*, vol. 387, pp. 1116–1124, 2016, doi: 10.1016/j.apsusc.2016.07.061.

[438] A. Ul, H. Khan, Y. Liu, R. Naidu, and C. Fang, "Interactions between zinc oxide nanoparticles and hexabromocyclododecane in simulated waters," *Environ. Technol. Innov.*, vol. 24, 2021.

[439] N. Rahman and M. Nasir, "Facile synthesis of thiosalicylic acid functionalized silica gel for effective removal of Cr(III): Equilibrium modeling, kinetic and thermodynamic studies," *Environ. Nanotechnology, Monit. Manag.*, vol. 14, no. May, p. 100353, 2020, doi: 10.1016/j.enmm.2020.100353.

[440] R. Satoh, S. Honma, H. Arafune, R. Shomura, T. Kamijo, and T. Morinaga, "In situ surface-initiated atom-transfer radical polymerization utilizing the nonvolatile nature of ionic liquids: A first attempt," *Polymers (Basel).*, vol. 13, no. 1, pp. 1–11, 2021, doi: 10.3390/polym13010061.

[441] A. Chiavola, E. D'amato, and C. Di Marcantonio, "Comparison of Adsorptive Removal of Fluoride from Water by Different Adsorbents under Laboratory and Real Conditions," *Water (Switzerland)*, vol. 14, no. 9, 2022, doi: 10.3390/w14091423.

[442] J. Qi, B. Li, P. Zhou, and X. Su, "Study on adsorption of hexavalent chromium by composite material prepared from iron-based solid wastes," *Sci. Rep.*, vol. 13, no. 1, pp. 1–12, 2023, doi: 10.1038/s41598-023-27414-9.

[443] Y. Alvarez-Galvan, B. Minofar, Z. Futera, M. Francoeur, and C. Jean-Marius, “Adsorption of Hexavalent Chromium Using Activated Carbon Produced from Sargassum ssp.: Comparison between Lab Experiments and Molecular Dynamics Simulations,” *Molecules*, vol. 27, no. 18, 2022, doi: 10.3390/molecules27186040.

[444] N. Nabbou, M. Belhachemi, M. Boumelik, T. Merzougui, D. Lahcene, and Y. Harek, “Removal of fluoride from groundwater using natural clay (kaolinite): Optimization of adsorption conditions,” *Comptes Rendus Chim.*, vol. 22, no. 2–3, pp. 105–112, 2019, doi: 10.1016/j.crci.2018.09.010.

[445] A. A. Ayalew, “Comparative adsorptive performance of adsorbents developed from kaolin clay and limestone for de-fluoridation of groundwater,” *South African J. Chem. Eng.*, vol. 44, no. October 2022, pp. 1–13, 2023, doi: 10.1016/j.sajce.2022.11.002.

[446] M. Hashemkhani, M. Rezvani Ghalhari, P. Bashardoust, S. S. Hosseini, A. Mesdaghinia, and A. H. Mahvi, “Fluoride removal from aqueous solution via environmentally friendly adsorbent derived from seashell,” *Sci. Rep.*, vol. 12, no. 1, pp. 1–13, 2022, doi: 10.1038/s41598-022-13756-3.

[447] P. K. Raul, R. R. Devi, I. M. Umlong, S. Banerjee, L. Singh, and M. Purkait, “Removal of fluoride from water using iron oxide-hydroxide nanoparticles,” *J. Nanosci. Nanotechnol.*, vol. 12, no. 5, pp. 3922–3930, 2012, doi: 10.1166/jnn.2012.5870.

[448] R. Araga, S. Soni, and C. S. Sharma, “Fluoride adsorption from aqueous solution using activated carbon obtained from KOH-treated jamun (Syzygium cumini) seed,” *J. Environ. Chem. Eng.*, vol. 5, no. 6, pp. 5608–5616, 2017, doi: 10.1016/j.jece.2017.10.023.

[449] A. Sarwar *et al.*, “Iron oxide (Fe3o4)-supported sio2 magnetic nanocomposites for efficient adsorption of fluoride from drinking water: Synthesis, characterization, and adsorption isotherm analysis,” *Water (Switzerland)*, vol. 13, no. 11, 2021, doi: 10.3390/w13111514.

[450] A. Elyahyaoui *et al.*, “Adsorption of chromium (VI) on calcium phosphate: Mechanisms and stability constants of surface complexes,” *Appl. Sci.*, vol. 7, no. 3, pp. 1–14, 2017, doi: 10.3390/app7030222.

[451] J. Ulatowska, Ł. Stala, and I. Polowczyk, “Comparison of Cr(VI) adsorption using synthetic schwertmannite obtained by Fe3+ hydrolysis and Fe2+ oxidation: Kinetics, isotherms and

adsorption mechanism," *Int. J. Mol. Sci.*, vol. 22, no. 15, 2021, doi: 10.3390/ijms22158175.

[452] V. Iashin, T. Wirtanen, and J. E. Perea-Buceta, "Tetramethylammonium Fluoride: Fundamental Properties and Applications in C-F Bond-Forming Reactions and as a Base," *Catalysts*, vol. 12, no. 2, 2022, doi: 10.3390/catal12020233.

[453] M. Masuku, J. F. Nure, H. I. Atagana, N. Hlongwa, and T. T. I. Nkambule, "Advancing the development of nanocomposite adsorbent through zinc-doped nickel ferrite-pinecone biochar for removal of chromium (VI) from wastewater," *Sci. Total Environ.*, vol. 908, no. June 2023, p. 168136, 2024, doi: 10.1016/j.scitotenv.2023.168136.

[454] M. H. Dehghani, M. Farhang, M. Alimohammadi, M. Afsharnia, and G. Mckay, "Adsorptive removal of fluoride from water by activated carbon derived from CaCl2-modified Crocus sativus leaves: Equilibrium adsorption isotherms, optimization, and influence of anions," *Chem. Eng. Commun.*, vol. 205, no. 7, pp. 955–965, 2018, doi: 10.1080/00986445.2018.1423969.

[455] F. Masoudi and A. Naghizadeh, "Silica nanoparticles for the removal of fluoride from aqueous solution : equilibrium , isotherms , kinetics , and thermodynamics," *Desalin. Water Treat.*, vol. 137, pp. 125–133, 2019, doi: 10.5004/dwt.2019.23182.

[456] P. Pillai, S. Dharaskar, M. Shah, and R. Sultania, "Determination of fluoride removal using silica nano adsorbent modified by rice husk from water," *Groundw. Sustain. Dev.*, vol. 11, no. March, p. 100423, 2020, doi: 10.1016/j.gsd.2020.100423.

[457] P. Kiprono, J. Kiptoo, E. Nyawade, and E. Ngumba, "Iron functionalized silica particles as an ingenious sorbent for removal of fluoride from water," *Sci. Rep.*, vol. 13, no. 1, pp. 1–13, 2023, doi: 10.1038/s41598-023-34357-8.

[458] T. Akafu, A. Chimdi, and K. Gomoro, "Removal of Fluoride from Drinking Water by Sorption Using Diatomite Modified with Aluminum Hydroxide," *J. Anal. Methods Chem.*, vol. 2019, 2019, doi: 10.1155/2019/4831926.

[459] F. C. Çavuşoğlu, G. Özçelik, and Ş. S. Bayazit, "Removal of toxic Cr(VI) from aqueous medium with effective magnetic carbon-based nanocomposites," *Turkish J. Chem.*, vol. 47, no. 6, pp. 1479–1496, 2023, doi: 10.55730/1300-0527.3629.

[460] R. Chen, P. Wang, M. Li, F. Tian, and J. Xiao, “Removal of Cr(VI) by magnetic Fe/C crosslinked nanoparticle for water purification: Rapid contaminant removal property and mechanism of action,” *Water Sci. Technol.*, vol. 78, no. 10, pp. 2171–2182, 2018, doi: 10.2166/wst.2018.497.

[461] K. Modaresahmadi, A. P. Khodadoust, and J. Wescott, “Adsorption of Fluoride from Water Using Aluminum-Coated Silica Adsorbents: Comparison of Silica Sand and Microcrystalline Silica,” *Separations*, vol. 11, no. 4, 2024, doi: 10.3390/separations11040125.

[462] M. P. Mannzhi and J. N. Edokpayi, “Defluoridation through the utilization of unmodified precipitate derived from a mucilaginous agricultural plant material,” *Results Mater.*, vol. 26, no. April, p. 100719, 2025, doi: 10.1016/j.rinma.2025.100719.

[463] W. Guo, H. Lin, H. Zhu, M. Lei, and J. Feng, “Preparation and application of magnesium oxide nanoparticles for superiorly fluoride removal,” *J. Alloys Compd.*, vol. 960, p. 170935, Oct. 2023, doi: 10.1016/J.JALLCOM.2023.170935.

[464] K. Das, U. Sukul, J. S. Chen, R. K. Sharma, and P. Banerjee, “Transformative and sustainable insights of agricultural waste-based adsorbents for water defluoridation: Biosorption dynamics, economic viability, and spent adsorbent management,” *Heliyon*, vol. 10, no. 8, p. e29747, 2024, doi: 10.1016/j.heliyon.2024.e29747.

APPENDIX

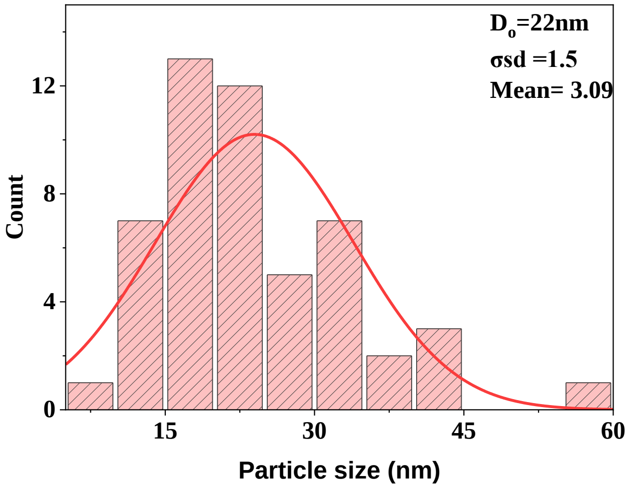

Fig. A 1. Particle size distributions of CHE capped ZnO NPs from SEM image J analysis

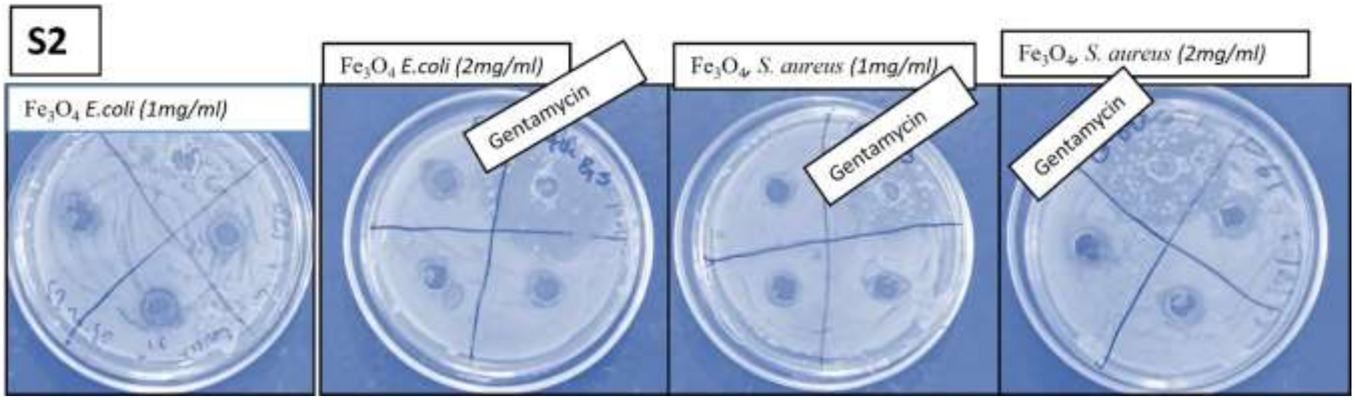

Fig. A2. Antimicrobial capacity of CHE capped Fe_3O_4 NPs

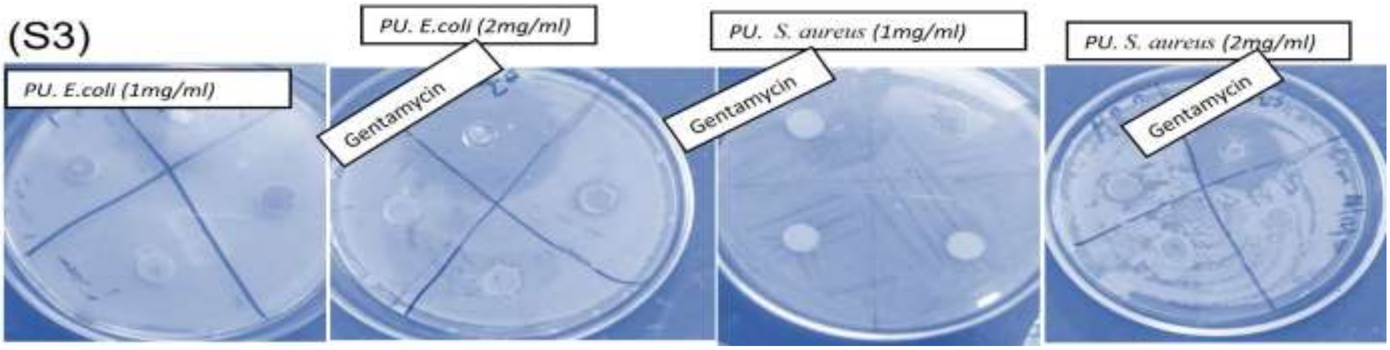

Fig. A 3. Antimicrobial capacity of PU